UNIVERSITÉ DE TOURS

ÉCOLE DOCTORALE : SSBCV

INSTITUT DE RECHERCHE SUR LA BIOLOGIE DE L'INSECTE

UNIVERSITY OF TWENTE

TWENTE GRADUATE SCHOOL

ROBOTICS AND MECHATRONICS

THÈSE présentée par :

Mourad JAFFAR-BANDJEE

soutenue le : **12 décembre 2019**

pour obtenir le grade de : **Docteur de l'université de Tours**

Discipline/ Spécialité : Biologie

Pheromone transport in multiscale pectinate antennae

Transfert de phéromone au sein des antennes pectinées multi-échelles

THÈSE dirigée par :

M. CASAS Jérôme	Professeur, Université de Tours
M. KRIJNEN Gijs	Professeur, University of Twente

RAPPORTEURS :

M. VAN LEEUWEN Johan	Professeur, Wageningen University & Research
M. RENOU Michel	Directeur de Recherche, INRA iEES Paris

JURY :

M. VENNER Kees (President)	Professeur, University of Twente
M. CASAS Jérôme	Professeur, Université de Tours
M. KRIJNEN Gijs	Professeur, University of Twente
M. VAN LEEUWEN Johan	Professeur, Wageningen University & Research
M. RENOU Michel	Directeur de Recherche, INRA iEES Paris
M. LEVY Frédéric	Directeur de Recherche, INRA Centre Val de Loire
M. GARDENIERS Han	Professeur, University of Twente

"Er zijn veel vlinders die ontkennen eerst rups te zijn geweest."

"There are many butterflies who deny having been a caterpillar first."

"Il y a beaucoup de papillons qui nient avoir été d'abord une chenille."

Gerd de Ley

Contents

1 Introduction **1**
- 1.1 Functional morphology . . . 1
- 1.2 Diversity of functions and shapes of antennae . . . 2
  - 1.2.1 Antennal shapes . . . 2
  - 1.2.2 Antenna diverse functions . . . 2
- 1.3 Insect olfaction is a major sense . . . 4
  - 1.3.1 Insect olfaction . . . 4
  - 1.3.2 Biological model: the pectinate antennae of *Samia cynthia* (Saturniidae) . . . 5
- 1.4 Olfaction is a physico-chemical transport process . . . 7
- 1.5 Objective of the thesis . . . 9

2 Introduction en français **11**
- 2.1 Morphologie fonctionnelle . . . 11
- 2.2 Diversité des fonctions et des formes d'antennes . . . 12
  - 2.2.1 Formes d'antennes . . . 12
  - 2.2.2 Diversité des fonctions des antennes . . . 13
- 2.3 L'olfaction est un sens majeur pour les insectes . . . 15
  - 2.3.1 L'olfaction chez les insectes . . . 15
  - 2.3.2 Modèle biologique : les antennes pectinées de *Samia cynthia* (Saturnidae) . . . 16
- 2.4 L'olfaction est un phénomène de transport physico-chimique . . . 16
- 2.5 Objectifs de la thèse . . . 20

3 Additive Manufacturing and Insect Science **23**
- 3.1 Abstract en Français . . . 23
- 3.2 Abstract . . . 23
- 3.3 Introduction . . . 24
- 3.4 Additive manufacturing . . . 24
- 3.5 Biomaterials and structure . . . 25
  - 3.5.1 Structural materials . . . 27

3.5.2 Architecture . . . 27
3.6 Bioinspired locomotion . . . 29
3.6.1 Actuators . . . 29
3.6.2 Bioinspired robots . . . 29
3.6.3 Flying robots . . . 29
3.7 Bioinspired sensors . . . 30
3.8 Discussion . . . 30
3.9 Conclusion . . . 31
3.10 Conflicts of interest . . . 31
3.11 Acknowledgements . . . 31
3.12 Interesting articles . . . 32

4 3D-Printing cylinders **33**
4.1 Résumé en Français . . . 33
4.2 Introduction . . . 33
4.3 3D-Printing of cylinders . . . 35
4.3.1 Materials and Methods . . . 35
4.3.2 Results . . . 37
4.3.3 Experimental observations . . . 38
4.4 Mechanical modelling of 3D printed cylinders . . . 43
4.4.1 Forces exerted on the cylinders in post-processing . . . 43
4.4.2 Longitudinal stress in homogeneous beams . . . 44
4.4.3 Longitudinal stress in lamellar beam . . . 46
4.4.4 Lamellar beam with bending and shear . . . 48
4.5 Models versus experimental data . . . 50
4.5.1 Model based indices . . . 50
4.5.2 Correction for the real shape of the cylinders . . . 51
4.5.3 Results: predictive value of model based indices . . . 53
4.6 Discussion . . . 56
4.7 Conclusion . . . 56

5 Leakiness of the macrostructure **59**
5.1 Résumé en français . . . 59
5.2 Introduction . . . 59
5.3 Materials and methods . . . 61
5.3.1 Real and surrogate antennae . . . 61
5.3.2 Flow measurements . . . 64
5.4 Results . . . 72
5.4.1 PIV measurements . . . 72
5.4.2 Fitting leakiness relationships . . . 76
5.5 Discussion . . . 77
5.5.1 Validity of the assumptions . . . 77
5.5.2 Similarity of the dynamics in different fluids . . . 77
5.5.3 Boundary layers superposition and its influence on leakiness 78
5.5.4 Flow capture ratio . . . 78

6 Mass capture model **83**
6.1 Résumé en Français . . . 83
6.2 Introduction . . . 83
6.3 Material and Methods . . . 85
6.3.1 Natural antennae . . . 85
6.3.2 Modeling mass transfer . . . 87
6.3.3 Experiments . . . 93
6.3.4 Combining the model and the PIV experiment . . . 98
6.4 Results . . . 100
6.5 Discussion . . . 103
6.5.1 Assumptions of the model . . . 103
6.5.2 The efficiency of the antenna is the product of two conflicting trade-offs . . . 105
6.5.3 Implications for the moth behavior and the antennal geometry 107
6.5.4 Geometry of antenna and flow dynamics determine capture efficiency . . . 108
6.6 Appendix . . . 110
6.6.1 Equivalent heat and mass transfer parameters . . . 110
6.6.2 Determination of the diffusive coefficient of the pheromones 112
6.6.3 Validity of the 2 dimensional assumption of the velocity field 114
6.6.4 Dependence of η_s on v_∞ . . . 114
6.6.5 Comparison of single cylinders either in a longitudinal or in a transversal flow . . . 115
6.6.6 Square and triangle distributions . . . 117
6.6.7 Gaussian odor pulse . . . 119
6.6.8 Extrapolation of the formula of Miyatake and Iwahita . . . 129

7 General Discussion **131**
7.1 Résumé en Français . . . 131
7.2 Introduction . . . 131
7.3 Multi-scale geometry . . . 132
7.4 Combining the two levels . . . 139
7.4.1 First method: the experimental approach . . . 139
7.4.2 Second method: the multiplicative method . . . 139
7.4.3 Third method: the equivalent cylinders . . . 142
7.4.4 Efficiency of the antenna . . . 148
7.4.5 Comparison with the previous models . . . 150
7.5 Functional morphology . . . 152
7.5.1 Pectinate or cylindrical antennae ? . . . 152
7.5.2 Orientation of the sensilla . . . 155
7.5.3 Efficiency, antennae surface and pheromone diffusive coefficient . . . 155
7.5.4 Comparison with other types of antennae . . . 158
7.6 Conclusion . . . 159

8 Abstract **179**

9 Abstract in French **181**

10 Abstract in Dutch **183**

11 Acknowledgments **185**

12 About the author **189**

List of Figures

1.1 Diversity of insect antennae (Reproduced from [1]) 3

1.2 Pectinate antenna of the male *Samia cynthia*. 6

1.3 Microstructure of the antenna of *Samia cynthia* composed of one ramus and the sensilla it supports. a: side view. b: cross section. The red arrow shows the direction of the airflow. 7

2.1 Diversité des antennes d'insectes (Reproduit à partir de [1]) 13

2.2 Antenne pectinée d'un mâle de l'espèce *Samia cynthia* 17

2.3 Microstructure de l'antenne de *Samia cynthia* composée d'un rami et des sensilles qu'il porte. a: vue de côté. b: section. La flèche rouge indique la direction du flux d'air. 18

3.1 Principle of Additive Manufacturing processes. a: 3D model of ant (Openscad v2015.03-2), b: Slicing of the 3D model (Openscad v2015.03-2), c: Layer-by-layer building process (Slic3r v1.2.9), d: Printed model. 25

3.2 Application of Additive Manufacturing to insect-inspired biomimetics. a: Dragonfly-inspired wing [2]; b: Honeybee-inspired needles [3]; c: Biomimetic spiderweb [4]; d: Micro air vehicle with insect-inspired wings [5]; e: Robot arm building a cocoon-like structure in a similar way as silkworm [6]; f: Artificial antenna structure inspired from moth [7]; g: Multifunction beetle-inspired leg [8]; h: Natural and artificial shells for hermit crab preference tests [9] . . 28

4.1 Attempt to fabricate cylinders with several 3D printers. 35

4.2 Distribution of the cylinders on the support ($D = 10$, $L = \frac{d}{L} = 30$) 36

4.3 Measurement of the cross section of the cylinders. The two directions used to measure the diameter are perpendicular. d_1 is the diameter measured in the horizontal direction, which is also the intersection between the cross section and the horizontal plane (shaded area). d_2 is the diameter in the perpendicular direction, which is also the direction of the building direction projected on the plane of the cross section. 37

4.4 Examples of cylinders after fabrication and post-processing steps. . 38

4.5 Relative length of cylinders of diameter $D = 5$ after fabrication for aspect ratio's $L = 10$, $L = 20$, $L = 30$ and $L = 50$. All cylinders were measured, including broken ones. 41

4.6 Relative length of cylinders of diameter $D = 10$ after fabrication for aspect ratio $L = 10$ and $L = 20$. All cylinders were measured, including broken ones. 41

4.7 Relative length of cylinders of diameter $D = 10$ after fabrication for aspect ratio $L = 30$ and $L = 50$. All cylinders were measured, including broken ones. 42

4.8 Diameters of cylinders with $D = 10$, $L = 20$ and $\alpha = 15^\circ$. (a) distal end of the cylinder showing a narrowing of the cross section which may be due to the layer-by-layer building process. (b) the focus plane is a slightly behind the distal end and the orientation of the layers are still visible on the sides of the cross section. (c) basal end of the cylinder showing the alteration of the cross section due to the cutting of the cylinder. (d) the focus plane is slightly behind the basal end to reveal an undisturbed cross section. 42

4.9 Homogeneous beam with a uniformly-distributed load 44

4.10 Orientation of the layers (red lines) in a part of the beam. The axis of the beam is the x-axis. $\sigma_{\max}$ is the maximum stress determined in the previous section. N is the component of the force normal to the plane of the layers and T is the force component tangential to the xy-plane (*i.e.* the shear-stress along the layer-interfaces). . . . 46

4.11 Curve of the cylinder depending on the position x 49

4.12 Left: displacement curves under increasing load as a function of x/L for α=10, 20, and 30°. Right: normalised tangential load T/P depending on x/L for the same angles. 50

4.13 Number of cylinders still intact after processing versus Index1 (top), Index2 (middle) and Index3 (bottom). Presentation is on a linear scale. 54

4.14 Number of cylinders still intact after processing versus Index1 (top), Index2 (middle) and Index3 (bottom). Presentation is on a logarithmic scale. 55

5.1 Illustration of an antenna of *Samia cynthia* and the 3D printed surrogate structure. In a. The structure composed of the flagellum and rami is visible. Note that the rami are not completely parallel and overlap at their tips. b. Focus on the tip of a ramus to reveal the sensilla. c. Simplified model of the gross morphology of the natural antenna. d. Picture of the actual printed surrogate structure (named Str_{50}). Like all of our 3D printed structures, this structure is scaled-up by a factor α=10 compared to the biological model. This model bears N_{rami}=2× 50 rami and has an effective surface S_{eff}=7,5 mm^2. 62

5.2 Experimental setup and definition of variables. This velocity field was obtained for the structure Str_{50} at a velocity of $3.21\,\text{mm}\,\text{s}^{-1}$ (equivalent air velocity: $0.5\,\text{m}\,\text{s}^{-1}$) in water. The arrow shows the direction of the flow. 66

5.3 Setup of the PIV experiment. a: setup of the PIV experiment. b: lasersheet. We can see that the laser sheet is wide enough to cover at least a complet interrami space. 67

5.4 a. Illustration of the slice method used to determine the leakiness of the structures. b. Relative proportion of the flux through a section of a structure located upstream and downstream of it. The location of the structure is shown by the black line. The value of the leakiness, as determined by the relative flux at the entrance of the structure, is shown by the horizontal red line. This graph was drawn for the case of structure Str_{50} at water velocity of $6.41\,\text{mm}\,\text{s}^{-1}$ (equivalent air velocity: $1\,\text{m}\,\text{s}^{-1}$). The measured leakiness is equal to 0.32. c and d. Effect of the change of effective surface on the flux inside the structure and estimation of the flow capture ratio. 71

5.5 Flow around the surrogate structures, seen from the side. a: Laminar flow around structure Str_{40} at oil velocity of $3.21\,\text{mm}\,\text{s}^{-1}$, equivalent to air velocity of $0.01\,\text{m}\,\text{s}^{-1}$. b: Stable separated vortex ring in the wake of structure Str_{40} at oil velocity of $64.1\,\text{mm}\,\text{s}^{-1}$, equivalent to air velocity of $0.2\,\text{m}\,\text{s}^{-1}$. c: Unsteady wake of structure Str_{40} at water velocity of $12.8\,\text{mm}\,\text{s}^{-1}$, equivalent to air velocity of $2\,\text{m}\,\text{s}^{-1}$. The gray arrows show the direction of the flow. 73

5.6 Influence of the effective surface S_{eff} on the flow in a cross section of the 3D printed scaled-up structures, with a constant diameter D_{rami}=500 µm. The velocities are normalized by the far-field corresponding velocity. 74

5.7 Leakiness of the structures and fitted curves. 75

5.8 Variation of the flow capture ratio depending on the number of rami and the air velocity. a: Variation of the flow capture ratio of the structures with changes of effective surface at different flow velocities. b: Normalized flow capture ratio depending on air velocity and number of rami. The normalisation was done by dividing the flow capture ratio by the maximum flow capture ratio obtained for all the designs at the same air velocity. The white dotted lines show the range of moth flight velocities and the gray horizontal line highlights the performance of the natural design of the moth. . . . 80

6.1 Definition of the different variables refering to velocities. v_∞ is the far-field velocity. v_n is the mean velocity of air between the sensilla. The structure represents a ramus and its sensilla viewed from the top. . . . 86
6.2 Electron Microscopy pictures of the antenna. a: the macrostructure composed of the flagellum and rami is visible. b: focus on the tip of a ramus to reveal the sensilla. . . . 86
6.3 Experimental and theoretical approaches used to calculate the antennal capture efficiency. a: picture of the microstructure obtained by Electron Microscopy. b: virtual object designed to mimic the microstructure. c: simplified microstructure with straight sensilla. d: Array of semi-infinite cylinders. The direction of the flow is indicated by the arrow : the cylinders face the flow. The number of cylinders is infinite in the directions orthogonal to the direction of the flow. The local mass transfer coefficient is determined as if it were in the case of semi-infinite cylinders but the total mass transfer is integrated only from the tip to the point where the length of the integrated portion of cylinder is equal to the length of the sensillum (red part of the cylinder). e: 3D printed microstructure used in the PIV experiments to determine leakiness. . . . 87
6.4 Control volume used to derive equation 6.13 . . . 91
6.5 Print of RS1 and RS2 from right to left. . . . 94
6.6 PIV experiment. a, setup of the experiment. b, velocity field obtained from PIV. . . . 96
6.7 Absolute equivalent air velocity fields from the PIV data for several far-field air velocities. . . . 96
6.8 Velocity field obtained with PIV. The white line pictures out the location of the flux integration to determine the mean velocity v_n of the fluid between the sensilla and the leakiness of the antenna. In this case the far-field velocity used in the experiment was $5.34\,\mathrm{mm\,s^{-1}}$ in oil which is equivalent to $0.5\,\mathrm{m\,s^{-1}}$ in air. Equivalent air velocities displayed in the picture. . . . 98
6.9 Combination of the model and the experiments to obtain the capture efficiency of the microstructure. . . . 99
6.10 Absolute mass flux reaching a sensillum depending on the air velocity v_n. . . . 100

6.11 Capture efficiency of the infinite model of semi-infinite sensilla depending on the air velocity v_n. The capture efficiency is a relative value so it is bounded between 0 and 100%. 101
6.12 Leakiness of the antenna. The data was determined in oil experiments but is displayed depending on the equivalent air velocities v_∞. 102
6.13 Capture efficiency η_s of the model of sensilla depending on the air velocity v_∞. 102
6.14 Capture rate of the antenna compared to leakiness and model capture rate. 103
6.15 Evolution of the mass flux F_{loc} captured along the sensillum for a far-field concentration c_∞ of $1\,g\,m^{-3}$. 104
6.16 Relative importance of the 1st half of the sensillum. 104
6.17 Local Péclet number for an air velocity $v_\infty = 1\,m\,s^{-1}$. Scale is in power of ten : 0 means that the Péclet number equals 1, 1 means a Péclet number of 10 etc. In the case of this logarithmic scale, a Péclet number above 0 means that advection is the most important phenomenon whereas a Péclet number below 0 means that diffusion is the main one. At the location of the antenna, and behing it, there is no value of velocity, so, the value was arbritrarily set at 0.01 in order to avoid trouble with the logarithmic scale. 107
6.18 Gas chromatogram obtained by Bestmann *et al* [10]. Label 1 refers to (4*E*,6*E*,11*Z*)-4,6,11-Hexadecatrienal, label 2 to (4*E*,6*E*,11*Z*)-4,6,11-Hexadecatrienyl acetate. The height of peak 1 is equal to 1/5 of the height of peak 2. 113
6.19 Measurement of the y-component. The oil velocity is equal to $2.14\,mm\,s^{-1}$ (Equivalent air velocity: $0.2\,m\,s^{-1}$). The arrow shows the direction of the flow. 114
6.20 Efficiency of the antenna represented either depending on v_n (red line) or depending on v_∞ (blue line) 115
6.21 Comparison between the drag of a transversal cylinder and a longitudinal one. Diameter and length were chosen according to the moth sensillum. 116
6.22 Comparison between the mass flux on a transversal cylinder and a longitudinal one. Diameter and length were chosen according to the moth sensillum. 116
6.23 Comparison of model capture efficiency in the case of a square or triangle array 118
6.24 Diffusion profiles at various time instants calculated according to equation 6.69 with n_{max}=2000 (top) and 20 only (bottom). $D = 5 \times 10^{-6}\,m^2/s$, $L = 150 \times 10^{-6}\,\mu m$, $c_0 = 3 \times 10^{12}\,/m^3$ 123
6.25 Output flux vs time as calculated from equation 6.71 taking $n_{max} = 200$ (blue line) and using the first order only (red). Parameters as for Figure 6.24. Dashed line indicates τ_{dif} from equation 6.72. . . . 124

6.26 Domain of simulation. The red lines are symmetric boundary conditions to simulate an infinite array of sensilla. This allows us to focus only on a quarter of the domain, in light red. The brown circles represent the sensilla viewed from the top. 130
6.27 Comparison of the relative capture of the sensilla calculated with the model or through FEM simulations. 130

7.1 Cylinder modeling a sensillum transversal to the flow and viewed from the top. v_0 is the far-field velocity, c_0 is the far-field concentration, a is the radius of the circle and r and θ are the polar coordinates. Reproduced from [11] 135
7.2 Analytical leakiness and simulation mass transfer 136
7.3 Analytical leakiness and simulation mass transfer. Reproduced from [12]. 137
7.4 Experimental leakiness and simulated mass capture. Reproduced from [13]. 137
7.5 Comparison of the leakiness of a single microstructure (RS1) with the one of pair of microstructures sitting side by side (RS1x1) . . . 140
7.6 Leakiness of the whole antenna using the multiplicative method. . 141
7.7 Drag of a ramus alone (blue dots), drag of a sensillum alone (green dots), drag of a ramus bearing a sensillum (red dots) and sum of the drag of a ramus alone and a sensillum alone (black dots). The value were determined using simulations (Comsol, Comsol Inc, Stockholm, Sweden). The sum of the drag of one ramus and the drag of one sensillum is $\approx 40\%$ higher than the drag of a ramus bearing one sensillum. 142
7.8 Approach of the second method. Infinite arrays of infinitely long structures (1 and 2) are convenient to model in simulations through the use of symmetric boundary conditions. The simplified antenna modeled by a macrostructure with equivalent cylinders (3) has a finite dimension and a relatively simple shape compared to the real antenna (4) which allows to run simulations to determine the leakiness. 143
7.9 Because the ramus has periodic rows of sensilla, we restricted the simulation domain to one row of five sensilla. The ramus is 25 µm high and has a diameter of 50 µm. We modeled a row of infinite rami using periodic boundary conditions shown in red. The top and bottom periodic boundary conditions shown in c are not displayed in a and b in order to improve the clarity of the figures. 144
7.10 Determination of the diameter of the equivalent cylinder to the microstructure at air velocity $v_{\mathrm{n,eq}} = 0.5\,\mathrm{m\,s^{-1}}$. The diameter is equal to 124.4 µm. The drag per cylinder and per unit of length is determined at this velocity for several diameters (black dots). A linear regression is then applied (green line) and the drag of the microstructure at this velocity (red line) is used to determine the diameter of the equivalent cylinder. 145

7.11 Diameter of the equivalent cylinder that has an equal drag as the ramus and sensilla, depending on the air velocity 146
7.12 Determination of the far-field velocity $v_{\infty,\mathrm{eq}}$ for a given equivalent diameter $\varnothing_{\mathrm{eq}}$ and its associate air velocity $v_{\mathrm{n,eq}}$. Here, $\varnothing_{\mathrm{eq}} = 124.4\,\mu\mathrm{m}$, $v_{\mathrm{n,eq}} = 0.5\,\mathrm{m\,s^{-1}}$ and $v_{\infty,\mathrm{eq}} = 2.3\,\mathrm{m\,s^{-1}}$. 147
7.13 Leakiness calculated by using the method of equivalent cylinders compared to the leakiness obtained with the multiplicative method and the data obtained from the PIV experiment and the experimental data of Vogel [14]. 148
7.14 Efficiency of the entire antenna. The leakiness is the leakiness of the macro and microstructure combined, the local capture efficiency refers to the efficiency of the infinite array of sensilla to capture the molecules among the flux that flows through the array. The efficiency of the antenna is the capture efficiency of the whole antenna and the efficiency of the microstructure was defined in Chapter 6 and is the efficiency of a microstructure alone. 149
7.15 Relative capture by the distal half of the sensilla. The relative capture was calculated in the case of the study of the entire antenna (red line) and compared with the case of the study of the microstructure alone (black line) (Chapter 6). 150
7.16 Definition of the reference flux. 153
7.17 Efficiency of the pectinate antenna compared to the one of a single flagellum, ramus or sensillum transversal to the flow. Flagellum3000 refers to a flagellum which would be as long as a normal flagellum but with a diameter equal to the width of a pectinate antenna which is around 3000 µm large. 154
7.18 Mass captured by the different structures: a bar flagellum, a ramus, a sensillum transversal to the flow, a pectinate antenna and a flagellum with a diameter of 3000 µm. The far-field concentration was set at $1\,\mathrm{mol\,m^{-3}}$. 155
7.19 Pheromone captured by a transversal and a longitudinal sensillum. The far-field concentration is set at $1\,\mathrm{mol\,m^{-3}}$. 156
7.20 Drag of a transversal and a longitudinal sensillum. 156

Chapter 1

Introduction

1.1 Functional morphology

Functional morphology investigates how shape and function are linked. Indeed, shape might be an important parameter in the performance of an organ or a group of organs. A good example of the relation between function and shape lies in the diversity of limb shapes among the Tetrapods. Limbs can have a variety of functions: they can be used to walk, run, swim, fly, jump, climb, hang, dig or handle objects. These numerous functions can be compared with the diversity of limb shapes such as fins, wings, legs and arms, each one having a specific shape in order to perform its function efficiently.

The same kind of relations could be made between the function and shape of an antenna. However, antennae functions are very diverse and the antennae of a given species are not restricted to one single function. They actually bear a combination of sensors or others appendages [15] and fulfill several tasks [16, 17, 18]. Beware, this multi-function aspect of the antenna must not hide the fact that antennae might also not be the only organs to fulfill a given function. In some insects, flow sensing can be done with hairs located on the cerci [19]. Olfactory sensors can be found on the maxillary palps [20, 21] and sensilla detecting vibration during flight can be located on wings [22]. However, given their multi-functional nature, antennae are important sensory organs for insects.

Natural selection says that only the fittest individuals in a population survive and reproduce. In the case of a stable environment, it implies that, after many generations, the descendants of the surviving individuals have acquired traits that are beneficial for their fitness in this given environment. A common expectation from natural selection is that the organisms are then said to be adapted to their environment. Also, because an individual with slightly better performance is more likely to pass on its genes, its traits should be, after a certain time, common among

the population. It is thus tempting to believe that every part of an organism is optimized to fulfill its function. Gould and Lewontin [23] warned against such shortcuts and reminded that organisms are functional entities that cannot be divided into several independent parts. Thus, ontogeny and phylogeny constraints, or even physical constraints, can prevent a trait of an organism to be optimized for its function.

Ontogeny constraints come from the developmental steps which have been shown to be highly-conservative in the early stages [24]. A well-known example of a non-optimized trait is the recurrent laryngeal nerve which goes from the brain to the larynx after a detour around the heart. Thus, the recurrent laryngeal nerve is approximately twice the length of the neck despite the fact that it links the brain and the larynx which are relatively close. As a consequence, this nerve is a few meters long in giraffes [25] and is expected to have been even longer in extinct sauropod dinosaurs [26]. Eventually, the design of the recurrent laryngeal nerve is not the most optimized one due to developmental constraints.

Ontogeny constraints are parts of the wider group of phylogenetic constraints [27]. Phylogenetic constraints are limitations on future evolution due to previously-developed traits. For example, insects are small-sized organisms and the commonly-accepted reason is that their size is limited by their tracheal respiratory system [28] which is not efficient for big sizes. An argument in favor of this theory is the existence of giant insects in the late Paleozoic era when the atmospheric oxygen level was higher [29]. A different evolutionary path led to the apparition development of lungs in Mammals, allowing them to reach far bigger sizes, such as the blue whale [30] which can reach 30 m in length.

1.2 Diversity of functions and shapes of antennae

1.2.1 Antennal shapes

Antennae are "mobile, segmented, paired appendages" [31] located on the head of insects. They exhibit a wide range of shapes (Figure 1.1). They can have very cylindrical shapes or very complex ones.

1.2.2 Antenna diverse functions

Antennae are important organs in insects as they can fulfill a wide range of functions. Many antennae have a major olfactory role. They can be involved in long-distance olfaction as it is the case of male moths which can detect female pheromones several hundreds meters away [32] or some flies of the genera *Lucilia* and *Chrysomia* attracted by the scent of the flowers of the genus *Rafflesia* [33, 34] (both visual and olfactory cues are actually used by the flies to localize the flowers). Cuticular hydrocarbons, low-volatile molecules due to their chemical structure and

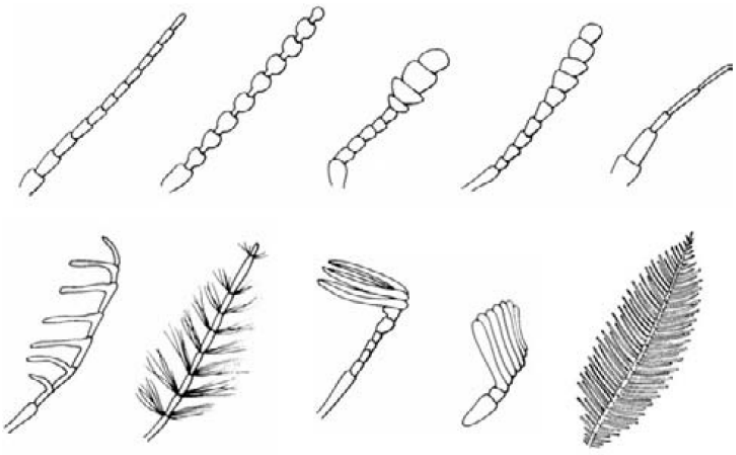

Figure 1.1: Diversity of insect antennae (Reproduced from [1])

waterproof properties [35], are involved in short-distance olfaction. They are used for example by social insects to perform nest recognition [36]. They require a direct contact with the antennae to be detected [37] and involve gustatory sensilla [38] even though it has been shown that contactless close-range detection is also possible [39, 40].

Antennae can also be used to perceive sounds. Contrary to tympaneal ears, they do not detect the pressure variations of the sound but they instead detect the movement of air generated by the sound. In mosquitoes, the capacity to hear through the antennae was discovered by Johnston [41] who gave his name to the Johnston's organs which have a key role in sound detection. Male mosquitoes locate females by the sound they make during flight and their plumose antennae have resonance frequencies close to the one of the female flight sounds [42]. Other insects, such as honey bees [43], use the same principles to hear.

It is interesting to notice that the Johnston's organs, used in the sound detection by the mosquitoes, are actually mechanosensory organs which detect the movements of the antenna. They can be involved in other functions of the antenna. In some Coleoptera (Gyrinidae) living at the surface of the water, antennae are used to detect preys through the vibrations they generate at the surface of the water. In this case, the antennae touch the water and are moved by the vibrations. The movement of the antenna is then detected by the Johnston's organs [44].

These same organs are also involved in flight control, in *Manduca sexta* moths for example [45]. Antennae vibrate during flight and their movement is altered by the Coriolis force. This change is detected by the mechanosensory Johnston's organs [22, 46] and the information is used to correct the trajectory of the insect.

Antennae can be used in a similar way to measure air flow and wind orientation [47]. It has also been shown that insects can detect electric fields. This the case of bees [48] and cockroaches [49] for example. In this case again, the Johnston's organs have a central role. The antennae of the insects get electrically charged during walk or flight [50, 51]. As they enter into an electric field, the antennae are deflected and the change of position is mechanically detected by the Johnston's organs [52]. Antennae have also a tactile function [53]. They then rely not only on Johnston's organs, as they are mechanosensors, but also on a variety of sensilla such as campaniform and marginal sensilla [54]. Tactile antennae are used to detect objects [54], as locomotory guides for example [55].

Antennae can fulfill a few more functions such as thermo- and hygro-sensing [56]. They can be involved in circadian clock mechanisms necessary for the monarch butterfly, for example, to find its way during migration [57]. Antennae can also be used by males to grip females [58, 59] or to repel rival males [15]. Even more surprising, some beetles living in water use their antennae as snorkels to suck air while staying underwater [60, 61]. Antennae of early stages of *Hydrochara caraboides* (previously known as *Hydrophilus caraboides L.*) have also been observed helping the mandibles to grind and knead prey [62].

1.3 Insect olfaction is a major sense

1.3.1 Insect olfaction

Almost all antennae can perceive odors, whatever shape they have [63]. A few examples of antennae without any chemoreceptive function exist ([64, 65] according to [66]) but they are quite rare, as far as I know. Moreover, these insects can still perceive odors thanks to the olfactory sensilla that they have on their labial palps. Chemoreception, the detection of chemical substances, is divided into olfaction and taste. Olfaction is usually related to air-borne chemicals and taste to aqueous ones although the distinction can also be done in terms of distance of detection [67]. Olfaction is for distance detection whereas taste is restricted to contact detection. I will use the following definition: "detection of volatile chemical compounds" [68].

Olfaction is mainly used to find and locate food. In the case of phytophagous insects, plant volatiles are detected by the insects and guide them to the emitter [69]. Haematophagous insects such as *Triatoma infestans* (Hemiptera) use carbon dioxyde and other odors to find their hosts [70].

Odors can be used to find proper ovipositions sites. This is for example the case of many parasitoids which use odors to find prey to lay their eggs in. The volatiles detected by the parasitoids may come from the plant where the hosts live [71, 72] or directly from the host such as sexual pheromones that are emitted to attract mates but can also be smelled by parasitoids [73]. Mosquitoes find oviposition sites

using olfactory clues that can be very similar to the ones used for host-seeking [74].

Communication among social insects is mainly done through olfaction, by means of pheromones. Pheromones were defined as "substances which are secreted to the outside by an individual and received by a second individual of the same species, in which they release a specific reaction" [75]. A wide group of pheromones consists of cuticular hydrocarbons which can be used in many cases: from nest recognition, to determination of the dominance status, to formation of social groups [76]. Pheromones can also be used to attract mates, warn of danger, guide conspecifics to resources or mark territory [77, 78] and they are not restricted to insects [79].

Olfaction has a key role in mate-seeking. Many species using sexual pheromones to attract mates. This is especially the case among Lepidoptera. In this order, in the majority of species, females release tiny amounts of sexual pheromones [80] to attract males even though some rare cases of males releasing and attracting females have been recorded [81]. Females can be detected a few hundreds meters away [32]. In some families of Lepidoptera such as Bombycidae and Saturniidae, larvae acquire fat reserves that are consumed by the imago which has no functional mouth parts and, thus, cannot feed [82, 83]. As a consequence, the imago stage lasts only between five and ten days. During this short period of time, the male must find a female mate to reproduce by detecting her sexual pheromone. There seems thus to be a larger pressure on males to have antennae efficiently detecting low levels of pheromones. Detection should also be very specific to ensure that males are attracted by a female of their own species.

1.3.2 Biological model: the pectinate antennae of *Samia cynthia* (Saturniidae)

In this thesis, I focused on the Saturniidae family and more specifically on the species *Samia cynthia*. Indeed, *Samia cynthia* does exhibit the lifestyle previously described and it has, as well, very complex antennae called pectinate antennae (Figure 1.2). These antennae are composed of a basal scape, a pedicel and a flagellum [84]. The specifity of pectinate antennae lies in their flagellum which supports secondary branches called rami. The flagellum is actually divided in smaller segments called flagellomeres. Each flagellomere bears four rami so the antenna is termed quadripectinate. The rami support the trichodea sensilla which are hair-like structures on which the chemical detectors are located (Figure 1.3). In *Samia cynthia*, the rami are distributed symmetrical on two sides of the flagellum (Figure 1.2). On the male antenna, the sensilla are located on one side of the rami, facing the flow (Figure 1.3). In comparison, females have narrower antennae due to shorter rami, and their sensilla are shorter and distributed all around the rami. In this work, I focused exclusively on male antennae and their sensilla facing the flow.

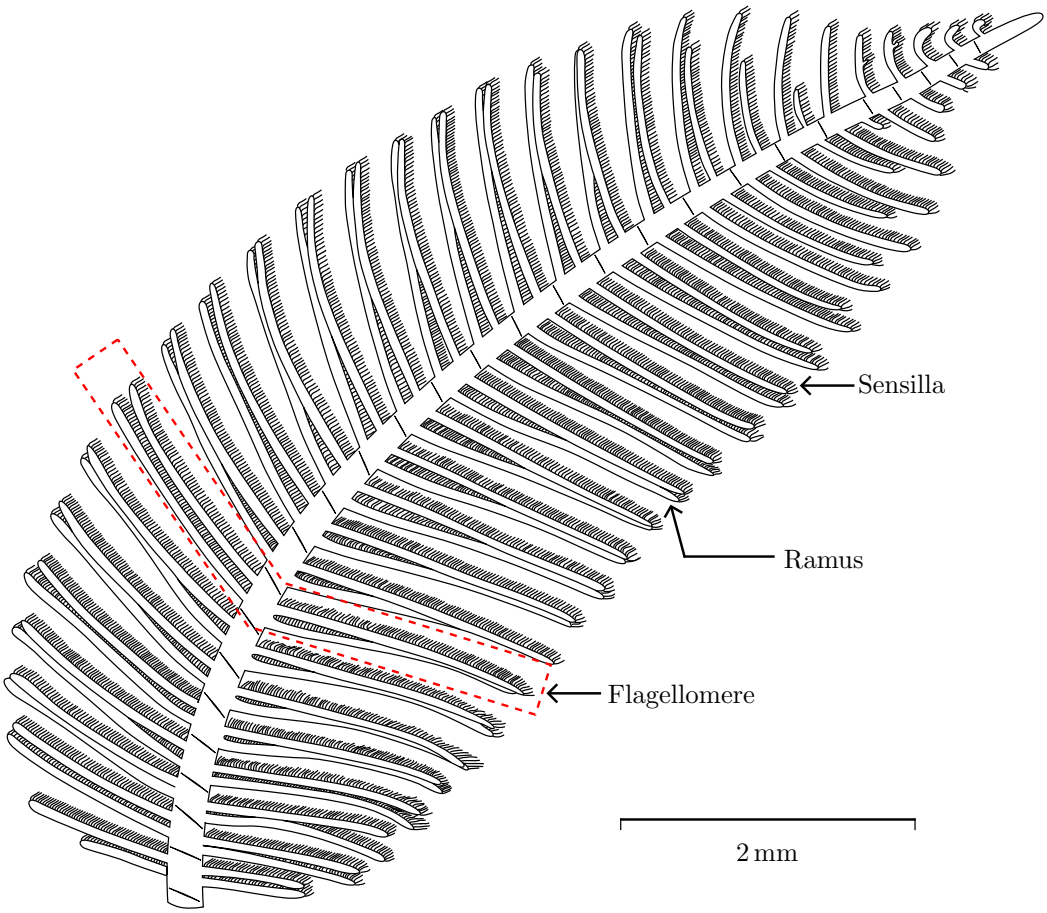

Figure 1.2: Pectinate antenna of the male *Samia cynthia*.

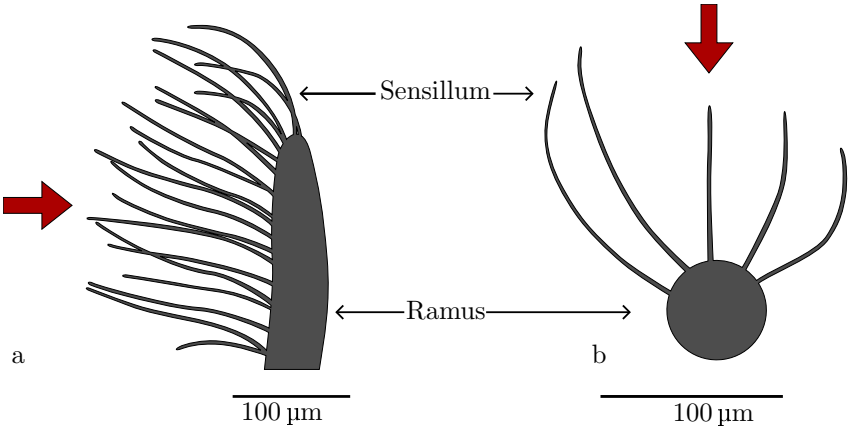

Figure 1.3: Microstructure of the antenna of *Samia cynthia* composed of one ramus and the sensilla it supports. a: side view. b: cross section. The red arrow shows the direction of the airflow.

1.4 Olfaction is a physico-chemical transport process

The olfaction process can be divided into several steps involving either the emitter or the receiver of the signal as well as the environment which carries it.

The signal has first of all to be produced and emitted, by the calling female in our case. Sexual pheromones are usually a blend of chemicals [85] or even geometrical isomers of the same molecules [86]. The proportion of each component is conserved among populations [87] although males respond to a higher range of blend proportions [88, 87, 89]. Females have tiny amounts of pheromones in their glands, meaning that the pheromone concentration in air is low. However, the relation between production and emission is not completely clear yet [80]. Plant volatiles can also be part of the chemical blend [90] which attracts mates and this phenomenon is not restricted to Lepidoptera, as Coleoptera have been found to use it too [91, 92]. In the case of *Samia cynthia*, the sexual pheromone is composed of two compounds [10, 93]: (4E,6E,11Z)-4,6,11-Hexadecatrienal and (4E,6E,11Z)-4,6,11-Hexadecatrienyl acetate. For more information on the chemistry of sexual pheromones in Lepidoptera, see [94].

Moth emission of sex pheromone is not constant. Females periodically extrude their glands [95, 96] to create pulses of pheromone. Moreover, turbulence in air tends to break the chemical signal into discontinuous patches, creating plumes of relatively high pheromone concentration separated by clean air [97, 98] (see [99] regarding plant volatiles). These two phenomena generate a periodic chemical signal which is necessary to trigger a response from the males [100, 101].

Before being detected by the chemical sensors of the moth, the pheromone

molecules must first be captured by the antenna, from the air which carries them. This is a problem of mass transfer. Mass transfer is determined by the mass transport equation (1.1) which states that only the air field velocity $\vec{v}$, the diffusive coefficient D and the boundary conditions (which depend on the geometry of the antenna) determine the concentration of pheromone c in the air and the pheromone flux at the surface of the antenna.

$$\frac{\partial c}{\partial t} + (\vec{v} \cdot \nabla)c = D\nabla^2 c \tag{1.1}$$

As a consequence, the shape of the antenna has a primordial importance at this step of the olfactory process. Indeed, the shape of the antenna has an influence on how the air flows around it and how the molecules are brought in its vicinity. Some models have already been developed to determine the proportion of molecules that arrive at the surface of the antenna [11, 102, 12]. However, because of the difficulty generated by the complex shape of the antenna, these models did not take the specific shape of the pectinate antennae into account. In this thesis, I developed a model to determine the capture efficiency of the pectinate antenna of *Samia cynthia* based on its specific geometry.

The sensillum cuticle is impermeable to pheromone molecules. Access between the exterior air and the interior haemolymph of the sensillum is reduced to the pores which are apertures of around 10 nm of diameter and represent only a small portion of the total surface [103]. Three mechanisms were proposed to explain how molecules could get to the pores. Firstly, only molecules that randomly fall on the pores could be captured [104]. Secondly, a mechanism of reduction of dimensionality has been proposed by Adam and Delbrück [105]. In this theory, pheromone molecules get stuck on the surface of the sensillum when they reach it. However, the interaction is loose enough to allow the molecules to diffuse at the surface of the sensilla and, after a certain time, find a pore. An alternative theory proposes that the random walk of molecules ensures that a molecule reaching the surface of a sensillum and rebounding on it would rebound many times on the surface and, thus, explore a wider surface, enhancing its probability to randomly find a pore [106]. Currently, given the difficulty of studying the chemicals present on the surface of the sensilla [107], neither theories have been experimentally tested.

Once they have crossed the pore openings, pheromone molecules are surrounded by odor binding proteins. Pheromones are usually amphiphile molecules and odor binding proteins help them to solubilized in the haemolymph, which is an aqueous solution. The odor binding proteins then transport the pheromone molecules to an odorant receptor linked to an olfactory sensory neuron, where the pheromone molecule is actually detected. An odorant-degrading enzyme then inactivates the pheromone molecule [108, 109].

One pheromone molecule is enough to fire one neuron. However, neurons can also fire spontaneously and, thus, generate a background noise. To overcome this

noise, it has been calculated that 200 molecules are necessary to overcome the background noise and trigger an antennal pulse [110]. Once a plume of pheromone has been detected, the male moth uses an anemotactic strategy [111] to find the source of the pheromone, that is, the emitting female. They fly upwind until they get out of the plume and they then display a zigzag trajectory to get back into the plume [112, 113, 114, 115]. If the male eventually finds the emitting female, courtship begins, involving pheromones [116, 117] emitted by the male, as well as other signals such as ultrasounds [118].

1.5 Objective of the thesis

This thesis focuses on the odor capture step of the olfaction process. The objective is to determine how the geometry of a pectinate antenna modifies the flow of air to favor mass transfer of the pheromone molecules to its surface. I then compare the olfactory performance of the pectinate antenna with the performance of a cylindrical-shaped one. The justification of this choice lies in the fact that Lepidoptera possess mainly cylindrical-shaped and pectinate antennae and that pectinate antennae independently evolved at least 13 times in several distinct families of moths [119]. Pectinate antennae are found in other orders of insects, such as Coleoptera and Hymenoptera, giving cues that pectinate antennae should be efficient at detecting odors.

The efficiency of the antenna is determined by two phenomena. Firstly, an antenna deflects a portion of the air flow that it encounters. Thus only a proportion of the air flux does flow through the antenna. This proportion is termed leakiness. Secondly, among the proportion of the flow going through the antenna, only a part of the pheromone molecules are effectively captured by the sensilla. To simplify the problem, I split the antenna in two levels: the macrostructure with the flagellum and the rami, and the microstructure composed of one ramus and its sensilla. I used several techniques to determine the performance of a pectinate antenna in capturing pheromone molecules: Additive Manufacturing, Particle Image Velocimetry, semi-analytical models of heat transfer and Finite Element simulations.

Additive Manufacturing, also known as 3D printing or Rapid Prototyping, is a term regrouping manufacturing processes that offer a greater freedom regarding the range of possible shapes thanks to their particular way of building objects. Desired 3D shapes are first designed on a computer. The object is then sliced in multiple layers and sent to the 3D printer which build the layers one after the other. In **Chapter 3**, the potential of Additive Manufacturing in the research field of insect science is reviewed with the latest works involving Additive Manufacturing to study insects. Improvements of Additive Manufacturing inspired from the insect world are also considered. This review emphasizes the benefits of both research fields to collaborate.

In **Chapter 4**, structures similar to the macro- and micro-structures of the antenna are built using Additive Manufacturing processes. Experiments are conducted and models developed to better understand how the anisotropic mechanical properties of 3D printed materials reduce the possibilities of Additive Manufacturing to produce high-aspect ratios cylinders. I focused on one specific 3D printer, the Objet Eden 260 (Stratasys, Eden Prairie, Minnesota, USA) and especially investigate cylinders whose diameters are only a few multiples of the smallest producible features by this 3D printer.

Particle Image Velocimetry was developed in the 1980's [120] and is a technique that allows to visualize and measure velocity fields. The fluid is seeded with particles that are chosen in order to be neutrally buoyant and a laser is used to illuminate the particles. Usually, laser sheets are used and give 2D information on the flow [121, 122]. Images are then correlated to determine the velocity field. This technique has already been successfully used in the study of insect fluid dynamics [123, 124, 125]. In **Chapter 5**, I use Particle Image Velocimetry to experimentally determine the leakiness of the macrostructures of the antenna on a range of air velocities encountered by moths in nature. Nowadays, tomo-particle image velocimetry has also been developed to give the complete 3D velocity field [126, 127].

Chapter 6 focuses on the pheromone capture by the microstructure. Heat and mass transfer have analogue equations. Thus, the technique to solve them are sometimes the same and, in the engineering field, they are usually taught together [128]. Moreover, given their industrial use, engineers have studied heat transfer in many geometrical configurations. I use the analogy of heat and mass transfer to apply heat transfer results to the pectinate antenna where mass transfer occurs and, combined with PIV measurements, I determine the capture efficiency of the microstructure of the antenna.

Chapter 7 is a general discussion about the previous chapters and shows complementary results. To obtain the efficiency of the entire antenna, results on both the macro- and micro-structures have to be combined. To meet this objective, I developed a method through simulations of fluid dynamics to determine the leakiness of the entire antenna. Fluid dynamics and mass transport simulations are then ran to compare the efficiency of a pectinate antenna with the one of a cylindrical-shaped antenna, which are the two shapes encountered among Lepidoptera [119]. I close the thesis by a large, comparative view on insect antennal architecture.

Chapitre 2

Introduction en français

2.1 Morphologie fonctionnelle

La morphologie fonctionnelle s'intéresse au lien entre fonction et forme. En effet, la performance d'un organe ou d'un groupe d'organes peut fortement dépendre de sa forme. La diversité de forme des membres au sein des Tétrapodes en est un bon exemple. Les membres accomplissent des fonctions différentes comme marcher, courir, nager, voler, sauter, grimper, se suspendre, creuser ou manipuler des objets. Ces nombreuses fonctions sont à mettre en relation avec la diversité des membres tels que les nageoires, les ailes, les pattes et les bras, chacun ayant une forme spécifique dans le but d'accomplir efficacement leur fonction.

Une relation similaire pourrait être faite entre la fonction et la forme d'une antenne. Cependant, les antennes présentent une très grande diversité de fonctions et une antenne d'une espèce donnée accomplit généralement plusieurs fonctions à la fois. Les antennes présentent en effet une combinaison de senseurs ou d'appendices [15] et accomplissent plusieurs tâches [16, 17, 18]. Il faut cependant garder à l'esprit que l'antenne n'est pas forcément le seul organe à accomplir certaines fonctions. Chez certains insectes, les cerques portent des poils qui détectent les flux d'air [19]. Des senseurs olfactifs peuvent également être présents sur les palpes maxillaires [20, 21] et des sensilles détectant les vibrations durant le vol ont été localisées sur certaines ailes[22]. Cependant, étant donné leur capacité à remplir de multiples fonctions, les antennes sont des organes sensoriels importants pour les insectes.

La sélection naturelle dit que seuls les individus les plus adaptés d'une population survivent et se reproduisent. Dans le cas d'un environnement stable, cela implique que, après plusieurs générations, les descendants des individus qui ont survécu ont acquis des traits bénéfiques à leur survie dans cet environnement donné. A cause de la sélection naturelle, on s'attend généralement à ceux que les

organismes des individus soit adapté à leur environnement. De plus, comme un individu qui a de meilleures performances est plus à même de passer ses gènes à la génération suivante, ses caractéristiques devrait, après plusieurs générations, être répandues au sein de la population. Il est ainsi tentant de croire chaque élément d'un organisme est optimisé pour remplir la fonction qui lui est dévolue. Gould et Lewontin [23] ont mis en garde contre de tels raccourcis et ont souligné que les organismes sont des entités fonctionnelles qui ne peuvent pas être décomposées en plusieurs sous-parties indépendantes. Ainsi, les contraintes ontogéniques et phylogénétiques, ou encore les contraintes physiques, peuvent empêcher une sous-partie d'un organisme d'être complètement optimisée pour remplir sa fonction.

Les contraintes ontogéniques résultent du processus développemental qui est fortement conservé, surtout dans les premiers stades [24]. Un exemple bien connu concerne le caractère non-optimisé du nerf laryngé récurrent qui part du cerveau pour rejoindre le larynx après avoir fait un détour au niveau du cœur. Ainsi, le nerf laryngé récurrent fait approximativement deux fois la longueur du cou malgré le fait qu'il relie le cerveau et le larynx qui sont relativement proches. En conséquence, ce nerf mesure plusieurs mètres chez la girafe [25] et est supposé avoir été encore plus long chez certains dinosaures [26]. Au final, le parcours du nerf laryngé récurrent e peut pas être optimisé à cause de contraintes développementales.

Les contraintes ontogéniques font partie d'une groupe plus vaste, les contraintes phylogénétiques [27]. Les contraintes phylogénétiques correspondent à des limitations sur les possibilités futures d'évolution à cause de caractères qui ont été développés antérieurement. Par exemple, les insectes sont des organismes de petite taille, la raison communément admise étant que leur taille est limitée par leur système respiratoire trachéal [28] qui n'est pas assez efficace pour des organismes de grande taille. Un argument en faveur de cette théorie est l'existence d'insectes géants au Paléozoïque supérieur quand la concentration atmosphérique en oxygène était plus élevée [29]. Un chemin évolutif différent a mené à l'apparition de poumons chez les Mammifères, leur permettant d'atteindre des tailles beaucoup plus importantes, comme le rorqual bleu [30] qui peut atteindre les trente mètres de long.

2.2 Diversité des fonctions et des formes d'antennes

2.2.1 Formes d'antennes

Antennae are "mobile, segmented, paired appendages" [31] located on the head of insects. They exhibit a wide range of shapes (Figure 2.1). They can have very cylindrical shapes or very complex ones.

Les antennes sont des "mobile, segmented, paired appendages" (appendices

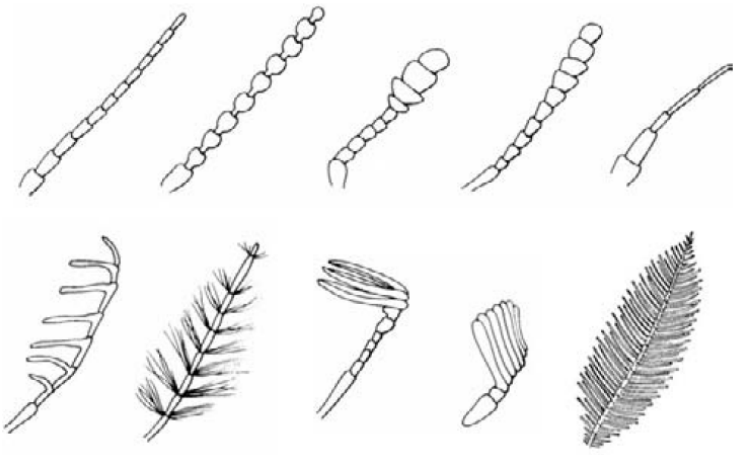

FIGURE 2.1: Diversité des antennes d'insectes (Reproduit à partir de [1])

mobiles, segmentés et appariés) [31] situés sur la tête des insectes. Elles peuvent prendre une grande variété de formes : certaines sont cylindriques alors que d'autres adoptent des formes beaucoup plus complexes (Figure 2.1).

2.2.2 Diversité des fonctions des antennes

Les antennes sont des organes importants pour les insectes car elles remplissent de nombreuses fonctions. Beaucoup d'antennes ont un rôle majeur pour l'olfaction. Elles peuvent être impliquées dans l'olfaction à grande distance. C'est le cas de certains papillons mâles qui peuvent détecter les phéromones émises par les femelles à plusieurs centaines de mètres [32] ou encore de certaines mouches des genres *Lucilia* et *Chrysomia* qui sont attirées par l'odeur des fleurs du genre *Rafflesia* [33, 34] (ces mouches utilisent également des indices visuels pour localiser les fleurs). Les hydrocarbones cuticulaires, qui sont généralement supposés être peu volatiles du fait de leur structure chimique et de leur propriété hydrophobique [35], sont impliqués dans l'olfaction à courte distance. Ils sont par exemple utilisés par les insects sociaux dans la reconnaissance de nid [36]. Ils sont détectés par contact direct des antennes [37], notamment par des sensilles gustatives [38] même si il a été montré qu'une détection à faible distance sans contact était possible [39, 40].

Les antennes peuvent aussi être utilisées pour percevoir des sons. Contrairement aux tympans, elles ne détectent pas les variations de pressions mais le mouvement de l'air généré par le son. Chez les moustiques, la capacité des antennes à entendre a été découverte par Johnston [41] qui a donné son nom à l'organe de Johnston, organe qui a un rôle-clé dans la détection des sons. Les moustiques mâles localisent les femelles par le son qu'elles émettent en vol et leurs antennes

plumeuses ont des fréquences de résonance proche de celles générées par le vol des femelles [42]. D'autres insectes, comme les abeilles mellifères [43], utilisent le même principe pour entendre.

Il est intéressant de noter que les organes de Johnston, utilisé dans la détection des sons par le moustique, sont en fait des organes mécanosensoriels qui détectent les mouvements de l'antenne. Ils peuvent également être impliqués dans d'autres fonctions des antennes. Chez certains Coléoptères (Gyrinidae) vivant à la surface de l'eau, les antennes détectent les vibrations de la surface de l'eau émises par les proies de l'insecte. Dans ce cas, les antennes sont au contact de l'eau et bougent avec le mouvement de la surface. C'est ce mouvement des antennes qui est ensuite détecté par les organes de Johnston [44].

Ces mêmes organes sont aussi impliqués dans le contrôle du vol , chez le papillon *Manduca sexta* par exemple [45]. Les antennes vibrent durant le vol et leur mouvement est altéré par les forces de Coriolis. Ce changement est détecté par les organes mécanosensoriels de Johnston [22, 46] et cette information est utilisée pour corriger la trajectoire de l'insecte. Les antennes sont utilisées d'une manière similaire pour mesurer des flux d'air ainsi que le sens du vent [47]. Il a aussi été montré que les insectes peuvent détecter des champs électriques. C'est par exemple le cas des abeilles [48] et des cafards [49]. Dans ce cas également, les organes de Johnston ont un rôle central. Durant la marche ou le vol, les antennes des insectes acquièrent une charge électrique [50, 51]. Quand un champ électrique apparaît, la position des antennes est modifiée et c'est ce changement de position qui est détecté par les organes de Johnston [52]. Les antennes ont aussi une fonction tactile [53] qui repose non seulement sur les organes de Johnston, qui sont des mécanosenseurs, mais également sur une variété de sensilles telles que les sensilles campaniformes et marginales [54]. La fonction tactile des antennes est utilisée pour détecter des objets [54], en tant que guide pour la locomotion par exemple [55].

Les antennes remplissent encore d'autres fonctions comme la détection de la température et de l'humidité[56]. Elles peuvent être impliquées dans les mécanismes de régulation de l'horloge circadienne, nécessaire au papillon monarque, par exemple, pour trouver son chemin durant la migration [57]. Les antennes sont parfois utilisées par les mâles pour agripper les femelles [58, 59] ou repousser des rivaux [15]. Plus surprenant encore, certains coléoptères vivant sous l'eau utilisent leurs antennes comme des tubas pour aspirer l'air tout en restant sous la surface de l'eau [60, 61]. Les antennes des premiers stades larvaires du coléoptère *Hydrochara caraboides* (anciennement connu sous le nom de *Hydrophilus caraboides L.*) ont été observées aider les mandibules à broyer des proies [62].

2.3 L'olfaction est un sens majeur pour les insectes

2.3.1 L'olfaction chez les insectes

Quasiment toutes les antennes peuvent percevoir des odeurs, quelque soit leur forme [63]. Quelques exemples d'antennes dépourvues de récepteurs chimiques ont été découverts ([64, 65] d'après [66]) mais ces cas sont rares, d'après ce que j'ai pu lire dans la littérature. De plus, ces insectes peuvent quand même percevoir des odeurs par le biais de sensilles olfactives localisées sur leurs palpes labiaux. La détection de composés chimiques est divisée en deux groupes, l'olfaction et le gustation. L'olfaction est généralement reliée aux composés chimiques volatiles (dans l'air) et la gustation aux composés présent en solution aqueuse bien que la distinction puisse également être faite en terme de distance de détection [67]. L'olfaction concerne alors la détection à distance alors la gustation est limitée à la détection par contact. J'utiliserai la définition suivante : "detection of volatile chemical compounds" (détection de composés chimiques volatiles) [68].

L'olfaction est principalement utilisée pour trouver et localiser de la nourriture. Dans le cas des insectes phytophages, certains volatiles émis par les plantes sont détectés par les insectes et les guident vers l'émetteur [69]. Les insectes hématophages tels que *Triatoma infestans* (Hemiptera) utilisent le dioxyde de carbone entre autres odeurs pour trouver leurs hôtes [70].

Les odeurs peuvent être utilisées pour trouver des sites de ponte. C'est le cas par exemple de nombreux parasitoïdes qui utilisent les odeurs pour trouver leurs proies dans lesquelles ils pondent leurs œufs. Les volatiles détectés par les parasitoïdes peuvent venir de la plante où se trouve l'hôte [71, 72] ou alors directement de l'hôte par le biais, par exemples de phéromones sexuelles émises pour attirer les mâles mais qui peuvent aussi être détectées par les parasitoïdes [73]. Les moustiques trouvent leur site de ponte à l'aide d'indices olfactifs qui peuvent être très proches de ceux utilisés pour la recherche d'hôte [74].

La communication entre les insectes sociaux se fait principalement par l'olfaction, au moyen de phéromones. Les phéromones sont définies en tant que "substances which are secreted to the outside by an individual and received by a second individual of the same species, in which they release a specific reaction" (substances secrétées par un individu et détectées par un second individu de la même espèce, chez qui elles déclenchent une réaction spécifique) [75]. Un large groupe de phéromones est constitué des hydrocarbones cuticulaires qui sont utilisés à de nombreuses fins : pour la reconnaissance des nids, la détermination du statut de dominance ou encore la formation de groupes sociaux [76]. Les phéromones sont aussi utilisées pour attirer des partenaires, prévenir d'un danger, guider les membres d'un groupe vers des ressources ou marquer un territoire [77, 78] et leur utilisation n'est pas restreinte aux seuls insectes [79].

L'olfaction joue un rôle-clé dans la recherche de partenaire. De nombreuses espèces ont recours aux phéromones sexuelles pour attirer des partenaires. C'est particulièrement le cas chez les Lépidoptères. Au sein de cet ordre, chez la majorité des espèces, les femelles émettent de très faibles quantités des phéromones sexuelles [80] pour attirer les mâles bien que dans de rares cas, ce sont les mâles qui attirent les femelles [81]. Les femelles sont détectées à plusieurs centaines de mètres de distance [32]. Dans certaines familles de Lépidoptères, comme les Bombycidae et les Saturnidae, les chenilles constituent des réserves de graisse qui sont utilisées au stade adulte par les imagos qui ne possèdent pas de parties buccales fonctionnelles et ne peuvent donc pas se nourrir [82, 83]. En conséquence, le stade adulte ne dure qu'entre cinq et dix jours. Durant cette courte période, le mâle, pour se reproduire doit trouver une femelle grâce aux phéromones que cette dernière a émises. Il semble donc y avoir une importante pression sur les mâles pour avoir des antennes qui détectent efficacement de faibles concentrations de phéromones sexuelles. La détection doit également être très spécifique pour que les mâles ne soient attirés que par les femelles de leur propre espèce.

2.3.2 Modèle biologique : les antennes pectinées de *Samia cynthia* (Saturnidae)

Dans cette thèse, je me suis focalisé sur la famille des Saturnidae et plus spécifiquement sur l'espèce *Samia cynthia*. En effet, *Samia cynthia* suit un mode de vie similaire à celui décrit précédemment et possède, de plus, des antennes très complexes qualifiées d'antennes pectinées (Figure 2.2). Ces antennes sont composées d'un scape basal, d'un pédicelle et d'un flagelle [84]. La spécificité des antennes pectinées repose dans leur flagelle qui porte des branches secondaires appelées ramis. Le flagelle est en fait divisé en petits segments, les flagellomères. Chaque flagellomère supportant quatre ramis, l'antennes est qualifiée de quadripectinée. Les ramis supportent les sensilles trichodea qui sont des structures ressemblant à des poils dans lesquelles sont situés les détecteurs chimiques (Figure 2.3). Chez *Samia cynthia*, les ramis sont distribués symétriquement de chaque côté du flagelle (Figure 2.2). Sur l'antenne mâle, les sensilles sont situées sur une face du rami, face au flux d'air (Figure 2.3). En comparaison, les femelles ont des antennes plus étroites découlant de ramis plus courts, et leurs sensilles sont également plus courtes et distribuées tout autour du rami. Dans ce travail, je me suis concentré exclusivement sur les antennes mâles et leurs sensilles faisant face au flux d'air.

2.4 L'olfaction est un phénomène de transport physico-chimique

Le processus d'olfaction peut être divisé en plusieurs étapes impliquant soit l'émetteur du signal, soit le receveur ou encore l'environnement qui transporte le message chimique.

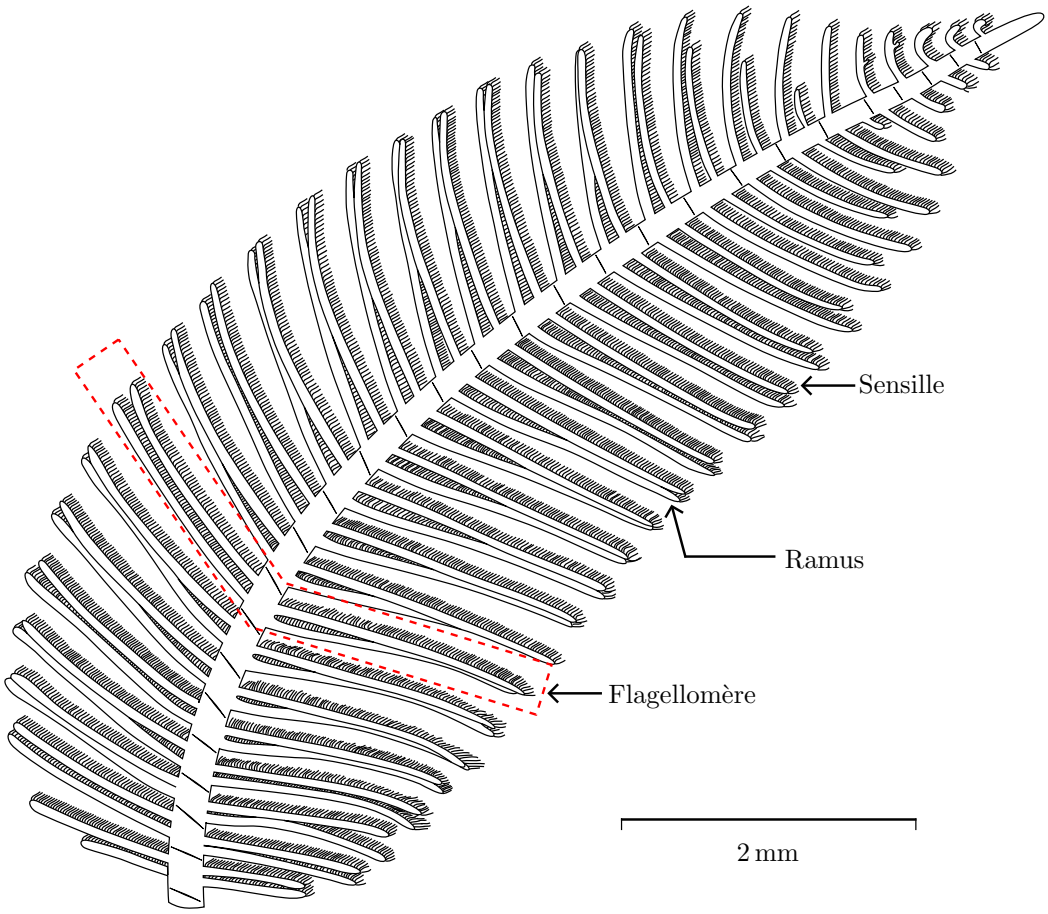

FIGURE 2.2: Antenne pectinée d'un mâle de l'espèce *Samia cynthia*

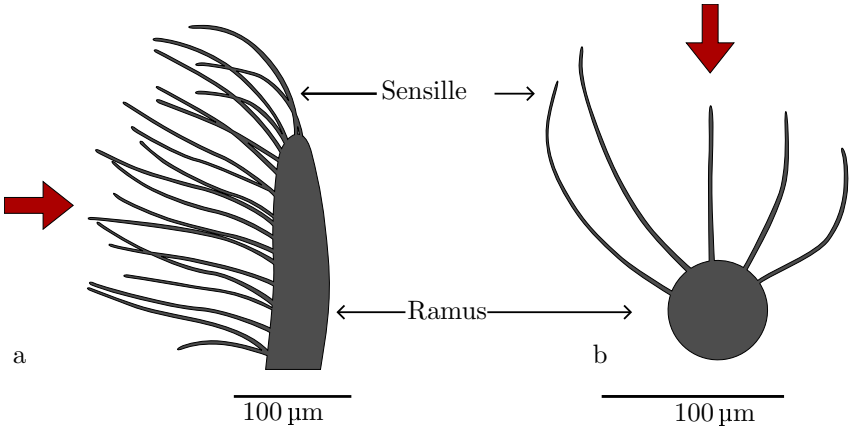

FIGURE 2.3: Microstructure de l'antenne de *Samia cynthia* composée d'un rami et des sensilles qu'il porte. a : vue de côté. b : section. La flèche rouge indique la direction du flux d'air.

Le signal doit tout d'abord être produit et émis, par la femelle dans notre cas. Les phéromones sexuelles sont généralement un mélange de plusieurs composés chimiques [85] ou même d'isomères de la même molécules [86]. La proportion de chaque composé est conservé au sein d'une population [87] bien que les mâles puissent répondre à une plus large plage de mélanges [88, 87, 89]. Les femelles ont de très faibles quantités de phéromones dans leurs glandes, impliquant que la concentration des phéromones dans l'air est faible. Cependant, la relation entre production et émission n'est toujours pas bien comprise [80]. Les volatiles émis par les plantes peuvent également faire partie du mélange [90] qui attire les mâles et ce phénomène n'est pas restreint aux Lépidoptères. Il a par exemple été trouvé chez des Coléoptères [91, 92]. Dans le cas de *Samia cynthia*, la phéromone sexuelle est composée de deux molécules [10, 93] : le (4E,6E,11Z)-4,6,11-Hexadecatrienal et le (4E,6E,11Z)-4,6,11-Hexadecatrienyl acetate. Pour plus d'informations sur la chimie des phéromones sexuelles chez les Lépidoptères, voir [94].

L'émission des phéromones chez les papillons n'est pas constante. Les femelles exposent periodiquement leurs glandes [95, 96] afin de créer des pulses de phéromone. De plus, la turbulence de l'air a tendance à casser le message chimique en patchs discontinus, créant des pulses de phéromone en concentration relativement élevée séparés par de l'air vie de toute phéromone [97, 98] (voir [99] pour les volatiles de plantes). Ces deux phénomènes génèrent un signal chimique périodique qui est nécessaire pour déclencher une réponse des mâles [100, 101].

Avant d'être détecté par les senseurs chimiques du papillon, les molécules de phéromone doivent d'abord être capturées par l'antenne, à partir de l'air qui les transporte. C'est un problème de transfert de masse. Les transfert de masses sont déterminés par l'équation de transfert de masse (2.1) qui dit que seuls le champ de vitesse de l'air $\vec{v}$, le coefficient de diffusion D et les conditions de bord

(qui dépendent de la géométrie de l'antenne) déterminent la concentration en phéromone $c$dans l'air et le flux de phéromone à la surface de l'antenne.

$$\frac{\partial c}{\partial t} + (\vec{v} \cdot \nabla)c = D\nabla^2 c \tag{2.1}$$

En conséquence, la forme de l'antenne a une importance primordiale dans cette étape du processus d'olfaction. En effet, la forme de l'antenne influence comment l'air s'écoule et amène les molécules dans son voisinage. Des modèles ont déjà été développés pour déterminer la proportion de molécules qui arrivent à la surface d'une antenne [11, 102, 12]. Cependant, à cause de la difficulté impliquée par la forme complexe de l'antenne, ces modèles ne prennent pas en compte la forme spécifique de l'antenne pectinée. Dans cette thèse, j'ai développé un modèle permettant de déterminer l'efficacité de capture d'une antenne pectinée de *Samia cynthia* sur la base de sa géométrie spécifique.

La cuticule des sensilles est imperméable aux molécules de phéromones. L'accès entre l'air extérieur et la lymphe à l'intérieur des sensilles est réduit aux pores qui sont des ouvertures de 10 nm environ et qui ne représente qu'une petite partie de la surface totale de l'antenne [103]. Trois mécanismes ont été proposés pour expliquer comment les molécules atteignent les pores. Premièrement, seules les molécules qui tombent aléatoirement dans les pores sont capturées [104]. Deuxièmement, un mécanisme de réduction de dimensionalité a été proposé par Adam et Delbrück [105]. Selon cette théorie, les molécules de phéromone restent attachées à la surface de l'antenne après l'avoir impactée. Cependant, cette interaction est suffisamment souple pur permettre aux molécules de diffuser sur la surface de l'antenne et, après un certain temps, trouver aléatoirement un pore. Une troisième théorie alternative propose que la marche aléatoire des molécules dans l'air permette à une molécule atteignant la surface d'une sensille de rebondir plusieurs fois et, ainsi, d'explorer une plus grande surface, ce qui augmenterait ses chances de tomber dans un pore [106]. A ce jour, étant donnée la difficulté d'étudier les composés chimiques à la surface des sensilles [107], aucune théorie n'a pu être testée expérimentalement.

Une fois entrées dans les pores, les molécules de phéromone sont entourées par des protéines (OBP : Odor Binding Proteins). Les phéromones sont généralement des molécules amphiphiles et les OBP les aident à se solubiliser dans la lymphe qui est une solution aqueuse. Les OBP transportent les molécules de phéromone à un récepteur d'odeur relié à un neurone sensoriel olfactif, où les molécules sont détectées. Une enzyme dégrade ensuite et inactive les molécules de phéromone [108, 109].

Une molécule de phéromone est suffisante pour déclencher un spike dans un neurone. Cependant, les neurones peuvent se déclencher spontanément et, ainsi, génèrent un bruit de fond. Il a été estimé que 200 molécules sont nécessaires pour dépasser le bruit de fond et généré un impulse de l'antenne [110]. Une

fois que le pulse d'odeur a été détecté, le papillon mâle utilise une stratégie anémotactique [111] pour trouver la source de la phéromone, c'st-à-dire la femelle. Ils volent à contrecourant du vent jusqu'à ce qu'ils sortent du pulse de phéromone et entament alors une série de zigzags pour le retrouver [112, 113, 114, 115]. Si au final le mâle trouve la femelle, la parade commence et implique des phéromones émises par le mâle [116, 117] ainsi que d'autres signaux comme des ultrasons par exemple [118].

2.5 Objectifs de la thèse

Dans cette thèse, je me suis concentré sur l'étape de capture d'odeur durant le processus d'olfaction. L'objective est de déterminer comment la géométrie de l'antenne pectinée modifie le flux d'air pour favoriser le transfert de masse de molécules de phéromone sur sa surface. J'ai ensuite comparé la performance olfactive d'une antenne pectinée avec celle d'une antenne cylindrique. Ce choix est justifié par le fait que les Lépidoptères possèdent majoritairement des antennes cylindriques ou pectinées et que les antennes pectinées sont apparues indépendamment treize fois dans plusieurs familles distinctes [119]. On trouve des antennes pectinées chez d'autres ordres d'insectes comme les Coléoptères et les Hyménoptères, ce qui renforce l'idée que ces antennes devraient être efficaces à capturer des odeurs.

L'efficacité de l'antenne est déterminé par deux phénomènes. Premièrement, une antenne dévie une partie du flux d'air qu'elle rencontre. Ainsi, seulement une proportion du flux d'air passe effectivement à travers l'antenne. Cette proportion est appelée perméabilité. Deuxièmement, parmi le flux d'air qui passe à travers l'antenne, seule une partie des molécules est effectivement capturée par les sensilles. Pour simplifier le problème, j'ai divisé l'antenne en deux niveaux : la macrostructure avec le flagelle et les ramis, et la microstructure composée d'un rami et de ses sensilles. J'ai ensuite utilisé plusieurs techniques pour déterminer la performance d'une antenne pectinée à capturer des molécules de phéromone : Impression 3D, Vélocimétrie par Image de Particle (PIV), modèle de transfert de chaleur semi-analytique et simulation par éléments finis.

L'impression 3D, aussi connue sous le nom de Fabrication Additive ou Prototypage Rapide, est un terme regroupant des processus de fabrication qui offrent une grande liberté en terme de formes grâce à leur façon particulière de fabriquer les objets. Les formes désirées sont d'abord conçues en 3D sur ordinateur. L'objet est ensuite numériquement découpé en tranches et envoyé à l'imprimante 3D qui le fabrique tranche par tranche. Dans le **Chapitre 3**, une synthèse est faite sur le potentiel de l'impression 3D dans le domaine de la recherche en biologie de l'insecte et passe en revue les derniers travaux impliquant l'impression 3D dans l'étude d'insectes. Des améliorations de l'impression 3D inspirées du monde des insectes sont aussi considérées. Cette synthèse met l'accent sur les bénéfiques réciproques qu'amènerait une collaboration entre ces deux domaines de recherche.

Dans le **Chapitre 4**, des structures similaires aux macro- et micro-structures de l'antenne ont été fabriquées par impression 3D. Des expériences ont été conduites et des modèles développés afin de mieux comprendre comment les propriétés anisotropiques des matériaux imprimés réduisent les possibilités de l'impression 3D de fabriquer des cylindres long et fins. Je me suis concentré sur une imprimante 3D, l'Objet Eden 260 (Stratasys, Eden Prairie, Minnesota, USA) et j'ai surtout étudié des cylindres dont le diamètre est égal à quelques multiples seulement du plus petit détail que l'imprimante 3D était capable de produire.

La Vélocimétrie par Image de Particules a été développée dans les années 1980 [120] et est une technique qui permet de visualiser et mesurer une champ de vitesse. Le fluide est ensemencé de particules qui sont choisies pour avoir une flottabilité neutre et un laser est utilisé pour illuminer les particules. Généralement, des nappes laser sont utilisée et produisent des informations en 2D du fluide [121, 122]. Les images sont ensuite corrélées pour déterminer le champ de vitesse. Cette technique a déjà été utilisée pour étudier la dynamique des fluides autour d'insectes [123, 124, 125]. Dans le **Chapitre 5**, j'ai utilisé la Vélocimétrie par Image de Particules pour déterminer expérimentalement la perméabilité des macrostructures de l'antenne sur une plage de vitesses rencontrées par le papillon dans la nature. De nos jours, la tomo-Vélocimétrie par Image de Particules a été développé pour mesurer le champ de vitesse en 3D [126, 127].

Le **Chapitre 6** se concentre sur la capture de phéromone par la micro-structure. Comme les transferts de masse et de chaleur découlent d'équations similaires, les techniques utilisées pour les résoudre sont parfois les mêmes et, dans le domaine de l'ingénierie , ils sont généralement enseignés en même temps [128]. De plus, étant donné leur utilité dans l'industrie, les ingénieurs ont étudié les transferts de chaleur dans de nombreuses configurations géométriques. J'ai utilisé l'analogie entre transferts de chaleur et de masse pour appliquer un résultat de transfert de chaleur à l'antenne pectinée où des transferts de masse ont lieu. Combiné avec des mesures de PIV, j'ai déterminée l'efficacité de capture de la microstructure de l'antenne.

Le **Chapitre 7** présente une discussion générale à propos des chapitres précédents et montre des résultats complémentaires. Pour obtenir l'efficacité de l'antenne entière, les résultats des macro- et micro-structures doivent être combinés. Pour remplir cet objectif, j'ai développé une méthode, à l'aide de simulation en dynamique des fluides, pour déterminer la perméabilité de l'antenne entière. Des simulations de dynamique des fluides et de transfert de masse ont ensuite été réalisés pour comparer l'efficacité d'une antenne pectinée avec celle d'une antenne cylindrique, qui sont les deux formes rencontrées chez les Lépidoptères [119]. Je conclus cette thèse par un point de vue comparatif sur l'architecture des antennes.

Chapter 3

Additive Manufacturing and Insect Science

3.1 Abstract en Français

L'impression 3D est devenue un outil efficace pour étudier des solutions biomimétiques inspirées des insectes. En effet, elle permet de fabriquer des objects de forme 3D complexes et utilise des matériaux avec des propriétes spécifiques, tels que les matériaux mous. Des biomatériaux aux biostructures, l'impression 3D offre des nombreuses possibilités en termes de design et de fonctions. Récipro-quement, des solutions technologiques inspirées des insectes peuvent améliorer les processus d'impression 3D utilisés, par exemple, pour produire des structures biocompatibles qui peuvent héberger des cellules. Nous pensons que, grâce à ses progrès continus, l'impression 3D aura un rôle croissant dans le développement de solutions inspirées des insectes.

3.2 Abstract

Additive Manufacturing has become an efficient tool to study insect-inspired biomimetic solutions. Indeed, it can build objects with intricate 3D-shapes and use materials with specific properties, such as soft materials. From biomaterials to biostructures or biosensors, Additive Manufacturing allows more possibilities in terms of design and functions. Reciprocally, insect-inspired technological solutions can be implemented to enhance Additive Manufacturing processes providing for example biocompatible structures that can successfully host living cells. We believe that, thanks to its continuous progress, Additive Manufacturing will play a growing role in the development of insect-inspired solutions.

3.3 Introduction

Biological systems are a wonderful source of inspiration to find solutions for a large variety of problems. Nature had millions of years to develop efficient and original ways to deal with challenges, e.g. varying from all kinds of locomotion to group organization, from abiotic constraints to predator evasion. Even if not all these solutions might be relevant for human applications, they may reveal interesting phenomena or mechanisms.
Insects, and in a broader sense arthropods, have a large range of ecological conditions: they can crawl on the ground, swim, fly, live in caves in complete darkness [129] or even survive space conditions ([130], Panarthropoda clade). Moreover, being part of the same phylogenetic group, they had to evolve various solutions based on the same basic tools and materials, e.g. all the cuticles and hard parts of insects contain chitin [131] with various mechanical properties. Insects are thus a rich and promising group for biomimetics [132].
However, insects are of relatively small size so it is sometimes difficult to study them. As the 3D-shape of an organ or any other part of interest is also closely linked with its function, manufacturing small-size objects with specific 3D-shapes would be a great help to investigate insect-related mechanisms. Well-known photolithography based fabrication technologies such as MEMS, CNC milling or moulding are wonderful technologies to produce a variety of objects but they have their limitations, e.g. size-wise or in producing various kinds of 3D shapes (Table 3.1). On the other side, even if it cannot reach the small size of insects, Additive Manufacturing (AM), with 3D printing its most well-known representative, produces highly customizable objects with far more freedom regarding their 3D-shapes than traditional manufacturing technologies.

Technology	Photolithography	Additive Manufacturing	CNC	Moulding
Dimensionality	2,5-D (stratified)	3D	3D, limited	3D, limited
Fabrication	Batchwise	Piecewise	Piecewise	Batchwise
Materials	Inorganic	Organic	Inorganic	Organic
	Mostly stiff	Stiff and flexible	Stiff	Stiff and flexible
	Linear	Creep, hysteresis	Linear	Creep, hysteresis
Resolution	nm - µm	µm - mm	0.1 µm - mm	µm - mm
Initial costs	High	Low	Low	High
$/piece	Low	High	High	Low
Customisation	None	Per piece	Per piece	None
Lead time	Long	Short	Short	Long

Table 3.1: Comparison of the characteristics of various traditonnal manufacturing processes with Additive Manufacturing, adapted from [133], CNC = Computer Numerical Control

3.4 Additive manufacturing

AM literally entails the class of fabrication technologies that are based on adding materials, rather than removing (e.g. etching, milling, spark erosion, etc.) from a piece. It is best known for 3D printing, e.g. a layer-by-layer manufacturing

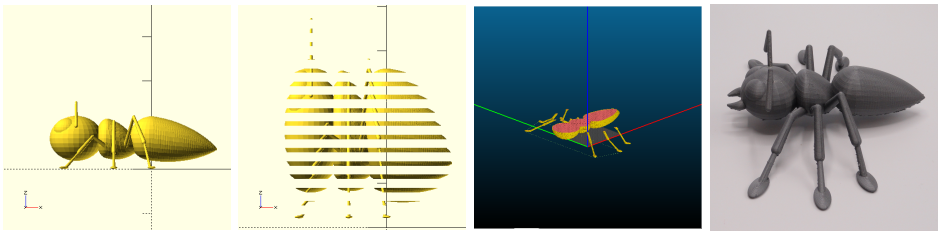

a b c d

Figure 3.1: Principle of Additive Manufacturing processes. a: 3D model of ant (Openscad v2015.03-2), b: Slicing of the 3D model (Openscad v2015.03-2), c: Layer-by-layer building process (Slic3r v1.2.9), d: Printed model.

process. Because of this particular process (Figure3.1), 3D printing can produce all possible 3D-shaped objects as long as it does not collapse during building, e.g. by gravitational forces [134].

AM is divided in 7 kinds of processes depending on how each additional layer of material is created [135] (Table 3.2). The choice of process is a critical one as it defines which kind of materials can be used in the process, the resolution that can be obtained and if there are any limits on the range of possible 3D-shapes. For example, Stereolithography (SLA) is a process where the new layer of material is cured by UV light within a layer of liquid photopolymers. Materials are thus restricted to photopolymers or materials that can be functionalised using photopolymers. Also, overhanging structures need support to be produced [136]. Alternatively, FDM (Fused Deposition Modelling) is a highly customizable process: here molten material is extruded through a nozzle. By combining several nozzles, it is possible to use several materials with various properties or colors [137] or even to create one's own material [138]. Another process often used in biomimetics research is Polyjetting. Here, droplets of material are jetted by a printer head to create each new layer. By adding more print nozzles, it is possible to use multiple materials in the same print or even create materials by mixing various components [139].
Progress has also been made with respect to materials with special properties. Conductive materials are now available [140] as well as soft materials [141] or even piezoelectric materials [142]. These kinds of materials are critical to produce actuators and sensors.

3.5 Biomaterials and structure

Insects are small and lightweight and they can synthesize materials with a large range of differing properties depending on the needed functionality of the material. Some of them are termed composite materials and obtain their mechanical properties from both the properties and the spatial arrangement of their constituents. From a broader point of view, structures built by arthropods, such as spider webs,

Category	Description	Advantages and disadvantages	Material resolution	Capability of multiple materials printing
Stereolithography	Stereolithography Apparatus (SLA) and DLP (Digital Light Processing) cure a layer of photopolymers with laser light point-by-point or a surface all at once	+ High dimensional accuracy and transparent material available − Restricted to photopolymers, time consuming material changing, material contamination and need of support structure	Good	Poor
Material extrusion	Fused or room-temperature materials are extruded through a nozzle. Ex: Fused Deposition Modeling (FDM) and 3D-bioprinting	+ Easy and cheap mechanisms, good materials properties, living cells can be incorporated − Relatively low dimensional accuracy and mechanical strength	Medium	Good
Powder bed fusion	Powder particles are fused together using a power source such as laser, heat or electron beam. Ex: Selective Laser Sintering (SLS) or Electron Beam Melting (EBM)	+ Wide range of materials, great material properties, high material strength, no need of support structure − Thermal stress, degradation, accuracy limited by the particle size of materials, material contamination when changing to other materials, require atmosphere control for metals	Low	Fair
Directed energy deposition	Materials, in the shape of powders or wires, are melted using a laser or electron beam and deposited according to a desired shape. Ex: direct metal deposition	+ Wide range of materials, great material properties − Low dimensional accuracy, thermal stress, requires atmosphere control, requires machining process to finish the part	High	Fair
Sheet lamination	Sheets of materials are cut and bound together. Ex: Ultrasonic Additive Manufacturing (UAM) uses ultrasounds to merge layers of metal	+ Fast process, high dimensional accuracy − Great amount of scrap, delamination, requires changeover when changing materials	Low	Fair
Material jetting	Material drops are jetted from printheads in a similar way as 2D-printing.	+ Fast process, wide range of materials, materials mixing on droplet scale, good accuracy − Limited to jettable materials, clogging problem	High	Excellent
Binder jetting	A binder is jetted on a bed of powder to stick the particles together. This process was originally known under the name 3D-Printing	+ Low temperature & fast process − High porosity, low surface quality, accuracy limited by particle size, difficult to remove trapped materials	Medium	Good

Table 3.2: Characteristics of the different AM processes, adapted from [143]

can give new ideas to architecture [144].

3.5.1 Structural materials

Biomaterials possess properties that make them special in regards to their human-made counterparts. They are lightweight, synthesizable in water solutions and biodegradable [145]. Many biomaterials are also composite materials: they are composed of several materials that are deposited in such a way that the resulting composite material can have better mechanical properties then any of its constituents [146]. This is for example the case of insect cuticle which is a mix of chitin nanofibers, water and various proteins and whose Young modulus varies from 1 kPa to 20 GPa [131].

AM and biomaterials can benefit from each other. Firstly, AM can play an important role in the development and use of composite and structural materials. Indeed, the possibility to produce and study such materials [146] has already been demonstrated. Water-repellent surface structures of springtails were also successfully reproduced and enhanced with AM to become repellent for almost any liquid [147]. Secondly, AM and more specifically FDM can produce materials with anisotropic properties by, for example, printing materials that are composed of a matrix and parallel fibers [148] as it is the case in silk [149]. The other way around, biomaterials can give new opportunities to AM, especially in 3D bio-Printing [150]. However, in traditional FDM, a filament of plastic is molten and made to flow through a nozzle. As 3D bio-printing concerns cells, a substance which can flow at room temperature and which is biocompatible and biodegradable is necessary. Bio-inks based on spider silk fibers have been created to meet these criteria [151].

On a larger scale, the two-way interaction still holds. AM can learn from insects how to design and produce 3D-shapes. This is especially the case for FDM which process is similar to the extrusion of silk by insects. An FDM nozzle put on a robot arm (Kukka arm) was shown to be able to mimick the cocoon construction process of a silkworm [6] (Figure3.2e).

3.5.2 Architecture

AM can help studying biostructures that have optimized load distribution such as honeycombs [152] and spiderwebs [4] (Figure3.2c). Those bio-structures have concrete applications, in architecture for example. Frei Otto who popularized lightweight structures was inspired by spiderwebs among others [144]. On the micro-scale, geometries of the stings of mosquitoes [153] and bees [3] were reproduced to create high-quality needles (Figure3.2b).

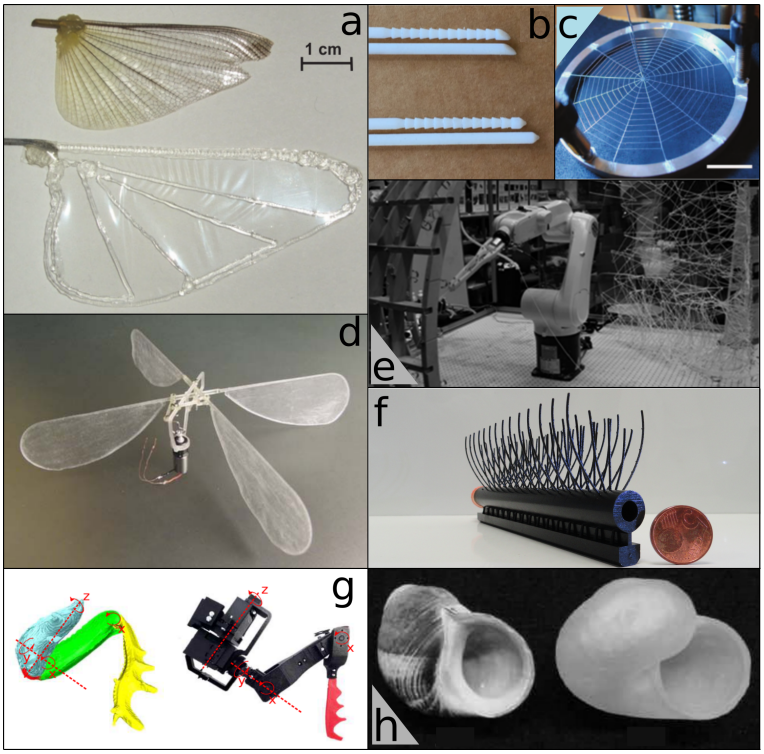

Figure 3.2: Application of Additive Manufacturing to insect-inspired biomimetics. a: Dragonfly-inspired wing [2]; b: Honeybee-inspired needles [3]; c: Biomimetic spiderweb [4]; d: Micro air vehicle with insect-inspired wings [5]; e: Robot arm building a cocoon-like structure in a similar way as silkworm [6]; f: Artificial antenna structure inspired from moth [7]; g: Multifunction beetle-inspired leg [8]; h: Natural and artificial shells for hermit crab preference tests [9]

3.6 Bioinspired locomotion

Insects live in very diverse ecological environments. Thus, they developed various strategies to move depending on whether they walk on solid or liquid surfaces, fly in the air or swim in water. Consequently, insects are a great source of inspiration for small-sized robots as they developed lightweight and efficient solutions to locomotion. The 3D-shape of organs such as wings or legs play a significant role in the performance of locomotion. AM can produce such complex 3D-objects and, thus, help to better understand the mechanisms of locomotion. These solutions can then be implemented to design better robots.

3.6.1 Actuators

Before being able to produce a full robot, AM must develop the capability to produce actuation. To this end, fabrication of the required actuators is a challenge, as they are composed of mobile parts, need ample energy supply and effective and efficient transduction mechanisms. Thanks to the development of soft materials for AM, it is now possible to produce soft actuators [154]. Actuators inspired from biological muscle fibers have even been developed [155]. However, this is a new development and another solution is to embed traditional actuators within 3D-printed parts [156].

3.6.2 Bioinspired robots

Locomotion is an important field for robotics [157]. Better understanding the physics of the various modes of locomotion of insects, such as walking and crawling, is crucial in designing better robots. In this regard, beetle [8] and leafhopper [158] legs have been investigated with the help of AM in order to understand how their shapes were linked to their functions (Figure3.2g). A similar approach was conducted to better understand the physics of insect crawling [159, 160]. However, only the bodies of the crawling robots were built with AM technologies. Traditional actuators were then assembled with the robot. Cutkosky and his team [161] used another manufacturing process called Shape Deposition Manufacturing (SDM), a process which combines moulding, parts embedding and assembly, to produce their walking robot inspired from cockroach because it is a straightforward method to embed actuators. The recent development of Hybrid Deposition Manufacturing, a technology comparable to SDM but with more parts being produced by 3D printing [162], could give Additive Manufacturing an important role in this domain.

3.6.3 Flying robots

Biomimetic flying robots have been under study for almost 30 years [163] and insects have gained a special focus as an effective source of inspiration [164]. Indeed, insects are small and some of them have excellent flying capabilities. They

perform flapping-wing flight which requires flexible wings [165]. Most of the work about insect-inspired flying robots has thus been dealing with wing shape and flexibility. Although CNC milling [166] was also used, Additive Manufacturing is a more convenient tool to investigate how wing geometry is related to flight performance. Most of the time, only the frame of the wing was produced with AM and subsequently a film was applied to mimick the membrane [167, 2] (Figure3.2a). Richter *et al* [5](Figure3.2d) were the only ones to completely produce wings with AM technology. Wing flapping physics has received ample attention and AM can help produce customized mechanical parts [5, 168].

Insect-inspired biomimetic AM can have surprising applications, for example in a culinary context: inspired by the rove beetle, a cocktail boat was put into motion on a water surface using the Marangoni propulsion [169].

3.7 Bioinspired sensors

Insects have evolved multiple sensors to interact with their environment. Here again, the 3D-shape of the sensors can have a profound importance and, thus, AM could be an efficient tool to investigate or reproduce biosensors [170].

Moth antennae are very sensitive olfactory sensors and they have a complex 3D-shape. Thanks to AM, it was possible to partly reproduce this shape and investigate its efficiency [171]. Arthropod eyes are also a good source of inspiration for biosensors. Studies and production of biomimetic eyes have been undertaken [172], showing the high interest in this kind of sensors. However, only during the last years was AM able to print micro-optics [173, 174] and a project to produce a biomimetic eye entirely through AM is currently in progress [175]. A last kind of biomimetic sensor developed with AM is an acoustic device inspired from a locust [176] thanks to the new possibility to use piezoelectric materials.

The literature about AM and insect-inspired sensors is actually quite recent. However, with the continuing technological developments of AM, accuracy is increased and a broader range of materials is available. We believe that this progress will help to accelerate design and study biosensors with AM in the near future.

3.8 Discussion

Additive Manufacturing is a group of evolving technologies. Processes are improved, accuracy is increasing, printers become cheaper and an increasing variety of materials is now usable such as flexible and/or conductive materials. This progress gives AM an increasing potential to produce objects with specific properties. For example some biomaterials display gradient properties which may be reproduced by e.g. polyjetting. However, AM is not always used for its enabling capabilities: it may as well just be a method to conveniently and cheaply produce

simple objects that help studying certain phenomena [177].

A dichotomy can be observed between the investigations aiming at mimicking the shape of an insect, or one of its organs, for technological applications, and those where the mechanisms are investigated in a biological context. In the former case, the challenge is usually a technical one: for example, Richter *et al* succeeded in manufacturing a flying robot [5]. In the latter case, AM is a very useful tool as it allows to produce similar objects with different parameters to better understand how they affect the performance of the real animal [2].

AM can also be used to investigate insect-environment interactions: artificial shells (Figure3.2h) and flowers with various geometrical parameters were offered to respectively hermit crab [9] and tobacco hawk moth [178] to determine their preferred choice. However, the accuracy of the chosen AM process can have a strong influence as the result might not be detailed enough to lure real insects [179].

Products built with AM processes undergo changes overtime or during the cooling period. With the development of smart materials, 4D printing tries to increase this change and integrate it in the design of the object. The objective is to change the shape or the function of an object depending on time or on the environmental conditions [180]. 4D-printed biomimetic structures [181] may give access to new design opportunities in insect biomimetics in the future.

3.9 Conclusion

As this survey shows, Additive Manufacturing using insects as templates is in its early days but is burgeoning. We expect to see major breakthroughs in a not too distant future. Indeed, the major technologies are already available: printing tiny details or huge structures, printing with different materials, or ones which change over time or over space. However, the challenge lies in the integration of technologies which may be principally not impossible but conceptually hard to realize in practice (e.g. extending photo polymerization technology, e.g. Nanoscribe (https://www.nanoscribe.de/en/), to multimaterial printing). The market will drive the speed of this evolution and, once this integration is achieved, we will see a flurry of very realistic and functional insect bio-inspired parts being produced, with levels of detail true to the real structures.

3.10 Conflicts of interest

The authors declare no conflict of interest.

3.11 Acknowledgements

This research was supported by the Region Centre-val-de-Loire.

3.12 Interesting articles

**[136] : Stereolithography process was enhanced to generate water support structures which are easily removable.

*[147] : The authors reproduced micro-structures at the surface of some insects called sprintails and that are known to be water-repellent. Thanks to Additive Manufacturing, they could modify the geometry of the structures so the surface would become repellent to any liquid.

**[4] : With the use of Additive Manufacturing, the roles of single thread mechanical strength and spider web geometry in the overall mechanical strength of a spiderweb is better understood.

*[3] : Needles with designed inspired from honeybee sting give less pain than traditional needles.

**[155] : Pneumatic soft actuators designs were inspired by the arrangement of fiber in muscles and were fabricated through Additive Manufacturing.

*[160] : Caterpillar locomotion is mimicked by a 3D-printed soft robot.

*[167] : Thanks to Additive Manufacturing, very realistic dragonfly-inspired wings were fabricated and the authors showed the importance of the membrane of the wing in its overall mechanical resistance.

*[173] : Micro-optics were successfully fabricated with Additive Manufacturing.

*[176] : An acoustic device inspired by locust and built with Additive Manufacturing gave insights to better design frequency-selective devices.

Chapter 4

3D-Printing cylinders

4.1 Résumé en Français

Dans le but de fabriquer des modèles artificiels d'antennes, nous nous sommes intéressés à l'impression 3D de cylindres longs et fins. En effet, les antennes pectinées possèdent de nombreux éléments, les ramis et les sensilles, qui ont une telle géométrie. Plus précisément, nous nous sommes intéressés à une imprimante 3D en particulier, l'Objet Eden 260 (Stratasys, Eden Prairie, Minnesota, USA) et nous avons imprimé des cylindres dont le diamètre était égal à quelques multiples du plus petit détail possible qui correspondait à la taille d'une goutte de matériel produite par l'imprimante 3D. Nous avons fait varié le diamètre, la longueur et l'orientation du cylindre par rapport à la direction de fabrication. Nous avons ensuite développé des modèles de mécaniques des matériaux afin d'expliquer comment les paramètres étudiés influencent le succès de fabrication des cylindres.

4.2 Introduction

To understand how pectinate antenna capture pheromone molecules in air, the first step is to study how air flows through the antenna. We decided to resort to an experimental approach using a Particle Image Velocimetry setup (see Chapter 6). However, before doing any experiment of fluid dynamics, we have to build the artificial models of the antennae which will be used in the experiments. Given the complex shape of the natural antennae (Chapter 1), Additive Manufacturing is a convenient tool because it allows great freedom of designs and is particularly adapted to fabricate custom objects in little time. However, as we will argue, 3D technologies are not yet developed sufficiently to print objects with the great dynamic range of scales as found in nature. Therefore in this chapter it is our aim to investigate what the minimum dimensions are that we can print with various printers and which still give us robust structures. To this end we will 3D print

a variety of cylinders and observe how they withstand the 3D printing and post-processing process. Some models to understand the experimental findings will be introduced and compared.

As a reminder, a pectinate antenna is composed of a long flagellum, two rows of rami and numerous sensilla. There are almost 4 orders of magnitude of difference between the smallest details of the antenna (the diameter of the sensilla) and its total size. Currently, no Additive Manufacturing process is able to handle such a wide span of orders of magnitude. Our approach consists of splitting the antenna in two levels: the macrostructure, composed of the flagellum and the rami (see Chapter 5), and the microstructure, composed of one ramus and its sensilla (for more details, see Chapter 6). In both cases, the structure is composed of numerous cylinders with high aspect ratios (Table 4.1), the rami in the case of the macrostructure and the sensilla in the case of the microstructure. The capacity of Additive Manufacturing to produce long cylinders is thus a key parameter to build the artificial models of antennae that we want to use in our experiments.

	Length	Diameter	Aspect ratio
Flagellum	1 cm	200 µm	50
Rami	1500 µm	50 µm	30
Sensilla	150 µm	3 µm	50

Table 4.1: Characteristics of the cylinders modeling the various elements of an antenna. The aspect ratio is defined as the ratio of the length of a cylinder over its diameter.

We tried several Additive Manufacturing processes in order to find one which could 3D-print the artificial models that we needed. We tried the Nanoscribe (Karlsruhe, Germany). This 3D-printer uses two-photon polymerization to build microscale objects. To our knowledge, this is currently the commercial 3D-printer with the highest resolution. However, we did not succeed in fabricating a scaled-down microscale model (Figure 4.1a) even though one successful attempt has been reported in the literature [171].

We also made a try with a Digital Light Processing printer, the Miicraft (Jena, Germany) which relies on photopolymers that cure under UV light. A digital micromirror device determines where the UV light touches the surface of the photopolymer vat and cures the phtopolymeres. We attempted to build straight cylinders using this process but also failed, most likely due to capillary effects (Figure 4.1b).

Eventually, we resorted to two 3D-printers, the Form 2 (Formlabs, Somerville, Massachussetts, USA), Figure 4.1c and the Objet Eden 260 (Stratasys, Eden

Prairie, Minnesota, USA), Figure 4.1d. The former relies on photopolymerisation (for more details, see Chapter 6) and the latter on material jetting.

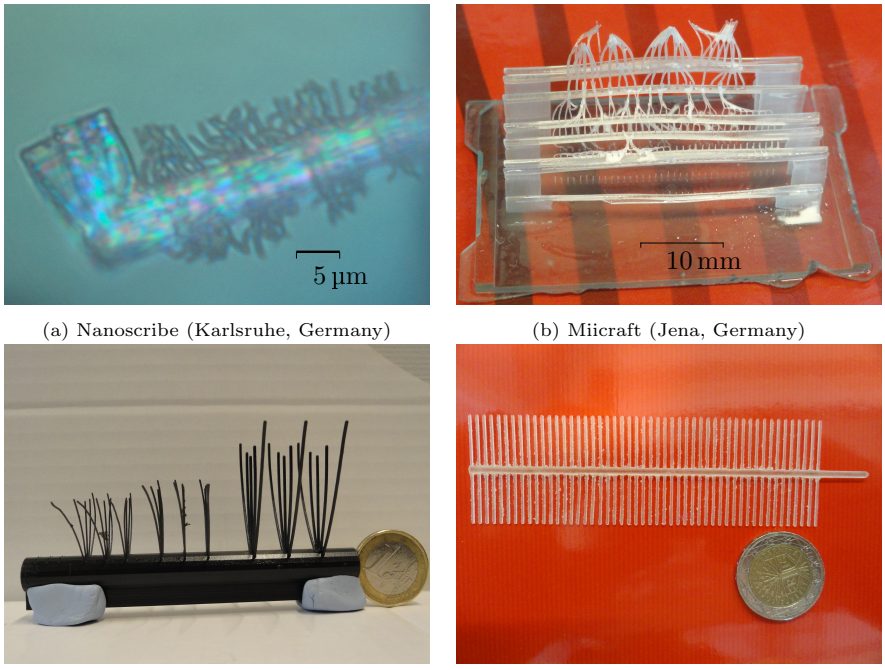

(a) Nanoscribe (Karlsruhe, Germany)

(b) Miicraft (Jena, Germany)

(c) Form 2 (Formlabs, Somerville, Massachussetts, USA)

(d) Objet Eden 260 (Stratasys, Eden Prairie, Minnesota, USA)

Figure 4.1: Attempt to fabricate cylinders with several 3D printers.

Given the difficulties we faced to 3D-print cylinders with high aspect ratio, we decided to investigate the limiting factors which prevent to 3D-print long cylinders with small diameters. We focused solely on one 3D-printer, the Objet Eden 260 (Stratasys, Eden Prairie, Minnesota, USA). We 3D-printed cylinders with several diameters, aspect ratios and orientation to the building direction. We then developed a few models to try to predict the survival of the cylinders.

4.3 3D-Printing of cylinders

4.3.1 Materials and Methods

We 3D-printed batches of cylinders with various diameters and aspect ratios. The 3D-printer was an Objet 260 (Stratasys, Eden Prairie, Minnesota, USA) and we used the VeroWhite material (Stratasys, Eden Prairie, Minnesota, USA). The resolution of the printer was set at 42 µm in the horizontal plane and 32 µm in the

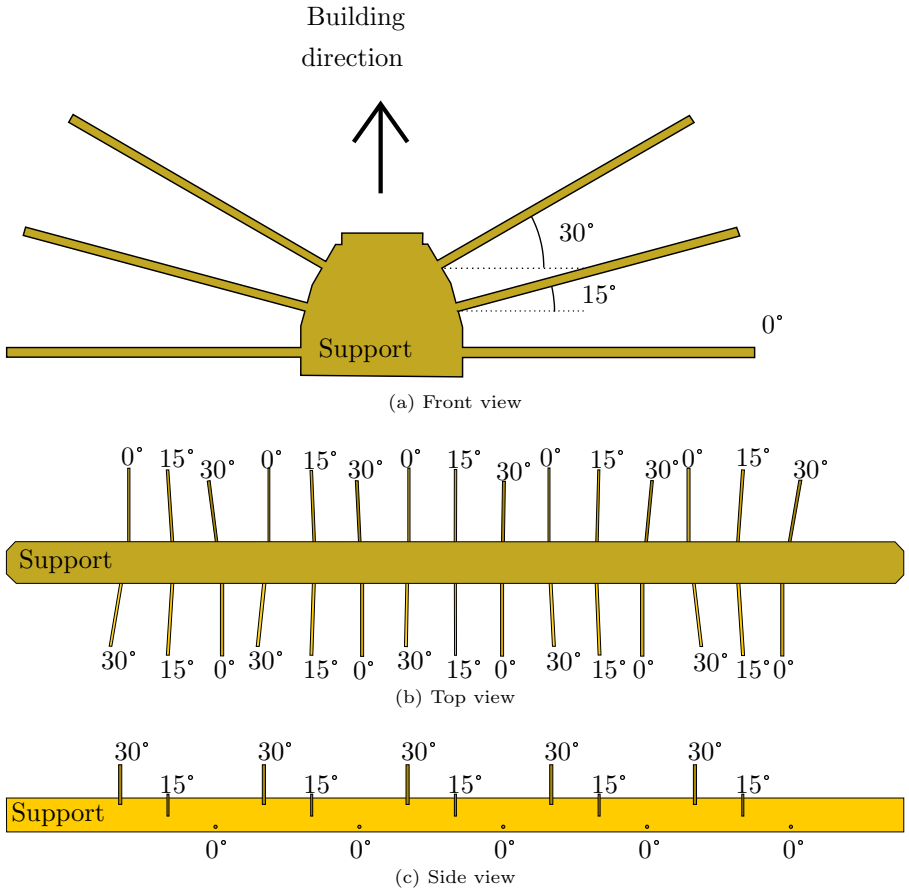

Figure 4.2: Distribution of the cylinders on the support ($D = 10$, $L = \frac{d}{L} = 30$)

building direction. We chose 5 diameters D $\{5, 10, 20, 30, 50\}$ expressed in multiples of the horizontal resolution. For example a diameter $D = 5$ is equal to $5 * 42\,\mu m = 210\,\mu m$. We defined the aspect ratio L as the ratio of the length L on the diameter d and chose 4 ones $\{10, 20, 30, 50\}$. Thus, the length of a cylinder of diameter $D = 20$ and aspect ratio $L = 30$ is $20 * 30 * 42\,\mu m = 25\,200\,\mu m$. We also investigated the influence of the orientation with respect to the vertical axis with three angles α $\{0°, 15°, 30°\}$.

For a given set of diameter, aspect ratio and angle, 10 replica were printed. The 10 replica of each of the 3 angles of a set of diameter and aspect ratio were printed on the same support cylinder and, hence, in the same fabrication run. We varied the angles of the cylinders according to the scheme shown in Figure 4.2.

The cylinders were 3D-printed surrounded by a support material (Objet Support SUP705, Stratasys, Eden Prairie, Minnesota, USA) which is water-soluble.

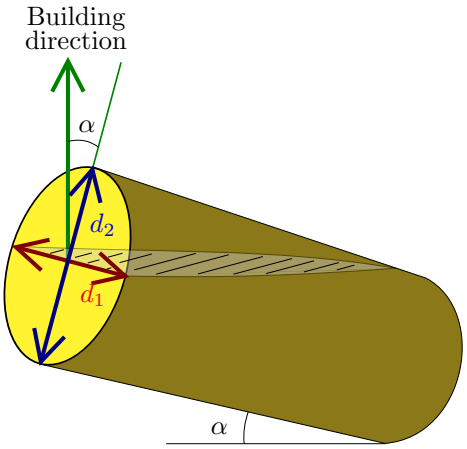

Figure 4.3: Measurement of the cross section of the cylinders. The two directions used to measure the diameter are perpendicular. d_1 is the diameter measured in the horizontal direction, which is also the intersection between the cross section and the horizontal plane (shaded area). d_2 is the diameter in the perpendicular direction, which is also the direction of the building direction projected on the plane of the cross section.

The support material was dissolved in a water solution with 2% sodium hydroxyde and 1% sodium metasilicate in a support cleaning apparatus SCA-1200HT (Stratasys, Eden Prairie, Minnesota, USA).

After removal of the support material, we took a picture of each cylinder and measured them using Inkscape software (V0.91, inkscape.org). Four measurements were done: at each extremity the diameter was measured in the horizontal direction and in the building direction projected on the cross section (Figure 4.3). The focus-point in the pictures was set a little behind the extremity of the cylinder to ensure that what we measured was the actual diameter of the cylinder. Indeed, at the distal end, some narrowing of the cylinder occurred, maybe due to drop-wise approximation of the intended structure as inherent in the 3D printing process. At the basal end we had to cut the cylinder from the support. We had to accept that the cutting process could locally alter the shape of the cross section.

4.3.2 Results

After removal of the support material, we could observe which cylinders survived the fabrication and post-processing steps (see e.g. Figures 4.4a and 4.4b). We considered that a cylinder survived if it looks straight and complete *i.e.* there is no sign of failure. In Table 4.2, we report the number of cylinders, out of ten replica, which were considered to have survived.

We also measured the length of all cylinders, including the broken ones. Only results for the cylinders with diameters $D = 5$ or $D = 10$ are displayed (respectively Figures 4.4, 4.5, 4.6 and 4.7) because the cylinders with larger diameters

almost all survived the fabrication processes and had relative lengths close to 100%. The cylinders with the smallest diameters and the highest aspect ratios are the most likely to break.

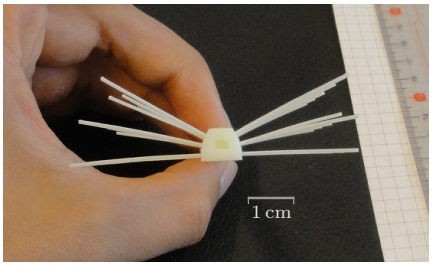

Front view

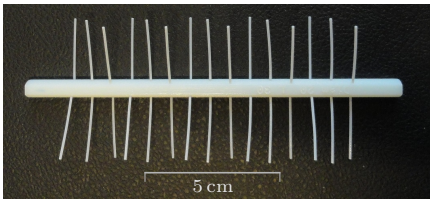

Top view

(a) $D = 20$ and $L = 30$. All cylinders survived fabrication and post-processing

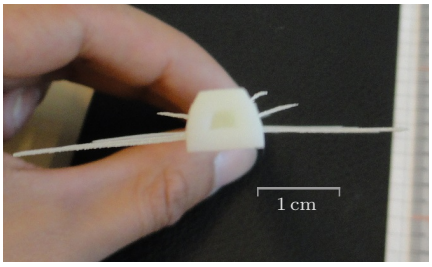

Front view

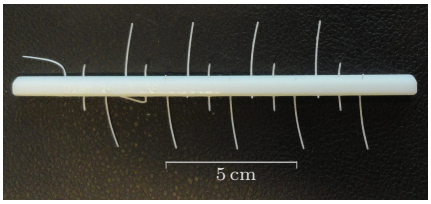

Top view

(b) $D = 10$ and $L = 50$. Only cylinders with an angle $\alpha = 0°$ survived. Cylinders with $\alpha = 15°$ broke at comparable positions. Cylinders with $\alpha = 30°$ mostly dissapeared.

Figure 4.4: Examples of cylinders after fabrication and post-processing steps.

Measured diameter values are reported in table 4.3. There is no measurement for $D = 5$ and $\alpha = 30°$ because the remaining parts of the cylinders after post-processing were either non existent or too short.

4.3.3 Experimental observations

Looking at the experimental results, see Tables 4.2 and 4.3 we can make some some observations.

- Not unexpectedly we see that there is a rather strong trend that thicker beams better survive the fabrication and post-processing steps.
- Overall there is a tendency that the larger the aspect ratio the more likely the beams are to break
- The angle α plays an important role in the survival ratio of the beams where larger angles seem to result in smaller number of surviving cylinders.
- We make an important observation with respect to the resulting lengths after fabrication and post-processing. For point loads at the tips and for homogeneous loading, the stress on the beams is maximum at the point where they

	$L = 10$	$L = 20$	$L = 30$	$L = 50$
$D = 5$				
$\alpha = 0^\circ$	10	10	10	9
$\alpha = 15^\circ$	6	3	2	0
$\alpha = 30^\circ$	0	0	0	0
$D = 10$				
$\alpha = 0^\circ$	10	10	10	9
$\alpha = 15^\circ$	10	8	6	0
$\alpha = 30^\circ$	0	0	0	0
$D = 20$				
$\alpha = 0^\circ$	10	10	10	10
$\alpha = 15^\circ$	10	10	10	10
$\alpha = 30^\circ$	10	10	10	9
$D = 30$				
$\alpha = 0^\circ$	10	10	10	10
$\alpha = 15^\circ$	10	10	10	10
$\alpha = 30^\circ$	10	10	9	10

Table 4.2: Number of cylinders (out of 10) which survived the fabrication and post-processing steps. Survival means that the cylinder is more or less straight and has no sign of failure.

are attached to the support. However, we see many cylinders that actually break at other positions and will pay attention to this in section 4.4.4.

- With respect to the diameters of the fabricated cylinders the main observation is that cylinders designed with a small diameter ($D = 5$ and $D = 10$, equivalent to, respectively, 210 µm and 420 µm) were not faithfully produced by the 3D-printer. Cylinders with a diameter $D = 5$ displayed a mean diameter down to $D = 3.38$ (67% of the desired diameter) in the case $L = 10$ and $\alpha = 0^\circ$, and up to $D = 12$ (240% of the desired diameter) in the case $L = 30$ and $\alpha = 0^\circ$. There is also a constant bias between the diameters measured in the two perpendicular directions: d_1-values (horizontal direction) are longer than the ones in the perpendicular direction d_2. The ratio of d_1 over d_2 can even reach 3 ($D = 5$, $L = 10$, $\alpha = 15^\circ$).

In the next section we will introduce some models in order to see if the above observations can be understood from a theoretical point of view.

		$L=10$		$L=20$		$L=30$		$L=50$	
		(D)	(µm)	(D)	(µm)	(D)	(µm)	(D)	(µm)
$\alpha = 0°$									
$D=5$	d_1	10.2 (0.93)	426 (39)	11.14 (0.76)	468 (32)	12.0 (2.9)	505 (123)	11.3 (0.9)	474 (37
	d_2	3.38 (0.35)	142 (15)	3.96 (0.36)	166 (15)	4.53 (2.55)	190 (107)	3.79 (0.61)	159 (26
$D=10$	d_1	14.6 (1.1)	612 (47)	14.0 (0.7)	589 (31)	15 (1.6)	630 (66)	14.6 (1.2)	613 (50)
	d_2	8.4 (1.5)	352 (62)	9.3 (0.9)	392 (38)	8.9 (1.0)	375 (43)	8.4 (1.4)	354 (61)
$D=20$	d_1	17.8 (0.5)	749 (22)	17.3 (0.6)	727 (24)	17.2 (0.4)	721 (15)	17.4 (0.6)	731 (24)
	d_2	20.9 (0.4)	879 (17)	20.7 (0.7)	870 (30)	20.7 (0.7)	870 (31)	20.7 (0.6)	870 (27)
$D=30$	d_1	28.2 (0.8)	1185 (35)	28.0 (1.0)	1175 (44)	27.9 (0.9)	1170 (36)	28.1 (1.1)	1179 (44)
	d_2	29.7 (0.9)	1246 (36)	30.2 (0.9)	1267 (39)	30.0 (0.7)	1261 (27)	29.7 (0.7)	1248 (32)
$D=50$	d_1								
	d_2								
$\alpha = 15°$									
$D=5$	d_1	10.3 (1.4)	431 (58)	9.1 (1.4)	381 (60)	10.7 (0.9)	451 (39)	10.5 (0.6)	441 (24)
	d_2	3.4 (1.1)	145 (46)	3.8 (1.7)	158 (77)	3.7 (0.7)	155 (30)	4.1 (0.8)	171 (35)
$D=10$	d_1	13.4 (0.9)	562 (37)	13.6 (0.68)	573 (28)	14.0 (1.3)	589 (54)	13.8 (1.6)	581 (68)
	d_2	7.5 (0.7)	315 (31)	7.9 (0.9)	330 (38)	7.7 (1.2)	324 (52)	5.9 (1.9)	247 (80)
$D=20$	d_1	21.1 (0.5)	886 (20)	20.9 (0.5)	877 (20)	21.3 (0.6)	893 (27)	22.0 (1.0)	922 (40)
	d_2	17.8 (0.7)	746 (28)	17.1 (0.4)	718 (18)	17.2 (0.6)	723 (23)	17.8 (0.9)	749 (37)
$D=30$	d_1	29.5 (1.0)	1241 (44)	30.2 (0.5)	1268 (19)	30.9 (0.6)	1297 (24)	30.6 (0.7)	1286 (28)
	d_2	26.7 (0.5)	1122 (23)	26.2 (0.6)	1101 (25)	26.8 (0.6)	1127 (24)	27.2 (1.0)	1143 (42)
$D=50$	d_1	48.9 (0.9)	2053 (40)	48.8 (1.1)	2049 (46)				
	d_2	45.9 (1.0)	1927 (40)	45.8 (1.0)	1926 (43)				
$\alpha = 30°$									
$D=5$	d_1								
	d_2								
$D=10$	d_1	13.4 (2)	564 (8)	13.4 (0.2)	564 (7)	17.0 (2.3)	713 (0.1)		
	d_2	10.2 (0.4)	430 (18)	9.2 (0.3)	387 (12)	10.2 (2.3)	428 (98)		
$D=20$	d_1	21.6 (0.9)	907 (40)	22.0 (0.5)	923 (21)	22.1 (0.7)	926 (30)	26.0 (4.7)	1091 (199)
	d_2	17.4 (0.4)	732 (18)	17.3 (0.5)	725 (20)	17.3 (0.5)	725 (22)	17.1 (1.1)	718 (47)
$D=30$	d_1	30.2 (0.8)	1270 (33)	30.0 (0.5)	1261 (19)	30.8 (0.6)	1295 (24)	33.2 (5.2)	1394 (218)
	d_2	27.3 (0.7)	1148 (31)	27.0 (0.5)	1133 (19)	26.6 (0.7)	1119 (28)	26.8 (1.4)	1124 (61)
$D=50$	d_1	48.7 (1.4)	2045 (58)	48.5 (1.3)	2038 (56)				
	d_2	48.0 (1.1)	2014 (45)	47.4 (1.6)	1989 (66)				

Table 4.3: Mean and standard deviation (in brackets) of the diameter of the cylinders depending on the design-diameter, the aspect ratio and the angle of the layers. The diameters are measured in two directions (Figure 4.3) and their values are given in two units. Firstly in multiples of the droplet size (a cylinder with diameter $D = 5$ is expected to have a diameter which is five times the droplet size) and secondly in µm.

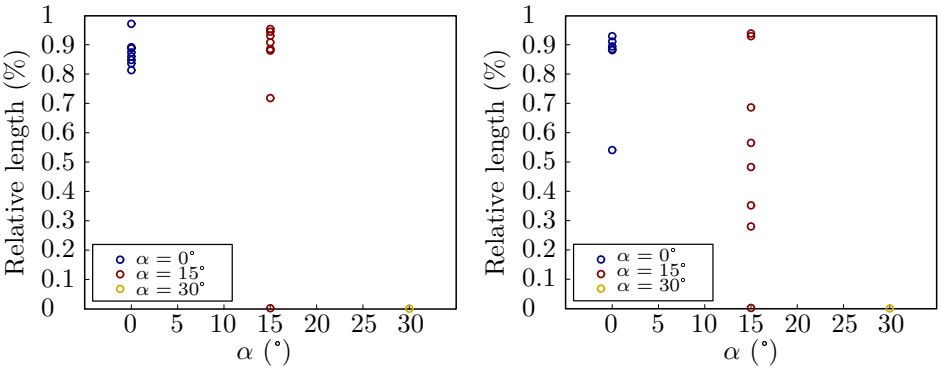

(a) Aspect ratio $L = 10$

(b) Aspect ratio $L = 20$

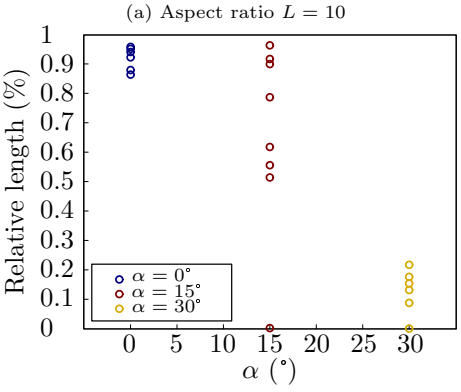

(c) Aspect ratio $L = 30$

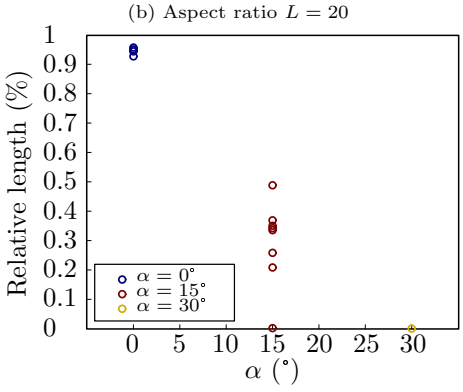

(d) Aspect ratio $L = 50$

Figure 4.5: Relative length of cylinders of diameter $D = 5$ after fabrication for aspect ratio's $L = 10$, $L = 20$, $L = 30$ and $L = 50$. All cylinders were measured, including broken ones.

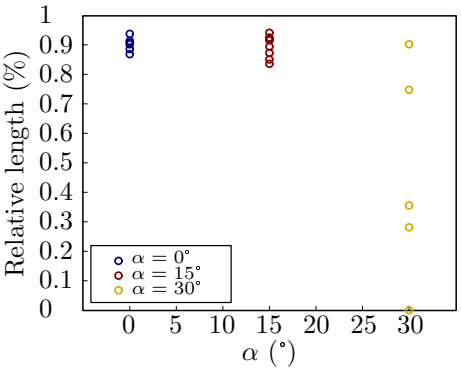

(a) Aspect ratio $L = 10$

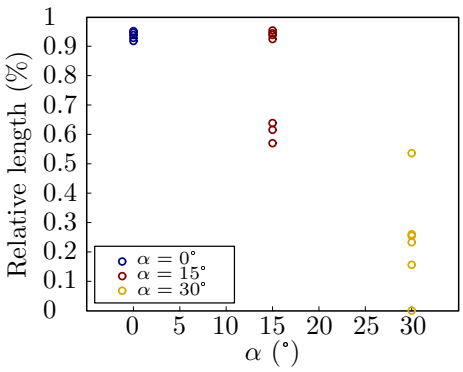

(b) Aspect ratio $L = 20$

Figure 4.6: Relative length of cylinders of diameter $D = 10$ after fabrication for aspect ratio $L = 10$ and $L = 20$. All cylinders were measured, including broken ones.

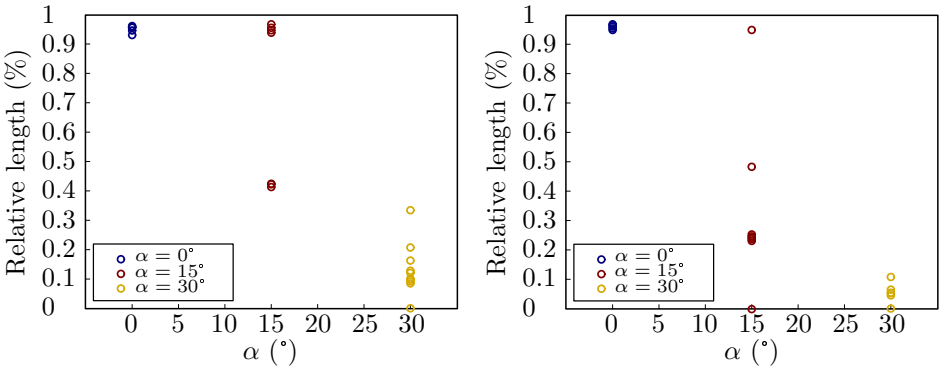

(a) Aspect ratio $L = 30$ (b) Aspect ratio $L = 50$

Figure 4.7: Relative length of cylinders of diameter $D = 10$ after fabrication for aspect ratio $L = 30$ and $L = 50$. All cylinders were measured, including broken ones.

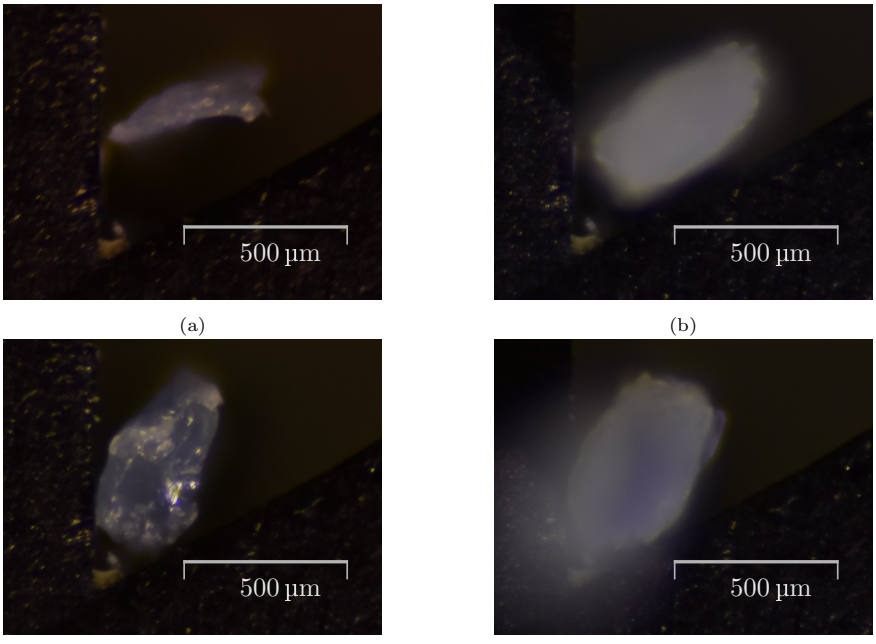

(a) (b)

(c) (d)

Figure 4.8: Diameters of cylinders with $D = 10$, $L = 20$ and $\alpha = 15°$. (a) distal end of the cylinder showing a narrowing of the cross section which may be due to the layer-by-layer building process. (b) the focus plane is a slightly behind the distal end and the orientation of the layers are still visible on the sides of the cross section. (c) basal end of the cylinder showing the alteration of the cross section due to the cutting of the cylinder. (d) the focus plane is slightly behind the basal end to reveal an undisturbed cross section.

4.4 Mechanical modelling of 3D printed cylinders

In the 3D printing proces of the cylinders there is little reason they brake as the cylinders are covered in a soluble support material (see section 4.3.1). However, during post-processing the structures are flushed with the dissolver fluid. As the support material is increasingly dissolved the cylinders get more exposed to the hydrodynamic forces and eventually the breaking off of the cylinders is dependent on both the exerted loads and the shear and/or normal yield stress. Evidently, the latter is affected by the laminar structure inherent in layer-wise fabrication.

In this section we first look at the possible loading conditions, then continue with a simple model for a homogeneous beam. Eventually we consider the possible effects associated with the laminar nature of the beams.

4.4.1 Forces exerted on the cylinders in post-processing

Uniformly-distributed force

Cylinders most likely break during post-processing which consists of a turbulent aqueous solution which dissolves the support material. A simple way to model the force exerted by the water on the cylinders is to consider that it is equal to the drag force:

$$F_d = \frac{1}{2} C_d S \rho v^2 \tag{4.1}$$

with C_d the drag coefficient (nondimensional),
S, the frontal surface of the cylinders (m^2),
ρ, the density of the fluid ($\mathrm{kg\,m^{-3}}$),
v, the velocity of the fluid ($\mathrm{m\,s^{-1}}$).

In the case of the drag force, the model of a uniformly-distributed load is the most appropriate one. Equation 4.1 gives a load p:

$$p = \frac{1}{2} C_d d \rho v^2 \tag{4.2}$$

Cylinder independent force

During fabrication, the cylinders are covered with a support material. The support material is very flexible so it does not add any substantial mechanical stiffness to the cylinders. However, it increases the drag to be supported by the cylinders. In first approximation, we consider that the diameter of the cylinder + support material is independent of the diameter of the cylinders and equal to d_S. We obtained the following drag force:

$$F_d = \frac{1}{2} C_d L d_S \rho v^2 \tag{4.3}$$

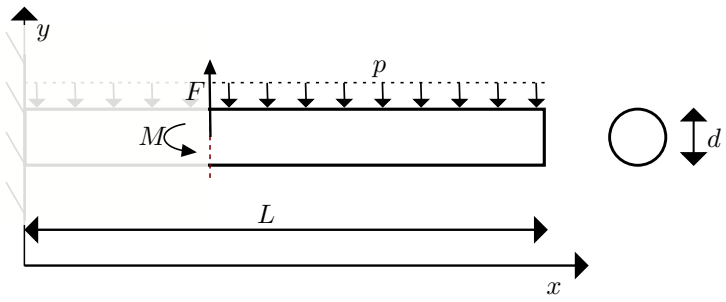

Figure 4.9: Homogeneous beam with a uniformly-distributed load

Thus the load per unit of length is:

$$p = \frac{1}{2} C_d d_S \rho v^2 \tag{4.4}$$

4.4.2 Longitudinal stress in homogeneous beams

The simplest model to describe the cylinders is by assuming them to be homogeneous, prismatic cylinders of circular cross-section. Despite the laminate nature of the cylinders, which will certainly be reflected in survival statistics, it seems a reasonable first approximation for modeling the loads on the beams at various positions. Two models of internal stress, resulting from the loading by the environment during the fabrication and post-processing, are considered: a beam of length L with uniformly-distributed load p (Figure 4.9) and the same beam but now with a concentrated load P at the tip of the cylinder, where.

$$P = Lp \tag{4.5}$$

We take the origin of the x-axis at the base of the cylinder. A distributed load p pointing in the negative y direction is exerted on the beam. To determine the stress within the cylinder, the force equilibrium is determined for the free body section of the beam from a coordinate x to the tip (Figure 4.9).

From the equilibrium relation for the forces in the y-direction, we obtain, with F and p positive in the direction of the arrows displayed in Figure 4.9:

$$F = p(L - x) \tag{4.6}$$

Note that F is also the shear force along the y-direction, which is increasing with decreasing x. Similarly the z-moment equilibrium, with moments taken positive in the counterclockwise direction, gives,:

$$M = \int_x^L (x' - x) p dx' = \frac{p}{2} (L - x)^2 \tag{4.7}$$

We can then determine the local stress in the beam according to the flexure formula. In the current case only the longitudinal stress due to moment is taken into consideration. This longitudinal local stress σ_x is:

$$\sigma_x(x, y) = \frac{M(x)y}{I} \tag{4.8}$$

with I the moment of inertia of the circular section. In our case of a circular section,

$$I = \frac{\pi d^4}{64} \tag{4.9}$$

with d the diameter of the cross section. We obtain

$$\sigma_x(x, y) = \frac{p}{2}(L - x)^2 y \frac{64}{\pi d^4} \tag{4.10}$$

Thus, at a given section, at $y = \frac{d}{2}$

$$\sigma_{x,\max}(x) = p(L - x)^2 \frac{16}{\pi d^3} \tag{4.11}$$

And the maximum horizontal stress, at $x = 0$, is

$$\sigma_{\max} = pL^2 \frac{16}{\pi d^3} \tag{4.12}$$

The situation with a point load of $P = pL$ is very much comparable and leads to a maximum stress of:

$$\begin{aligned} \sigma_{\max}(x) &= pL(L - x)\frac{32}{\pi d^3} \\ \sigma_{\max} &= pL^2 \frac{32}{\pi d^3} \end{aligned} \tag{4.13}$$

i.e. this means that the maximum stress is a factor of 2 more than for the distributed load.

Consequences

The results of the previous section are well-known [182]; they show that the maximum longitudinal stress, σ_x, occurs at the base of the cylinder. Not taking into account the lamellar nature of the beams it is thus likely that the cylinders break most likely at this location. We also found that at a cross-section, at given position x, the maximum stress occurs at the surface of the cylinder. Comparison of

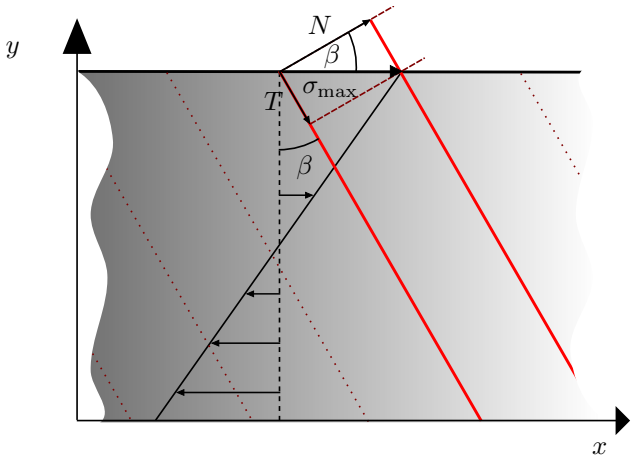

Figure 4.10: Orientation of the layers (red lines) in a part of the beam. The axis of the beam is the x-axis. $\sigma_{\max}$ is the maximum stress determined in the previous section. N is the component of the force normal to the plane of the layers and T is the force component tangential to the xy-plane (*i.e.* the shear-stress along the layer-interfaces).

equations 4.12 and 4.13 shows that for a given total load, P, the cylinders are less likely to break for the distributed load. However, these models are concerned with the longitudinal stress but have neither taken into account the stress that may occur in the transverse direction nor the laminate nature of the cylinders. This will be addressed in the following sections.

4.4.3 Longitudinal stress in lamellar beam

In the first model of a lamellar beam, we model the beam as a superposition of homogeneous layers as our cylinders are 3D-printed layer after layer. The objective is to study how the orientation of the layers with the axis of the cylinder can alter the mechanical properties of the beam. We assume that the stress distribution in a lamellar beam is similar to a homogeneous beam. We are then able to determine how the orientation of the layers changes the mechanical strength of the beam.

We consider that the weakness of the beam lies in the inter-layer cohesion. We determine the stress perpendicular to the plane of the layer and how it changes with the orientation of the layers (Figure 4.10). Layers have an orientation β with the yz-plane ($\beta = \frac{\pi}{2} - \alpha$). The interesting value is the normal stress N which determines the stress perpendicular to the layers, as the interlayer cohesion is the element that is the most likely to fail.

Uniformly-distributed load

Using the expression found in equation 4.11, we find that:

$$N(x) = \cos(\beta)p(L-x)^2\frac{16}{\pi d^3}$$
$$T(x) = \sin(\beta)p(L-x)^2\frac{16}{\pi d^3} \tag{4.14}$$

and

$$N_{\max} = \cos(\beta)pL^2\frac{16}{\pi d^3}$$
$$T_{\max} = \sin(\beta)pL^2\frac{16}{\pi d^3} \tag{4.15}$$

Assuming the distributed load to be caused by a homogeneous drag-force, equation 4.2, and according to equation 4.15, the maximal stress is:

$$N_{\max} = \cos(\beta)\frac{8}{\pi}C_d\rho v^2\left(\frac{L}{d}\right)^2 \tag{4.16}$$

It is surprising to note that, everything else being constant, the maximum stress is only dependent on the aspect ratio $\left(\frac{L}{d}\right)^2$.

Cylinder independent load

If the distributed load is independent of the diameter of the cylinders, the maximum load perpendicular to the layer is (equation 4.4):

$$N_{\max} = \cos(\beta)\frac{8}{\pi}C_d d_S\rho v^2\left(\frac{L}{d}\right)^2\frac{1}{d}$$
$$T_{\max} = \sin(\beta)\frac{8}{\pi}C_d d_S\rho v^2\left(\frac{L}{d}\right)^2\frac{1}{d} \tag{4.17}$$

In this case, the maximum load, for a given aspect ratio $\frac{L}{d}$, is proportional to the diameter L/d^2.

Concentrated load

We consider now a less realistic model: a force P is concentrated at the tip and independent of the cylinder geometry (equation 4.13):

$$N(x) = \cos(\beta)\sigma_{x,\max} = \cos(\beta)P\,(L-x)\,\frac{32}{\pi d^3}$$
$$T(x) = \sin(\beta)\sigma_{x,\max} = \sin(\beta)P\,(L-x)\,\frac{32}{\pi d^3} \tag{4.18}$$

The maximum load is:

$$N_{\max} = \cos(\beta) PL \frac{32}{\pi d^3}$$
$$T_{\max} = \sin(\beta) PL \frac{32}{\pi d^3} \tag{4.19}$$

Thus, for a given aspect ratio $\frac{L}{d}$, the maximum stress is proportional to d^{-2}.

Consequences

In all three stress distributions, the maximum stress is located at the surface of the cylinder and the stress normal to the layers is related to the orientation with a dependence in $\cos(\beta)$. Thus, the best orientation is for $\beta = \frac{\pi}{2}$: in this situation the stress normal to the inter-layer surface is equal to 0. At the same time the shear stress is maximum for this angle. The maximum normal and shear yield stresses along the layer interface of the 3D printed cylinders will eventually be decisive for how the cylinders will break. However, the presented models still all predict that maximum loading is at the position where the cylinders sit on the support ($x = 0$).

4.4.4 Lamellar beam with bending and shear

Some cylinders, in our experiments, did not break at the base of the cylinder. Instead they broke some distance away from the support (Figure 4.4b). The model we developed so far cannot predict such behavior because the moment is always the highest at the support where the cylinder is attached, which therefore is the location where the cylinders are the most likely to break.

Thus, we now consider a model where the bending of the cylinder of length L is a function of the position x and the loading P and where the shear-force along the laminar interfaces changes accordingly over the length of the cylinders (Figure 4.11a). The loading P is parallel to the x-axis and exerts a point load that tends to bend the cylinder. The bending of the cylinder is dependent on x and the angle between the cylinder at location x and the x-axis is termed γ. As a reminder, β is the angle between the layers and the cross sections of the cylinder. We define a third angle, δ, which is the angle between the layers and the x-axis (Figure 4.11b).

A free body diagram exerted on the distal part of the cylinder (Figure 4.11b) shows that the moment exerted on the cross section at location x is, if we assume that the variation of the angle γ remains small:

$$M(x) = P(L - x) \sin(\gamma(x)) \tag{4.20}$$

We also have:

$$M(x) = EI \frac{\mathrm{d}^2 v}{\mathrm{d}x^2} = EI \frac{\mathrm{d}\beta}{\mathrm{d}x} \tag{4.21}$$

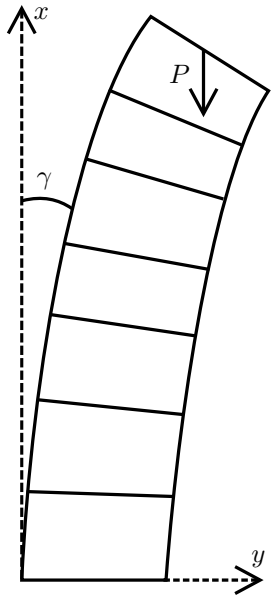

(a) Curved cylinder with an angle γ with the x-axis dependent on x

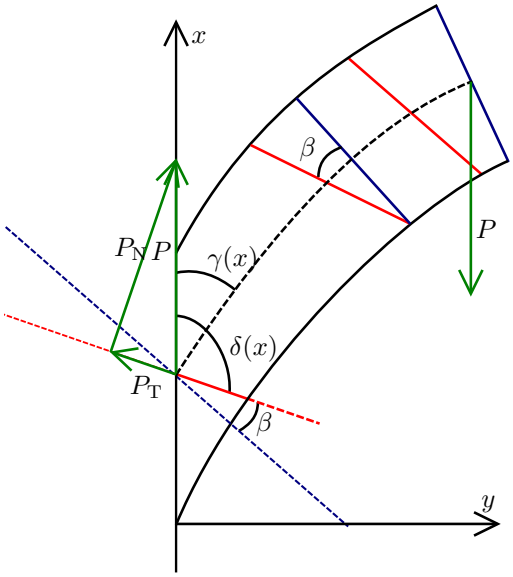

(b) Free body diagram applied on a part of the cylinder and definition of the angles. The blue lines are cross section perpendicular to the principal axis of the cylinder. The red lines show the orientation of the layers.

Figure 4.11: Curve of the cylinder depending on the position x

with E, the Young modulus of the material (Pa), I, the moment of inertia of the cylinder (m^4) and $v(x)$, the displacement of the neutral axis in the y direction at position x.

We integrate $\frac{d\beta}{dx}$ and consider the variations of $\gamma(x)$ with x to be negligible. In other words, we consider $\sin(\gamma(x))$ to be almost constant and approximate it with $\gamma_0 = \gamma(0)$. We obtain:

$$\gamma(x) \approx \frac{P}{EI}\left(Lx - \frac{x^2}{2}\right)\sin(\gamma_0) + \gamma_0 \tag{4.22}$$

and, consequently,

$$\delta(x) = \frac{\pi}{2} - \beta + \frac{P}{EI}\left(Lx - \frac{x^2}{2}\right)\sin(\gamma_0) + \gamma_0 \tag{4.23}$$

We thus obtain:

$$\begin{aligned} P_T &= -P\cos(\pi - \delta(x)) \\ &= -P\cos\left(-\beta + \gamma_0 + \frac{P}{EI}\left(Lx - \frac{x^2}{2}\right)\sin(\gamma_0)\right) \\ &= -P\cos\left(-\beta + \gamma_0 + \frac{PL^2}{EI}\left(\frac{x}{L} - \frac{x^2}{2L^2}\right)\sin(\gamma_0)\right) \end{aligned} \tag{4.24}$$

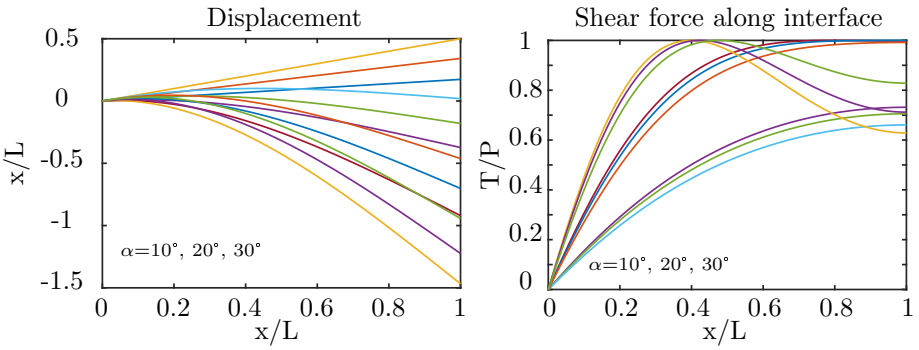

Figure 4.12: Left: displacement curves under increasing load as a function of x/L for α=10, 20, and 30°. Right: normalised tangential load T/P depending on x/L for the same angles.

The maximum shear force in the layer interface is obtained for different values of $\frac{x}{L}$ depending on the angle of the layer β, see Figure 4.12. As the maximum shear stress is not located at the base of the cylinder, it means that other locations of the cylinders are susceptible to failure and it may explain why some cylinders that we 3D-printed did break but not at the base (Figure 4.4b).

4.5 Models versus experimental data

We recorded the number of cylinders that were still standing on the support after printing and post-processing. The number of failed cylinders was taken as a measure of the stress exerted by the fluid on the cylinders. If this stress is high, there is a higher probability of breaking so the number of standing cylinders should be small. In all our models the maximum stress is a function of the orientation β, the aspect ratio L/d and the diameter of the cylinders d. In the following we will try to correlate the number of surviving cylinders with appropriately chosen indices.

4.5.1 Model based indices

According to equation 4.16, in the model of uniformly-distributed load, the maximum normal force $N_{\max}$ has the following relation:

$$N_{\max} = K_1 \cos(\beta) \left(\frac{L}{d}\right)^2 \tag{4.25}$$

with $K_1 = \frac{8}{\pi} C_d \rho v^2$. If model 1 is valid, then the number of cylinders should decrease with increasing values of $\cos(\beta) \left(\frac{L}{d}\right)^2$. We define Index1 as:

$$\text{Index1} = \cos(\beta) \left(\frac{L}{d}\right)^2 \tag{4.26}$$

In the case of a point load, we will call this Model 2, we found a different relation (equation 4.19):

$$N_{\max} = K_2 \cos(\beta) \frac{L}{d} \frac{1}{d^2} \tag{4.27}$$

with $K_2 = P\frac{32}{\pi}$. We define Index2 as:

$$\text{Index2} = \cos(\beta) \frac{L}{d} \frac{1}{d^2} \tag{4.28}$$

We define a third index, Index3, for the situation of a cylinder diameter independent drag-force. According to the expression of $N_{\max}$ taken from equation 4.17 we have:

$$N_{\max} = K_3 \cos(\beta) \left(\frac{L}{d}\right)^2 \frac{1}{d} \tag{4.29}$$

with $K_3 = \frac{8}{\pi} C_d d_S \rho v^2$

$$\text{Index3} = \cos(\beta) \left(\frac{L}{d}\right)^2 \frac{1}{d} \tag{4.30}$$

4.5.2 Correction for the real shape of the cylinders

For low values of diameters, the cross section of the cylinder is not a circle anymore but rather a rectangle. The moment of inertia of the cylinder is thus changed a bit. From pictures of the cross sections of the cylinders, we found that the cross sections can be considered circular for diameters superior or equal to 20. In the cases of diameters equal to 5 or 10, we modeled the cross section as a rectangle whose dimensions were determined experimentally.

The main differences are the two following ones: the moment of inertia changes depending on the cross section and the drag coefficient of a circular cross section is approximately half as large as for a square cross section. Hence, for a rectangular section of base b and height h:

$$I = \frac{bh^3}{12} \tag{4.31}$$

Model 1: Uniformly distributed load

Hence, for a rectangular cross section the maximum normal stress is:

$$N_{\max} = 3 \cos(\beta) p \frac{L^2}{bh^2} \tag{4.32}$$

The distributed load is assumed to be generated by the drag of the fluid on the cylinder. The coefficient drag C_d is the one for a square cross section and is thus equal to two times the one of a circular cross section:

$$F_d = \frac{1}{2}\frac{C_d}{2}\rho v^2 L d = Lp \tag{4.33}$$

For a rectanguler cross section, we thus obtain:

$$F_d = \frac{1}{2}C_d \rho v^2 L b = Lp \tag{4.34}$$

Leading to the maximum stress:

$$N_{\max} = \frac{3}{2}\cos(\beta) C_d \rho v^2 \left(\frac{L}{h}\right)^2 \tag{4.35}$$

We redefine Index1 as:

$$\text{Index1} = \frac{4}{\pi}\cos(\beta)\left(\frac{L}{d}\right)^2 \tag{4.36}$$

For diameters equal to 5 or 10, we use the rectangle formula and obtain:

$$\text{Index1} = \frac{3}{2}\cos(\beta)\left(\frac{L}{h}\right)^2 \tag{4.37}$$

Model 2

We used the same approach with a concentrated load independent of the size or shape of the cylinders. We get for diameters equal to 5 or 10 and rectangular cross sections:

$$\text{Index2} = 6\cos(\beta)\frac{L}{bh^2} \tag{4.38}$$

We also model the load in a different way, assuming a linear dependence of the load with the length of the cylinder and obtain the following alternative index for rectangular cross sections:

$$\text{Index2b} = 3\cos(\beta)\left(\frac{L}{h}\right)^2 \frac{1}{b} \tag{4.39}$$

	Index1	Index2	Index2b	Index3
Loading	Distributed load	Point load	Point load $\propto L$	Distributed load
Model	$\cos(\beta)\left(\frac{L}{d}\right)^2$	$\cos(\beta)\frac{L}{d}\frac{1}{d^2}$		$\cos(\beta)\left(\frac{L}{d}\right)^2\frac{1}{d}$
Corrected				
$(d \leq 10)$	$\frac{3}{2}\cos(\beta)\left(\frac{L}{h}\right)^2$	$6\cos(\beta)\frac{L}{bh^2}$	$3\cos(\beta)\left(\frac{L}{h}\right)$	
$(d > 10)$	$\frac{4}{\pi}\cos(\beta)\left(\frac{L}{d}\right)^2$	$\frac{32}{\pi}\cos(\beta)\frac{L}{d}\frac{1}{d^2}$	$3\cos(\beta)\left(\frac{L}{h}\right)$	

Table 4.4: Overview of introduced indices

Summary of indices

In the previous sections we have introduced a number of possible indices based on varying assumptions on the loading of the beams during the post-processing process. These indices are summarised in Table 4.4.
It is worthwhile noting that

- Some indices are functional quite comparable (e.g. Index2b and Index3)
- The model based indices do not take fabrication imperfections and deviations from the design values into account. The corrected values are used to attempt to do this.
- All indices have the same dependence on the angle β.

4.5.3 Results: predictive value of model based indices

In Figure 4.13 we show a scatter-plot of the number of cylinders out of 10 that survived the fabrication and post-processing steps as a function of the various indices. We restrict ourselves to Index1, Index2 and Index3[1]. The colors used in the plot refer to the four dissimilar diameters as these seem to play a more dominant role than either the length or the angle. Obviously, all 3 indexes seem to be correlated with a decline in surviving cylinders as the indices increase, as was expected. However, the amount of scatter makes it hard to draw any conclusions as to which index is the most predictive.

Figure 4.14 shows again the number of surviving cylinders, but this time as function of the $^{10}\log$ of the indices, plotted over a range of 5 decades. Compared to the linear representation this logarithmic plots more clearly show that these indices can be predictive within about an order of magnitude. E.g. for Index1 it is observed that the number of surviving cylinders decays from 10 to 0 in about a change of Index1 from about 100 to about 1000. The plots for Index2 and Index3 show similar graphs but with more scatter than the one for Index1. From this analysis, it seems that Index1 and, thus Model 1, has the best correlation with the measurements. However, differences with Index2 and Index3 have not been quantified yet.

[1]The results for Index2b were very similar to those for Index3 and provided no additional insights.

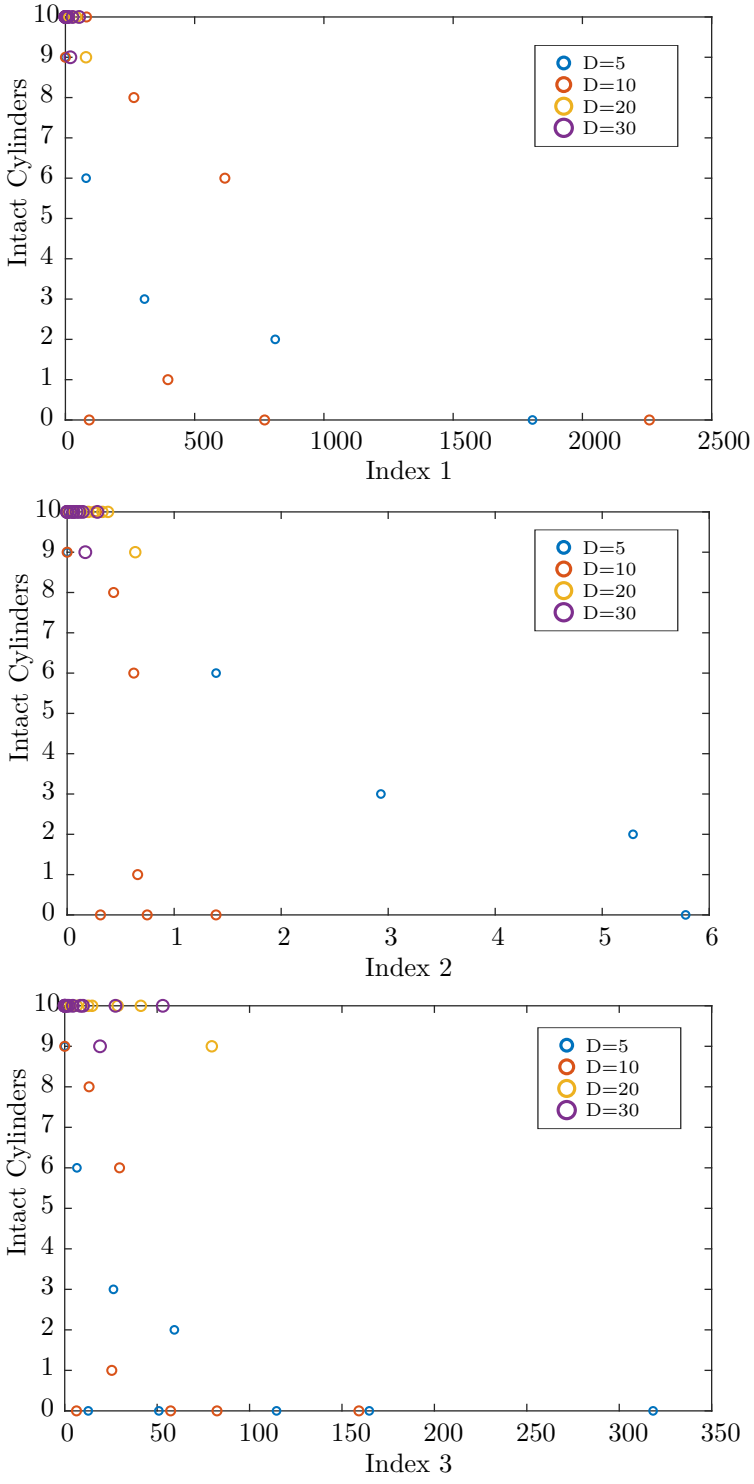

Figure 4.13: Number of cylinders still intact after processing versus Index1 (top), Index2 (middle) and Index3 (bottom). Presentation is on a linear scale.

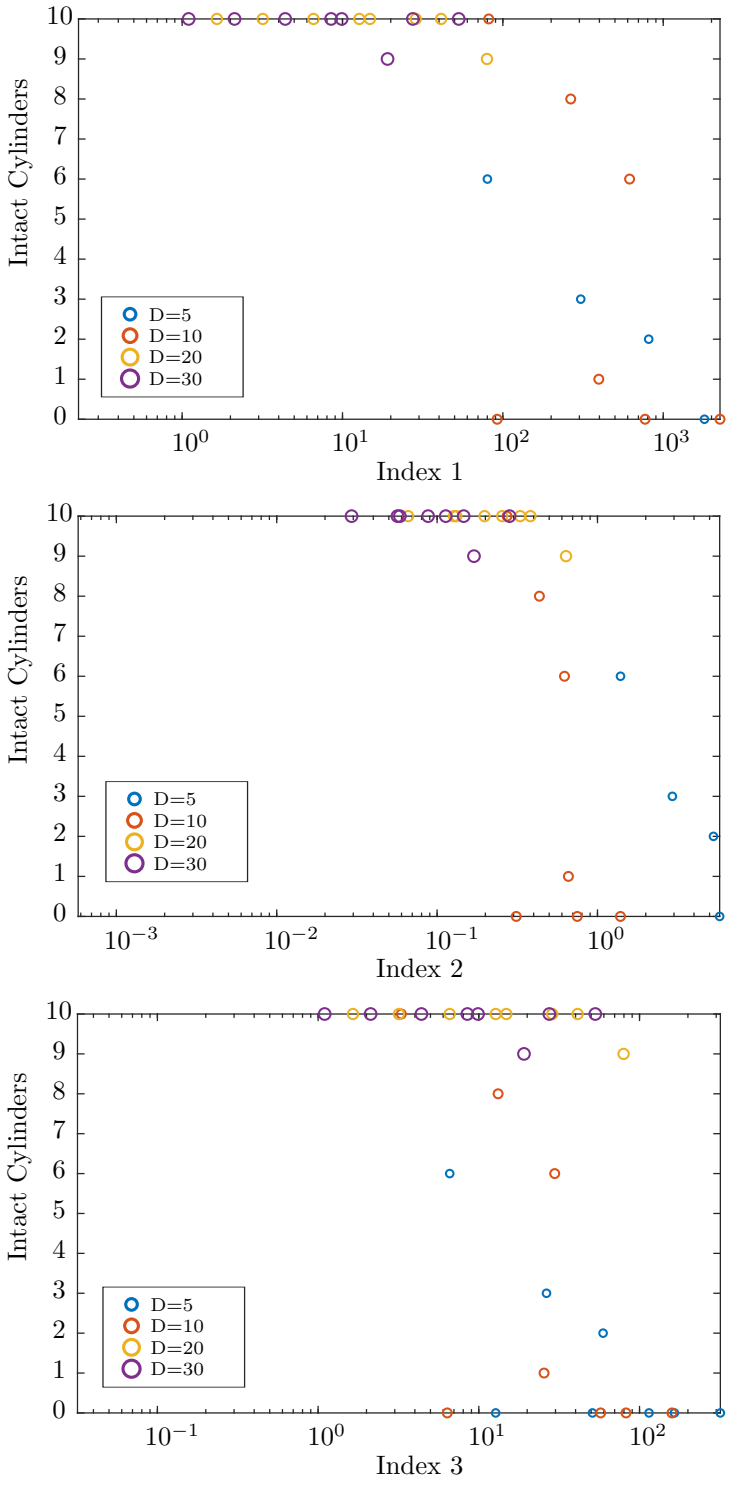

Figure 4.14: Number of cylinders still intact after processing versus Index1 (top), Index2 (middle) and Index3 (bottom). Presentation is on a logarithmic scale.

4.6 Discussion

For small size diameters (5 and 10 times the dot size), the 3D-printer is not able to faithfully produce a circular cylindrical shape. The cross section is stretched in the horizontal direction and flattened in the perpendicular one. Thus, the circular section becomes ovoid with the long axis being up to three times longer than the smaller one.

We thought of three reasons to explain such a phenomenon. Firstly, the 3D-printer might be programmed to have a minimum size in the horizontal plane. Secondly, when the material is jetted, it might spread a bit before being cured, explaining why the diameter is larger in the horizontal plane and shorter in the perpendicular direction. Thirdly, during the post-processing step, the aqueous solution might slightly delaminate the layers.

We tested one homogeneous beam model and several variations to try to explain the survival ratio of the cylinders based on their mechanical properties. Several shortcomings may explain why our model fails to fit with our experimental data, e.g. we do not know the exact loading conditions during post-processing, our models are primarily based on homogeneous beam theory and only linear, i.e. only valid for small deflections.

To get some insight into the influence of the laminar nature on the survival ratio we also theoretically investigated the influence of the 3D-printed material on survival ratios. In this model we looked in some detail at the stresses that may occur along the interface of the layers, a bond which is generally found to be less strong than in the other directions. In our model the beams are composed of layers of material but the mechanical properties within a layer are uniform and isotrope. However, our 3D-printer actually jets material droplet by droplet and curing happens along one direction of the horizontal plane. Thus, the real material is expected to be also anisotropic in the horizontal plane.

The models we developed are valid for small deflections. The cross sections of the cylinders are assumed to stay in the same plane and keep their original shape. After complete curing, our cylinders are quite resistant and require strong mechanical loading to break. Thus, the small deflection model might not be suitable to our problem as large deflections occur. However, nonlinear models dealing with large elastic deformations are more complex and usually require simulations to be solved, often obscuring insight as well.

4.7 Conclusion

We have made a first attempt to develop a model that can help to predict the survival ratio of 3D-printed thin cylinders but our model poorly fits the experimental data. By developing a more complex model, we showed that failure can occur at

different location along the cylinder, depending partly on the orientation of the layers. This model might explain the observations we made about cylinders that were broken at a medium distance between the base and the tip of the cylinder.

Chapter 5

Leakiness of the macrostructure

5.1 Résumé en français

La perméabilité, c'est-à-dire la proportion d'air qui passe à travers l'antenne au lieu d'être déviée autour, est un paramètre-clé pour comprendre le fonctionnement des antennes pectinées. Cependant, la capacité d'une structure à capturer des molécules est un compromis entre une grande perméabilité pour capter une grand partie du flux et une large surface de contact afin de capturer le plus possible de molécules. Or une large surface de contact implique une diminution de la perméabilité. Dans ce chapitre, nous avons étudié comment la perméabilité évolue en fonction de la surface de contact. Pour cela, nous nous sommes intéressé à la macrostructure des antennes : nous avons fait varié le nombre de rami et avons mesuré expérimentalement la perméabilité par Vélocimétrie par Image de Particules (PIV). Pour cela, nous avons imprimé des modèles d'antennes agrandis à l'aide d'imprimantes 3D et nous avons observé leur perméabilité dans de l'eau et de l'huile afin de conserver le même nombre de Reynolds que les antennes dans l'air. Nous avons trouvé que chaque structure (avec un nombre de rami fixé) a une plage de vitesse d'efficacité maximale qui diffère d'une antenne à l'autre. En revanche, le design des antennes de papillons semble conçu pour être robuste, c'est-à-dire fonctionner efficacement sur une large plage de vitesses correspondant à celles rencontrés par le papillon dans la nature.

5.2 Introduction

In many moth species, olfaction is a key sense for successful reproduction. After emergence, female imagos call for males by releasing tiny amounts of sexual pheromones [183] carried by the wind over large distances of up to several hundred meters [32] and detected by males with the help of their antennae [184]. When encountering an antenna of a male moth, the pheromone molecules must be first

captured, before being carried to and detected by the sensors located within the sensilla of the antenna. In the Saturniidae family, these antennae have a particular shape and are termed pectinate antennae (Figure 5.1a). They are composed of one main branch, the flagellum, which supports many secondary branches, the rami. Numerous small hairs, the sensilla, hosts of the sensors, are located on the rami. In our work, we focused on the antenna of one single species, *Samia cynthia*.

In this work, we study the pheromone capture step, when molecules in air reach the surroundings and the surface of an antenna. This step consists of a mass transfer between the air and the surface of the antenna. At low concentrations, which is the case for moth sexual pheromones, mass transfer depends only on the flow of air through the antenna and on the diffusive coefficient of the pheromone in air. At very high concentrations, mass conservation and, thus, the respective densities of air and pheromone, would need to be taken into account. Given the complex shape and multi-scale nature of the antennae, determining the flow of air around them through analytical models is a very difficult task. One of the difficulties lies in the fact that an antenna is a complex object with finite dimensions. Thus, air can flow between the rami and sensilla, or around the entire antenna. We are particularly interested in the proportion of air that flows within the antenna instead of around it, called leakiness in accordance with several previous studies [185, 13]. In other contexts, porosity, which is closely linked with leakiness (at a given velocity, a very porous structure allows more fluid to pass through it compared to a less porous one), has been shown to play an important role in the fluid dynamics around permeable disks [186]. It is an important measure in the context of olfaction, as it gives an upper limit of the proportion of pheromone molecules that can be captured and detected by an organ.

Leakiness is a complicated property to be determined because it depends both on the macroscale and on the microscale of the antennae. Furthermore, the leakiness of a permeable structure also varies with air velocity. Cheer and Koehl [187] determined the leakiness of an antenna, but they reduced the number of rami to two. This trick was actually a powerful one as it allowed them to calculate the interaction between the two rami while keeping the geometry simple enough to be able to solve it analytically. Indeed, an analytical approach is likely to be too complex in the case of an entire structure. Consequently, the leakiness of the entire organ has been experimentally measured, but without any variation of the geometry of the antenna [14, 188, 13, 189].

As we were interested in the influence of the entire architecture of antennae, we resorted to experiments and decided to measure the leakiness with a Particle Image Velocimetry (PIV) setup on scaled-up, 3D printed antennae. PIV is mainly used in experimental fluid mechanics and in biology to obtain time-resolved velocity measurements and related properties in fluids [124, 190]. We adapted the fluid viscosity and velocity to keep the Reynolds number correspondingly with the situation in nature, which ensures that the dynamics for real antennae and for our artificial structures are similar [191, 192].

A moth antenna is a multi-scale object: its length is approximately 1 cm whereas its sensilla are only a few micrometers thick. Thus, there are four orders of magnitude between these two extremes. We resorted to 3D printing to produce antennae with various geometrical parameters. 3D printing is a very convenient tool as it gives a greater freedom of designs compared to traditional manufacturing processes. It also allows to produce single customized objects. Currently, no Additive Manufacturing technology is able to span over four orders of magnitude [193]. As a consequence, we limit our modeling to one level, the structure composed of the flagellum and rami (Figure 5.1a) and we choose in a first approximation to neglect the effect of the second, lower level on the flow around the antennae. This second level is the microstructure (Figure 5.1b), composed of one ramus and its sensilla. This assumption will be discussed. We changed the number of rami to investigate whether the natural configuration of 50 rami of 50 µm diameter is in some ways optimal in terms of leakiness and flow capture for varying wind speeds. Changing the number of rami results in a change of effective surface (or frontal area) of the antenna. We postulate that an increase of the effective surface allows an antenna to support more sensilla, where the chemical detectors are located.

5.3 Materials and methods

5.3.1 Real and surrogate antennae

Morphology of the moth antennae

We first proceed with the characterization of the main morphological features of *Samia cynthia* antennae. Cocoons were ordered from the OPIE (Office for Insects and their Environment, Guyancourt, France). After one or two weeks, the imagos emerged and were directly put in a freezer. The moths were then dried at room temperature for a month. We used Electron Microscopy (Quanta 450, FEI, Hillsboro, Oregon, USA) in our observations.

An antenna is 1 cm long on average (Figure 5.1a). The flagellum is divided in smaller segments called flagellomeres and each flagellomere bears two pairs of rami, one on each side, perpendicular to the flow direction. The most distal flagellomeres may bear only two rami, one on each side. So, on average, one antenna has 100 rami perpendicular to the flow, 50 on each side.

3D printed antennae

Because of 3D print limitations, but also to observe the velocity field in more details, we scaled-up our artificial structures by a factor of 10 relative to the natural ones and adjusted both the fluid velocities and viscosities. The Naviers-Stokes equations ensure that configurations of similar geometries with equal Reynolds

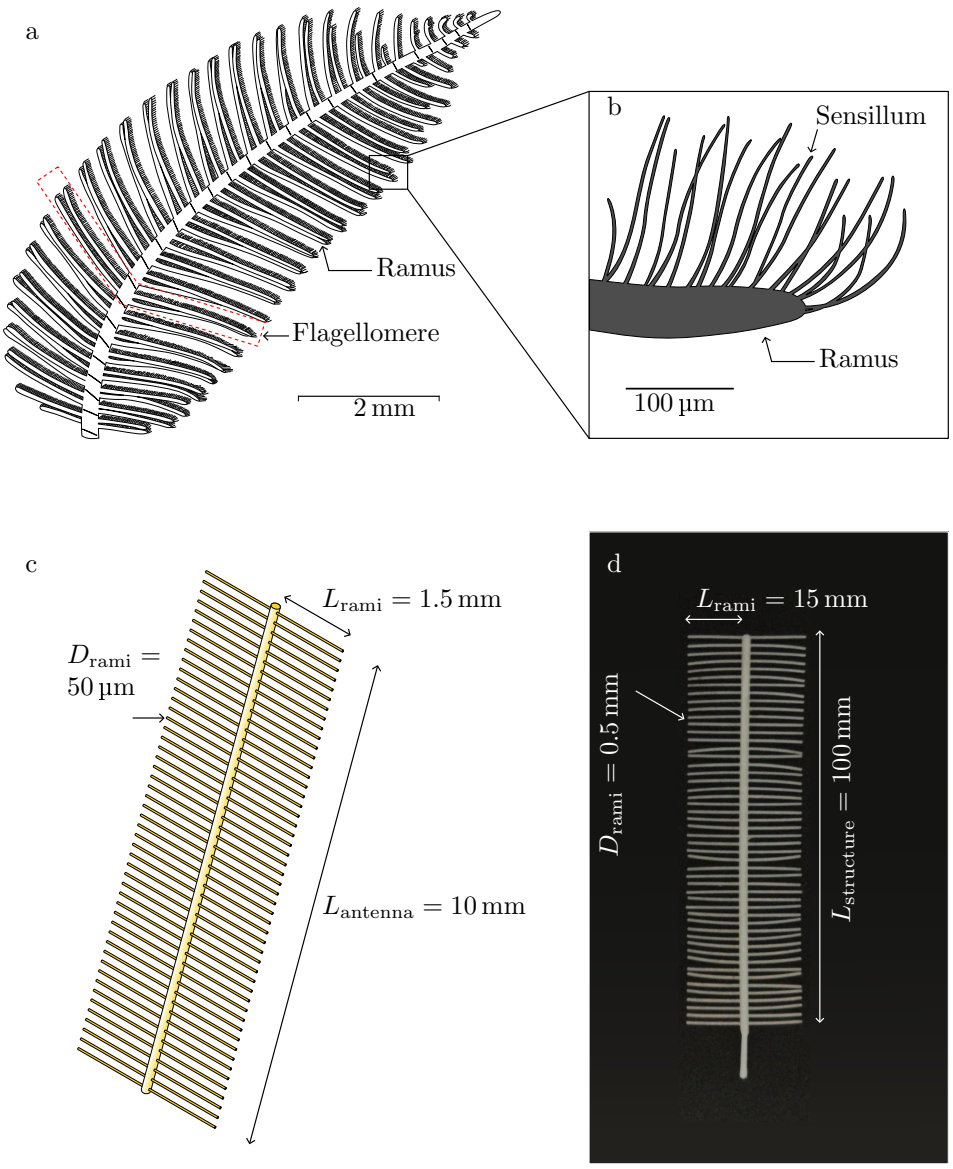

Figure 5.1: Illustration of an antenna of *Samia cynthia* and the 3D printed surrogate structure. In a. The structure composed of the flagellum and rami is visible. Note that the rami are not completely parallel and overlap at their tips. b. Focus on the tip of a ramus to reveal the sensilla. c. Simplified model of the gross morphology of the natural antenna. d. Picture of the actual printed surrogate structure (named Str_{50}). Like all of our 3D printed structures, this structure is scaled-up by a factor α=10 compared to the biological model. This model bears N_{rami}=2× 50 rami and has an effective surface S_{eff}=7,5 mm^2.

numbers have similar flow profiles: for example, their non-dimensionalized velocities or accelerations are equal [194]. This particularity of the Naviers-Stokes equations is convenient as it allows to scale-up the geometries by adjusting the two other parameters which are the fluid velocity and the fluid viscosity (Equation 5.1). To change the fluid viscosity over the entire range of values of biological relevance, we had to change the fluid nature (*i.e.* viscosity). To cover the entire range of interesting Re-values, we worked in both water and rapeseed oil. We then adjusted the fluid velocities to keep the Reynolds number constant.

$$\mathrm{Re} = \frac{Lv}{\nu} \tag{5.1}$$

with Re, the Reynolds number (non-dimensional),
L, the characteristic length m,
v, the characteristic velocity, $\mathrm{m\,s^{-1}}$,
ν, the kinematic viscosity of the fluid, $\mathrm{m^2\,s^{-1}}$.

From now on, the 3D printed artificial-antennae surrogate are termed *structures* and the different designed *structures* are described by the term *Str#* (*Str* standing for 3D printed surrogate structure). For instance, Str_{50} was designed to mimic the real antennae, scaled by a factor 10, as it also has 50 rami of diameter 500 µm on each side of the flagellum (thus 100 rami in total). Furthermore, to investigate the influence of the size of the gap between rami and the influence of the effective surface area S_{eff}, we built structures with $\{30, 40, 60, 70\}$ rami on each side of the flagellum, respectively labeled $\{Str_{30}, Str_{40}, Str_{60}, Str_{70}\}$. The rami were evenly spaced along the flagellum. We defined the *effective surface* as the projected surface of the structure of rami (neglecting the projected surface area of the flagellum which is kept constant):

$$S_{\mathrm{eff}} = 2 \cdot N_{\mathrm{rami}} \cdot D_{\mathrm{rami}} \cdot L_{\mathrm{rami}} \tag{5.2}$$

with N_{rami} the number of rami on one side of the flagellum,
D_{rami} the diameter of the rami and
L_{rami} the length of the rami.

Furthermore, we defined the total surface of the structure S_{t}, bounded by its lateral extent, as:

$$S_{\mathrm{t}} = 2 \cdot L_{\mathrm{struc}} \cdot L_{\mathrm{rami}} \tag{5.3}$$

with L_{struc} the length of the structure.

	N_{rami}	D_{rami} (µm)	S_{eff} (mm^2)	Capture surface ratio $\frac{S_{\text{eff}}}{S_{\text{t}}}$	Scale
Str_{30}	30	500	450	0.15	10
Str_{40}	40	500	600	0.20	10
$\mathbf{Str_{50}}$	**50**	**500**	**750**	**0.25**	**10**
Str_{60}	60	500	900	0.30	10
Str_{70}	70	500	1050	0.35	10

Table 5.1: List of the structures and their various geometrical parameters. The parameters displayed in bold are the ones equivalent to the moth antenna.

Given the specific shape of each of our structures, we resorted to 3D printing to build them. Indeed, 3D printing is convenient to build customized objects [193]. However, there are still some limitations depending on the specific type of 3D printing. We resorted to poly-jetting, using an Objet Eden 260 (Stratasys, Eden Prairie, Minnesota, USA) which is a material jetting 3D printer: droplets of material are jetted to build the object layer by layer. The benefit of the Eden 260 is the use of support material which allows designs with overhanging parts. However, the material support must be removed and this step can be tricky in case of numerous thin cylinders, as it is the case here. The voxel resolution of this 3D printer is around ≈42 µm diameter times a thickness of ≈16 µm, giving smallest printed details of around a few hundreds of micrometers [195]. All structures were designed using Openscad (version 2015.03-2) [196]. Using a single row of rami on each side of the surrogate allowed us to conveniently take off the support material.

5.3.2 Flow measurements

We resorted to a Particle Image Velocimetry (PIV) [197] set-up to visualize the velocity field. This experimental technique consists of seeding a fluid with micrometric particles that are assumed to follow the fluid motion. A laser sheet is then used to illuminate the particles in a given plane. A camera in the perpendicular direction records the position of the particles at regular times. The fluid velocity field is extracted from these pictures through the use of a correlation algorithm which compares a picture with the one taken at the next time step [198].

Scaling up and description of the experiments

We investigated a wide range of relative velocities between the air and the antenna to cover air flows through an antenna on a resting moth or, equivalently, flows through an antenna during moth flight. Thus, we used biologically relevant air velocities of 0.01, 0.02, 0.05, 0.1, 0.2, 0.5, 1, 2 and 5 m s^{-1}. Because of the technological limitations of the poly-jetting process, we scaled-up our artificial structure by a factor 10 as previously explained. Equation 5.1 shows that, in order to keep the Reynolds number constant, the velocity and/or the viscosity of the fluid must be adjusted. Adjusting velocities in our PIV experiments is bounded by practical considerations related to achievable accelerations and required minimum

time for measurements. Therefore, instead of working in air (kinematic viscosity of $15.6\,\mathrm{mm^2 s^{-1}}$ at 25 °C and 1 bar) we decided to run our experiments in water and in oil for their appropriate kinematic viscosities ($1\,\mathrm{mm^2\,s^{-1}}$ for water at 20 °C and $50\,\mathrm{mm^2\,s^{-1}}$ for heated rapeseed oil at 29 °C). This way of doing is commonly encountered in fluid dynamics and flight aerodynamics [191].

The water and oil velocities (Table 5.2) were adapted in order to keep the Reynolds number equal to the ones in air according to :

$$v_{\mathrm{water}} = \frac{1}{\alpha}\frac{\nu_{\mathrm{water}}}{\nu_{\mathrm{air}}} v_{\mathrm{air}} \tag{5.4}$$

$$v_{\mathrm{oil}} = \frac{1}{\alpha}\frac{\nu_{\mathrm{oil}}}{\nu_{\mathrm{air}}} v_{\mathrm{air}} \tag{5.5}$$

with v_{water} the far-field water velocity
ν_{water} the water kinematic viscosity
v_{oil} the far-field oil velocity
ν_{oil} the oil kinematic viscosity
$\alpha = 10$ the scaling factor.

Velocity in *air* ($\mathrm{m\,s^{-1}}$)	0.01	0.02	0.05	0.1	0.2	0.5	1	2	5
Velocity in *water* ($\mathrm{mm\,s^{-1}}$)					1.28	3.21	6.41	12.8	32.1
Velocity in *oil* ($\mathrm{mm\,s^{-1}}$)	3.21	6.41	16	32.1	64.1	160			

Table 5.2: Summary of the PIV experiments and corresponding velocities in air, water and oil.

We ran two experiments for each structure. In both cases, the flow is parallel to the z-axis, the laser sheet is parallel to the xz-plane and the camera is in the y-direction (Figure 5.2). For experiments in water, the equivalent velocities of the lowest velocities in air are too small to get any good measurements. Likewise at large velocities in air, the velocities in oil are too high to be practical. We thus switched between rapeseed oil and water to be able to explore the entire velocity range. Note that at the equivalent velocities in air of 0.2 and $0.5\,\mathrm{m\,s^{-1}}$ the measurements in water and oil overlap, allowing us to observe the consistency of our measurements.

Particle Image Velocimetry setup

The structures were immersed into a tank filled with water or rapeseed oil (Figure 5.3). To generate a constant flow, we fixed the structure on a support and moved the tank of fluid at the desired velocity. In this configuration, the laser

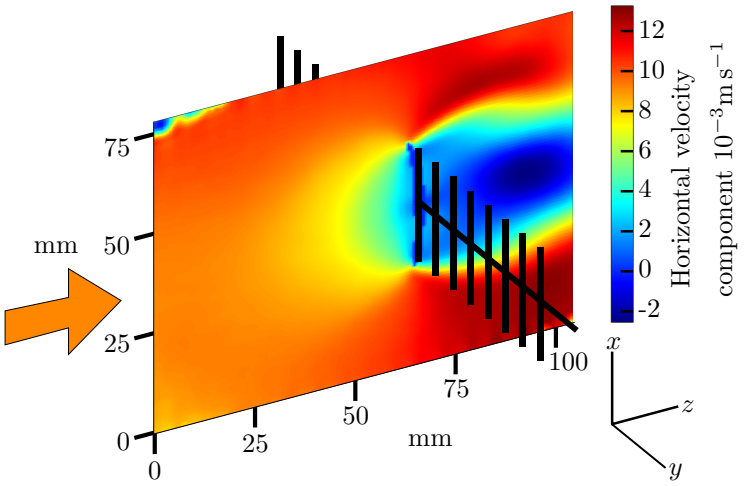

Figure 5.2: Experimental setup and definition of variables. This velocity field was obtained for the structure Str_{50} at a velocity of $3.21\,\mathrm{mm\,s^{-1}}$ (equivalent air velocity: $0.5\,\mathrm{m\,s^{-1}}$) in water. The arrow shows the direction of the flow.

source and the camera were also fixed. Motion of the tank was realized by means of a motorized linear axis (LST1000D-T3, Zaber Technologies, Vancouver, British Columbia, Canada). We added a cover made of hard plastic at the surface of the water to prevent the formation of waves during the acceleration phase. Hollow glass particles covered with silver (10 µm, SUGS-10, Dantec Dynamics, Skovlunde, Denmark) were used to track the fluid movements. A $1.5-2$ mm wide laser sheet was generated by a continuous laser source (MGL-F, 532 nm, 2 W CNI, Changchun, China) equipped with a cylindrical lens. Details of the velocities used in the two experiments in water and oil are summed up in Table 5.2.

A high-speed camera (Phantom 9.1, Vision Research, Perth, Australia) was used to record the motion of the particles. We wanted to have a complete view of the flow and equipped the camera with a 35 mm lens (AF-S DX, Nikon, Tokyo, Japan) of aperture 1/4. The field of view was then equal to 105×77 mm. The resolution of the pictures was set at 1632×1200 pixels. 100 pictures per second ($\Delta t = 10$ ms) were recorded except at 32.1, 64.1 and $160\,\mathrm{mm\,s^{-1}}$. At these two last velocities, we reduced the exposure time to 5 ms to prevent particles appearing as line-segments rather than points.

Raw image processing was done using the software package Davis (Davis 8.3, Lavision, Gottingen, Germany). Processing consisted of extracting the velocity field from the pictures taken by the camera. The first step was subtraction of the background noise resulting mainly from the reflection of the laser light by the static object in the flow. It allowed us to keep only the flowing particles. We then applied a mask at the location of the structure and we chose an adaptive cross-correlation algorithm with 50% overlapping. The interrogation windows were chosen between

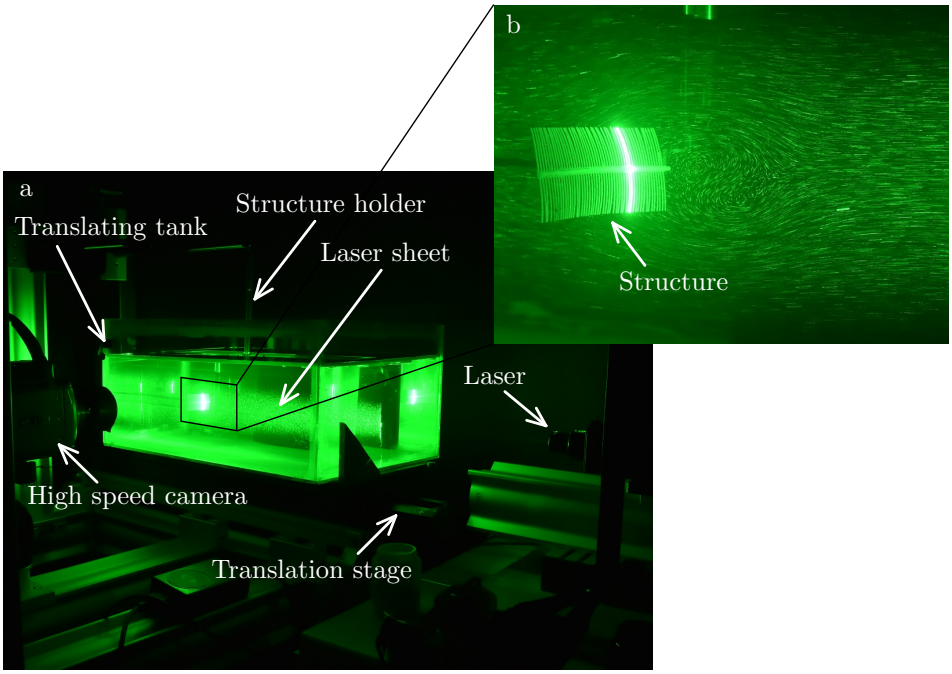

Figure 5.3: Setup of the PIV experiment. a: setup of the PIV experiment. b: lasersheet. We can see that the laser sheet is wide enough to cover at least a complet interrami space.

24 and 32 pixels. The capacity of the cross-correlation to accurately determine the velocities depends on the displacement, in number of pixels, of the particles between two correlated pictures. The maximum measured velocity, $v_{\max}$, is defined according to equation 5.6 and the minimum one, $v_{\min}$, is defined according to equation 5.7. The ratio of minimum and maximum velocities indicates the span of the dynamical range of velocity measurements.

$$v_{\max} = \frac{L}{\Delta t}\frac{L_{\mathrm{IW}}}{N_{\mathrm{L}}} \tag{5.6}$$

$$v_{\min} = \frac{L}{\Delta t}\frac{0.1}{N_{\mathrm{L}}} \tag{5.7}$$

with L, the length of the field of view ($L = 105\,\mathrm{mm}$),
N_{L}, the number of pixels ($N_{\mathrm{L}} = 1632\mathrm{px}$),
L_{IW}, the size, in pixels, of the interrogation window ($L_{\mathrm{IW}} = 24 - 32\mathrm{px}$),
Δt, the time between two pictures.

The term 0.1 (in pixel) in equation 5.7 refers to the minimum pixel displacement that the algorithm can detect. 0.1 means it can detect sub-pixel displacement. In the case of $\Delta t = 10\,\mathrm{ms}$, the minimum velocity is $0.613\,\mathrm{mm\,s^{-1}}$, which is almost equal to the minimum velocity in water ($0.641\,\mathrm{mm\,s^{-1}}$) and higher than the minimum velocity in oil ($0.21\,\mathrm{mm\,s^{-1}}$). To achieve a larger velocity measurement dynamical range, we decided to decrease the minimal detectable velocity, by increasing the time between two pictures, as explained above. This was done by taking one picture every 50 pictures and one every 70 pictures in the case of the lowest oil velocity, giving a minimum detectable velocity of, respectively, $0.0123\,\mathrm{mm\,s^{-1}}$ and $0.0088\,\mathrm{mm\,s^{-1}}$. The maximum velocity for $\Delta t = 10\,\mathrm{ms}$ is equal to $147\,\mathrm{mm\,s^{-1}}$ and is sufficient for our entire range of velocities. For a given velocity, on a given structure, we determined the time-evolution of the velocity field, using several subset pairs of images and a suitable time gap to obtain an appropriate dynamical range of measurable velocities. As we studied steady-state flows, we then averaged the time-resolved velocity fields to determine the steady-state velocity field.

Estimation of the leakiness and definition of the flow capture ratio

We consider our structure to be a homogeneous permeable object. It means that the leakiness is also homogeneous and can be assessed from the evaluation of flow velocities in a single plan. However, because the structure has a finite size, edge effects occur, influencing locally the leakiness. As it has a high aspect ratio, *i.e.* it is longer than wide, edge effects are relatively more important in the width direction, that is, in the direction along the rami (x-axis, Figure 5.2). Thus, we can expect more variations along a ramus (x-axis) than along the flagellum (y-axis).

We thus decided to measure the flow in a xz plane located approximately in the middle of the structure. There are however important velocity variations whether a ramus is included or not in this plane. In our experimental set up, the laser sheet has however a given width of 1.5 - 2 mm. Indeed, it is difficult to produce very thin laser sheet. An ideal infinitely-thin laser sheet would also encounter few particles and, thus, could not produce good enough pictures. Thanks to the width of the laser sheet, our measurements provided a mean of the velocity fields of many planes including planes with and without including a ramus (Figure 5.3b) and, thus, gave us a mean velocity field in a middle section of the structure.

Our method to measure leakiness Le consists of looking at the spatial decrease of the flux ϕ as we get closer to the structure. However, given the geometry of our measurement setup, the exact flux at the precise position of the structure is inaccessible, because it is hidden by the structure itself. We thus integrated the measured flow through a segment parallel to the x-direction and as wide as the structure and followed the evolution of this flux as the segment is gradually moved closer to the structure (Figure 5.4.a). Thanks to the continuity of the flux, we can then determine the flux ϕ_{rami} within the structure (Figure 5.4.b). Several estimations of the leakiness for the same structures showed that this method gives an estimate with an interval of leakiness of 5%. Then, we multiplied this 2D flux by the length of the structure to get the total flux. We used this method in the rest of this work to determine the leakiness of the structure.

In order to assess the effectiveness of a structure we need to take two related effects into account. Obviously, structures with large leakiness Le have a large flux passing through them, a prerequisite for pheromone uptake. At the same time, if the large leakiness is due to a very sparse structure, *i.e.* if there are few rami in the structure and the distance between the rami is large, the chances for capturing any of the pheromone molecules in the structure are rather low. Hence, we also need to take into account the relatively available rami surface. Taking both effects into account, from the combined estimation of the leakiness and of the structure effective surface (S_{eff}, see Table 5.1 for details), we define a new parameter which reflects the efficiency of the artificial structure, the flow capture ratio F_{c}. This ratio is defined as the product of two ratios, (i) the leakiness Le and (ii) the capture surface ratio of a structure. This is the fraction of the effective surface over the total surface bounded by the lateral extent of the structure, i.e. $S_{\text{eff}}/S_{\text{t}}$ (see table 5.1 for numerical values):

$$F_{\text{c}} = \frac{S_{\text{eff}}}{S_{\text{t}}}\text{Le} \tag{5.8}$$

Figures 5.4.c and 5.4.d illustrate the expected effect of a change of structure effective surface S_{eff} on this flow capture ratio. For the structure Str_{30} with 30 rami, having a relatively small effective surface $S_{\text{eff},30}$ (Figure 5.4.c), the leakiness is relatively important; it means that the flux ϕ_{Str30} is relatively large. We can

therefore expect on one side a large flow capture ratio $F_{\mathrm{c}30}$, due to the large leakiness of this sparse structure, but on the other side we can also expect a small flow capture ratio, due to the small effective surface. We now consider a second structure, Str_{70} with 70 rami and thus a larger effective surface $S_{\mathrm{eff},70} > S_{\mathrm{eff},30}$ as illustrated in figure 5.4.d. The leakiness of this second structure is reduced compared to the first one, as the flux ϕ_{Str70} between the rami decreases. This may translate into a reduction of the expected flow capture ratio $F_{\mathrm{c}70}$. At the same time, there might be an increase of effective surface due to an increase of the flow capture ratio F_{c70}. The trade-off between these two conflicting effects (ie an increase of effective surface and a decrease of leakiness) greatly affects the flow capture ratio. Moreover, due to boundary layer effects, leakiness and therefore the flow capture ratio, also greatly depend on the flow velocity.

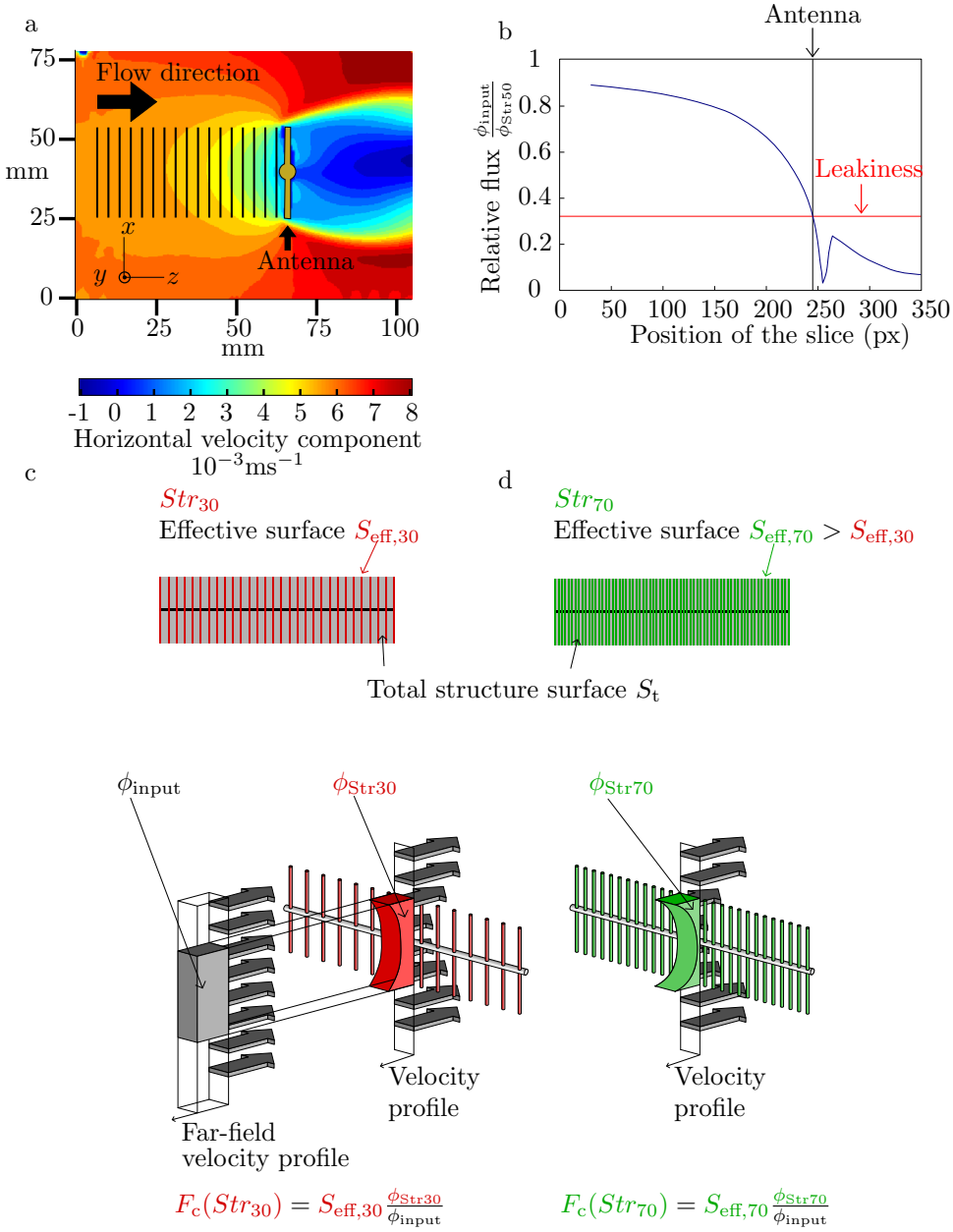

Figure 5.4: a. Illustration of the slice method used to determine the leakiness of the structures. b. Relative proportion of the flux through a section of a structure located upstream and downstream of it. The location of the structure is shown by the black line. The value of the leakiness, as determined by the relative flux at the entrance of the structure, is shown by the horizontal red line. This graph was drawn for the case of structure Str_{50} at water velocity of 6.41 mm s^{-1} (equivalent air velocity: 1 m s^{-1}). The measured leakiness is equal to 0.32. c and d. Effect of the change of effective surface on the flux inside the structure and estimation of the flow capture ratio.

5.4 Results

5.4.1 PIV measurements

When the flow encounters a structure, part of the fluid flows through the structure and part of the flow goes around the structure (Figure 5.5). As expected, the wake of the structure is particularly affected by the change of flow regime, *i.e.* by the increase of flow velocity. At low velocities, the flow is laminar and symmetrical, and converges behind the structure (Figure 5.5a). At high velocities, the wake is turbulent and we note the presence of shedding vortices, even though some vortices are still maintained behind the flagellum (Figure 5.5c). In between, at medium velocities, a separated vortex ring is present in the wake of the structures (Figure 5.5b) and the distance between the vortex ring and the structure depends on the fluid velocity. In their work on dandelion seed flight [186], the authors identified its porosity as a key design feature that enables the formation of the separated vortex ring. Our pectinate antenna is also a porous object and is another striking example of this new class of fluid behaviour around fluid-immersed bodies. Whether and how this might be beneficial in the context of olfaction needs dedicated work.

We have explored how the velocity fields in a cross section of the structures of constant ramus diameter are affected by the change of effective surface. To do so, we used several structures with increasing numbers of rami with constant diameter (see table 5.1 for more details). The whole matrix of measurements is large, since we explore nine different flow velocities (from $0.01\,\mathrm{m\,s^{-1}}$ to $5\,\mathrm{m\,s^{-1}}$) on five different designs, from Str_{30} ($N_{\mathrm{rami}} = 30$ and D_{rami}=500 µm, corresponding to an effective surface S_{eff} of $450\,\mathrm{mm^2}$) to Str_{70} ($N_{\mathrm{rami}} = 70$ and D_{rami}=500 µm, corresponding to an effective surface S_{eff} of 1050 µm). Figure 5.6a and 5.6b illustrate how the change of effective surface affects the flow around the structure at low velocity. Figure 5.6c and 5.6d illustrates how the change of effective surface affects the flow around it at high velocity. We limit the examples to the extreme cases. We use these measurements to estimate the evolution of leakiness with an increase of effective area, by integrating the evolution of the flux as we get closer to the structure. We determined that structures with numerous cylinders, *i.e.* more than the natural design (Str_{60} and Str_{70}, respectively 60 and 70 cylinders), had a lower leakiness than the ones with fewer cylinders than the natural design (FR Str_{30} and Str_{40}, respectively 30 and 40 cylinders) at a given air velocity, as expected (Figure 5.7). It is worth noticing that the scaling using constant Reynolds numbers works reasonably well: in the region where the ranges of Reynolds numbers in oil and water overlap, the water and oil data give almost the same leakiness (Figure5.7).

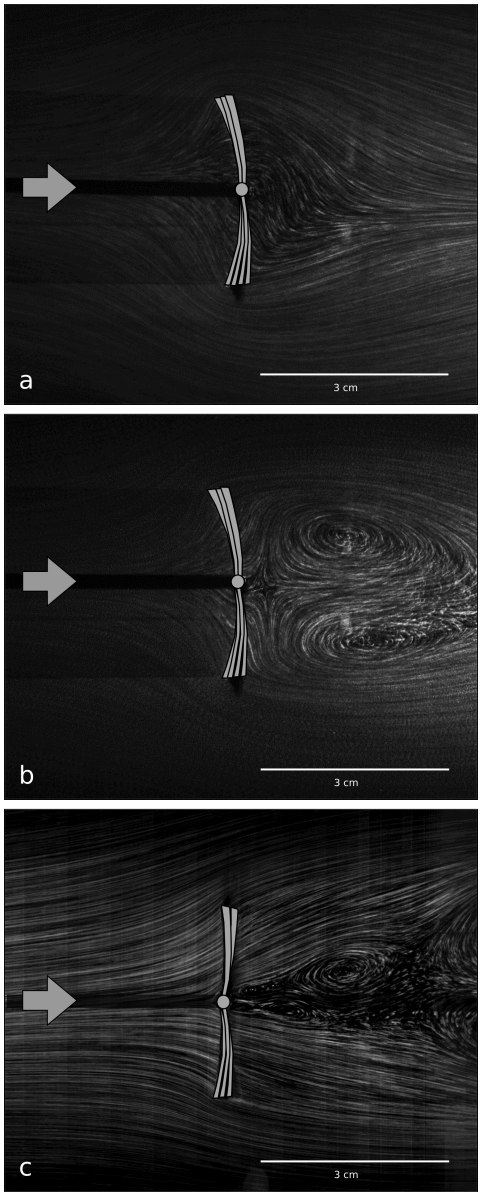

Figure 5.5: Flow around the surrogate structures, seen from the side. a: Laminar flow around structure Str_{40} at oil velocity of $3.21\,\mathrm{mm\,s^{-1}}$, equivalent to air velocity of $0.01\,\mathrm{m\,s^{-1}}$. b: Stable separated vortex ring in the wake of structure Str_{40} at oil velocity of $64.1\,\mathrm{mm\,s^{-1}}$, equivalent to air velocity of $0.2\,\mathrm{m\,s^{-1}}$. c: Unsteady wake of structure Str_{40} at water velocity of $12.8\,\mathrm{mm\,s^{-1}}$, equivalent to air velocity of $2\,\mathrm{m\,s^{-1}}$. The gray arrows show the direction of the flow.

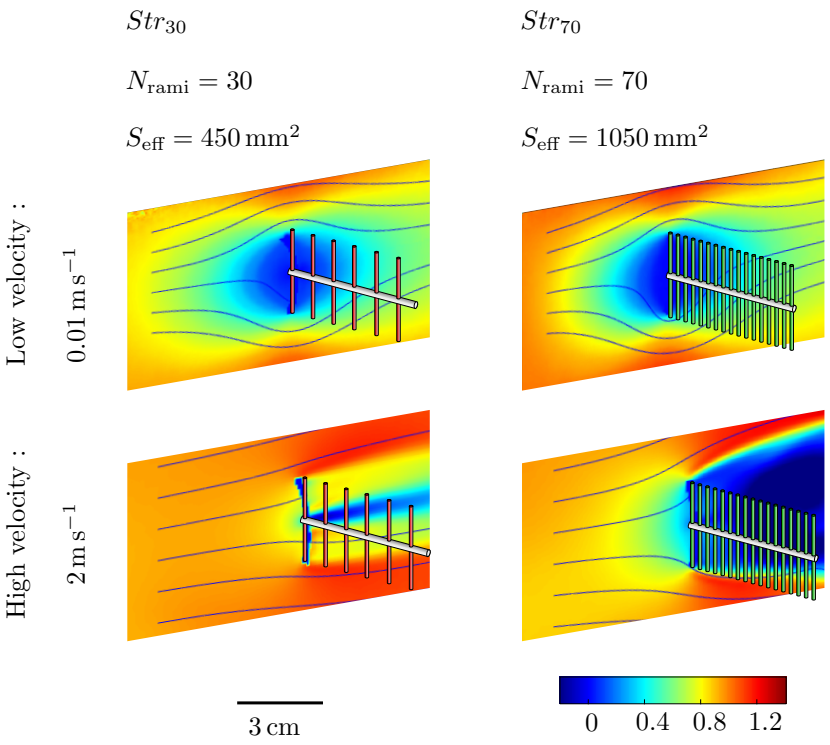

Figure 5.6: Influence of the effective surface S_{eff} on the flow in a cross section of the 3D printed scaled-up structures, with a constant diameter D_{rami}=500 µm. The velocities are normalized by the far-field corresponding velocity.

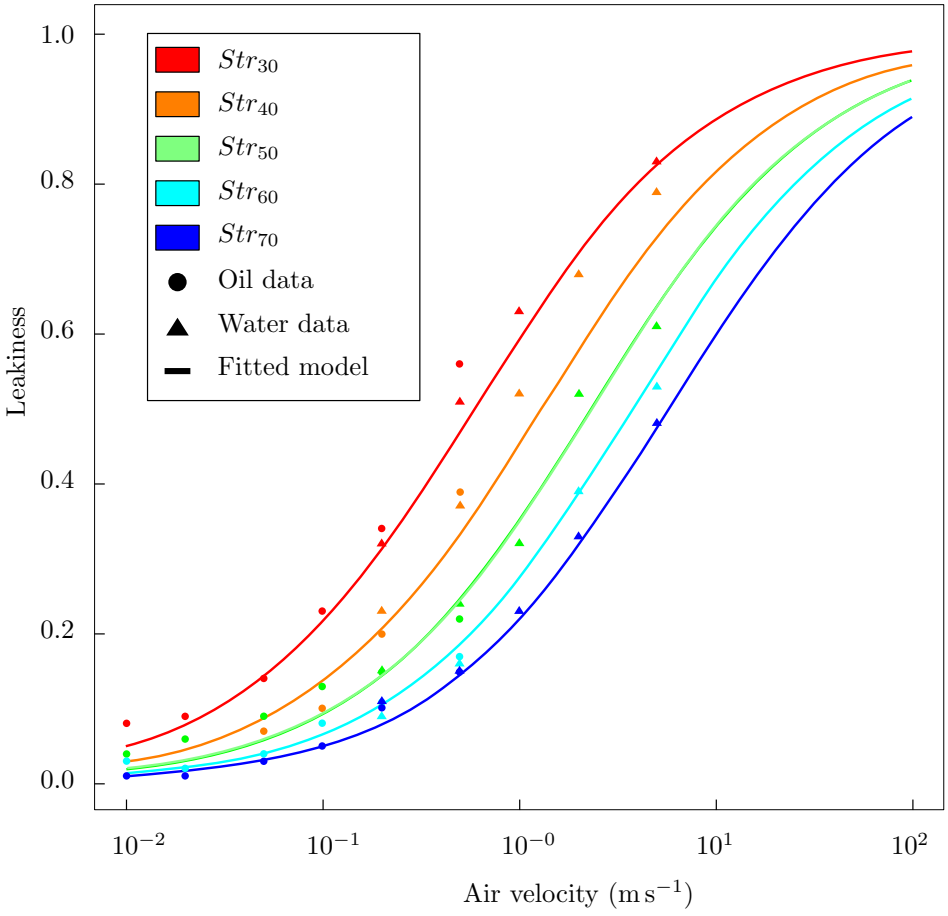

Figure 5.7: Leakiness of the structures and fitted curves.

5.4.2 Fitting leakiness relationships

The observed trends (Figure 5.7) suggest a general behavior: leakiness increases according to a sigmoidal function [14] and a reasonable fit can be obtained with:

$$\mathrm{Le} = \frac{v_\mathrm{n}^\alpha}{1 + v_\mathrm{n}^\alpha} \tag{5.9}$$

where v_n is the normalised far-field velocity, i.e. $v_\mathrm{n} = \frac{v_\infty}{v_{50\%}}$ and where $v_{50\%}$ is a normalising velocity coinciding with the velocity at which leakiness is 0.5. This is an important point for the sigmoid as it is the location of the maximum of variation. Indeed, at very low and very high velocities, the sigmoid is always close to 0 and 1 respectively. α can be used to tailor the slope to optimally fit the measured curves. We used the software RStudio (Version 1.0.136) to fit a sigmoid to each curve of leakiness using a least-square method, the non-linear regression function nls.

Structure	α	$v_{50\%}$	R^2
Str_{30}	0.748	0.475	0.996
Str_{40}	0.859	0.913	0.996
Str_{50}	0.660	2.435	0.980
Str_{60}	0.731	4.219	0.992
Str_{70}	0.703	5.554	0.998

Table 5.3: Parameters obtained from the non-linear regression for each structure. R^2 is the coefficient of determination.

The $v_{50\%}$ values as function of $S_\mathrm{eff}/S_\mathrm{t}$ show a nearly exponential relation. A reasonable predictive function is:

$$v_{50\%} = C \cdot (S_\mathrm{eff}/S_\mathrm{t})^\beta \tag{5.10}$$

Here again, we used the non-linear regression nls to determine the parameters and obtained:

$$C = 97.43 \tag{5.11}$$

$$\beta = 2.69 \tag{5.12}$$

with $R^2 = 0.980$, the coefficient of determination.

We then made a non-linear regression on all the data to determine a common α for all the structures. The velocities $v_{50\%}$ were calculated according to equation 5.10 using the parameters in 5.11 and 5.12. We obtained:

$$\alpha = 0.727 \tag{5.13}$$

with $R^2 = 0.983$, the coefficient of determination.

5.5 Discussion

5.5.1 Validity of the assumptions

A major postulate of our work, stated in the introduction, is that increasing the effective surface increases the number of sensilla and hence increases the capture probability of pheromone molecules. This postulate has a major implication. While sensilla require attachment points and hence a surface, increasing the effective surface while keeping the total surface constant is bound to fail: sensilla also need the empty spaces between the rami to function. Thus, while it is likely that the effective surface is a determining variable, it might not be the only one defining the overall capture efficiency.

The capture of odors is a mass transport problem where both advection and diffusion play a role. However, in some cases, studying only one of the processes may be sufficient to assess the olfactory efficiency of a structure. For example, understanding the change of leakiness regime (underlying a change in the advection process of the molecules) of the olfactory appendages of underwater crustaceans is sufficient to understand how they capture odors [199, 200]. Because the diffusion coefficient of molecules in water is low ($\approx 10^{-9}$ $m^2\,s^{-1}$ compared to 10^{-6} $m^2\,s^{-1}$ in air), crustaceans appendages need closely packed structures. However water cannot flow through them anymore, unless the appendages are actively moved to generate a flux. In a more general way, Waldrop *et al* [201] showed that leakiness and advection are important to understand underwater olfactory appendages, whereas diffusion is required to understand olfactory antennae in air. They also showed that pectinate antennae are an intermediary case in which both phenomena should be studied. Here, we focused on leakiness. Diffusion at the level of the sensilla is challenging [202] and studied in Chapter 6

5.5.2 Similarity of the dynamics in different fluids

The scaling of the antenna and the shift from air to water and oil depend on the fact that keeping the Reynolds number identical to the natural situation is sufficient to ensure similar dynamics. The range of water and oil velocities were defined so that their respective ranges of equivalent air velocities would overlap. The water and oil curves indeed fit broadly, in particular the ranking between treatments which is quite well conserved (Figure 5.7).

One of the reasons for the observed discrepancies in the two fluids might be that the lowest velocities in water were too low to enable good measurement of the fluid dynamics. At these water velocities ($0.641\,mm\,s^{-1}$ and $1.28\,mm\,s^{-1}$ corresponding to air velocities of $10\,cm\,s^{-1}$ and $20\,cm\,s^{-1}$ respectively), any small disturbance can have a big impact on the PIV measurement. For example, the laser sheet heats the structure and generates upward water flow. This phenomenon is indeed especially noticeable at low velocities for two reasons: firstly, the displacement of the fluid structure is low and the heat generated by the laser sheet is thus dissipated in

a small volume of water, giving rise to considerable temperature gradients. Secondly, the upward water velocity due to the difference of density is not negligible compared to the horizontal velocity.

Regarding the measurements made in oil, difficulties appeared at the equivalent air velocity of $50\,\mathrm{cm\,s^{-1}}$. Here, the oil velocity is $160\,\mathrm{mm\,s^{-1}}$. At this velocity, we had to decrease the opening time of the camera in order to have good images of the particles, rather than small lines due to their displacement. As a drawback, less light enters the camera and the images of the particles at the sides of the laser sheet are not sharp, leading to a loss of accuracy of the measurement of the velocity field.

5.5.3 Boundary layers superposition and its influence on leakiness

In all our measurements, leakiness increases with fluid velocity (Figure 5.7). This result was expected because the boundary layer around an object tends to be smaller at high velocities, allowing more fluid to pass through the structure. We observed that the transition between an almost non-permeable structure at low velocities and a highly permeable structure at high velocities occurs at air velocities ranging from $10\,\mathrm{cm\,s^{-1}}$ to $1\,\mathrm{m\,s^{-1}}$ (Figure 5.7). These air velocities are encountered by a moth in nature [203, 204]. Thus, the geometry of the structures seems to be adapted to have a high leakiness at the air velocities at which the antennae are known to function.

We have shown that the structures with numerous rami had a lower leakiness than the ones with fewer rami at a given air velocity (Figure 5.7). The variation of leakiness might be due to the extent with which boundary layers overlap. In the case of numerous cylinders, the cylinders are closer to each other and, then, more susceptible to have overlapping boundary layers compared to distant ones in which the boundary layers are more likely to have a weaker interaction with each other [19]. As a consequence, fewer pheromone molecules are available per sensillum in a denser structure. Sparser structures allow more air to pass through but the total surface of the antenna is reduced. From the point of view of molecular diffusion, it also means that air flows at higher velocities, giving little time to the pheromone molecules to diffuse to the sensilla. Diffusion at the level of the sensilla is specifically studied in Chapter 6.

5.5.4 Flow capture ratio

From the previous section, we understand the importance of the overlap of boundary layers around rami, eventually resulting in the reduction of the leakiness of the structure when its effective surface increases. The measurement of the leakiness alone does, however, give only a partial insight of the antenna efficiency. An antenna with a larger effective surface is supposed to bear more sensilla in contact

with the flow, and this might also influence the flow capture ratio defined previously. We now determine the overall flow capture ratio incorporating this effect. We simply define it as the product of the leakiness Le with the ratio of the effective surface of the structure S_{eff} over its total surface S_{t}. It represents the ratio of a given far field flux that can be caught by a given surface of rami bearing sensilla. The calculation of this flow capture ratio highlights the trade-off between the two effects previously identified.

Figure 5.8a represents the dynamics of the flow capture rate for different effective surfaces. At low flow velocity, it appears that a smaller effective surface is sufficient while a larger effective surface seems to be more efficient at high velocity. We observe that the average effective surface of the *Samia cynthia* antennae gives them an average efficiency over a wide range of fluid velocity.

From the sigmoid curves, we determined the leakiness of structures with different numbers of rami as well as their flow capture ratio. We used these fitted curves to calculate the leakiness of structures with a number of rami ranging from 10 to 80 and their respective flow capture ratio. In order to compare the flow capture ratios at all velocities and for all structures, we normalized the flow capture ratio at a given velocity by the maximum flow capture ratio obtained for all structures at the same velocity (Figure 5.8b). The justification to take a different normalizing flow capture ratio at each velocity is that we want to compare all the structures at a fixed velocity to determine which geometry is the more efficient one at this given velocity. Fitting an overarching sigmoidal model to the observed trends enables us to explore a wider range of structural architectures. We can see that there is no design that is optimized for all velocities. For designs with many rami, the flow capture ratio is very low at low velocities whereas designs with few rami perform poorly at high velocities. Actually, each design has a maximum of flow capture ratio spanning a range of air velocities. The maximum of flow capture ratio of the natural design (50 rami) is centered on the moth flight velocities.

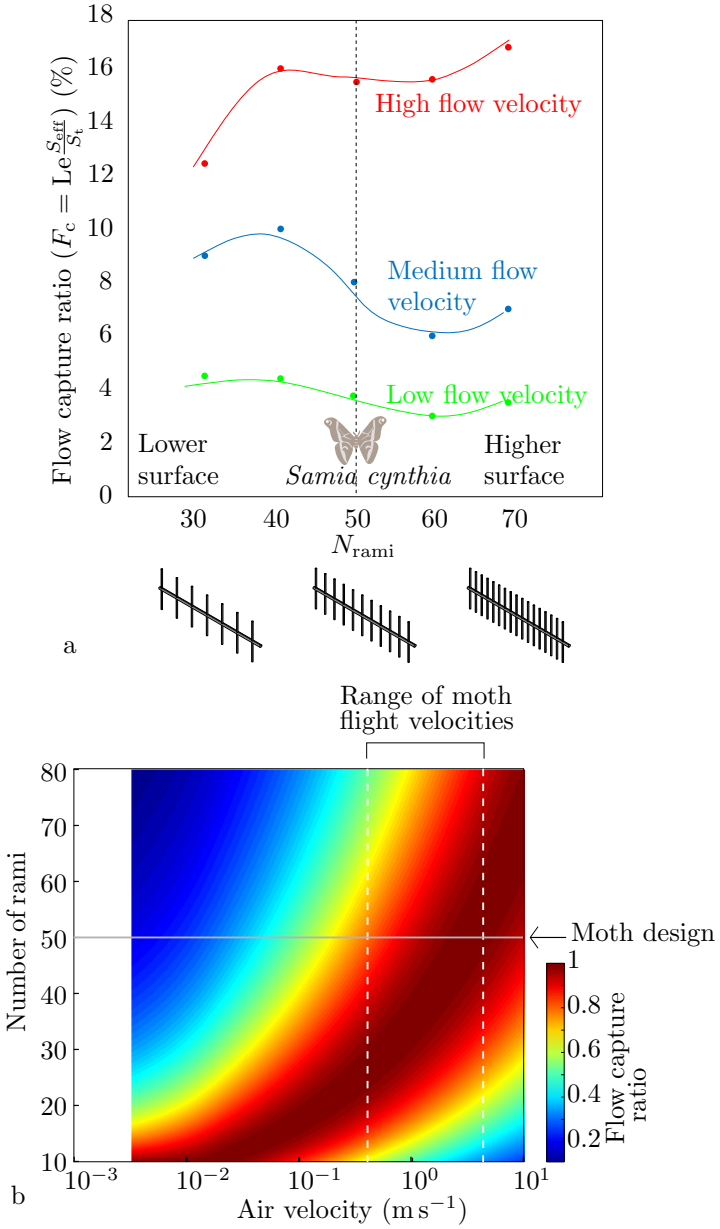

Figure 5.8: Variation of the flow capture ratio depending on the number of rami and the air velocity. a: Variation of the flow capture ratio of the structures with changes of effective surface at different flow velocities. b: Normalized flow capture ratio depending on air velocity and number of rami. The normalisation was done by dividing the flow capture ratio by the maximum flow capture ratio obtained for all the designs at the same air velocity. The white dotted lines show the range of moth flight velocities and the gray horizontal line highlights the performance of the natural design of the moth.

The architecture of real antennae has some slight differences relative to the surrogate ones which might be important. Indeed, rami of a pectinate antenna are not completely parallel, as can be seen in Figure 5.1a, and this seems to be the case for several species of moths [205]. The rami are almost equidistant at their base but get closer towards their tips, where they overlap. This change of inter-rami distance might have consequences on the flow capture ratio. At the base, the design is similar to our structure with 50 rami and the flow capture ratio is thus properly determined. However, as the rami overlap at the tip, we end up with a structure that ressembles that of 25 rami. In between, we can assume a continuum between the two extreme configurations. As a result, we can assume that the change of distance between the rami extends the range of air velocities towards the low velocities, where the antenna is efficient (Figure 6.29b). We therefore conclude that the overall architecture of pectinate antennae of insects is a robust design well-suited to function over a wide range of flow velocities.

Chapter 6

Mass capture model

6.1 Résumé en Français

Les senseurs chimiques étant situés dans les sensilles, nous nous sommes concentrés sur la capture de phéromone par les sensilles. Les sensilles ont été modélisées par des cylindres longitudinaux et pour résoudre le problèmes de masse du flux de phéromone sur la surface des sensilles, nous nous sommes tournés vers un modèle de transfert de chaleur dans une telle géométrie. Après avoir adapté les résultats du modèle à notre cas, nous avons pu calculé le flux de phéromone sur les sensilles et, combiné avec les résultats sur la perméabilité du chapitre précédent, l'efficacité de capture de la microstructure de l'antenne pectinée. Nos travaux ont également apporté une réponse physique au phénomène de lentille olfactive.

6.2 Introduction

In air, the concentration of pheromone is determined by the velocity of air and by the diffusive coefficient of the pheromone in air. However, the velocity of air close to the sensilla is influenced by the shape of the entire antenna. An antenna can increase its capture efficiency in two ways. The first parameter is the contact surface between the antenna and the air which increases with the size and the number of sensilla. The second parameter is related to how the air flows past the antenna. The antennae can be seen as a permeable object and, thus, air can either flow through the structure of the antennae or can be deflected around the whole antenna. In the second case, the molecules carried by the air are not available to the antennae. The proportion of air going through the antenna tends to decrease with the resistance to air of the antenna, for example, with the number of sensilla.

Saturniidae antennae have already been the subject of numerous studies. A part of them focused on the leakiness of the antennae, defined as the part of

the air flux that does flow through the antennae compared to the total incoming flux. This leakiness was either determined experimentally [14, 189] or through modeling [102]. Mass transfer from the air to surface of the antenna was also theoretically studied, either from an analytical [11] or numerical [206] point of view. They respectively studied antennae of *Bombyx mori* which are very similar to the ones of Saturniidaes, and antennules of marine crustaceans. Electroantenogram studies have the benefit of taking both leakiness and mass transfer into account. However, it is difficult to know the pheromone concentration in the air reaching the antenna. Humphrey and Haj-Hariri [12] were the first, to our knowledge, to develop a pseuso-analytical model that takes into account both the leakiness and the mass transfer of pheromone. However, their leakiness was a fixed parameter independent of the air velocity and of the particular geometry of the antenna.

In this chapter, we wanted to understand how the shape of the antenna supports the capture of molecules by altering the air velocity field around the sensilla. We put emphasize on the geometry of the antenna and determined the efficiency of the antenna or, in other words, the proportion of molecules it captures depending on the incoming mass flux of pheromone. We explored a large range of velocities in order to mimic the wind bringing air to the antennae of a moth or the air flow induced by the flight of a moth.

For practical reasons, we limited our study to one single species, *Samia cynthia*. Our first step was to describe the shape of the antennae. They can actually be divided in three levels: the flagellomere which is the main branch of the antennae, the rami which are secondary branches located perpendicularly on the flagellum and the sensilla where the chemical sensors are. The sensilla are mainly located on the rami. One important parameter that we wanted to investigate is the fact that the sensilla are oriented upstream, longitudinal to the flow of air. Because of the 4 orders of magnitude of difference between the diameter of the sensilla ($\approx$3 µm) and the total length of the antennae ($\approx$1 cm), we could not investigate a complete antenna. We had to split it in two levels of organization: a first level composed of the flagellomere and the rami, and a second one composed of one ramus and its sensilla. In this study, we focused exclusively on the second level that we call, from now on, the microstructure. We then used 3D printers to build large-scaled artificial microstructures. Using a Particle Image Velocimetry setup, we then visualized the air flowing around a microstructure and determined its leakiness. The air was actually slowed down by the presence of the microstructure and the measured leakiness quantified how much slower the air encountered the sensilla. This lower velocity was used as input for a model of mass transfer. The array of sensilla were modeled as an infinite array of longitudinal cylinders. This model was developped for heat transfer [207] and we adapted their results to our mass transfer problem thanks to the similarity between the phenomena of heat and mass transfer. We could then determine the efficieny of the microstructure to capture molecules in air and how the mass capture is distributed along the sensilla.

6.3 Material and Methods

Moth antennae exhibit a complex and multi-scale structure. There are almost four orders of magnitude between the entire length of the antenna ($\sim$ cm) and the diameter of sensilla ($\sim$ µm). Because of the difficulty to study either experimentally of through modelling such object, the antenna was dissociated in two levels: the macrostructure and the microstructure. The macrostructure is composed of the flagellum and the rami (Figure 6.2a), and the microstructure is composed of a ramus with sensilla (Figure 6.2b). We focused, in this paper, on the microstructure where the actual chemical sensors are located.

Two aspects of the antenna are particularly important and challenging to determine its capture efficiency: the particular geometry of the antenna and its leakiness due to its finite dimensions. We separately dealt with each aspect. Firstly, the antenna has an intricate shape with sensilla located on rami fixed on the flagellum (Figure 6.2). We simplified and modeled our antenna with a 2D-array of longitudinal cylinders whose diameters and lengths are comparable to the ones of the sensilla. We then adapted an analytical formula developed by Miyatake and Iwashita [207] for heat transfer to measure mass transfer between a fluid and an infinite array of horizontal cylinders. Secondly, the antenna is a finite permeable structure. In most studies, permeable structures are located within tubes [208, 209] so all the fluid particles have to go through the structure. However, our antenna is located in an open flow field: air can flow between the sensilla or around the whole structure. In order to determine the proportion of airflow going between the sensilla and carrying the molecules that can potentially reach the surface of the antenna, we ran experiments with Particle Image Velocimetry. According to Koehl [187], we called this proportion the leakiness of the antenna. This leakiness gives us the flux of air between the sensilla and, thus, also the mean air velocity between the sensilla. This value is important as it defines the air velocity used as input in the model of mass transfer previously developed (Figure 6.1).

To sum up our approach, we first reproduced the geometry of the moth antenna (Figure 6.3 a and b), then developped a model of mass transfer on a simplified geometry (Figure 6.3d), produced a 3D printed microstructure to determine its leakiness through Particle Image Velocimetry (PIV) (Figure 6.3e). Finally, we combined the results of both previous sections to calculate the capture efficiency of the microstructure.

6.3.1 Natural antennae

Moth cocoons of *Samia cynthia* were obtained from OPIE (Guyancourt, France). After emergence, moths were put in a freezer and dried at room temperature for a month. Then, the antennae were cut and put into a Scanning Electron Microscope (Quanta 450, FEI, Hillsboro, Oregon, USA) without any metal coating.

Sensillum density and shape were observed on the SEM pictures. The main observations were that the sensilla are located on the portion of the rami facing

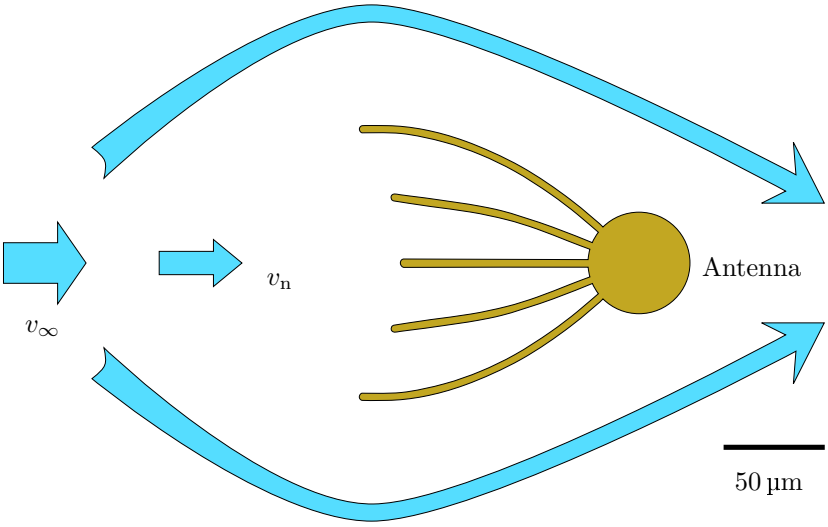

Figure 6.1: Definition of the different variables refering to velocities. v_∞ is the far-field velocity. v_n is the mean velocity of air between the sensilla. The structure represents a ramus and its sensilla viewed from the top.

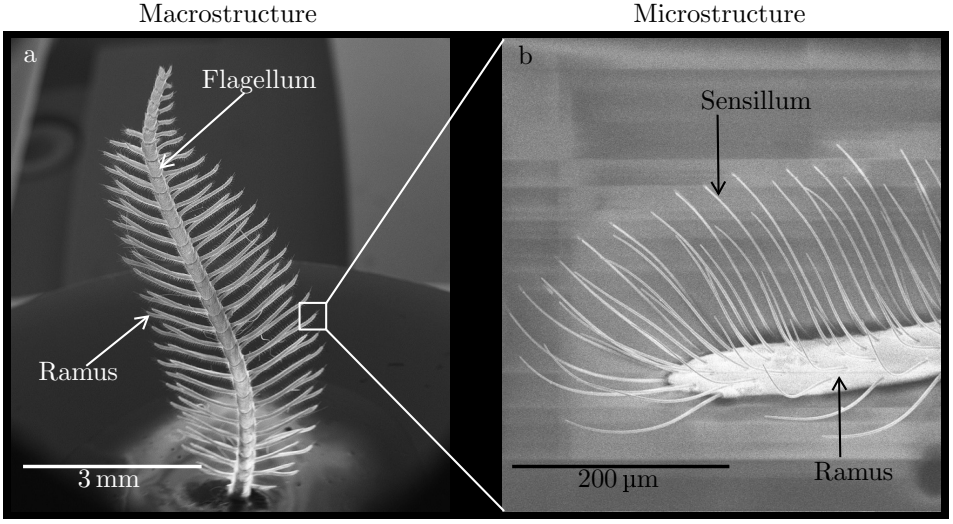

Figure 6.2: Electron Microscopy pictures of the antenna. a: the macrostructure composed of the flagellum and rami is visible. b: focus on the tip of a ramus to reveal the sensilla.

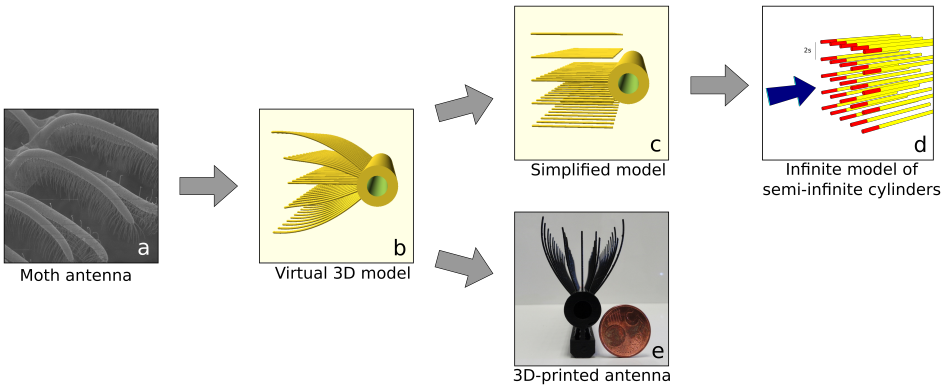

Figure 6.3: Experimental and theoretical approaches used to calculate the antennal capture efficiency. a: picture of the microstructure obtained by Electron Microscopy. b: virtual object designed to mimic the microstructure. c: simplified microstructure with straight sensilla. d: Array of semi-infinite cylinders. The direction of the flow is indicated by the arrow : the cylinders face the flow. The number of cylinders is infinite in the directions orthogonal to the direction of the flow. The local mass transfer coefficient is determined as if it were in the case of semi-infinite cylinders but the total mass transfer is integrated only from the tip to the point where the length of the integrated portion of cylinder is equal to the length of the sensillum (red part of the cylinder). e: 3D printed microstructure used in the PIV experiments to determine leakiness.

the flow. Sensilla are also curved in such a way that they are aligned with the flow of air coming to the antenna as shown in Figure 6.1. Measurements showed that the rami have a diameter of 50 µm and the sensilla are between 100 µm and 150 µm long for a diameter of 3 µm.

6.3.2 Modeling mass transfer

The goal of this part is to provide (i) a solution of the concentration c_s along a sensillum in a steady flow and (ii) derive an expression of the local mass transfer F_s along the sensillum.

The classical mass transport equation is:

$$\frac{\partial c}{\partial t} + (\vec{v}_{\text{air}}.\nabla)c = D\nabla^2 c \tag{6.1}$$

with c the concentration of pheromone in air
$\vec{v}_{\text{air}}$ the velocity of air
D the diffusive coefficient of pheromone in air.

The equation is not easy to solve given the complex, multi-scale geometry of the antenna and we resort to an approximate semi-analytical formulation. We modeled the antenna as a 2D infinite square array of sensilla and each sensillum is modeled as a semi-infinite cylinder with a diameter equal to the one of the sensilla

(Figure 6.3d). Because of the infinity of the array, every single cylinder behaves in the same way and it is thus convenient to reduce the study of this 'wall of sensilla' to the study of a single cylinder with appropriate boundary conditions that mimic the infinity of the array. We call this sensillum 'the average sensillum'. The use of semi-infinite cylinders to model sensilla is justified by the fact that it can model the effect of the sensilla facing the flow. However, because of its semi-infinity, it means that the array of sensilla absorbs all the molecules in the air flow. So, for the purpose of our study, we restrict the results starting from the tip of the cylinders and on a length equal to the one of a natural sensillum. We also assumed that the presence of the remaining part of the cylinders in the dowstream part of the model does not affect in a considerable manner the flow in the first part.

An analogous heat exchange model

Heat transfer in the case of arrays of semi-infinite longitudinal cylinders have been investigated by Miyatake and Iwashima [207] and we make use of the well-known similarity between heat and mass transfers to apply their model to our problem. Heat and mass transfers are indeed both convective phenomena characterized by a diffusion coefficient and by a similar transport equation (Table 6.3). Switching the thermal diffusivity α and the temperature T with, respectively, the mass diffusivity D and the pheromone concentration c is equivalent to switching from the heat equation to the mass one. As a consequence, heat transfer results can be adapted to mass transfer problems and *vice versa*. Boundary conditions must also be similar.

As the fluid flows between the cylinders, heat is exchanged between the cylinders and the fluid. By design of the model, the temperature on the cylinders is kept constant so it is the temperature of the fluid which varies. In the case of the antenna, the concentration on the surface of the sensillum is equivalently fixed, so the concentration in the fluid is the quantity that varies. From a biological point of view, it is reasonable to assume a concentration null at the surface of the sensillum given the very low concentration of pheromone molecules in air.

Reframing the model to our purpose

We first adapted heat transfer processes to mass transfer ones by using the analogies summarized in Table 6.3 (Appendix 6.6.1). We then ensured that our boundary conditions are equivalent to the boundary conditions of the heat transfer model. First, the sensilla are modeled as cylinders and are distributed in a square array of side $2s$ (Figure 6.3d). Second, the concentration at the surface of the sensilla c_{s} is assumed uniform and null. This is equivalent to considering that a pheromone molecule reaching the surface of the antenna is absorbed by the surface and cannot be released in the air again. Third, the far-field concentration c_{∞} is assumed uniform, implying that the antenna is reached by a filament of odor whose cross-section perpendicular to the flow direction is much bigger than the frontal area of

the antenna.

The results are determined in the steady-state case: fluid flow and mass transfer do then depend on space, but they are constant over time. Inflowing fluid has a constant and uniform velocity v_{n} (we assume in section 6.3.4 that this velocity is equal to the mean velocity of air at the entrance of the microstructure) as well as a concentration c_{∞}. The fluid is assumed to be fully laminar and the concentration at the surface of the sensilla c_{s} is also assumed null all over their lengths. The model determines the Sherwood number, a non-dimensional number that characterizes mass transfer by comparing the convective (advection and diffusion combined) mass flux between the fluid and the surface of the cylinders to the mass transfer due to diffusion alone.

$$\mathrm{Sh} = \frac{K_M L_{\mathrm{s}}}{D} \tag{6.2}$$

with K_M the coefficient of mass transfer ($\mathrm{m\,s^{-1}}$)
L_{s} the length of a sensillum (m)

The boundary layer increases along the sensillum and gets fully developed at infinity. By design, the flow regime is laminar, so turbulence cannot appear. In our case, the Reynolds number at the end of a sensillum, with a characteristic length equal to L_{s}, the length of the sensillum, and a velocity equal to $5\,\mathrm{m\,s^{-1}}$ is equal to 50, which is far lower than the Reynolds number required to have some turbulence. As the boundary layer increases along the sensillum, the Sherwood number goes down. Thus, Miyatake and Iwashima's model gives local values of the Sherwood number varying with z, the coordinate along the sensillum, as:

$$\mathrm{Sh}_{\mathrm{loc}}(z) = \left(f^2 + g^2 \mathrm{Gz}(z)^{2/3}\right)^{1/2} \tag{6.3}$$

with

$$f = \frac{4.00(1 + 0.509\psi)}{1 + 0.765\psi^{5/3}} \tag{6.4}$$

$$g = \frac{1.69(1 + 9.1\psi)}{(1 + 10.8\psi^{5/4})(4\sigma^2 - \pi)^{1/3}} \tag{6.5}$$

$$\mathrm{Gz}(z) = \frac{w_{\mathrm{mod}}}{Dz} \tag{6.6}$$

d_{s} the diameter of a sensillum (m)
s half distance between cylinders (m)
w_{mod} the volume flow rate of fluid per cylinder ($\mathrm{m^3 s^{-1}}$). In our model, $w_{\mathrm{mod}} =$

$v_\mathrm{n} 4s^2$ with v_n the far-field velocity of the fluid and $4s^2$ the frontal area in the case of a square distribution
σ the adimensionalized distance between cylinders $2s/d_\mathrm{s}$ (also termed pitch-to-diameter ratio in [207])
ψ the dimensionless spacing between cylinders, $\sigma - 1$
$\mathrm{Gz}(z)$ the local Graetz number
K_M, the coefficient of mass transfer, is obtained as:

$$K_M(z) = \frac{D}{L_\mathrm{s}} \left(f^2 + g^2 \mathrm{Gz}(z)^{2/3} \right)^{1/2} \tag{6.7}$$

At each position of the cylinder, the local mass transfer $F_\mathrm{loc}(z)$ on a slice of cylinder of length $\mathrm{d}z$ depends on the local mass transfer coefficient K_M and follows the expression:

$$F_\mathrm{loc}(z) = K_M(z) \left(c_\mathrm{f}(z) - c_\mathrm{s} \right) \tag{6.8}$$

with
$c_\mathrm{f}(z)$ the mean concentration of pheromone in the fluid at z (gm^{-3})
c_s the concentration at the surface of the cylinders supposed to be uniformly constant (gm^{-3}).

A mass balance on a slice of fluid around a cylinder (Figure 6.4) gives:

$$F_\mathrm{in}(z) - F_\mathrm{out}(z + \mathrm{d}z) = F_\mathrm{loc}(z) \pi d_\mathrm{s} \mathrm{d}z \tag{6.9}$$

with

$$F_\mathrm{in}(z) = w_\mathrm{mod} c_\mathrm{f}(z) \tag{6.10}$$

$$F_\mathrm{out}(z + \mathrm{d}z) = w_\mathrm{mod} c_\mathrm{f}(z + \mathrm{d}z) \tag{6.11}$$

As the concentration at the surface of the cylinders is considered uniform in space and constant in time due to the steady-state assumption, the concentration of pheromone in the fluid is bounded to vary according to:

$$w_\mathrm{mod} c_\mathrm{f}(z) - w_\mathrm{mod} c_\mathrm{f}(z + \mathrm{d}z) = K_M(z) \left(c_\mathrm{f}(z) - c_\mathrm{s} \right) \pi d_\mathrm{s} \mathrm{d}z \tag{6.12}$$

Thus, the variation of mean fluid concentration along a cylinder is given by:

$$-w_\mathrm{mod} \frac{\mathrm{d}c_\mathrm{f}}{\mathrm{d}z} = K_M(z) \pi d_\mathrm{s} \big(c_\mathrm{f}(z) - c_\mathrm{s} \big) \tag{6.13}$$

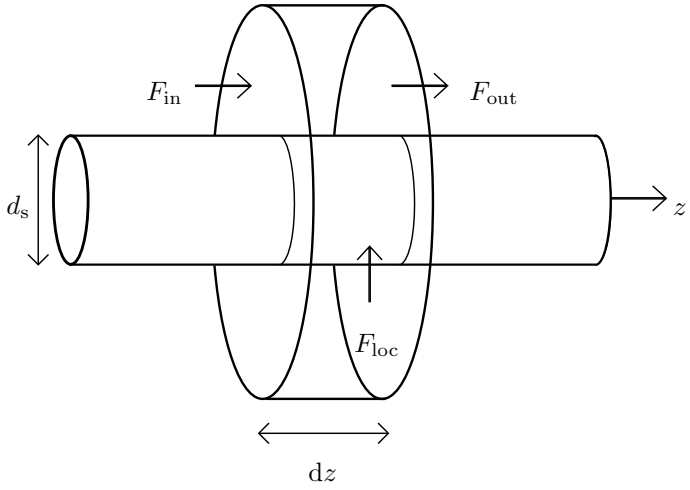

Figure 6.4: Control volume used to derive equation 6.13

The total mass flux F_{s} between the fluid and a sensillum is obtained by solving equations 6.8 and 6.13 and by integrating the local mass flux along a sensillum with a length L_{s}.

$$F_{\text{s}} = \int_0^{L_{\text{s}}} F_{\text{loc}}(z)\pi d_{\text{s}}\mathrm{d}z \tag{6.14}$$

For large values of z, the Graetz number becomes very small compared to 1 (equation 6.6) and the term $g^2\mathrm{Gz}(z)^{2/3}$ becomes negligible compared to f^2 in equation 6.7. The coefficient K_M becomes almost constant at high values of z and equation 6.13 becomes :

$$-w_{\text{mod}}\frac{\mathrm{d}c_{\text{f}}}{\mathrm{d}z} = K_M\pi d_{\text{s}}c_{\text{f}}(z) \tag{6.15}$$

If we define $\gamma = \frac{K_M\pi d_{\text{s}}}{w_{\text{mod}}}$ then we obtain:

$$c_{\text{f}} = c_\infty \exp(-\gamma z) \tag{6.16}$$

Comparison between the two terms $g^2\mathrm{Gz}(z)^{2/3}$ and f^2 shows that $g^2\mathrm{Gz}(z)^{2/3}$ becomes negligible for values of z at least of the order of the millimeter which is longer than the 150 µm of the sensilla. Thus, in our model we cannot use the asymptotic value of K_M to simplify the model. However, $g^2\mathrm{Gz}(z)^{2/3}$ acts like it increases the value of γ and the fluid concentration decreases faster than in the case of constant K_M.

Because we model an infinite array of sensilla, we can focus on one single sensillum in order to model the 'average' sensillum. We solved the system of

		Geometrical parameters	
L_{ant}	1 cm	Antenna length	Measurements
d_{s}	3 µm	Sensilla diameter	Measurements
L_{s}	150 µm	Sensillum length	Measurements
α	300	Scaling factor	
s	16 µm	Half distance between sensilla	Measurements
σ	10.7	Adimensionalized distance between cylinders	$\sigma = 2s/d_{\text{s}}$
ψ	9.7	Dimensionless spacing between sensilla	$\phi = \sigma - 1$
d_{s}		diameter of the cylinder in the heat transfer model, equivalent of the diameter of the sensillum for the mass transfer model	
S_{front}	m^2	Frontal area	Equations 6.22 and 6.23
		Experimental parameters	
v_{air}	m s^{-1}	Air velocity	
v_{oil}	m s^{-1}	Oil velocity	
v_{∞}	m s^{-1}	Far-field air velocity in the PIV experiment	
v_{n}	m s^{-1}	Mean air velocity close to the antenna	
c_{s}	g m^{-3}	Uniform concentration at the surface of the sensillum	
c_{∞}	g m^{-3}	Far-field concentration	
		Adimensionalized numbers	
Le		Leakiness	Equation 6.21
Re		Reynolds number in air	Equation 6.19
Sh		Sherwood number	Table 6.3
Sh_{loc}		Local Sherwood number	
Gz		Graetz number	Table 6.3
		Physical parameters	
ν_{air}	$15.6 \times 10^{-6}\ \text{m}^2\text{s}^{-1}$	Kinematic viscosity of air at 20 °C	
ν_{oil}	$50 \times 10^{-6}\ \text{m}^2\text{s}^{-1}$	Kinematic viscosity of rapeseed oil at 29 °C	
D	$4.5 \times 10^{-6}\ \text{m}^2\text{s}^{-1}$	Diffusive coefficient of pheromone	Appendix 6.6.2
w_{mod}	m^3s^{-1}	Volume flow rate per sensillum in the model	$w_{\text{mod}} = (4 * s^2 - \pi * (\frac{d_{\text{s}}}{2})^2) * v_{\infty}^{\text{mod}}$
w	m^3s^{-1}	Volume flow rate per sensillum in the experiment	$w = (4 * s^2 - \pi * (\frac{d_{\text{s}}}{2})^2) * v_{\infty}$
		Variables	
v_{n}	m s^{-1}	Mean fluid velocity at the entrance of the antenna	
w_{n}	m^3s^{-1}	Flux near the antenna, between the two mostly outward positioned sensilla	
w_{ref}	m^3s^{-1}	Flux taken for an equal surface as F_{through} for a fluid at velocity v_{∞}	
K_M	m s^{-1}	Mass transfer coefficient	
F_{in}	g s^{-1}	Mass flux going in the control volume described in Figure 6.4	
F_{out}	g s^{-1}	Mass flux going out the control volume described in Figure 6.4	
F_{loc}	$\text{g m}^{-2}\,\text{s}^{-1}$	Local mass flux going to the sensilla in Figure 6.4	
F_{s}	g s^{-1}	Total mass flux going to a sensillum	
c	g m^{-3}	Pheromone concentration in the fluid	
c_{f}	g m^{-3}	Mean concentration in the fluid between the sensilla depending on z	
η_{s}		Capture efficiency of a sensillum	
η_{ant}		Capture efficiency of the antenna	

Table 6.1: List of parameters used in the paper

equations 6.8 and 6.13 (Matlab R2015b 8.6.0.267246) and obtained the mass flux on one sensillum F_s using equation 6.14. We then calculated the capture efficiency η_s of the sensillum by dividing the mass flux previously determined F_s with the reference mass flux F_{ref}^{mod}. The reference mass flux is the volume flow rate per sensillum defined in the model times the far-field concentration :

$$F_{ref}^{mod} = w_{mod} c_\infty \tag{6.17}$$

The capture efficiency of a single sensillum becomes :

$$\eta_s = \frac{F_s}{F_{ref}^{mod}} \tag{6.18}$$

In this infinite model, sensilla are all equivalent. Thus, determining the capture efficiency of all sensilla requires only to multiply both the mass flux on a sensillum F_s and the reference flux F_{ref}^{mod} by the number of sensilla on the antenna. This is equivalent to multiply both the numerator and the denominator of η_s by the number of sensilla (equation 6.18). A mere simplification shows that it is equal to the one of a single sensillum.

A real antenna is however not infinite and leakiness accounts for that. The divergence of the flow arriving on an antenna has two consequences. Firstly, the airflow is slowed down by the presence of the antenna. The air flowing through the antenna v_{ant} has a lower speed than the far-field air velocity v_∞. The air flowing through the antenna v_{ant} is taken as the model far-field air velocity v_n (Figure 6.1). Secondly, a portion of air flows around the whole antenna and not through it so the molecules it carries are out of reach of the sensilla. The reference flux F_{ref} must then be defined depending on v_∞ and not v_n as it was the case for the reference flux of the model (equation 6.17).

We determined the value of leakiness of the antenna using a Particle Image Velocimetry (PIV) experiment.

6.3.3 Experiments

Fabrication of artificial antennae by Additive Manufacturing

Artificial antennae (Figure 6.5) were designed with Openscad (version 2015.03-2) and 3D printed with a Form 2 from Formlabs (Somerville, Massachusetts, USA) using Black Photoreactive Resin (Formlabs, Somerville, Massachusetts, USA). The antennae were scaled by a factor $\alpha = 300$ compared to natural ones for two reasons. Firstly, the artificial antennae should be big enough to measure the flow around them accurately. Secondly, the sensilla need to be thick enough to survive the mechanical loading during the building process. An artificial antenna was then 13 cm long, with a rami of 1.5 cm diameter and sensilla of 0.9 mm diameter.

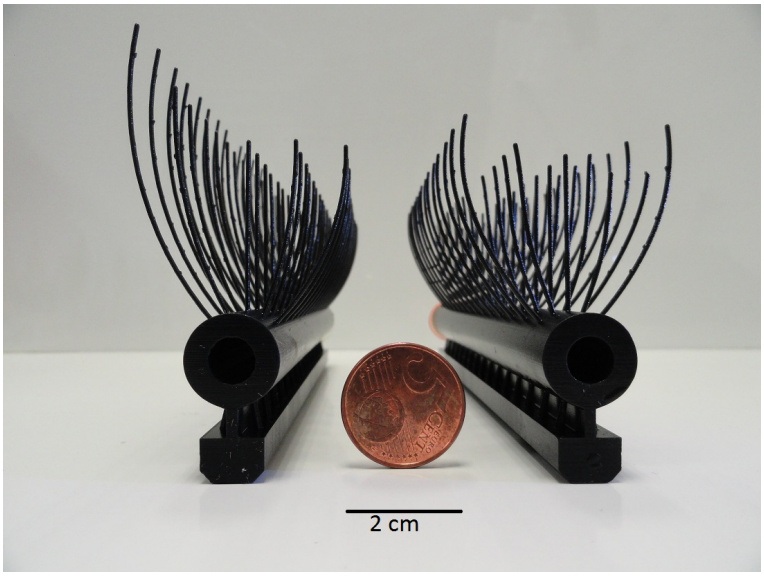

Figure 6.5: Print of RS1 and RS2 from right to left.

Particle Image Velocimetry

A wide range of velocities was used to cover the amplitude of flows through the antenna induced by wind on a resting moth, or flows through the antenna during a simulated moth flight. Thus, we considered an air velocity span of 3 orders of magnitude and choose the velocities $\{0.002, 0.005, 0.1, 0.2, 0.5, 1, 2, 5\}$ $\mathrm{m\,s^{-1}}$. In terms of Reynolds numbers, using the sensillum diameter as characteristic length, we get

$$\mathrm{Re} = \frac{d_\mathrm{s} * v_\mathrm{air}}{\nu_\mathrm{air}} \tag{6.19}$$

with d_s the diameter of the sensillum (3 µm), v_air the velocity of air, ν_air the kinematic viscosity of air ($15.6 \times 10^{-6}\,\mathrm{m^2\,s^{-1}}$ at 20 °C). These above velocities correspond to the range of Reynolds numbers of {0.004, 0.01, 0.02, 0.04, 0.1, 0.2, 0.4, 1}.

In order to keep the Reynolds number constant while working with antennae which are three orders of magnitude larger than the natural ones, we changed both the velocity and the kinematic viscosity of the fluid. Instead of working in air, we thus ran our experiments in rapeseed oil which has a measured kinematic viscosity of $50 \times 10^{-6}\,\mathrm{m^2 s^{-1}}$ at 29 °C (Rolling ball viscometer: Lovis 2000, Anton Paar, Graz, Austria). The oil velocities corresponding to the air velocities were determined using equation 6.20 and are indicated in Table 6.2.

$$\mathrm{Re} = \frac{d_\mathrm{s} * \alpha * v_\mathrm{oil}}{\nu_\mathrm{oil}} \tag{6.20}$$

with α, the scaling factor used to fabricate the artificial antennae,
v_{oil}, the oil velocity,
ν_{oil}, the oil kinematic viscosity.

Reynolds number	0.004	0.01	0.02	0.04	0.1	0.2	0.4	1
Air velocity v_{air} $\text{m}\,\text{s}^{-1}$	0.02	0.05	0.1	0.2	0.5	1	2	5
Experimental oil velocity v_{oil} $\text{mm}\,\text{s}^{-1}$	0.21	0.53	1.07	2.14	5.34	10.7	21.4	53.4

Table 6.2: Equivalent oil velocities. Reynolds numbers in both water and oil were equaled to determine the oil velocity corresponding to each air velocity that we wanted to investigate.

To generate a constant flow through an antenna, we fixed the antenna on a support and moved an aquarium filled with rapeseed oil using a motorized linear axis (LST1000D-T3, Zaber Technologies, Vancouver, British Columbia, Canada). The aquarium was made of glass, 50 cm long (in the direction of the flow), 30 cm wide and 25 cm deep. Hollow glass particles covered with silver (10 µm, SUGS-10, Dantec Dynamics, Skovlunde, Denmark) were used to track the fluid movements and were illuminated by a laser sheet of $1.5-2$ mm of thickness. The laser sheet was generated by a continuous laser source (MGL-F, 532 nm, 2 W CNI, Changchun, China) equipped with a cylindrical lens. Between 100 and 200 pictures per second ($\Delta t = 5 - 10$ ms) were recorded depending on the velocity of the fluid using a highspeed camera (Phantom 9.1, Vision Research, Perth, Australia) equipped with a 35 mm lens (AF-S DX, Nikon, Tokyo, Japan). The resolution of the pictures was $1632 * 1200$ and the field of view had a size of $105 * 78$ mm. We used the software Davis (Davis8.3, Lavision, Gottingen, Germany) to process our pictures. Depending on oil velocity, we analysed pairs of pictures separated by a temporal interval ensuring a correct estimation of velocity.

The microstructure was positioned perpendicular to the flow so that the sensilla faced it. The laser sheet was set parallel to the $x - z$ plane (Figure 6.6), approximately in the middle of the microstructure in order to avoid edge effects. The flow velocity field is then almost 2D in $x - z$ planes (Figure 6.7). However, because of the presence of sensilla, the component of the velocity in the y direction cannot be null. We ran experiments in the same disposition but with the laser sheet in the $y - z$ plane in order to check that the z-component of the velocity is negligible (Appendix 6.6.3). We also designed our microstructure with regularly-spaced rows of sensilla and compared the flow profile with the laser sheet positioned both on a row of sensilla and between two rows and found negligible differences between them.

Estimating leakiness

Leakiness (Le) measures the proportion of molecules that is available to the antenna. It is defined as the flux going through an object divided by the flux going

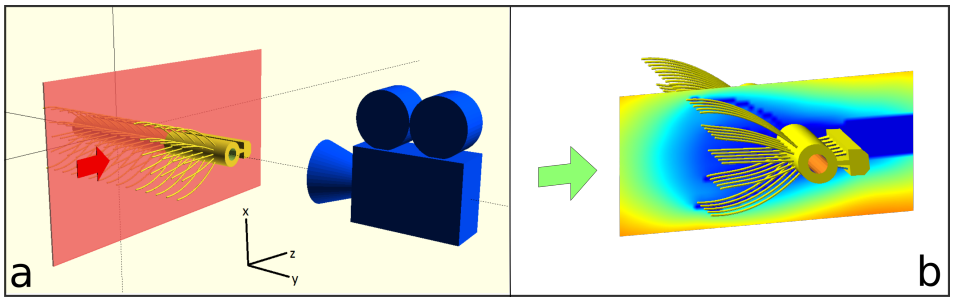

Figure 6.6: PIV experiment. a, setup of the experiment. b, velocity field obtained from PIV.

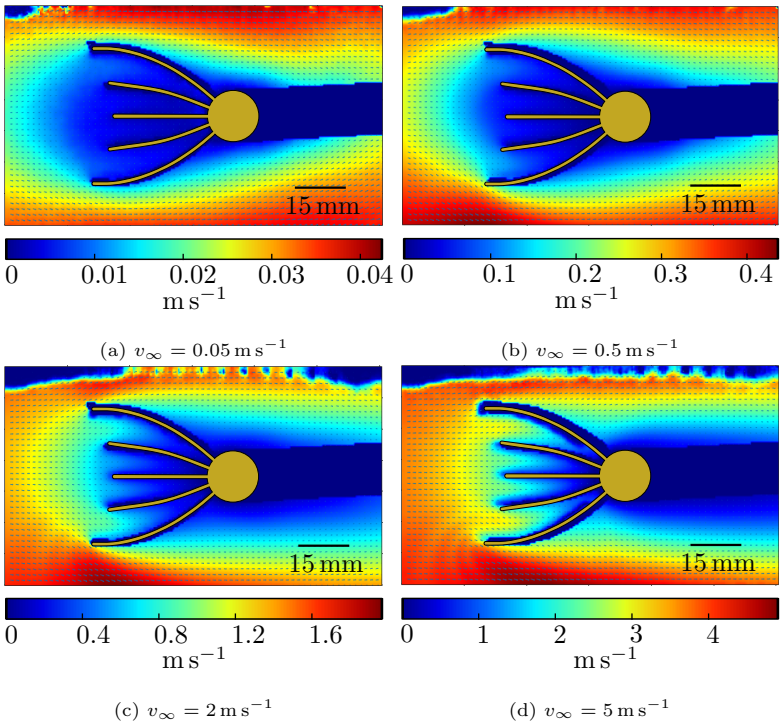

Figure 6.7: Absolute equivalent air velocity fields from the PIV data for several far-field air velocities.

through an equal frontal area, as if the object was absent [187]. The frontal area is equal to the surface resulting from the projection of the object on a plane perpendicular to the direction of the flow. Leakiness is thus the ratio of the measured flux and the reference flux. A leakiness equal to zero means that the structure is non-permeable. As the structure gets more permeable, leakiness increases until it reaches one, a completely permeable structure, equivalent to no structure at all. Because leakiness is a relative measure, it is identical in dynamically-scaled configurations or, in other words, in configurations with equal Reynolds number. It means that we can measure leakiness on a scaled-up antenna in oil and apply the resulting measurements to the real antenna in air.

As we are interested in the flow that brings molecules in the neighborhood of the sensilla, we compared the flux flowing between the mostly outward positioned sensilla of the antenna (the flux through the antenna) to the far-field flux through an equal area (the reference flux). The flux through the antenna is measured by means of the PIV velocity field. We integrated the velocity field on a line between the two most outward positioned sensilla (Figure 6.8) and multiplied it by one unit length in the y-direction (perpendicular to the plane of Figure 6.8) because we assume the antenna to be infinitely long in the y-direction. It is important to notice that the leakiness is the ratio of two fluxes through surfaces of equal area. The reference flux is the flux going through a surface of the same area as the one defined for the flux through the antenna, but with a velocity field equal to the far-field velocity field. In other words, we multiplied the distance between the two most outward positioned sensilla by one unit-length in the y-direction and by the far-field velocity, leading to the following expression of leakiness:

$$\mathrm{Le} = \frac{w_\mathrm{n}}{w_\mathrm{ref}} \tag{6.21}$$

with w_n the flux near the antenna, between the two mostly outward positioned sensilla of the antenna and w_ref the reference flux.

If we define :
v_n, the mean velocity at the entrance of the antennae where leakiness is determined,
v_∞, the uniform far-field velocity and
S_front, the frontal area,
we obtain

$$w_\mathrm{n} = v_\mathrm{n} * S_\mathrm{front} \tag{6.22}$$

$$w_\mathrm{ref} = v_\infty * S_\mathrm{front} \tag{6.23}$$

Combining equations 6.21, 6.22 and 6.23, we obtain:

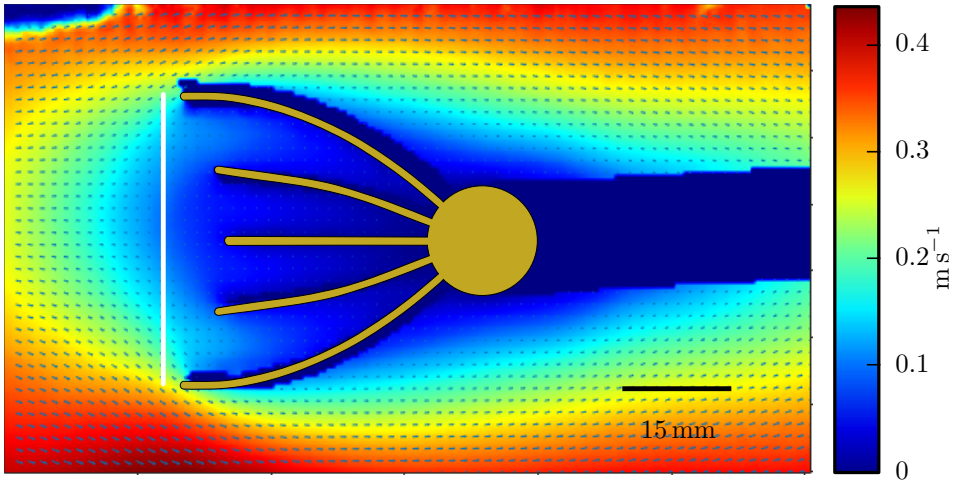

Figure 6.8: Velocity field obtained with PIV. The white line pictures out the location of the flux integration to determine the mean velocity v_n of the fluid between the sensilla and the leakiness of the antenna. In this case the far-field velocity used in the experiment was $5.34\,\mathrm{mm\,s^{-1}}$ in oil which is equivalent to $0.5\,\mathrm{m\,s^{-1}}$ in air. Equivalent air velocities displayed in the picture.

$$\mathrm{Le} = \frac{v_n}{v_\infty} \tag{6.24}$$

Or, equivalently,

$$v_n = \mathrm{Le} * v_\infty \tag{6.25}$$

Because the microstructure that we designed displays regularly-spaced rows of sensilla, we evaluated the leakiness for the velocity field with a laser sheet positioned both on a row and between two rows of sensilla. The leakiness of the microstructure was defined as the mean of these two local measures of leakiness.

6.3.4 Combining the model and the PIV experiment

The model of mass transfer adapted from Miyatake and Iwashita [207] gives the capture efficiency of a sensillum depending the velocity of the air coming on the sensillum. As an approximation, we considered the mean velocity v_n at the entrance of the antenna as the model far-field velocity (Figure 6.9).

The model gives the expression of the capture efficiency of a sensillum depending on v_n, $\eta_s(v_n)$ as well as the mass flux on a sensillum $F_s(v_n)$. The PIV experiment gives the relation between the far-field velocity v_∞ and the velocity at the entrance of the antenna, $v_n(v_\infty)$. By combining the model and the experimental sections, it is possible to express the capture efficiency of a sensillum depending on the far-field velocity v_∞, $\eta_s(v_\infty)$. We did the same for the mass flux on a sensillum $F_s(v_\infty)$. From now on, given the relation expressed in equation 6.25, we

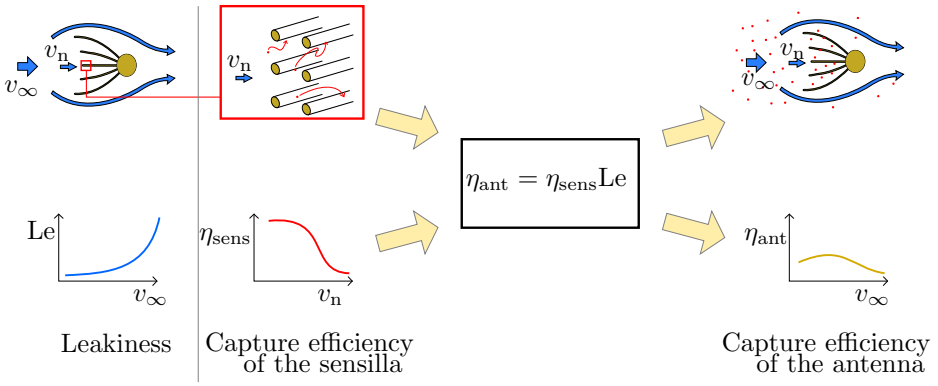

Figure 6.9: Combination of the model and the experiments to obtain the capture efficiency of the microstructure.

expressed all the values of the model depending on v_∞ and not v_n anymore.

To determine the efficiency of the antenna η_{ant}, we had to also take into account that a portion of air does not flow through the antenna. The easiest way to determine it is to go back to the mass flux on a sensilla $F_s(v_\infty)$ and define a new reference mass flux F_{ref} depending on v_∞.

$$F_{ref} = wc_\infty = 4s^2 v_\infty c_\infty \tag{6.26}$$

The capture efficiency of the antenna η_{ant} is defined as :

$$\eta_{ant}(v_\infty) = \frac{F_s(v_\infty)}{F_{ref}(v_\infty)} \tag{6.27}$$

By multiplying the numerator and denominator by $F_{ref}^{mod}(v_\infty)$ and using the expressions of the reference fluxes (equations 6.17 and 6.26), we obtained :

$$\eta_{ant}(v_\infty) = \frac{F_s(v_\infty)}{F_{ref}^{mod}(v_\infty)} \frac{v_n 4s^2}{v_\infty 4s^2} \tag{6.28}$$

According to equations 6.18, 6.24 and 6.25, we obtained :

$$\eta_{ant}(v_\infty) = \eta_s(v_\infty)\text{Le}(v_\infty) \tag{6.29}$$

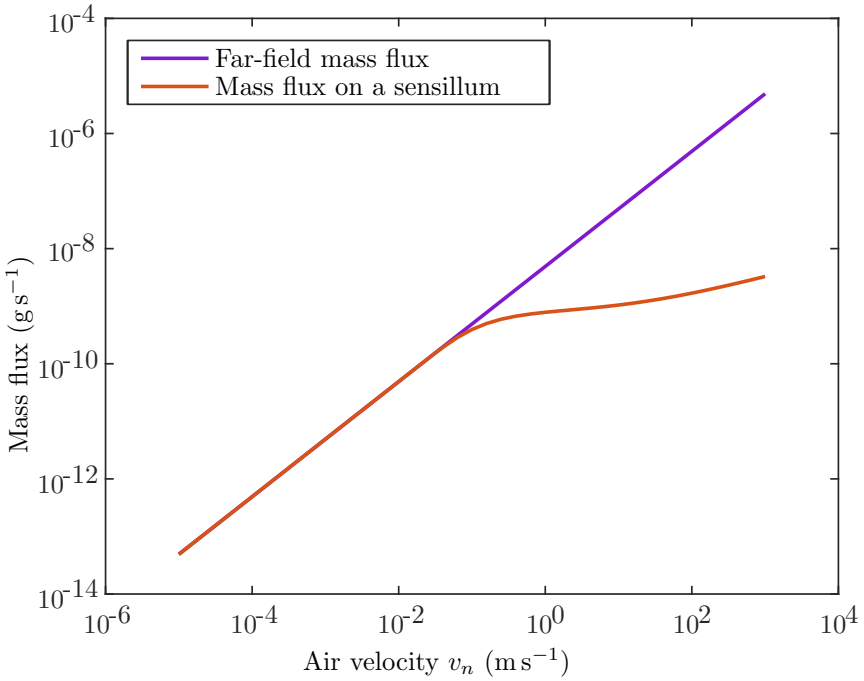

Figure 6.10: Absolute mass flux reaching a sensillum depending on the air velocity v_n.

6.4 Results

We focused first on the behavior of the model of mass capture so the variables are depending on v_n.

The absolute mass flux captured by the sensilla F_s was determined with a far-field concentration c_∞ of $1\,\mathrm{g\,m^{-3}}$. It increases with air velocity v_n. The rate of increase is linear for low velocities and gets flatter at high velocities (Figure 6.10).

The capture efficiency of the model η_s shows a quite different behavior, constantly decreasing (Figure 6.11). This difference is due to the fact that the model reference mass flux $F_\mathrm{ref}^\mathrm{mod}$ increases linearly with the far-field velocity v_n whereas the mass flux F_s increases more slowly (Figure 6.10). As a consequence, the model capture efficiency η_s, which is a relative value, decreases at high velocity.

From now on, we consider the whole microstructure so the variables are now depending on v_∞.

The measured leakiness Le of the antenna is increasing monotonously with the far-field velocity v_∞ (Figure 6.12). A drop of leakiness occurred at $0.1\,\mathrm{m\,s^{-1}}$ for structures with various geometries that we tested (unpublished data) so we think

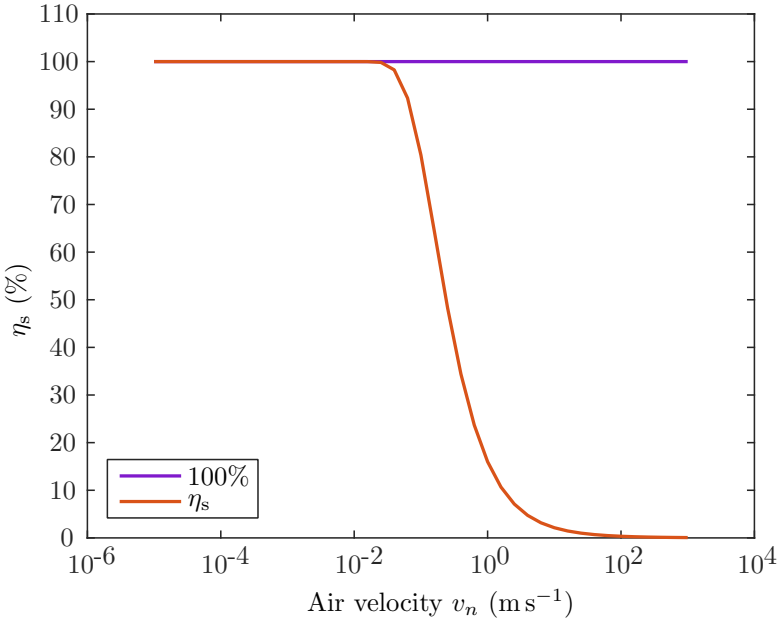

Figure 6.11: Capture efficiency of the infinite model of semi-infinite sensilla depending on the air velocity v_n. The capture efficiency is a relative value so it is bounded between 0 and 100%.

that the most likely explanation is that our linear motorized axis had some irregularities at this velocity.

We used the leakiness as a direct link between v_n and v_∞ (equation 6.25) to express η_s depending on v_∞ (Appendix 6.6.4). This mainly results in a shift of the curve in the direction of the high velocities (Figure 6.13).

In Figure 6.14, we see that the leakiness Le is growing whereas the efficiency of the model η_s is decreasing with increasing v_∞. The efficiency of the microstructure, η_{ant}, the product of the two curves (equation 6.29), displays a flat optimum around 0.5 m s^{-1}.

It is interesting to note that the mass flux is limited by both the leakiness of the antenna and the capture efficiency of the array of sensilla. At low velocities, the leakiness is the limiting factor as most of the air is flowing around the antenna. However, air flows slowly between sensilla and pheromone molecules have thus enough time to diffuse to the surface of the sensilla. At higher velocities, limited mass capture is due to the array of sensilla which is not efficient enough to capture a large portion of the molecules flowing between the sensilla. The transition occures around 0.2 m s^{-1}, *i.e.* in the middle of the optimal range of velocities.

The spatial distribution of capture shows a decrease of capture along the sensillum (Figure 6.15). By integrating these local capture rates F_{loc} (equation 6.8),

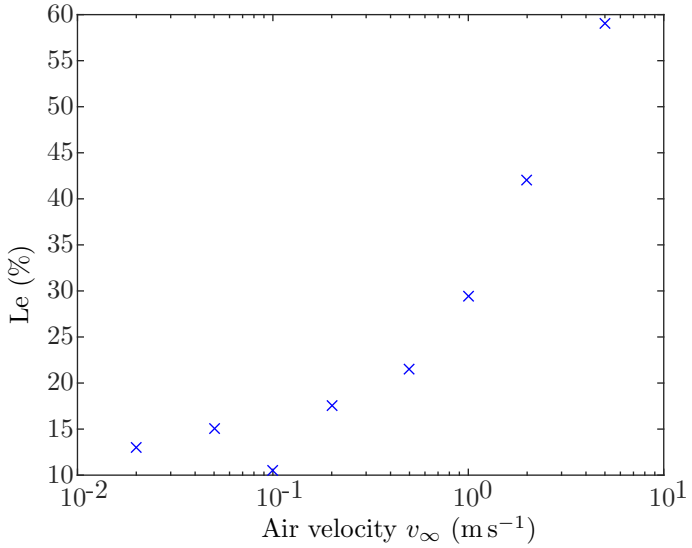

Figure 6.12: Leakiness of the antenna. The data was determined in oil experiments but is displayed depending on the equivalent air velocities v_∞.

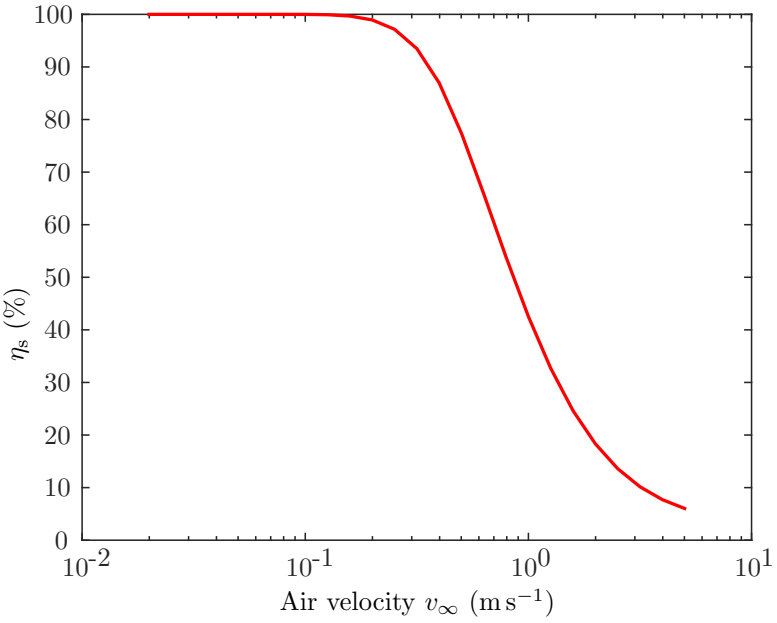

Figure 6.13: Capture efficiency η_s of the model of sensilla depending on the air velocity v_∞.

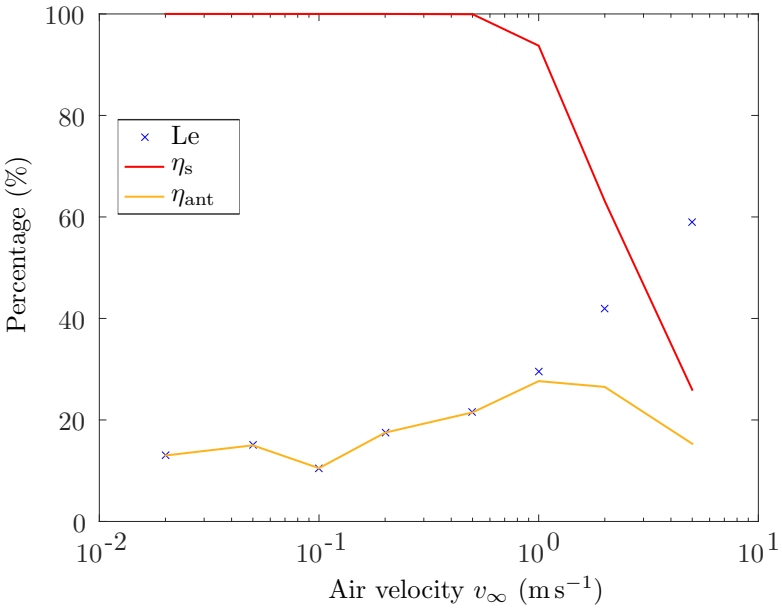

Figure 6.14: Capture rate of the antenna compared to leakiness and model capture rate.

we obtained the relative capture importance of each half of the sensillum (Figure 6.16). The first half of the sensillum captures more molecules and its relative importance depends on the air velocity.

Transversal and longitudinal cylinders to the flow were also simulated using Comsol in order to determine their drag and mass flux (Appendix 6.6.5).

6.5 Discussion

6.5.1 Assumptions of the model

We discuss in turns a number of assumptions regarding the printed antenna, the fluid dynamics experiments and the model, related to 1) the printed square arrangement of sensilla on the ramus which is an approximation of the real arrangement, 2) our choice of the sensillum to define the characteristic length, 3) the assumed infinite length of the antenna, 4) the assumed pheromone concentration at the sensillum surface and 5) the assumed stationary distribution of odor in the far-field in the model.

Let us consider the three first points, all related to the geometry of the antenna. We have used a square array of sensilla for simplicity, whereas real antennae are not as ordered. To assess the importance of this approximation, we computed the flow using a triangular array with the same density of sensilla (calculations in Appendix 6.6.6). This difference alters the efficiency of the antenna only marginally;

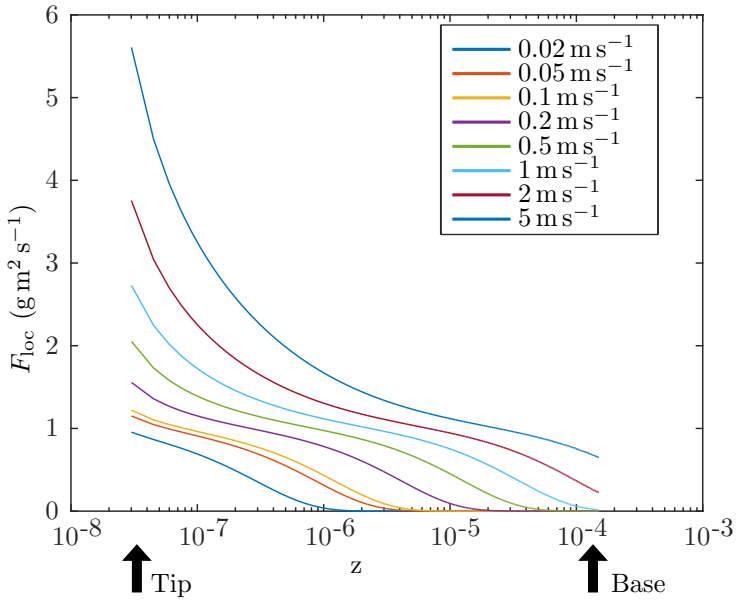

Figure 6.15: Evolution of the mass flux F_{loc} captured along the sensillum for a far-field concentration c_∞ of $1\,\text{g}\,\text{m}^{-3}$.

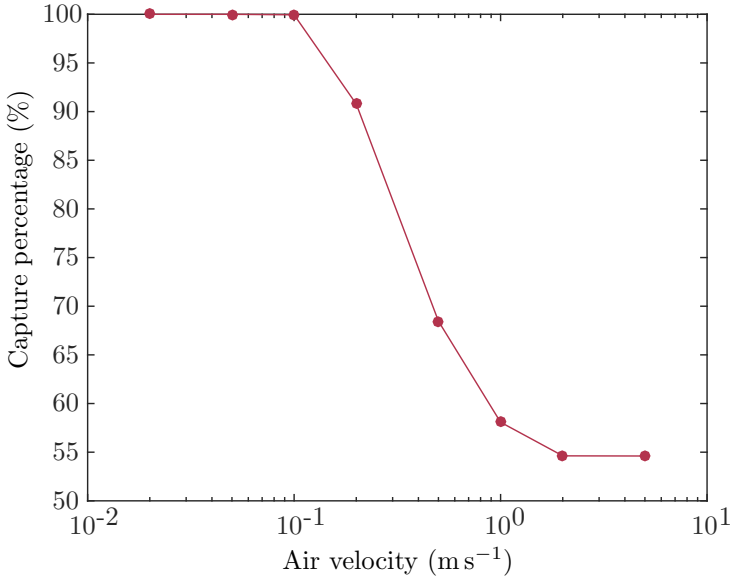

Figure 6.16: Relative importance of the 1st half of the sensillum.

what matters is the density of sensilla more than their arrangement. Secondly, there is not a single length value characteristic of an antenna due to its multi-scale nature. However, to determine the flow regime and the equivalent Reynolds number, we chose the sensillum diameter as the appropriate scale. This choice was made because we were interested in the flow between the dense rows of sensilla, because they are located upstream relative to the rami and the flagellum, and because they are the ones which bear the sensory pores. Finally, our PIV measurements were conducted with a laser sheet perpendicular to the axis of the rami and we considered the flow to be 2-dimensional in this plane. The laser sheet was located approximately in the middle of the antenna in order to avoid edge effects. Assuming the flow profile we obtained was representative of the flow profile of an infinitely-long microstructure, we extrapolated the results of our single measurement to the whole microstructure. The main benefit of this appraoch is that we could focus on an 'average' sensillum.

The concentration of odor at the surface of the sensillum was assumed to be always null. Two interpretations of this boundary conditon are possible. The pheromone molecules on the surface of the sensillum are processed so quickly that the surface concentration is indeed always close to zero. Alternatively, the pheromone molecules can stick on the surface of the sensilla and are not able to desorp. Given the very low concentration of pheromone in air, it is reasonable to consider that the carrying capacity of the surface is never reached or, from a reverse point of review, that the carrying capacity of a sensillum surface is infinite. Studying the physico-chemical properties and the adsorption-desorption coefficients at the surface of the sensillum is challenging and has been done only a few times, so we currently do not know exactly what happens to a molecule that reaches the sensillum surface [107].

The odor distribution is a key assumption in all the models published so far. We assumed a constant flux of pheromones, in coherence with the model of Miyatake and Iwashima [207] that we used as analogy was developed for a stationary heat flux. This is a strong approximation with reality: female moths release pulsed puffs [95, 96] and this signal is deformed by turbulence in air [99, 210]. Thus, moth antennae generally experience spatio-temporal puffs of pheromone, and even need a periodic signal to trigger a behavioral response [100, 101]. Our model cannot predict anything regarding temporal chemical patterns such as shape of the signal or value of the derivative of the concentration. However, if we consider the instant when the insect is within a plume or puff and totally surrounded by a pheromone cluster, then the assumption of steady-state is reasonable (Appendix 6.6.7).

6.5.2 The efficiency of the antenna is the product of two conflicting trade-offs

The capture performance of an antenna depends, among others, on two main features: its finite dimensions and its particular geometry [201]. The finite dimen-

sions imply that air can either flow between the sensilla or go around the whole antennal structure: leakiness defines the proportion of air that flows between the sensilla. This is thus an important parameter to take into account as an antenna cannot capture the pheromone molecules that are carried by the air going around it. Leakiness depends on the velocity by which the air approaches the antenna and the particular geometry of the antenna which forms, to lesser or higher degree, a resistance to the air flow. Leakiness furthermore determines the velocity of air between the sensilla. We have shown that a low leakiness improves pheromone capture because the molecules have sufficient time to be trapped by the sensilla surface due to diffusion only. So, the first feature, the finite dimension of the antenna, has a key impact on capture performance through leakiness. The capture efficiency is furthermore compounded by the specific geometrical arrangement of the sensilla, the second feature. The model of an infinite array of semi-infinite longitudinal cylinders facing the air flow captures the essence of this geometrical problem [207]. The outcome of our model is that the capture efficiency of an antenna is the product of the leakiness with the efficiency of that infinite model. As leakiness and efficiency of the infinite model are both defined as ratios ranging between 0 and 1, their product is also comprised between 0 and 1 and, more importantly, is always inferior to each term. Thus, for a given air velocity, the efficiency of the antenna is majored by their smallest value. In Figure 6.14, we can observe that, at low velocity, the leakiness is very small and is limiting the efficiency of the antenna whereas at high velocities, a higher proportion of air effectively goes between the sensilla. However, at these high velocities, only a small portion of the pheromone molecules diffuses to the sensilla. We conclude that an efficient antenna should have both a high leakiness and a small distance between sensilla. For an array of horizontal cylinders, the first condition implies a decrease of the drag due to a decrease in the length or the number of cylinders. The second condition requires an increase of the length or the number of cylinders. We thus observe a trade-off between these two limiting conditions, implying an optimum of efficiency, located at intermediate values of air velocities.

This trade-off between leakiness and capture efficiency can be understood in terms of advection and diffusion. A high leakiness is equivalent to a dominant advection contribution whereas a good capture efficiency requires a dominant diffusion contribution. The Péclet number is well-adapted to express that relative importance of advection and diffusion :

$$\mathrm{Pe} = \frac{v_{\mathrm{air}} * L_{\mathrm{s}}}{D} \tag{6.30}$$

In Figure 6.17, the Péclet number is above one in the main flow, upstream of the sensilla, and is reduced by one order of magnitude between the sensilla, showing that diffusion dominates advection between the sensilla.

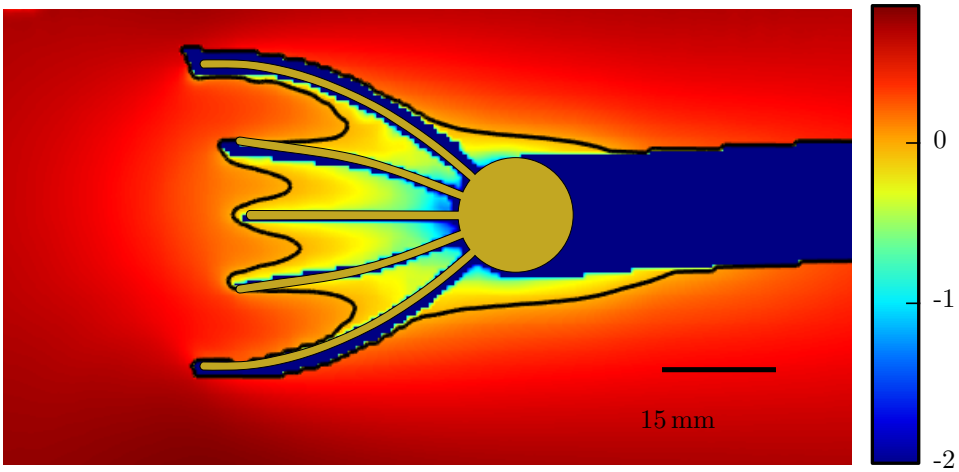

Figure 6.17: Local Péclet number for an air velocity $v_\infty = 1\,\mathrm{m\,s^{-1}}$. Scale is in power of ten : 0 means that the Péclet number equals 1, 1 means a Péclet number of 10 etc. In the case of this logarithmic scale, a Péclet number above 0 means that advection is the most important phenomenon whereas a Péclet number below 0 means that diffusion is the main one. At the location of the antenna, and behing it, there is no value of velocity, so, the value was arbritrarily set at 0.01 in order to avoid trouble with the logarithmic scale.

6.5.3 Implications for the moth behavior and the antennal geometry

As observed in previous works [205, 211, 212], the position of the sensilla relative to the supporting structure varies a lot from species to species, with all possibilities found in Nature. In this moth species as well as in *Bombyx mori*, sensilla are facing the flow. This is surprising as, for a given number of cylinders of a given length, the ones perpendicular to the flow are more efficient at capturing molecules than longitudinal horizontal ones, as we have confirmed (Figures 6.21 and 6.22). We have two explanations for this surprising geometry. First, the drag of perpendicular cylinders is higher. Indeed, for the same contact surface, perpendicular cylinders have a higher drag than longitudinal ones. Higher drag most likely reduces the leakiness of the antenna. Thus, without much increasing the drag of the whole antennae, longitudinal sensilla might greatly enhance the contact surface. Secondly, having the sensors ahead of the supporting structure enables them to extract more information, as other locations are quickly entrapped in the deflected zone produced by the larger sustaining structures, such as the rami and the flagellum.

Our reasoning has been done so far using the flow velocity experienced by the model of infinite array of longitudinal cylinders. By construction, the flow has then to pass through the array. If we now change the point of view and consider more realistic antenna of finite dimensions, then the relevant flow velocity is the far field one, the one we measured in the experiments. This shift of point of view

does not change any of the qualitative results, but produces a shift of the curve of capture efficiency to higher flow velocities (Appendix 6.6.4). This shift in efficiency locates the maximum efficiency of the antenna at far-field velocities of 0.5–1 $\mathrm{m\,s^{-1}}$, close to the flight velocities of the Saturniidae moths [203, 204]. This good match between our expectations and reality needs to be balanced with the fact that we studied flow only through a portion of the antenna with a single ramus and its sensilla. A real antenna is made of approximately 100 rami so that hydrodynamical interactions between the rami can be expected according to previous studies that measured the leakiness of whole antennae [14, 189]. Consequently, a decrease in leakiness for a complete antenna and a shift of the maximum efficiency of the antenna to even higher, but still realistic, velocities can be also expected for a complete antenna. Finer observations of the rami reveal that the rami are associated in pairs and that the distance between rami varies along their lengths. One implication could be that the local leakiness of the rami and the sensilla could depend on the distance with the neighbouring rami (see Chapter 5). On a more general scope, the distances between the elements constitutive of the antenna could have an influence on the leakiness such as the distance between the rami or between the sensilla. Thus, the various sections of the rami could be efficient at various velocities.

6.5.4 Geometry of antenna and flow dynamics determine capture efficiency

Our main contribution, relative to previously published work [11, 102, 12], lies in our attention to the detailed geometry of the antennae that is closer to Nature than of the previous models. Murray [11] introduced no geometry of the antenna whatsoever in his model and hence did not take into account leakiness. He was interested in another aspect of odor capture, the enhanced capture by molecules moving on a surface rather than in a volume. Somewhat more realistically, Humphrey and Haj-Hariri [12] modeled the 'interior' of the antenna as a uniform space, but the existence and hence the orientation of the sensilla then becomes irrelevant. They furthermore modeled the whole antenna as a permeable cylinder with a fixed leakiness that was not directly function of the geometry of the antenna and which was independent of air velocity. Cheer and Koehl [102], in a definitely more realistic work, opted for two sensilla transversal to the flow, for which they could obtain an estimate of leakiness. Very recently, Waldrop et al. [201] had the most realistic and versatile computational simulations, but the difficulty of keeping the nondimensional Reynolds, Schmidt and Péclet numbers in appropriate ratios makes any comparison with our experimental work rather difficult, beyond the already mentioned benefits of positioning the sensilla upfront of the antenna. All these works are exclusively theoretical and show the difficulty in determining leakiness, even for the simplest geometries. Our study is the third [14, 189] to tackle this problem experimentally and the only one which combines leakiness determination and mass transfer calculation.

This attention to the particular geometry, however, had its costs. Focusing on one particular geometry implie a lack of genericity towards the diversity of antenna shapes. The focus on geometrical aspects also forces us to a steady-state model, preventing the characterization of temporal patterns. However, a few time-dependent studies have been published. Humphrey and Haj-Hariri [12] calculated detection times and signal deformations through some assumptions of the transport equation. Schuech *et al.* [206] numerically solved the equation of mass transport to determine the mass flux on sensilla, in the case of perpendicular organs to the flow. His model allowed to look at temporal indicators such as dissymmetry of the chemical signal or concentration gradients. However, we wanted to investigate whether the longitudinal orientation of the sensilla was important for mass capture so we opted for a different approach by adapting a model used in heat transfer to the geometry at hand and testing it experimentally. The similarity between heat transfer and mass transfer is well-known in the area of engineering under the name of transport phenomena [128, 194]. The heat transfer equation and the mass transfer one are mathematically identical under certain assumptions, valid in our case: no natural convection in the heat transfer model and very low concentrations in the case of mass transfer. The analogy can be used however only if the biological mass transfer problem can be modeled with one of the geometries studied in heat transfer. This explains the paucity of works we could use, as heat exchange of an array of longitudinal cylinders is uncommon [207, 213, 214].

The use of proper analogies uncovers two positive implications for the surprising longitudinal orientation of the sensilla. Firstly, air is depleted of its pheromones molecules as it flows along the sensilla, so that pheromone concentration at the tip of the sensilla is the highest. Secondly, the fluid boundary layer is thin at the outwards looking tip and grows along the sensillum. Thus, the further downstream of the tip, the longer it takes for a molecule to cross this layer. These two reinforcing mechanisms can explain the 'olfactory lens" first described by Kaissling [188, 215], studied by Maitani *et al.* [107] and now accepted knowledge in the olfaction community. Undisclosed surface physico-chemical processes were assumed to produce such enrichment of odors at the tip of the sensors. We rather rationalize the existence of a passive process explaining this "olfactory lens" mechanism. The two mechanisms leading to the phenomonon of "olfactive lens" depend only on the geometry of the antenna. The sole study of the capture model could have predict it. However, the determination of the leakiness through PIV was necessary to know the importance of the phenomenon depending on the air velocities. The vast variety of antennal forms and orientation of sensors observed in insects will be understood only once similar endeavour is done on these geometries, as the intricacies of flow dynamics with complex geometries preclude any broad-brush statements about efficiency.

The model of Miyatake and Iwashita was developped for a close spacing of cylinders with a small range of pitch-to-diameter ratios σ ($\sigma \leq 4$). In the case of the antenna of the moth, the pitch-to-diameter ratio σ reaches 23.3. We ran simulations with Comsol to check that expanding the formula of Miyatake and Iwahita

to higher values of pitch-to-diameter ratios gave good results (Appendix 6.6.8).

6.6 Appendix

6.6.1 Equivalent heat and mass transfer parameters

Heat transfer	Mass transfer
Thermal diffusivity ($\mathrm{m^2 s^{-1}}$)	Mass diffusivity ($\mathrm{m^2 s^{-1}}$)
$\alpha = \frac{\lambda}{\rho c_p}$	D
Heat transport equation	Mass transport equation
$\frac{\partial T}{\partial t} + \left(\vec{v}.\vec{\nabla}\right) T = \alpha \nabla^2 T$	$\frac{\partial c}{\partial t} + \left(\vec{v}.\vec{\nabla}\right) c = \alpha \nabla^2 c$
Nusselt number	Sherwood number
$\mathrm{Nu} = \frac{hL_c}{\lambda}$ h, heat transfer coefficient ($\mathrm{Wm^{-2}s^{-1}}$) Lc, characteristic length (m) λ, thermal conductivity ($\mathrm{Wm^{-1}s^{-1}}$)	$\mathrm{Sh} = \frac{K_M L_c}{D}$ K_M, mass transfer coefficient ($\mathrm{m\,s^{-1}}$) Lc, characteristic length (m) D, diffusion coefficient ($\mathrm{m^2 s^{-1}}$)
Heat transfer coefficient	Mass transfer coefficient
$h = \frac{Q_c}{A \Delta T \Delta t}$ Q_c, heat energy from fluid to cylinders (J) A, exchange surface ($\mathrm{m^2}$) ΔT, temperature difference (K) Δt, time interval (s)	$K_M = \frac{M_c}{A \Delta c \Delta t}$ M_c, mass from fluid to rami g A, exchange surface ($\mathrm{m^2}$) Δc, concentration difference ($\mathrm{gm^{-3}}$) Δt, time interval (s)
Graetz number	Graetz number
$\mathrm{Gz}(z) = \frac{wc_p}{kz}$ w, mass flow rate of fluid per cylinder ($\mathrm{m^3 s^{-1}}$) c_p, heat capacity of the fluid at constant pressure ($\mathrm{JK^{-1}}$) k, thermal conductivity of the fluid ($\mathrm{Wm^{-1}s^{-1}}$)	$\mathrm{Gz_{mass}}(z) = \frac{w_{\mathrm{mod}}}{Dz}$ w_{mod}, volume flow rate of fluid per cylinder ($\mathrm{m^3 s^{-1}}$) D, coefficient of diffusion ($\mathrm{m^2 s^{-1}}$)

Table 6.3: Similarity of heat and mass transfers parameters

6.6.2 Determination of the diffusive coefficient of the pheromones

The pheromones of *Samia cynthia* were identified in 1989 in the subspecies *Samia cynthia ricini* [10]. It is actually a mix of two major components : (4*E*,6*E*,11*Z*)-4,6,11-Hexadecatrienal and (4*E*,6*E*,11*Z*)-4,6,11-Hexadecatrienyl acetate.
(4*E*,6*E*,11*Z*)-4,6,11-Hexadecatrienal has the following chemical formula $C_6H_{26}O$ and a molar mass of $234.4\,\mathrm{g mol^{-1}}$. The chemical formula of (4*E*,6*E*,11*Z*)-4,6,11-Hexadecatrienyl acetate is $C_{18}H_{30}O_2$ and its molar mass is $278.4\,\mathrm{g mol^{-1}}$.

From the chemical formula and molar mass, it is possible to determine an approximate diffusive coefficient in air for both pheromones [216].

(4*E*,6*E*,11*Z*)-4,6,11-Hexadecatrienal

All variables with an index A refer to (4*E*,6*E*,11*Z*)-4,6,11-Hexadecatrienal.

The diffusive coefficient of (4*E*,6*E*,11*Z*)-4,6,11-Hexadecatrienal in air is given by [216]:

$$\mathrm{Diff_A} = \frac{1.0868 T^{1.75}}{m_{\mathrm{A,Air}}^{1/2}(V_{\mathrm{A}}^{1/3} V_{\mathrm{Air}}^{1/3})^2} \tag{6.31}$$

with T the temperature taken at $T = 298\,\mathrm{K}$
$m_{\mathrm{A,Air}}$ the reduced mass of the pair air-(4*E*,6*E*,11*Z*)-4,6,11-Hexadecatrienal given by:

$$m_{\mathrm{A,Air}} = \frac{2 m_{\mathrm{A}} m_{\mathrm{Air}}}{m_{\mathrm{A}} + m_{\mathrm{Air}}} \tag{6.32}$$

and V_{A} and V_{Air} the dimensionless diffusion volumes of, respectively, (4*E*,6*E*,11*Z*)-4,6,11-Hexadecatrienal and air.

The diffusion volume of air is given in [217] and $V_{\mathrm{Air}} = 19.7$.
The diffusion volume of other molecules is given by their chemical formula. Each atom contributes to the diffusion volume depending on its nature : the diffusion volume of C is 15.9, the one of O is 6.11 and the one of H is 2.31. Thus, as the chemical formula of (4*E*,6*E*,11*Z*)-4,6,11-Hexadecatrienal is $C_6H_{26}O$, we obtained :

$$V_{\mathrm{A}} = 6 * 15.9 + 26 * 2.31 + 1 * 6.11 = 320.57 \tag{6.33}$$

However, the $\mathrm{Diff_A}$ coefficient is expressed in Torr $\mathrm{cm^2 s^{-1}}$. To obtain the result in $\mathrm{m^2 s^{-1}}$, $\mathrm{Diff_A}$ must be divided by $750 * 10^4$. We obtained the diffusive coefficient D_{A} :

$$D_{\mathrm{A}} = 4.73 \times 10^{-6}\,\mathrm{m^2 s^{-1}} \tag{6.34}$$

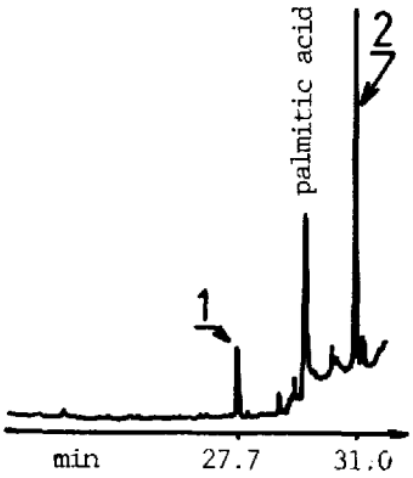

Figure 6.18: Gas chromatogram obtained by Bestmann *et al* [10]. Label 1 refers to (4*E*,6*E*,11*Z*)-4,6,11-Hexadecatrienal, label 2 to (4*E*,6*E*,11*Z*)-4,6,11-Hexadecatrienyl acetate. The height of peak 1 is equal to 1/5 of the height of peak 2.

(4*E*,6*E*,11*Z*)-4,6,11-Hexadecatrienyl acetate

All variables with an index B refer to (4*E*,6*E*,11*Z*)-4,6,11-Hexadecatrienyl acetate.

We used the same approach and obtained:

$$V_{\mathrm{B}} = 367.72 \tag{6.35}$$

and

$$D_{\mathrm{B}} = 4.44 \times 10^{-6}\,\mathrm{m^2 s^{-1}} \tag{6.36}$$

Diffusive coefficient

We take the weighted mean of the two diffusive coefficients depending on their relative abundance in the original mix of pheromone. Their relative abundances were extracted from the gas chromatogram done by Bestmann *et al* [10] : the surfaces under the peaks were approximated by their heights to the noise level. We found that (4*E*,6*E*,11*Z*)-4,6,11-Hexadecatrienyl acetate is 5 times more abundant than (4*E*,6*E*,11*Z*)-4,6,11-Hexadecatrienal. Thus :

$$D = \frac{D_{\mathrm{A}} + 5 * D_{\mathrm{B}}}{6} \tag{6.37}$$

So

$$D = 4.5 \times 10^{-6}\,\mathrm{m^2 s^{-1}} \tag{6.38}$$

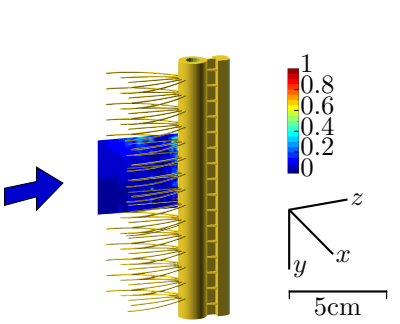

(a) Position of the microstructure. The laser sheet is parallel to the middle row of sensilla.

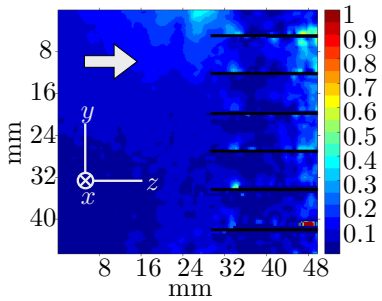

(b) Local absolute ratio of the y-component divided by the x-component of the velocity. The black lines show the location of the sensilla.

Figure 6.19: Measurement of the y-component. The oil velocity is equal to $2.14\,\mathrm{mm\,s^{-1}}$ (Equivalent air velocity: $0.2\,\mathrm{m\,s^{-1}}$). The arrow shows the direction of the flow.

6.6.3 Validity of the 2 dimensional assumption of the velocity field

We made all the measurements of the fluid velocity field in the $x-z$ plane, the plane of the laser sheet. The implicit assumption, here, is that the fluid displacement perpendicular to the plane of the laser sheet is negligible. However, in the case of the microstructure, due to the intrinsic 3D shape of the sensilla, there must be a non-null y-component in the velocity field. To measure its importance upstream of the sensilla, we ran a complementary measurement with the laser sheet parallel to the main axis ($y-z$ plane) of the microstructure (Figure 6.19a) and effectively found that the y-component of the velocity field is negligible close to the middle of the microstructure (Figure 6.19b).

6.6.4 Dependence of η_s on v_∞

The efficiency of the antenna η_s is determined with a far-field velocity v_n. However, equation 6.25 shows that v_n is also dependent on the far-field velocity v_∞ used in the PIV experiments. In other words, η_s is a function of v_n and v_n is a function of v_∞ :

$$\eta_s = f(v_n) \tag{6.39}$$

$$v_n = g(v_\infty) \tag{6.40}$$

with f and g two unknown functions. By combining equations 6.39 and 6.40, we obtain η_s as a function of v_∞ :

$$\eta_s = f(g(v_\infty)) \tag{6.41}$$

It is thus possible to represent the efficiency of the antenna η_s depending on v_∞. This is more informative as we are interested in determining the capture efficiency

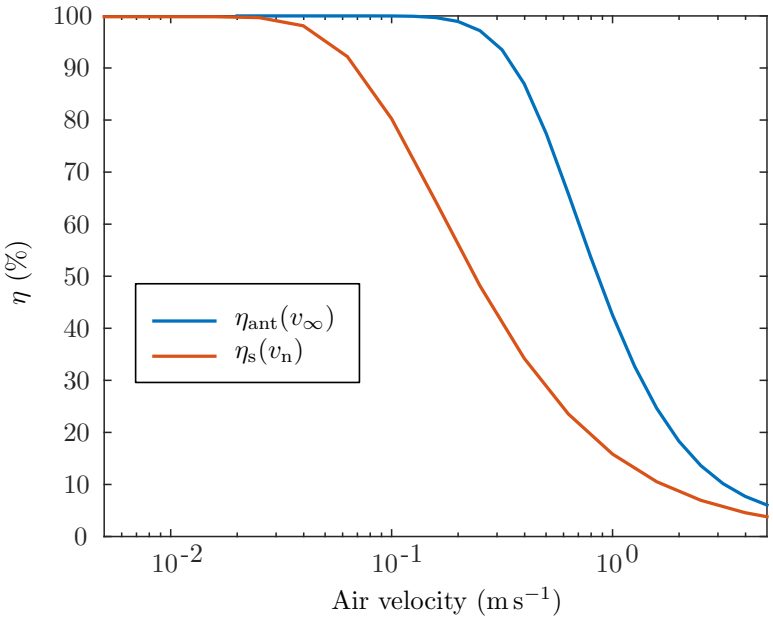

Figure 6.20: Efficiency of the antenna represented either depending on v_{n} (red line) or depending on v_∞ (blue line)

of a sensillum η_{s} for a given far-field velocity v_∞. To better see the difference, we displayed in Figure 6.20 the capture efficiency η_{s} two times, one depending on v_∞^{mod} ($f(v_\infty^{\mathrm{mod}})$) and the other depending on v_∞ ($f(g(v_\infty))$). We can then observe a shift of the curve to the highest velocities when it is represented depending on v_∞.

6.6.5 Comparison of single cylinders either in a longitudinal or in a transversal flow

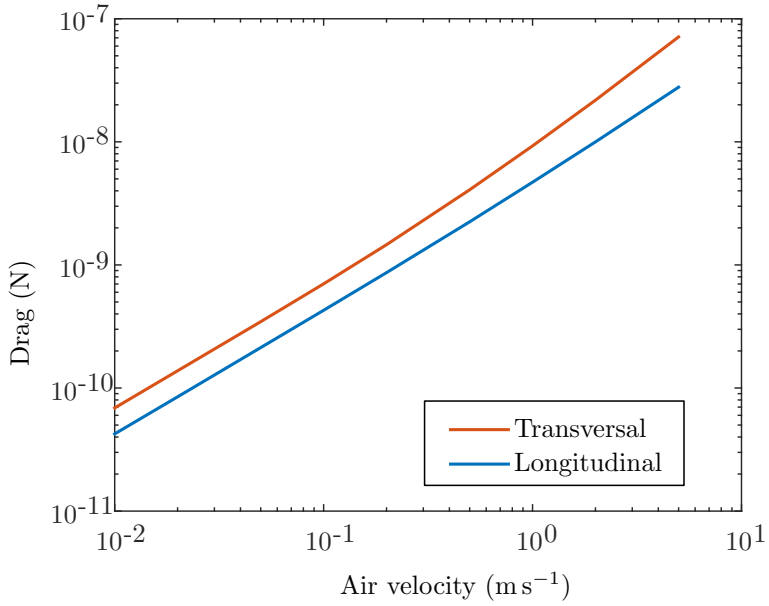

Figure 6.21: Comparison between the drag of a transversal cylinder and a longitudinal one. Diameter and length were chosen according to the moth sensillum.

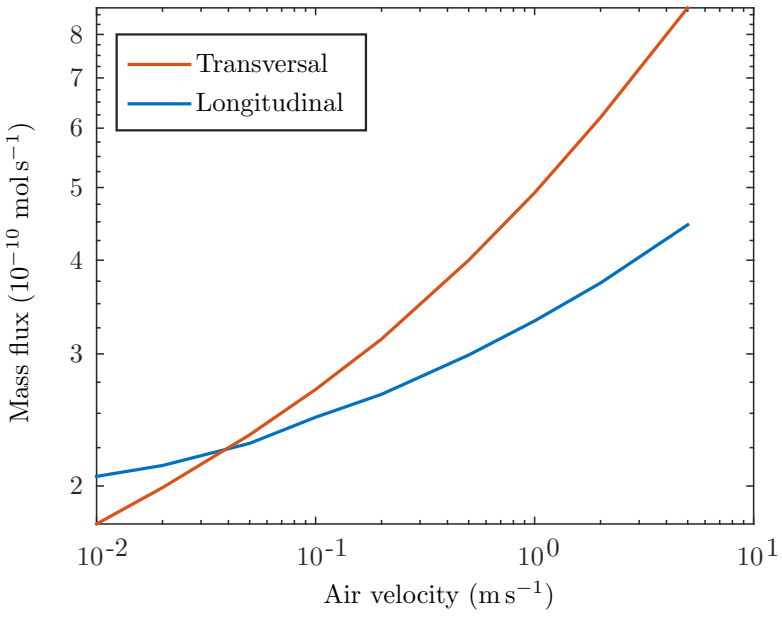

Figure 6.22: Comparison between the mass flux on a transversal cylinder and a longitudinal one. Diameter and length were chosen according to the moth sensillum.

6.6.6 Square and triangle distributions

To check the influence of the distribution of the sensilla, we also investigated a triangle distribution: the sensilla are located at the corners of an equilateral triangle of side $2s$.
Equations 6.4 and 6.5 become:

$$f = \frac{8.92(1 + 2.82\phi)}{1 + 6.86\phi^{5/3}} \tag{6.42}$$

$$g = \frac{2.34(1 + 24\phi)}{(1 + 36.5\phi^{5/4})(2sqrt(3)\sigma^2 - \pi)^{1/3}} \tag{6.43}$$

Because the density of sensilla must be equal, the volume flow rates per sensillum in the model and the experiment are equal to :

$$w_{\mathrm{mod}} = 4s^2 v_{\mathrm{n}} \tag{6.44}$$

(6.45)

$$w = 4s^2 v_{\infty} \tag{6.46}$$

(6.47)

In a triangular array, the volume flow rates are Thus, the distance between sensilla must change to adjust to the triangular array:

$$s_{\mathrm{triangle}} = \frac{s}{\sqrt{\cos\frac{\pi}{6}}} \tag{6.48}$$

Shifting to a triangle distribution has little effect on the capture rate (Figure 6.23).

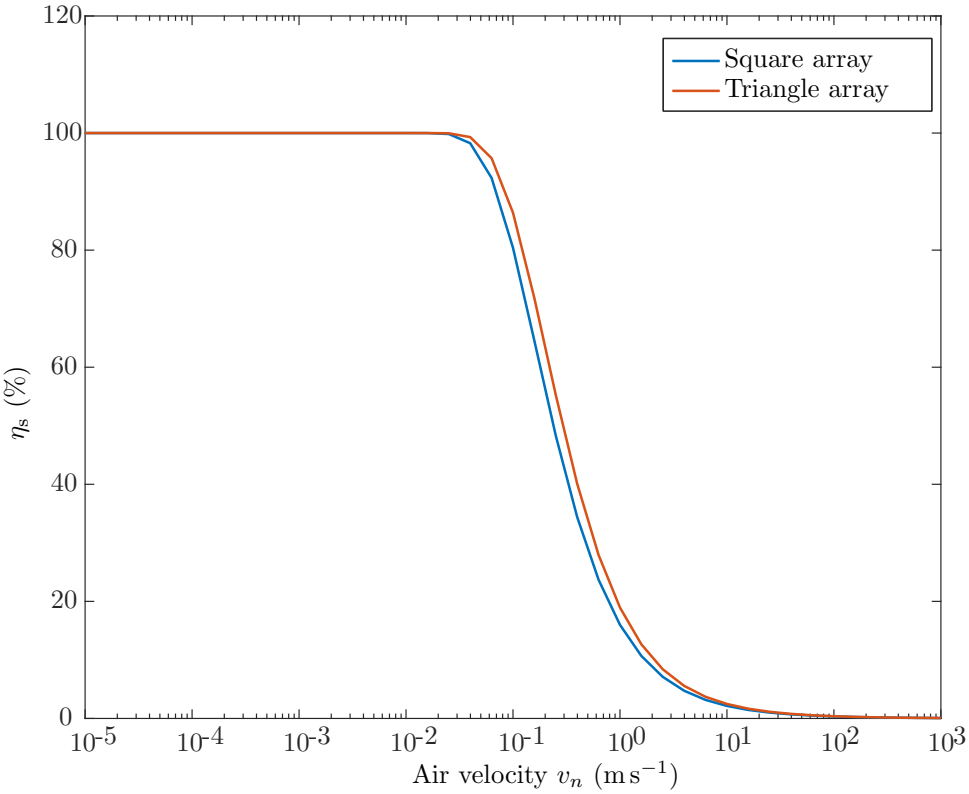

Figure 6.23: Comparison of model capture efficiency in the case of a square or triangle array

6.6.7 Gaussian odor pulse

Objective

The goal of this short excerpt is to determine to which extend the stationary model for pheromone pick-up by moth antennae, as derived on the basis of heat transfer in an infinite array of cylinders oriented parallel to a heated flow, can be used for (quasi-) dynamic odour pulses. In this stationary model, it is assumed that diffusive velocity in longitudinal direction is negligible relative to the advective velocity of the pheromone molecules. We will establish a model for the transverse diffusion and investigate the time-constant involved in this diffusion process. From that, we can predict what the minimum duration of pheromone pulses should be to have sufficient pick up of the molecules.

Model

We assume that a moth secretes a gaussian pulse with maximum s_0 and temporal pulse width of σ seconds:

$$s(t) = s_0 e^{-(t/\sigma)^2} \tag{6.49}$$

The pheromone pulse is picked up by a unidirectional homogeneous flow of speed v_0 such that the time dependent pulse is imprinted in a space dependent 1D pheromone pulse:

$$c(z,t) = c_0 e^{-\left\{\left(t-\frac{z}{v_0}\right)/\sigma\right\}^2} = c_0 e^{-\left\{\frac{t}{\sigma}-\frac{z}{v_0\sigma}\right\}^2} \tag{6.50}$$

with $l_0 = v_0\sigma$ the spatial pulse width and z the distance of the observer relative to the source. Assuming no pheromone adsorption or binding near the source, mass conservation requires that

$$\lim_{t\to\infty} = \int_{-t}^{+t} s(t')dt' = \lim_{z\to\infty}\int_{-z}^{+z} c(z',t_0)dz' \tag{6.51}$$

where t_0 is an arbitrary point in time and the primes indicate the integration variables. The equality yields

$$2\sqrt{\pi}\sigma s_0 = 2\sqrt{\pi}\sigma v_0 c_0 \quad \Rightarrow \quad c_0 = \frac{s_0}{v_0} \tag{6.52}$$

The spatio-temporal plume will propagate with time and deform due to both advection and diffusion. Hence the mass flux consists of two contributions:

$$\begin{aligned} \vec{J} &= \vec{J}_{\mathrm{a}} + \vec{J}_{\mathrm{d}} \\ &= \vec{v}c - D\nabla c \end{aligned} \tag{6.53}$$

The change in concentration per unit of time is given by:

$$-\frac{\partial c}{\partial t} = \nabla\cdot\vec{J} = \vec{v}\cdot\nabla c + c\nabla\cdot\vec{v} - D\nabla^2 c \tag{6.54}$$

Assuming incompressible flow ($\nabla \cdot \vec{v} = 0$) we find:

$$-\frac{\partial c}{\partial t} = \vec{v} \cdot \nabla c - D\nabla^2 c \tag{6.55}$$

In the stationary model based on heat exchange [207], it is assumed that only lateral diffusion, i.e. perpendicular to the direction of the sensilla, occurs. Here we restate this condition into: *lateral diffusion must be much faster than the timescale on which the changes in concentration along the longitudinal direction occur.* Splitting the velocity and derivatives into longitudinal and transverse components this leads to:

$$|D\frac{\partial^2 c}{\partial \perp^2}| \gg v_z \frac{\partial c}{\partial z} - D\frac{\partial^2 c}{\partial z^2} \tag{6.56}$$

The term on the left hand side depends on the specifics of the concentration profile in the boundary layers around the sensilla and, therefore, is rather complex. Here we approximate this term by assuming c at the sensillum surface is 0 and halfway between two sensilla (L, where the spacing is $2L$) it is $c(z)$, further assuming ideal sources and sinks and no depletion of the pheromone feed. This leads to[1]:

$$c(z)\frac{D}{L^2} \gg v_0 \frac{\partial c(z)}{\partial z} - D\frac{\partial^2 c(z)}{\partial z^2} \tag{6.57}$$

Using equation 6.50, we find:

$$\frac{D}{L^2} \gg \frac{2u}{\sigma} - 2D\frac{2u-1}{(v_0\sigma)^2} \tag{6.58}$$

where $u = \frac{t}{\sigma} - \frac{z}{v_0\sigma} \geq 0$, due to causality (a pulse cannot arrive before it has been secreted). Talking the minimum value of the right hand side under the assumption that $\sigma > \frac{D}{v_0^2}$ we find:

$$\sigma \ll \frac{L}{2v_0} \tag{6.59}$$

1D diffusion with fixed and time dependent boundary values

Diffusion following a step function

Diffusion profile We try to find a solution of the transverse part of equation 6.55,

$$\frac{\partial c}{\partial t} - D\nabla^2 c = 0, \tag{6.60}$$

[1]The expression $t_{\text{dif}} = \frac{L^2}{D}$ for diffusion time is actually based on the width of a Gaussian pulse, spreading with time in the absence of further sinks or sources. In our situation the sensilla act as sink, increasing the spreading of the pheromone

for diffusion in lateral direction, let us say x, and with boundary conditions

$$\begin{aligned} c(0,t) &= c_0 H(t) \\ c(L,t) &= 0 \end{aligned} \tag{6.61}$$

and initial condition:

$$c(x,0) = 0 \tag{6.62}$$

with $H(t)$ the Heavyside (step) function. The specified boundary conditions coincide with the situation in which no, or only negligible, depletion from the source at $x = 0$ occurs.

Solutions of this situation in case the first condition is not imposed, e.g. $L = \infty$, are hard to find in textbooks ([218] is a good reference but unfortunately does not cover this situation).

For the given situation, it is easy to find a particular solution:

$$c_{\mathrm{p}}(x,t) = c_0 \left(1 - \frac{x}{L}\right) \tag{6.63}$$

which does comply with equations 6.60 and 6.61. However, this solution is time-independent and may only be expected at larger time instances. Also note that the pheromone flux for this stationary solution is given by $-D\nabla c = -D\frac{c_0}{L}$. Next to the particular solution there are also solutions to the homogeneous differential equation:

$$\begin{aligned} c_{\mathrm{h}}(x,t) &= e^{-\lambda t}\left\{A\cos kx + B\sin kx\right\} \\ \lambda &= Dk^2 \end{aligned} \tag{6.64}$$

These solutions need to be further determined with respect to the boundary conditions imposed on them.

1. c_{p} fulfills the boundary condition at $x = 0$ for all t. This means there is no room for the cosine terms and subsequently $A = 0$.

2. c_{p} is also appropriate for the boundary condition at $x = L$ for all t. Hence we require that the sine terms in the homogeneous solution vanish at $x = L$ or in other words:

   $$k = \frac{n\pi}{L} \tag{6.65}$$

   where we restrict n to positive natural numbers.

3. Since k does not have a unique value we have a series expansion for the total concentration profile:

   $$c(x,t) = c_0 \left(1 - \frac{x}{L}\right) + \sum_{n=1}^{\infty} B_n e^{-\lambda_n t}\sin(k_n x) \tag{6.66}$$

   where the various B_n need yet to be determined.

4. Given the initial condition $c(x,0) = 0$ and from equation 6.66 we have:

$$\sum_{n=1}^{\infty} B_n \sin(k_n x) = -c_0 \left(1 - \frac{x}{L}\right) \tag{6.67}$$

5. To determine the coefficients B_n, we multiply equation 6.67 with $\sin(k_m x)$ and integrate over $x = 0 - L$:

$$\int_0^L \left\{ \sum_{n=1}^{\infty} B_n \sin(k_n x) \sin(k_m x) \right\} dx = -\int_0^L c_0 \left(1 - \frac{x}{L}\right) \sin(k_m x) dx$$

Reversing summation and integration, which is allowed because of the linear nature of both, and due to the orthogonality of the functions $\sin(k_m x)\sin(k_n x)$ on the interval $x = 0 - L$, all terms in the summation vanish, except when $m = n$. Hence we find:

$$B_n \frac{L}{2} = -\int_0^L c_0 \left(1 - \frac{x}{L}\right) \sin(k_m x) dx = -\frac{c_0}{k_n} \tag{6.68}$$

Putting together the results of equations 6.64, 6.66 and 6.68 we finally have:

$$\begin{aligned} c(x,t) &= 0 && t < 0 \\ &= c_0 \left(1 - \frac{x}{L}\right) - \frac{2c_0}{L} \sum_{n=1}^{\infty} \frac{e^{-Dk_n^2 t}}{k_n} \sin(k_n x) && t \geq 0 \end{aligned} \tag{6.69}$$

with k_n according to equation6.65. The above equation has been used to calculate the diffusion profiles for $D = 5 \times 10^{-6}\,\mathrm{m}^2/\mathrm{s}$, $L = 150 \times 10^{-6}\,\mu\mathrm{m}$, $c_0 = 3 \times 10^{12}\,/\mathrm{m}^3$ and for 7 orders of time ranging between 1 ns and 10 ms.

Outflux for step-function The output flux at $x = L$ can be calculated from minus the gradient of the concentration times the diffusivity:

$$J(L,t) = -D \frac{\partial c(x,t)}{\partial x}\bigg|_{x=L} \tag{6.70}$$

$$J(L,t) = -c_0 \frac{D}{L} \left\{ -1 - 2 \sum_{n=1}^{\infty} e^{-Dk_n^2 t} \cos(k_n x) \right\}\bigg|_{x=L}$$

$$\begin{aligned} J(L,t) &= 0 && t < 0 \\ &= c_0 \frac{D}{L} \left\{ 1 + 2 \sum_{n=1}^{\infty} e^{-Dk_n^2 t} (-1)^n \right\} && t \geq 0 \end{aligned} \tag{6.71}$$

Note that for $t = 0$ the coefficients B_n drop with n^{-1}. For $t > 0$ this drop off is faster because of the exponential term dropping off with α^{-n^2}. Hence, for $t > 1/Dk_n^2$ the contribution of the nth term drops quickly. In time, the response

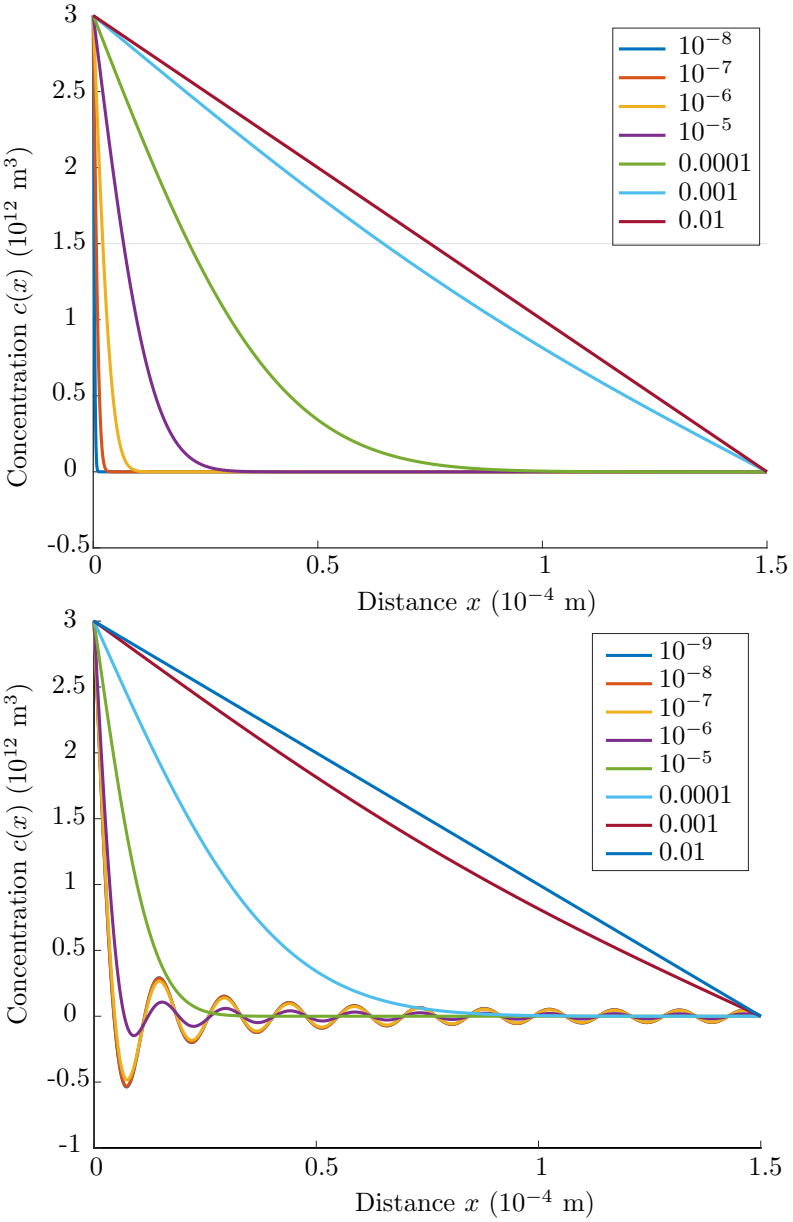

Figure 6.24: Diffusion profiles at various time instants calculated according to equation 6.69 with $n_{\max}$=2000 (top) and 20 only (bottom). $D = 5 \times 10^{-6}\,\mathrm{m}^2/\mathrm{s}$, $L = 150 \times 10^{-6}\,\mu\mathrm{m}$, $c_0 = 3 \times 10^{12}\,/\mathrm{m}^3$.

starts to reach the end of the spatial interval when the largest term, $n = 1$ starts

to decrease:

$$t > 1/Dk_1^2 = \frac{L^2}{D\pi^2} \equiv \tau_{\text{dif}} \tag{6.72}$$

Although this expression is by no means exactly defined, it is an easy estimation of the onset of saturation of the concentration in the structure.

The output flux has been calculated for a structure with the parameters as used for Figure 6.24. The predicted diffusion time-constant, according to equation 6.72 is 0.45 ms (-3.34 in Figure 6.25).

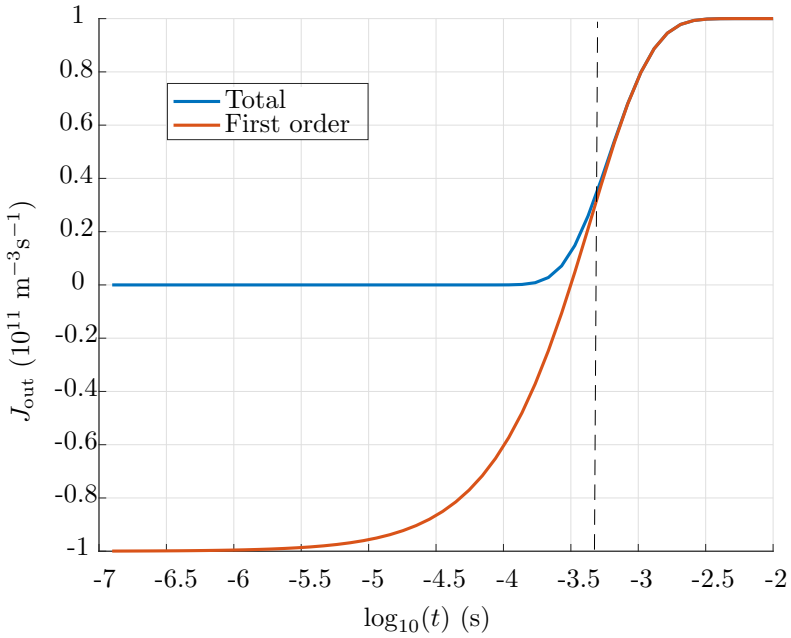

Figure 6.25: Output flux vs time as calculated from equation 6.71 taking $n_{\text{max}} = 200$ (blue line) and using the first order only (red). Parameters as for Figure 6.24. Dashed line indicates τ_{dif} from equation 6.72.

Negative step function Obviously, physically we may not expect any negative concentrations. However, once a positive step in the concentration has been made, an equal negative step can be added to it to return the input concentration back to 0. Here we look at such a negative step function with the purpose to later construct a rectangular pulse. In analogy with the previous positive step function,

equation 6.90, here we take as boundary and initial conditions:

$$\begin{aligned} c(0,t) &= -c_0 H(t) \\ c(L,t) &= 0 \\ c(x,0) &= 0 \end{aligned} \tag{6.73}$$

Following the same line of reasoning this will lead to a solution:

$$\begin{aligned} c(x,t) &= 0 && t < 0 \\ &= -c_0\left(1 - \frac{x}{L}\right) + \frac{2c_0}{L}\sum_{n=1}^{\infty}\frac{e^{-Dk_n^2 t}}{k_n}\sin(k_n x) && t \geq 0 \end{aligned} \tag{6.74}$$

and pheromone outflux:

$$\begin{aligned} J(L,t) &= 0 && t < 0 \\ &= -c_0\frac{D}{L}\left\{1 + 2\sum_{n=1}^{\infty} e^{-Dk_n^2 t}(-1)^n\right\} && t \geq 0 \end{aligned} \tag{6.75}$$

Rectangular pheromone pulse Combining the results of the previous two subsections we find for a rectangular pulse, centred around $t = 0$ and duration τ:

$$\begin{aligned} c(0,t) &= c_0\left\{H(t+\tau/2) - H(t-\tau/2)\right\} \\ c(L,t) &= 0 \end{aligned} \tag{6.76}$$

the solution:

$$\begin{aligned} c(x,t) &= 0 && t \leq -\tau/2 \\ &= c_0\left\{1 - \frac{x}{L}\right\} - \frac{2c_0}{L}\sum_{n=1}^{\infty}\frac{e^{-Dk_n^2(t+\tau/2)}}{k_n}\sin(k_n x) && -\tau/2 < t \leq \tau/2 \\ &= -c_0\frac{2}{L}\sum_{n=1}^{\infty}\frac{e^{-Dk_n^2(t+\tau/2)} - e^{-Dk_n^2(t-\tau/2)}}{k_n}\sin(k_n x) && t \geq \tau/2 \end{aligned} \tag{6.77}$$

The corresponding outflux is:

$$\begin{aligned} J(L,t) &= 0 && t \leq -\tau/2 \\ &= c_0\frac{D}{L}\left\{1 + 2\sum_{n=1}^{\infty} e^{-Dk_n^2(t+\tau/2)}(-1)^n\right\} && -\tau/2 < t \leq \tau/2 \\ &= c_0\frac{D}{L}\left\{2\sum_{n=1}^{\infty}\left\{e^{-Dk_n^2(t+\tau/2)} - e^{-Dk_n^2(t-\tau/2)}\right\}(-1)^n\right\} && t \geq \tau/2 \end{aligned} \tag{6.78}$$

Restricting the solution to the leading first order term ($n = 1$), we find:

$$\begin{aligned} J(L,t) &= 0 && t \le -\tau/2 \\ &= c_0 \frac{D}{L}\left\{1 - 2e^{-Dk_1^2(t+\tau/2)}\right\} && -\tau/2 < t \le \tau/2 \\ &= c_0 \frac{2D}{L}\left\{-e^{-Dk_1^2(t+\tau/2)} + e^{-Dk_1^2(t-\tau/2)}\right\} && t \ge \tau/2 \end{aligned} \tag{6.79}$$

This expression shows that the maximum pheromone outflux is obtained at $t = \tau/2$:

$$\begin{aligned} J(L)_{\max} &= J(L, \tau/2) \\ &= c_0 \frac{2D}{L}\left\{1 - e^{-Dk_1^2(\tau)}\right\} \end{aligned} \tag{6.80}$$

The maximum flux at the output, relative to the maximum possible flux, which would be the case for $\lim_{\tau\to\infty}$, is:

$$\eta(\tau) = \frac{J(L)_{\max}}{\lim_{\tau\to\infty} J(L)_{\max}} = 1 - e^{-\tau/\tau_{\text{dif}}} \tag{6.81}$$

The last result shows that the minimum duration of rectangular pulses to be 'reasonably' detectable should be on the order of $\tau = \tau_{\text{dif}} = L^2/D\pi^2$.

Response to Gaussian pheromone pulse From the solution equation 6.69, it is straight-forward to calculate the response to a delta pulse with content c_0:

$$h(t) = \frac{dc}{dt} = \sum_n \frac{2c_0}{Lk_n} \frac{e^{-Dk_n^2 t}}{Dk_n^2} \sin(k_n x) \tag{6.82}$$

Now that we have the pulse-response, we can calculate the overall response to a time dependent input concentration from:

$$c(x,t) = \int_{-\infty}^{t} C(\tau) h(t-\tau) d\tau \tag{6.83}$$

For the Gaussian pulses earlier introduced the response will be:

$$c(x,t) = \int_{-\infty}^{t} c_0 e^{-\left(\frac{\tau}{\sigma}\right)^2} \sum_{n=1}^{\infty} 2 \frac{e^{-Dk_n^2(t-\tau)}}{LDk_n^3} \sin(k_n x) d\tau \tag{6.84}$$

where σ is the pulse width and where we have neglected the time shift z/v_0. Restricting ourselves to the first order only, since this is the 'slowest component' and has the largest amplitude anyway, we find:

$$c(x,t) = 2c_0 \frac{\sin(k_1 x)}{LDk_1^3} \int_{-\infty}^{t} e^{-\left(\frac{\tau}{\sigma}\right)^2} e^{-Dk_1^2(t-\tau)} d\tau \tag{6.85}$$

Taking the relative outflow of pheromones at $x = L$:

$$\frac{J_{\mathrm{o}}}{J_{\mathrm{o,max}}} = \frac{D\left.\frac{\partial c(x,t)}{\partial x}\right|_{x=L}}{\frac{Dc_0}{L}} = \frac{2}{Dk_1^2}\int_{-\infty}^{t} e^{-\left(\frac{\tau}{\sigma}\right)^2} e^{-Dk_1^2(t-\tau)} d\tau \tag{6.86}$$

Clearly, when Dk_1^2 is much larger than $1/\sigma$, the input pulse will be detected faithfully. Hence the condition for the input pulse to be detectable is:

$$\frac{1}{\sigma} \ll D\frac{\pi^2}{L^2} \quad \Rightarrow \quad \sigma \gg \frac{L^2}{D\pi^2} = \tau_{\mathrm{dif}} \tag{6.87}$$

More precise:

$$\frac{J_{\mathrm{o}}}{J_{\mathrm{o,max}}} = \frac{2}{Dk_1^2} e^{-Dk_1^2 t} \int_{-\infty}^{t} e^{-\left(\frac{\tau}{\sigma}\right)^2} e^{Dk_1^2 \tau} d\tau \tag{6.88}$$

Despite the simplifications made, the above equation is not easily evaluated. A useful way may be to use Laplace or Fourier transforms of both functions, multiply them in the respective domain and transform back.

Harmonic driving of input concentration

Diffusion profile We try to find a solution of the transverse part of equation 6.55,

$$\frac{\partial c}{\partial t} - D\frac{\partial^2 c}{\partial x^2} = 0 \tag{6.89}$$

for diffusion in lateral direction with boundary conditions[2]

$$\begin{aligned} c(0,t) &= c_0\left\{1 + e^{j\omega t}\right\} \\ c(L,t) &= 0 \end{aligned} \tag{6.90}$$

where the physical concentration is given by $\Re\{c(x,t)\}$ and c_0 is the time-averaged concentration at $x = 0$. The specified boundary conditions coincide with the situation in which no, or only negligible, depletion from the source at $x = 0$ occurs and all pheromones are absorbed at $x = L$. We are interested in the stationary harmonic situation and therefore neglect possible transient effects. Consequently the homogeneous solutions of equation 6.89 are of no concern and we only look at a particular solution. Inspection of the equation suggests a trial function of the form:

$$c(x,t) = A\left\{1 - \frac{x}{L}\right\} + e^{j\omega t}\left\{Be^{kx} + Ce^{-kx}\right\} \tag{6.91}$$

Substitution of equation 6.91 into the diffusion equation (equation 6.89) results in the characteristic equation:

$$j\omega - Dk^2 = 0 \quad \Rightarrow \quad k = \pm\sqrt{j\frac{\omega}{D}} = \pm(1+j)\sqrt{\frac{\omega}{2D}} \tag{6.92}$$

[2]Note that the time-independent part is necessary to prevent negative concentrations.

The boundary conditions require:

$$\begin{aligned} c_0\left\{1+e^{j\omega t}\right\} &= A + e^{j\omega t}\left\{B+C\right\} \\ 0 &= e^{j\omega t}\left\{Be^{+kL}+Ce^{-kL}\right\} \end{aligned} \tag{6.93}$$

with solutions

$$\begin{aligned} A &= c_0 \\ B &= \frac{c_0}{1-e^{2kL}} \\ C &= \frac{-c_0 e^{2kL}}{1-e^{2kL}} \end{aligned} \tag{6.94}$$

resulting in the final solution:

$$\begin{aligned} c(x,t) &= c_0\left[\left(1-\frac{x}{L}\right)+e^{j\omega t}\left\{\frac{e^{kx}-e^{-kx}e^{2kL}}{1-e^{2kL}}\right\}\right] \\ &= c_0\left[\left(1-\frac{x}{L}\right)+e^{j\omega t}\left\{\frac{e^{k(x-L)}-e^{-k(x-L)}}{e^{-kL}-e^{kL}}\right\}\right] \end{aligned} \tag{6.95}$$

Short diffusion length approximation Clearly the concentration profile is strongly dependent on terms e^{kx} and e^{kL}. However, when $kx \leq kL \ll 1$ all these terms will differ decreasingly from 1. So in the short diffusion limit we find:

$$\begin{aligned} \lim_{kL\to 0} c(x,t) &\approx c_0\frac{e^{j\omega t}}{-2kL}\left\{1+kx-(1-kx)(1+2kL)\right\} \\ &= c_0\frac{e^{j\omega t}}{-2kL}\left\{1+kx-1+kx-2kL-2k^2xL)\right\} \\ &\approx c_0 e^{j\omega t}\left\{1-\frac{x}{L}\right\} \end{aligned} \tag{6.96}$$

in which only first order terms in kL have been retained. This expression looks suspiciously alike the particular solution for the concentration step case, which it should as the two should be identical for $\lim \omega \to 0$. Using equation 6.92 we can translate the short diffusion length condition as well in frequency terms:

$$kL \ll 1 \quad \Rightarrow \quad \omega \ll \frac{D}{L^2} \quad \Rightarrow \quad T \gg \frac{2\pi L^2}{D} \tag{6.97}$$

Note that this period scales exactly like the diffusion time-constant defined earlier (equation 6.72) but only has a different constant.

Outflux for harmonic driving and impedance The outflux of pheromones at the end of the diffusion length L can be calculated again according to equation 6.75 and now yields:

$$J(L,t) = -D\frac{\partial c(x,t)}{\partial x}\bigg|_{x=L} = Dc_0\left[\frac{1}{L}-\left\{\frac{2k}{e^{-kL}-e^{kL}}\right\}e^{j\omega t}\right] \tag{6.98}$$

Remark that for $\lim_{\omega \to 0}$ this coincides with the steady state solution after a step-function in the concentration, equation 6.75. On the other hand, the influx is given by:

$$J(0,t) = -D\frac{\partial c(x,t)}{\partial x}\bigg|_{x=0} = Dc_0\left[\frac{1}{L} - k\left\{\frac{e^{-kL}+e^{+kL}}{e^{-kL}-e^{+kL}}\right\}e^{j\omega t}\right] \tag{6.99}$$

Clearly, there are temporary differences between influx and outflux. These account for the 'charging' and 'discharging' of the volume with pheromone molecules, giving a capacitor-like contribution to the system. However, the time-averaged in and out fluxes from the harmonic contribution are 0 as can be easily inferred from the harmonic dependence of the flow:

$$< J(0,t) >= \frac{1}{T}\int_0^T Pe^{j\omega t}dt = \frac{P}{j\omega T}\, e^{j\omega t}\Big|_0^T = 0 \tag{6.100}$$

where $T = 2\pi/\omega$ and P is a constant depending on k and L. Obviously, the same holds for the outflux.

6.6.8 Extrapolation of the formula of Miyatake and Iwahita

The formula developed by Miyatake and Iwashita is valid at close spacing of the cylinders or, equivalently, low pitch-to-diameter ratios σ ($\sigma \leq 4$). In our model, the pitch-to-diameter ratio σ is equal to 11.3. We ran simulations with Comsol on an infinite array of sensilla (Figure6.26). We found that extrapolating the formula to higher values of pitch-to-diameter ratio σ is correct (Figure 6.27).

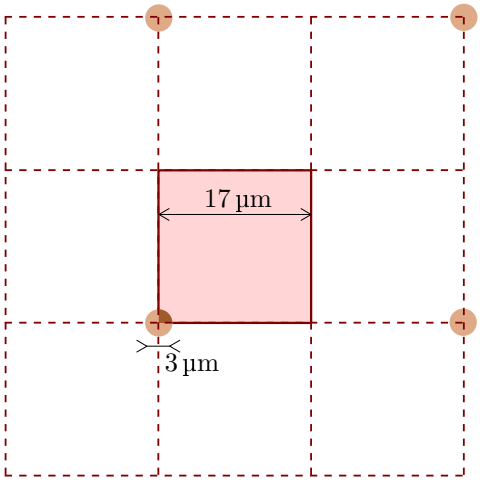

Figure 6.26: Domain of simulation. The red lines are symmetric boundary conditions to simulate an infinite array of sensilla. This allows us to focus only on a quarter of the domain, in light red. The brown circles represent the sensilla viewed from the top.

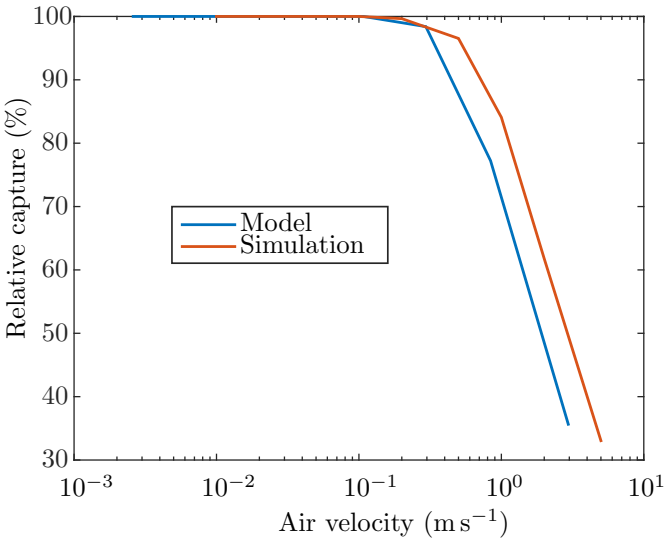

Figure 6.27: Comparison of the relative capture of the sensilla calculated with the model or through FEM simulations.

Chapter 7

General Discussion

7.1 Résumé en Français

Les résultats des chapitres précédents sont discutés afin de faire ressortir quels sont les paramètres qui déterminent la capture d'une antenne. Des résultats complémentaires sont également apportés. En effet, pour déterminer la capture d'une antenne pectinée, les résultats relatifs à la macrostructure et à la microstructure doivent être combinés. Nous avons donc développé une méthode pour calculer la perméabilité d'une antenne pectinée complète. Pour cela, nous nous sommes appuyés sur des simulations de dynamique des fluides par éléments finis. Au final, nous avons pu déterminer la capture d'une antenne pectinée et l'avons comparée à celle d'une antenne cylindrique.

7.2 Introduction

Moth antennae of *Samia cynthia* have an intricate 3D shape. They are composed of a main branch, the flagellum, where secondary branches, the rami, stand. These rami support sensory hairs called sensilla. In our work, we modeled each element of the antenna as a cylinder. Even with the help of this simplification, the antenna has a complex geometry, manly due to the important number of sensilla ($\approx$10 000) and their relative position, and also, due to the wide range of orders of magnitude between the element sizes. A solution to deal with such objects is to split them in several scales; two in our case. Thus, at the large scale, the antenna can be seen as a permeable plate whereas, at small scale, it can be modeled as an array of cylinders.

Two traits determine the efficiency of the antenna. Firstly, the leakiness, which is a measure of the proportion of flux that flows through the structure of the antenna and not around the entire antenna. This proportion is important as it allows to estimate an upper limit of the proportion of pheromone molecules that can be potentially captured by the antenna. Secondly, the capture rate of the sensilla,

which depends on their dimensions and orientation. The capture rate allows to evaluate the amount of pheromones being effectively captured, *i.e.* it determines the proportion of molecules captured in the fluid flowing between the structures of the antenna. Combining these two parameters (leakiness and capture rate), it is possible to estimate the efficiency of the antenna.

In this chapter, we will firstly discuss the impact of the multi-scale geometry of the antenna in the study of its efficiency as well as the different kinds of methods that can be used to solve such multi-scale problems. We will then investigate how to combine together the results obtained by using a scale-splitting technique. Finally, we will explore what the consequences are in terms of antenna design.

7.3 Multi-scale geometry

If we skip the scape and the pedicel which are basal segments, the antenna is composed of three elements: the flagellum, the rami and the sensilla. The flagellum is 1 cm long and 200 µm thick and divided in 25 segments called flagellomeres. Each flagellomere supports four rami, two on each side. The rami are cylinders, 1.5 mm long and 150 µm thick. On each ramus stand the sensilla. These tiny hairs host the chemical sensors that specifically recognize and detect the pheromone molecules. The hairs are 150 µm long and 3 µm thick. Thus, there is a huge dimensional gap between the length of the flagellum and the diameter of the sensilla which spans over four orders of magnitude. This gap has consequences on the methods used to study an antenna.

In an experimental approach, it might be convenient to directly work on a real antenna. However, real antennae are not regular objects with straight elements. They are instead composed of curved elements that are not of the same length and hide each other. Working on a more regular array of cylinders mimicking the antenna might thus be a solution. Artificial antennae also allow to vary the geometrical parameters in order to better understand the role of each element. However, the multi-scale geometry of the antenna is also a difficulty to deal with. It is indeed challenging to build an entire artificial antenna using Additive Manufacturing (as discussed in Chapter 4). Indeed, two main difficulties arise at this point. The first one comes from the tiny dimension of the antenna. The sensilla have a diameter of only 3 µm and a high aspect ratio that can reach 50 or more. Up to now, few Additive Manufacturing processes can reach such tiny dimensions. To our knowledge, the only commercial 3D printers that build accurate micro-metric features are from NanoScribe (Karlsruhe, Germany). These 3D printers rely on a two-photon polymerization process. This method can even build sub-micrometric features. However, the main limitation is that it cannot build a 1 cm long object. This is actually the second difficulty: the four orders of magnitude of the antenna are a problem for most printers. Even if we up-scaled the antenna, we could not find any 3D printer that could perform the task.

Also, from a modeling perspective, such a complex shape is a problem. Because there is a wide range of dimensions and a wide range of air velocities, the range of Reynolds number is also wide. Depending on which spatial dimension (between 3 µm and 1 cm) and air velocity (between $0.01\,\mathrm{m\,s^{-1}}$ and $5\,\mathrm{m\,s^{-1}}$) are chosen, the Reynolds number may vary between 0.002 and 3000. In this calculation, the kinematic viscosity of air was equal to $15.6 \times 10^{-6}\,\mathrm{m^2 s^{-1}}$. The Reynolds number compares the relative influence of the viscosity and the inertia in the flow. At low Reynolds numbers, viscous effects dominate the flow. At high Reynolds numbers, inertia is the dominating phenomenon. For Reynolds numbers close to 1, viscosity and inertia have both considerable contribution to the flow. In our case, we have Reynolds numbers much greater than 1, Reynolds numbers much less than 1 and Reynolds numbers close to 1. It is thus not possible to make any approximations to simplify the following Naviers-Stokes equations (7.1 and 7.2) which describe how air flows around the numerous elements of the antenna :

$$\frac{\partial \vec{v}}{\partial t} + (\vec{v} \cdot \nabla)\vec{v} = -\frac{\nabla p}{\rho} + \nu \nabla^2 \vec{v}, \tag{7.1}$$

$$\nabla \cdot \vec{v} = 0, \tag{7.2}$$

with $\vec{v}$ the air velocity ($\mathrm{m\,s^{-1}}$)
and ν the air viscosity ($\mathrm{m^2 s^{-1}}$).

Furthermore, either from an analytical or numerical point of view, the border conditions have a strong influence on how easy it is to solve the mass transfer and Naviers-Stokes equations. The intricate shape of the antennae with numerous sensilla makes it difficult to determine simple boundary conditions.

The division of the antenna in two levels allows us to study simpler structures and, thus, to have simpler boundary conditions. In an experimental approach, it makes the objects simpler and with a narrower range of orders of magnitude between the finest details and the total size of the structure. Each level is thus more easily built than the combination of both.

The equation of mass transfer which rules the pheromone capture by the antenna is the following:

$$\frac{\partial c}{\partial t} + (\vec{v} \cdot \nabla)c = D \nabla^2 c, \tag{7.3}$$

with c the mass concentration of pheromone in air ($\mathrm{g\,m^{-3}}$)
and D the diffusion coefficient of pheromone in air ($\mathrm{m^2\,s^{-1}}$).

The air velocity has an influence on the concentration of pheromone as shown in the term $(\vec{v} \cdot \nabla)c$. In the case of analytical modeling or simulation, it means that

the Naviers-Stokes and mass transfer equations should both be solved, which is not easy in the case of a complex object such as a moth antenna. From an experimental point of view, the problem could be studied by means of Particle Image Velocimetry (PIV) coupled with a technique of Planar Laser-Induced Fluorescence (PLIF). The PLIF technique uses fluorescent particles that diffuse in the fluid. The measure of the fluorescent intensity gives the concentration in fluorescent particles in the fluid. PLIF is also used to measure heat transfer. However, this technique is more difficult to use than single PIV and the fluorescent particles must be chosen with care [219, 220, 221]. Given the complexity of determining both fluid dynamics and mass transfer, it is sometimes easier to deal separately with each problem. Thus, to study the pheromone capture by a moth antenna, two complementary approaches are used in this work: (1) splitting the antenna in two levels to obtain simpler geometries and (2) solving the fluid dynamics and mass transfer separately.

Previous works have followed this approach but, each time, in a different manner. Murray [11] chose to focus on a single sensillum modeled as a cylinder. This approach is equivalent to split the antenna and focus on the smallest element. This is justified by the fact that the chemical detectors are located within the sensilla. Thus, understanding the mass transfer at the level of the sensilla is an important point. To simplify the problem and make it analytically solvable, Murray assumed the sensillum to be a cylinder transversal to a steady flow of air. He also assumed a constant pheromone concentration. As a consequence, the terms $\frac{\partial v}{\partial t}$ and $\frac{\partial c}{\partial t}$ in equations 7.1 and 7.3 drop, respectively. The approach of Murray provides two main benefits. The first one is that there is only one cylinder to deal with at a time. The second one is that the transverse cylinder, assumed to be infinite, can be modeled by a 2D circle (Figure 7.1), thus reducing the complexity of the problem. In such a configuration, the author was able to solve both the fluid dynamics and mass transfer problems at the finest level of detail. The first, coarser, level of the antenna takes into account the interaction between the sensilla and is modeled as a multiplying factor of the capture rate of the sensilla. This factor is extrapolated from a study of aerosol capture by closely-packed parallel circular cylinders [222]. As a summary, the first level of the antenna is simplified and modeled as a multiplicative factor and the mass transfer is calculated on the second level, which has a very simple shape.

Cheer and Koehl [102] also modeled the sensilla as cylinders transversal to the flow. However, they were also interested in the influence of the rami that support the sensilla and, like the sensilla, modeled them as cylinders transversal to the flow too. The authors looked at a new parameter that could have a major influence on the efficiency of an antenna: the leakiness. Antennae are composed of many elements that generate a resistance to the air flow. Thus, air partly flows through the antenna or around the entire structure. Leakiness may be negligible in the case of highly permeable objects but it has two major consequences on structures with low to medium leakiness. Firstly, the pheromone molecules in the portion of air flowing around the entire structure are not available for capture by the sensilla. Secondly, a low leakiness means a slower air velocity than the far-field one. For

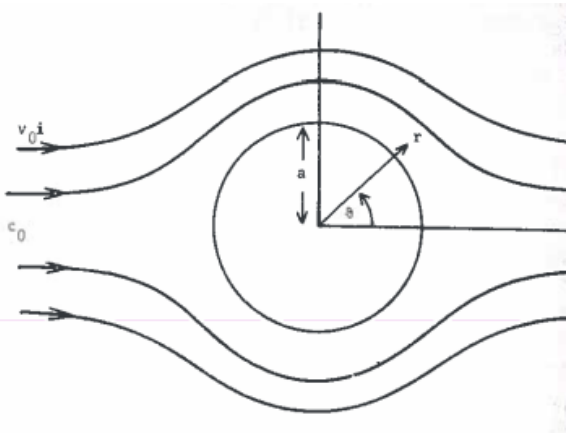

Figure 7.1: Cylinder modeling a sensillum transversal to the flow and viewed from the top. v_0 is the far-field velocity, c_0 is the far-field concentration, a is the radius of the circle and r and θ are the polar coordinates. Reproduced from [11]

example, a leakiness of 0.1 means that only 10% of the pheromone molecules can potentially be captured by the sensilla. However, it also means that the air flows 10 times slower, giving more time to the pheromone molecules to diffuse to the surface of the sensilla (see discussion of Chapter 6). Determining the leakiness of a structure such as a moth antenna is not an easy task: Cheer and Koehl achieved it by solving the velocity profile in two steps. The first step was to determine how air flows between two transversal cylinders (mimicking two rami) at *intermediate* Reynolds number. The mean velocity between the rami was then used as far-field velocity to find the velocity field around two transversal cylinders at *low* Reynolds number (Figure 7.2a). Interestingly, the authors had to use two different models of fluid flowing between two cylinders. At the level of the rami, the Reynolds number is high and inertia cannot be neglected anymore. Nevertheless, they could simplify the inertia term according to the Oseen approximation [223]: The non-linear term $(\vec{v}\cdot\nabla)\vec{v}$ is changed by $(\vec{v}_\infty\cdot\nabla)\vec{v}$. At the level of the sensilla, the Reynolds number drops and they could use a model that the two authors previously developed for low Reynolds numbers [187]. A major drawback of this analysis is that it only deals with the fluid dynamics and does not determine the pheromone capture by the antenna. This work is extended further by Schuech *et al* [206] who ran simulations to determine the mass capture by an infinite row of cylinders mimicking the sensilla (Figure 7.2b). The drawback of considering an infinite array is that it cannot determine the leakiness because the infinity of the array forces the fluid to flow entirely between the cylinders. However, the benefit of such a model is that it is convenient to run simulations on: in an infinite array of evenly-spaced cylinders, only one cylinder with appropriate boundary conditions is sufficient to determine the behavior of the entire array.

To avoid the complexity of analytically calculating the leakiness of the antenna, Humphrey and Haj-Hariri [12] split the antenna in three levels and modeled the

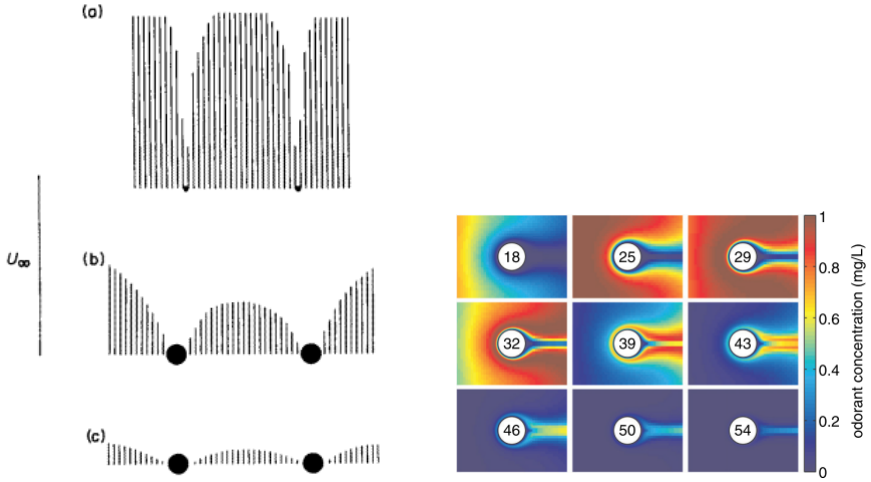

(a) Varying leakiness between two cylinders. Reproduced from [187]

(b) Pheromone concentration around a sensillum in an infinite row. Reproduced from [206]

Figure 7.2: Analytical leakiness and simulation mass transfer

first one as a permeable cylinder (Figure 7.3a) with a given leakiness (equal to 5 and 10%). Using approximations, they determined the flow profile around the permeable cylinder as well as the mass transport of pheromone at the entrance of the cylinder. Inside the permeable cylinder, there are sensilla but there is no space dependence anymore, the concentrations are uniform and a mass balance determines the concentration of pheromone in the air inside the antenna and on the surface of the sensilla (Figure 7.3b). The concentration at the surface of the pores (located on the surface of the sensilla) is considered to be equal to the concentration at the surface of the sensilla. The depletion of pheromones, due to the pheromone molecules entering into the tubule, is considered to be negligible. Eventually, the pheromone molecules enter the tubules through the pores and migrate to the end of the tubules where they are detected (Figure 7.3c). This model is interesting because it gives an analytical solution to temporal chemical variations and tackles the mass transfer problem at the two levels of the antenna. However, the leakiness is a fixed parameter that is independent of the air velocity. Experiments conducted by Vogel [14], and confirmed by our work (Chapter 5), showed that the leakiness does actually depend on air velocity.

Because of the complexity to analytically calculate leakiness and mass transfer, Loudon and Koehl [13] directly measured the leakiness on a real moth antenna using an experimental set-up equipped with a hot-wire anemometer (Figure 7.4a). They then conducted random-walk simulations using the air velocity profile they measured to determine how many molecules would reach the surface of the sensilla (Figure 7.4b).

Given the complexity of the antenna, all these previous studies had to give

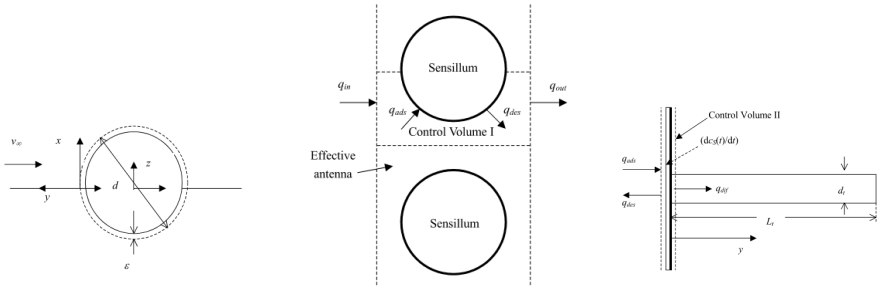

(a) First level: a permeable cylinder.

(b) Second level: the sensilla.

(c) Third level: the surface of the sensilla ans the tubules.

Figure 7.3: Analytical leakiness and simulation mass transfer. Reproduced from [12].

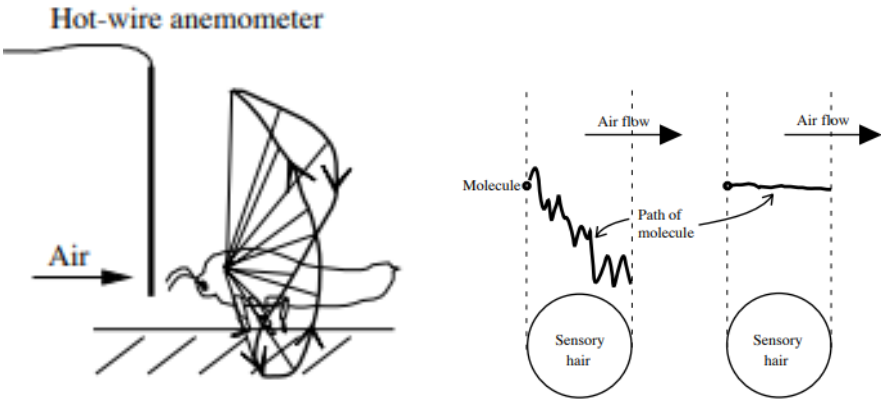

(a) Experimental set-up to determine the leakiness.

(b) Simulation to determine the random walk of a pheromone molecule.

Figure 7.4: Experimental leakiness and simulated mass capture. Reproduced from [13].

up on some aspects to gain on other ones. Hence, Murray [11] could completely define analytically the fluid dynamics and mass transfer around the sensilla. However, his model was developed for the case of a flow steady state and he did not calculate the leakiness of the antenna, which is an important parameter. A major work is the study of Cheer and Koehl [102]. They focused on determining the leakiness but, in order to keep calculations doable, they had to consider only two sensilla and not a row of them. They also did not look into the mass transfer problem. Humphrey and Haj-Hariri [12] could investigate the temporal pattern of a chemical signal reaching the antenna. However, their estimated leakiness was a fixed parameter independent of the velocity. They also greatly simplified the geometry of the antenna by modeling the array of sensilla and rami by a permeable cylinder. Last, Loudon and Koehl [13] measured the leakiness on a real moth antenna and simulated the random walk of pheromone molecules. They could not determine the temporal pattern of the chemical signal in contrast to Humphrey and Haj-Hariri [12]. From these studies arises the conclusion that a single model can hardly be expected to capture the functioning of a moth antenna in its entire nature and that we must choose which aspects to focus on.

As for ourselves, we were interested in the shape of the antenna and how it is related to olfactory performance. One point to notice is the fact that the sensilla were so far always modeled as cylinders transversal to the flow. *Samia cynthia*, our biological model, bears sensilla pointing forward. In the Saturniidae family, Schneider and Kaissling [205, 211] as well as Steinbrecht [212] observed that the sensilla were either on the front side of the rami or on the front and back sides. This result was later confirmed [224] in the sub-family of the Saturniinae (our study species, *Samia cynthia*, belongs to this sub-family). Thus, a better way to model them is in using a cylinder longitudinal to the flow. The second point is that we wanted to investigate how leakiness depends on the shape of the antenna and how it varies according to the air velocity.

To tackle this problem, we split our antenna in two levels. The first one (called the macrostructure) comprised the flagellum and the rami and the second level (called the microstructure) was made of one ramus and its sensilla. Using a PIV set-up, we determined the leakiness of each level and even varied the shape of the macrostructure to see how it would affect leakiness. We then modeled the microstructure as an infinite array of longitudinal cylinders to determine the mass transfer from the air to the surface of the sensilla using a model of Miyatake and Iwashita [207]. Originally, this model was developed for heat transfer. However, given the similarity of the heat and mass transfer equations, we could adapt the results of the study to our mass transfer needs. The last step, developed below, is now to combine the results of the two levels to determine the efficiency of the entire antenna.

7.4 Combining the two levels

In chapter 6, we combined the leakiness of the microstructure with the capture efficiency of an infinite array of cylinders to determine the capture efficiency of the microstructure. However, to obtain the capture efficiency of the entire antenna, we should consider the leakiness of both the first and the second levels (macro- and microstructure) and combine them to obtain the leakiness of the entire antenna. We developed three methods to combine the two levels: the first one is an experimental approach, the second one combines the leakiness of the two levels using the multiplicative assumption (defined below) and the third one resorts to the concept of drag to generate a macrostructure which takes the microstructure into account.

As a reminder, the first level refers to the macrostructure which, in our antenna, is composed of the flagellum and the rami. The second level refers to the microstructure and is composed of one ramus and its sensilla.

7.4.1 First method: the experimental approach

In the PIV setup described in Chapter 6, we measured the leakiness of two microstructures side-by-side. The advantage of this configuration is that it was still possible to run the experiments in our tank and that it took into account interaction between two microstructures. However, the difference of leakiness between a single microstructure and two ones side-by-side is small (Figure 7.5). One of the main reasons of this surprising result might be the limited size of the tank. Two microstructures side-by-side occupy a non-negligible part of the cross-section of the tank. Thus, the oil might have been partially forced to flow between the sensilla compared to an ideal infinite tank due to wall effects.

7.4.2 Second method: the multiplicative method

Splitting the antenna in two levels is a good approach to simplify the analytical resolution of the problem but it also requires to combine the two levels back in order to obtain results related to the entire antenna, and not just a part of it. Cheer and Koehl [102] faced this problem as they split the antenna with the rami on one side and the sensilla on the other side. They considered that the rami would greatly influence the air velocity field and determined what the small sensilla would face. However, they did not consider that the sensilla could also feed back on the flow velocity field around the rami or, equivalently, they considered this impact of the sensilla to be negligible. In this approach, the first level determines the large-scale velocity field and the flow velocity profile encountered by the second level. The second level determines the small-scale velocity profile but does not have any impact on the large-scale one. This is an assumption, and it needs to be tested.

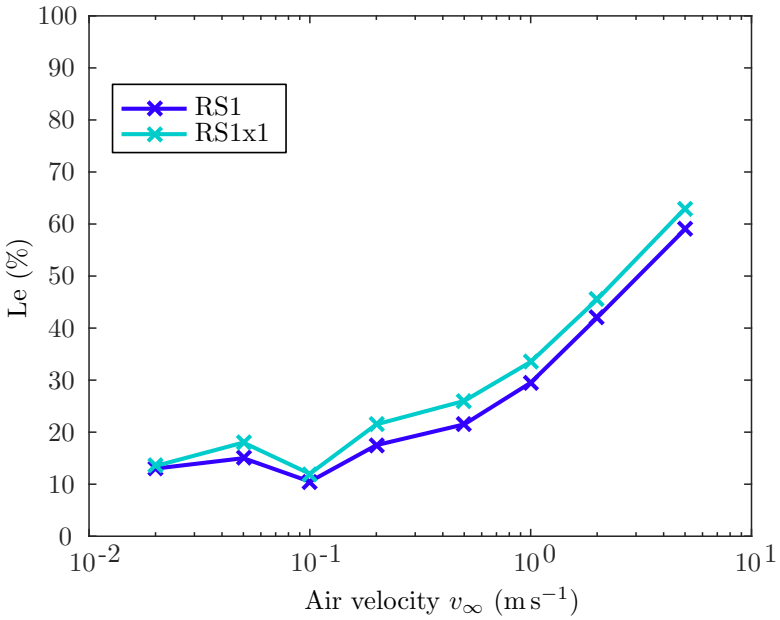

Figure 7.5: Comparison of the leakiness of a single microstructure (RS1) with the one of pair of microstructures sitting side by side (RS1x1)

For each far-field velocity v_∞ that we studied, we determined the corresponding leakiness at the first level, Le_1 and at the second level, Le_2. However, the first level influences the far-field velocity of the second level too, by slowing down the air. Thus, the real far-field velocity of the second level should be $v_\infty * \mathrm{Le}_1$. We then interpolated the leakiness of the second level on these new far-field velocities, $v_\infty * \mathrm{Le}_1$. Thus, the total leakiness is the product of the leakiness at each level, $\mathrm{Le}_1 * \mathrm{Le}_2$. According to this approach, we obtained a total leakiness $v_\infty * \mathrm{Le}$, which is lower than the leakiness of each level (Figure 7.6).

Multiplying the leakinesses of the two levels together might be interpreted as similar to adding the drag generated by the two levels. Indeed, drag has been shown to be closely linked to the pressure drop, which itself is closely linked to the leakiness [225]. The drag can be seen as a force opposing to the flow: the higher the drag, the lower the flow and, consequently, the lower the leakiness. With this method, the drag of the total antenna would be the drag of the first level plus the drag of the second level. This approach is justified in the case of sensilla that are small compared to the diameter of the rami and when the rami and the sensilla lay in the same 2D plane and are all transversal to the flow. However, in our case, the rami are transversal but the sensilla are longitudinal to the flow and located *upstream* of the rami, *i.e.* the rami and the sensilla do not lay in a plane perpendicular to the flow. The sensilla length ($\approx 150\,\mu\mathrm{m}$) is furthermore larger than the rami diameter ($50\,\mu\mathrm{m}$). Thus, the multiplicative method might be too coarse.

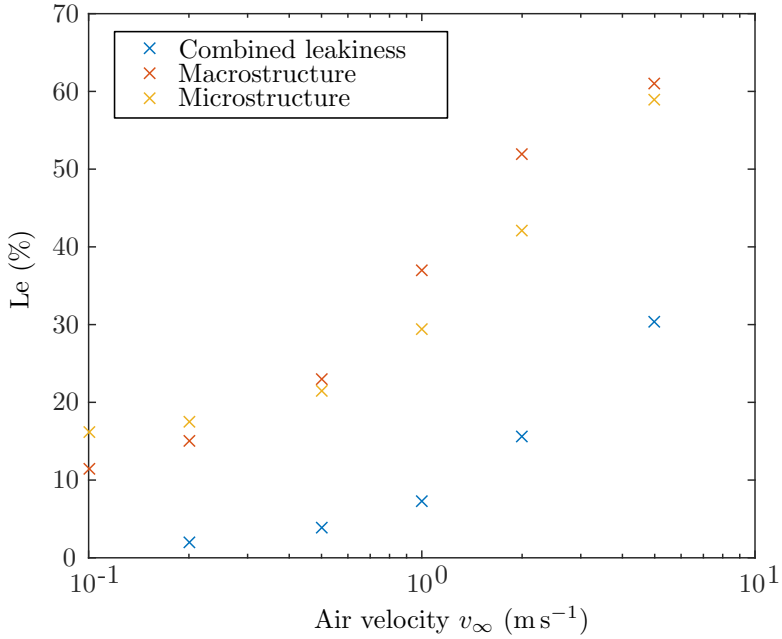

Figure 7.6: Leakiness of the whole antenna using the multiplicative method.

To control the validity of the multiplicative method, we ran simulations on Comsol (Comsol Inc, Stockholm, Sweden). We wanted to compare the sum of the drag of a single ramus (transversal to the flow) and a single sensillum (longitudinal to the flow) with the drag of a ramus supporting one sensillum. If the sum of the drag of a ramus alone plus the drag of a sensillum alone is equal to the drag of a ramus supporting one sensillum, we then consider that the multiplicative method to determine the leakiness is applicable to our structure of interest. Else, we have to find a new method to take into account the interaction between the rami and the sensilla. We investigated the drag at several air velocities $\{0.01, 0.02, 0.05, 0.1, 0.2, 0.5, 1, 2, 5\}\,\mathrm{m\,s^{-1}}$. The transversal cylinder, mimicking a ramus, had a diameter of 50 µm and the longitudinal ones, mimicking sensilla, were 150 µm long with a diameter of 3 µm. We considered an infinitely-long ramus and an infinite array of sensilla and used periodic boundary conditions to decrease the domain of simulation. To keep coherence with our PIV experiments, we considered one sensillum every 25 µm. Thus, the ramus was modeled as a slice of cylinder 25 µm long. In the simulation with a ramus and one sensillum, we positioned the sensillum upstream of the ramus.

The main result of this analysis is that the sum of the drag of a ramus alone and a sensillum alone is higher by around 40% than the drag of a ramus supporting a sensillum (Figure 7.7). As a consequence, it is not valid to multiply the leakinesses at each level to obtain the one of the entire antenna.

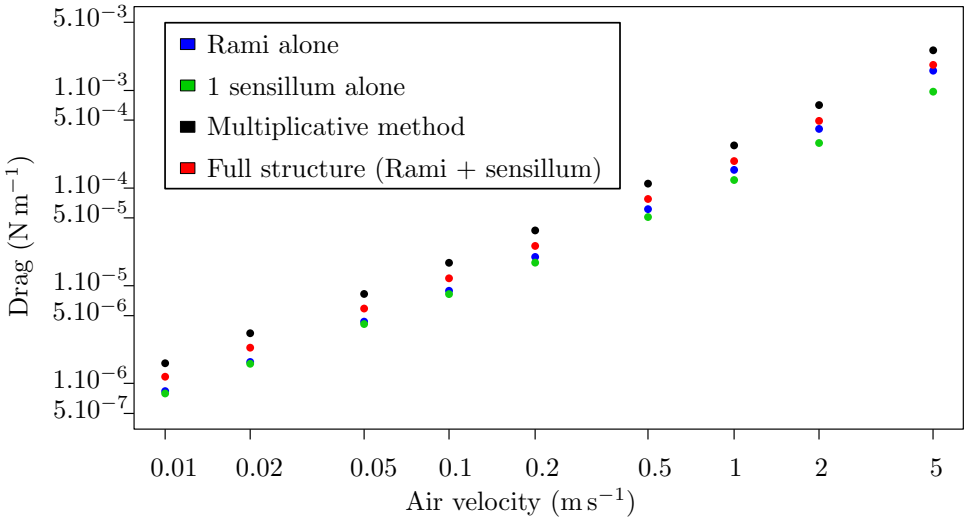

Figure 7.7: Drag of a ramus alone (blue dots), drag of a sensillum alone (green dots), drag of a ramus bearing a sensillum (red dots) and sum of the drag of a ramus alone and a sensillum alone (black dots). The value were determined using simulations (Comsol, Comsol Inc, Stockholm, Sweden). The sum of the drag of one ramus and the drag of one sensillum is $\approx 40\%$ higher than the drag of a ramus bearing one sensillum.

7.4.3 Third method: the equivalent cylinders

Given the results of the simulations, we could not simply multiply the leakiness of the two levels to obtain the leakiness of the antenna. An alternative method is to model the entire microstructure by an equivalent cylinder with appropriate diameter based on considerations on the drag (Figures 7.8.1 and 7.8.2). Such an approach was already used in a study [186] on dandelion seeds where the porous dandelion seeds were compared with impermeable cylinders with an equal drag. We then substitute each ramus of the macrostructure by this equivalent cylinder (Figure 7.8.4). The idea is to measure the leakiness on the macrostructure (1st level) while still taking into account the influence of the microstructure (2nd level) on the flow. In other words, we want the macrostructure supporting equivalent cylinders to have the same leakiness as the one of a complete antenna which can be seen as a macrostructure whose cylindrical rami have been replaced by microstructures. Given the relation between leakiness and drag [225], we assumed that, if the equivalent cylinders have the same drag as the microstructures, the macrostructure with equivalent cylinders and the complete antenna would have the same leakiness.

The key point is to remind that we are interested in the drag of the microstructure alone but embedded in a complete antenna, which means that the microstructure is located within a row of microstructures which interact with each other. Let us consider the edge effects to be negligible. At close range, we model the antenna as an infinite row of infinitely long microstructures and we determine, through simulations, the drag per unit of length of such an infinite microstructure (Fig-

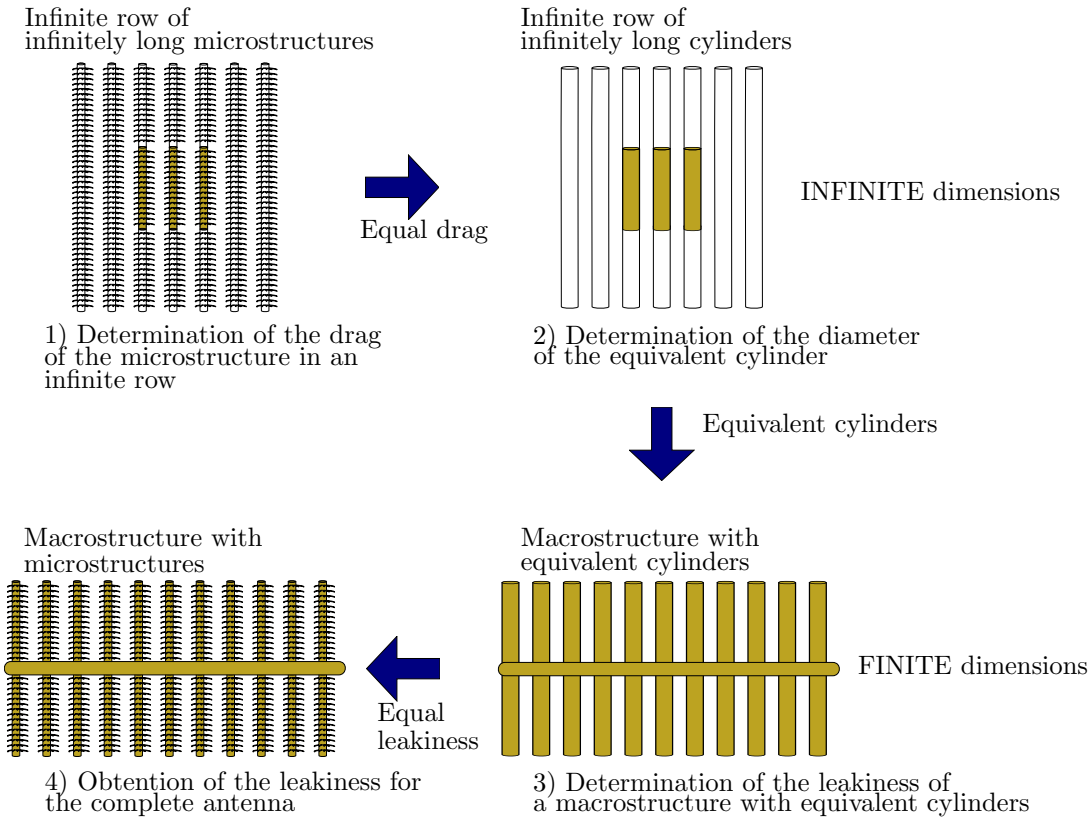

Figure 7.8: Approach of the second method. Infinite arrays of infinitely long structures (1 and 2) are convenient to model in simulations through the use of symmetric boundary conditions. The simplified antenna modeled by a macrostructure with equivalent cylinders (3) has a finite dimension and a relatively simple shape compared to the real antenna (4) which allows to run simulations to determine the leakiness.

ure 7.8.1). The diameter of the equivalent cylinder is then chosen in such a way that the drag per unit of length of the equivalent cylinder, standing in an infinite row of infinitely long cylinders with same diameter *i.e.* in the same configuration, is equal to the one of the microstructure defined above. The distance between microstructures in the first case, and equivalent cylinders in the second one, is kept the same. This procedure ensures that, for a given velocity v_{n}, the drag of the microstructure and the equivalent cylinder is the same, as is the flux between the microstructures or the equivalent cylinders.

For a given far-field velocity $v_{\mathrm{n,eq}}$ of the microstructure, we determined the drag d through simulations of a cylinder 25 µm high with 5 sensilla and appropriate periodic boundary conditions to obtain an infinite ramus in an infinite row (Figure 7.9). At this velocity $v_{\mathrm{n,eq}}$, we also determined the drag of a cylinder in the same configuration, *i.e.* an infinite cylinder in an infinite row, depending on its diameter. We simulated a single cylinder and used the same boundary conditions

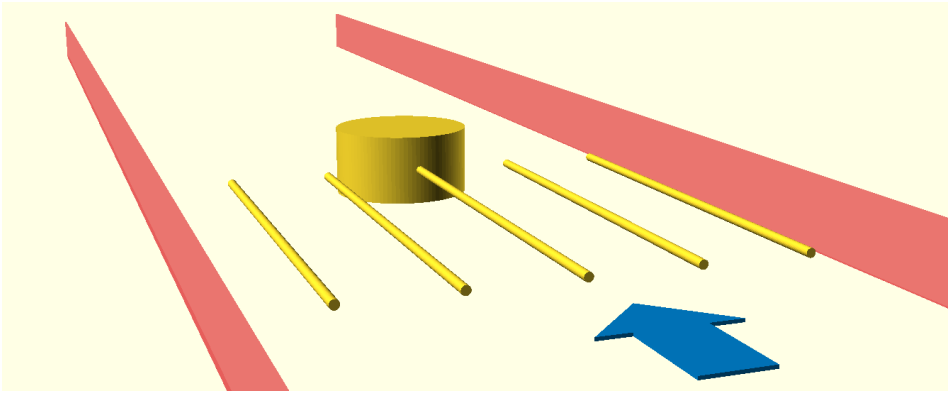

(a) 3D view of the ramus and its five sensilla. The blue arrow shows the direction of the flow.

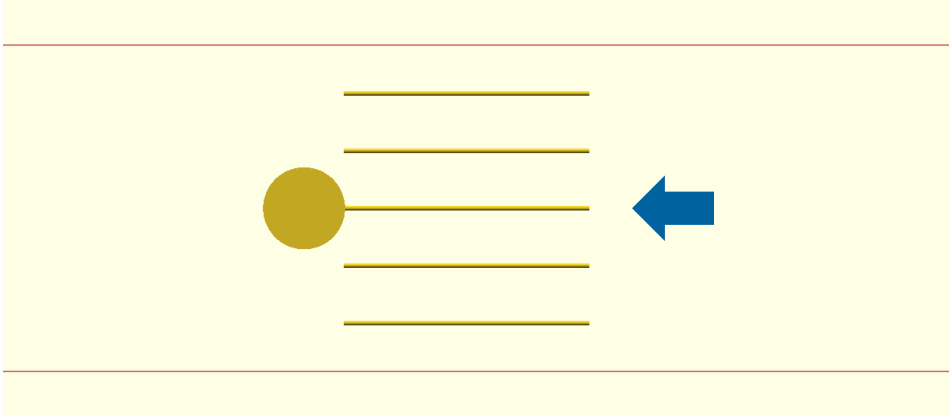

(b) Top view. The blue arrow shows the direction of the flow

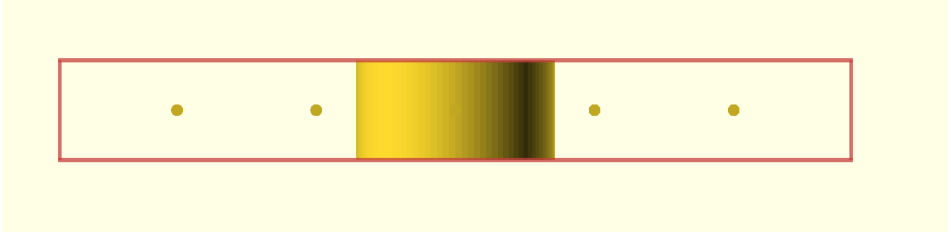

(c) Front view

Figure 7.9: Because the ramus has periodic rows of sensilla, we restricted the simulation domain to one row of five sensilla. The ramus is 25 µm high and has a diameter of 50 µm. We modeled a row of infinite rami using periodic boundary conditions shown in red. The top and bottom periodic boundary conditions shown in c are not displayed in a and b in order to improve the clarity of the figures.

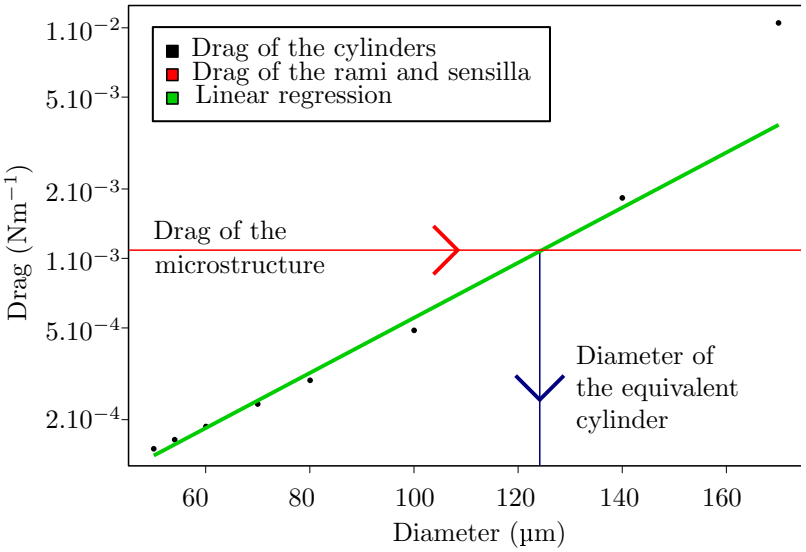

Figure 7.10: Determination of the diameter of the equivalent cylinder to the microstructure at air velocity $v_{n,eq} = 0.5\,m\,s^{-1}$. The diameter is equal to 124.4 µm. The drag per cylinder and per unit of length is determined at this velocity for several diameters (black dots). A linear regression is then applied (green line) and the drag of the microstructure at this velocity (red line) is used to determine the diameter of the equivalent cylinder.

as in the case of a ramus with sensilla. We selected the diameter $\varnothing_{eq}$ that had the same drag d. However, this equivalent cylinder is only valid at the velocity $v_{n,eq}$. For example, at velocity $v_{n,eq} = 0.5\,m\,s^{-1}$, we determined the drag of a cylinder in a row depending on its diameter as well as the drag of the ramus and the five sensilla. We did a linear regression on the drag depending on the diameter using all the points except the one for a diameter of 160 µm because the trend deviated from linearity. We determined the diameter of the equivalent cylinder $\varnothing_{eq}$ that had a drag equal to the one of a ramus and its sensilla at this given velocity (Figure 7.10). Using this method, we obtained the equivalent diameter at each velocity (Figure 7.11).

We also know that:

$$v_n = v_\infty Le_1 \tag{7.4}$$

with v_n, the mean air velocity close to the antenna,
v_∞, the far-field velocity of the antenna,
and Le_1, the leakiness of the macrostructure

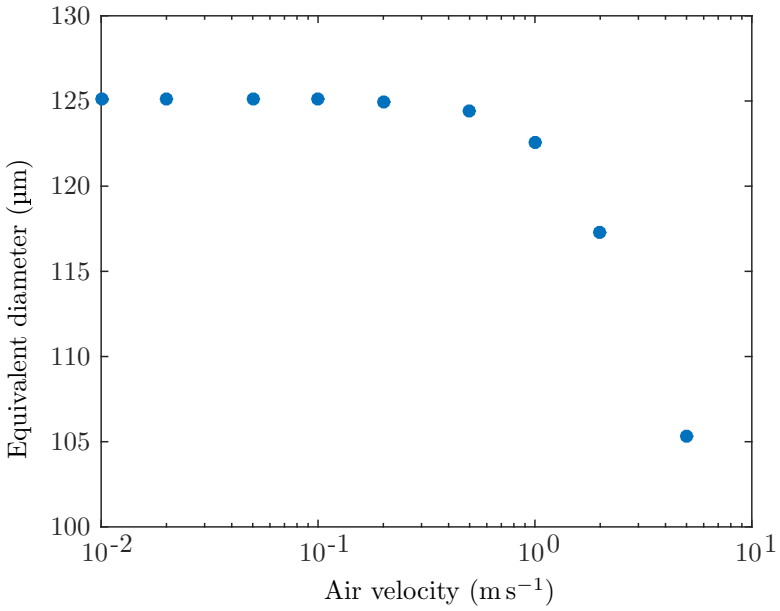

Figure 7.11: Diameter of the equivalent cylinder that has an equal drag as the ramus and sensilla, depending on the air velocity

We then ran simulations to determine the leakiness of the *macro*structure of the antenna with rami having a diameter equal to each of the equivalent diameters that were previously found. Because of symmetry, we ran simulations only on a quarter of the macrostructure and used appropriate periodic boundary conditions to reconstruct the entire row of rami.

From the simulations, we know the relation between the far-field velocity v_∞ and the leakiness of the macrostructure Le_1. According to equation 7.4, we can determine the velocity at the entrance of the microstructure v_n depending on the far-field velocity v_∞. We reversed the relation and determine the far-field velocity v_∞ required to obtained a velocity v_n. To achieve this objective, we did a linear regression on v_n depending on v_∞ in the range of $\{0.1, 0.2, 0.5, 1\}\mathrm{m\,s^{-1}}$ where the relation was linear. During this operation, we obtained both the far-field velocity $v_{\infty,\mathrm{eq}}$ and the leakiness Le_1 for each velocity $v_{\mathrm{n_{eq}}}$ associated to a given equivalent diameter $\varnothing_\mathrm{eq}$ (Figure 7.12).

The advantage of this method is that we bypass the estimation of the leakiness of the microstructure. The influence of the microstructure on the flow is captured by the drag which was used to determine the diameter of the equivalent cylinders. Thus, the leakiness of the macrostructure Le_1 is the leakiness of the entire antenna.

The leakiness we obtained using this method (Figure 7.13) is actually not too

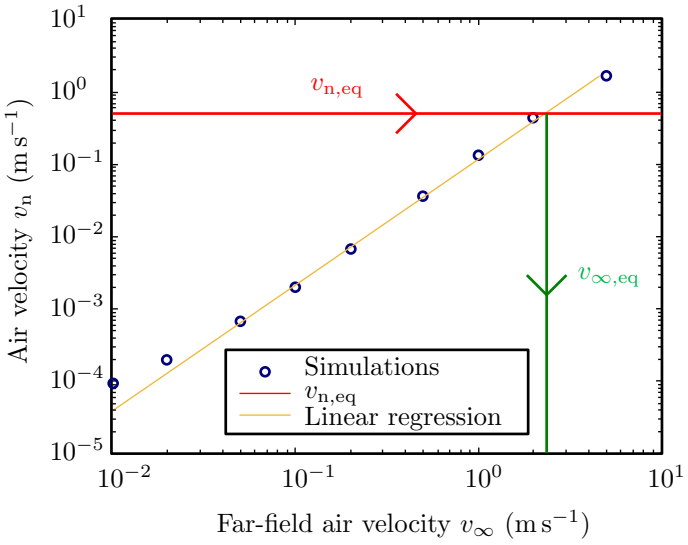

Figure 7.12: Determination of the far-field velocity $v_{\infty,\mathrm{eq}}$ for a given equivalent diameter $\varnothing_{\mathrm{eq}}$ and its associate air velocity $v_{\mathrm{n,eq}}$. Here, $\varnothing_{\mathrm{eq}} = 124.4\,\mu\mathrm{m}$, $v_{\mathrm{n,eq}} = 0.5\,\mathrm{m\,s^{-1}}$ and $v_{\infty,\mathrm{eq}} = 2.3\,\mathrm{m\,s^{-1}}$.

different from the leakiness obtained using the multiplicative method in the previous section. It is also close to the experimental data of Vogel [14]. The reason may lie in the fact that ensuring equal drag of the microstructure and the equivalent cylinder might not be enough to ensure equal leakiness. The 40% difference between the multiplicative method and the method of equivalent cylinders might also be negligible compared to the few orders of magnitude covered by the drag. Other reasons could be that Vogel did not work on the same species and used a single anemometer to measure the leakiness of the entire antenna.

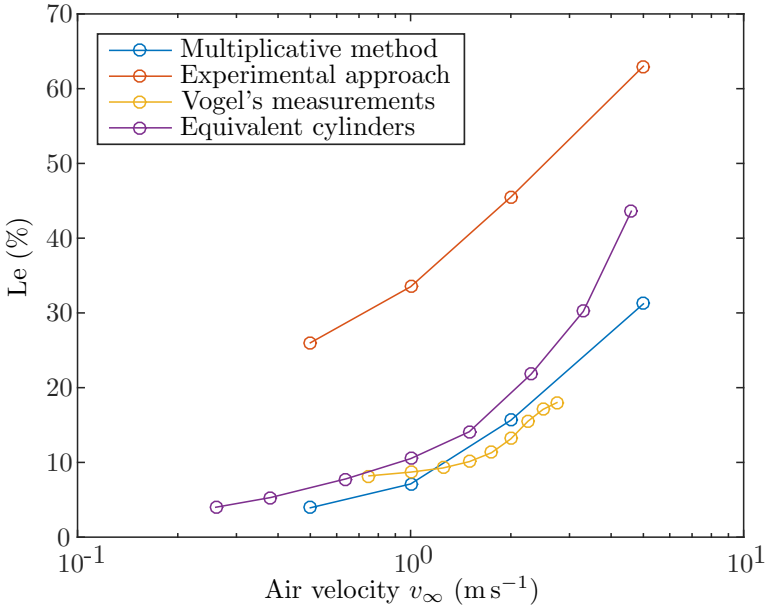

Figure 7.13: Leakiness calculated by using the method of equivalent cylinders compared to the leakiness obtained with the multiplicative method and the data obtained from the PIV experiment and the experimental data of Vogel [14].

7.4.4 Efficiency of the antenna

Thanks to the method developed in the previous section, we determined the leakiness of the complete antenna with all the rami and all the sensilla. We now model the antenna as an array of longitudinal sensilla with a leakiness determined in the previous section. Using the model of Miyatake and Iwashita [207], we determined the capture efficiency of the antenna (Figure 7.14). There is a flat maximum around 2 m s^{-1}: the antenna is thus efficient on a wide range of moth flight velocities.

Combining the two levels of the antenna tends to decrease the leakiness compared to the sole study of the microstructure (Chapter 6). Thus, for a given air velocity, the airflow inside the structure tends to be slower and molecules have more time to diffuse. Thus, the tip of the sensilla facing the flow captures more molecules than the base of the sensilla: the distal half of a sensillum captures between 60% and 100% of the total amount of captured molecules (Figure 7.15). This phenomenon of concentrated capture at the tip of the sensilla was already shown during the study of the microstructure alone (Chapter 6). However, here, we show that considering the entire antenna increases this unbalance of capture between the two halves of the sensilla.

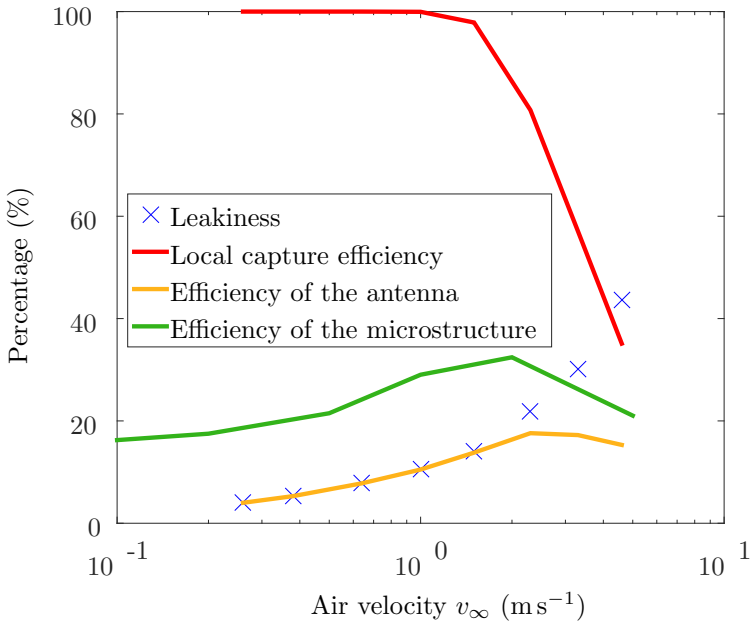

Figure 7.14: Efficiency of the entire antenna. The leakiness is the leakiness of the macro and microstructure combined, the local capture efficiency refers to the efficiency of the infinite array of sensilla to capture the molecules among the flux that flows through the array. The efficiency of the antenna is the capture efficiency of the whole antenna and the efficiency of the microstructure was defined in Chapter 6 and is the efficiency of a microstructure alone.

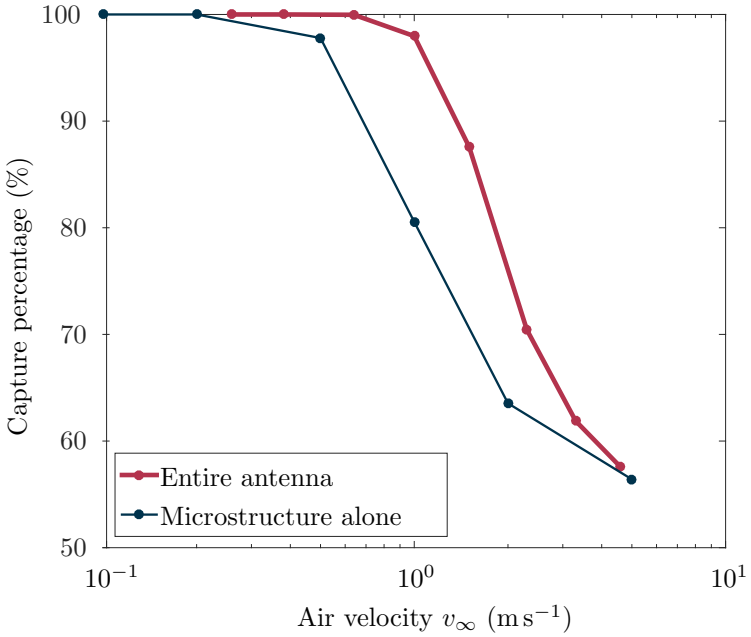

Figure 7.15: Relative capture by the distal half of the sensilla. The relative capture was calculated in the case of the study of the entire antenna (red line) and compared with the case of the study of the microstructure alone (black line) (Chapter 6).

7.4.5 Comparison with the previous models

In our work, we combined several approaches to determine the olfactory efficiency of the pectinate antenna. We resorted to experiments, modeling and simulations to reach our objective. However, the validity of our model is limited to steady-state cases, either from the fluid dynamics point of view or from the pheromone concentration point of view. In other words, the air flow, as well as the pheromone concentration, are constant.

The complex multi-scale shape of the antenna was actually the main difficulty. Choices had to be made. We wanted to focus on the physics that drive the pheromone capture depending on the geometry of the antenna. We had thus to simplify the other aspects of the antenna, such as the fluctuating air flow and the temporal pattern of the pheromone signal. Other works focused on other aspects and, thus, chose to model the antenna in different ways. For example, Humphrey and Haj-Hariri [12] investigated the temporal pattern of the chemical signal detected by the antenna. Thus, They did not model the geometry of the antenna in a faithful way, but instead, they focused on the temporal variations in the pheromone signal.

Cheer and Koehl [187] wanted to determine the leakiness of an antenna depending on its geometry. However, they had to simplify it (two rami + two sensilla) in

order to keep the analytical calculations doable. They modeled the rami and the sensilla as cylinders transversal to the flow in the same way as Murray [11] did. This is a difference with the way we modeled our sensilla, longitudinal to the flow. From a biological point of view, this difference is justified by the fact that the direction of the sensilla varies from one species to an other. Cheer and Koehl [102] found that the sensilla of *Actias luna* were oriented at 45° to the flow direction. Murray, working on *Bombyx mori*, observed that the sensilla were distributed all around the rami [11]. From our own observations through Scanning Electron Microscopy, we found that the sensilla of *Samia cynthia* are oriented towards the flow, pointing forward.

A common and usual approximation [102, 12, 13, 14, 189, 226] in the study of moth antenna is to consider that the antennae are perpendicular to the flow. To our knowledge, only one study [227] looked at the influence of the orientation of pectinate antennae (on *Lymantria dispar* and *Bombyx mori*) and observed that the antennae were perpendicular to the flow during sniffing. The authors also showed that the antennae were more efficient when perpendicular to the flow. We could find in the literature some further pictures of moths showing that the antenna seem to be kept perpendicular to the air flow during flight [204, 228]. Overall, such information is rare despite being key.

Observing the antennae during flight might also be important for another reason: it has been shown that antennae vibrate during flight [45, 229]. The vibration frequency is close to the one of the wing beat, between 8 and 16 Hz in the Saturniidae family [229]. Due to the vibrations, the airflow through the antenna is expected to be periodic. However, we do not know of any observation of the phase between the beating of the wing and the oscillation of the antennae. If the two phenomena are in phase, then the amplitude of the periodic component of the flow is increased and, thus, key to understand the antenna whereas in the reverse case, the periodic component of the flow might be reduced.

Moths actually perform active sensing by moving wings to generate an airflow through the antenna. This behavior is called sniffing. Sniffing also generates periodic airflow. Loudon and Koehl [13] found that the frequency of the wing beat and the airflow is around 48 Hz for *Bombyx mori* and that the amplitude of the unsteady component of the flow accounts for 6-32% of the total flow. Their study is interesting because it is the first one, to our knowledge, to deal with periodic airflow during pheromone capture. However, even if they did measure air velocities in the periodic airflow generated by wing beating, they used the mean air velocity at the front of the antenna and a steady-state model (combination of Darcy law and model of Cheer and Koehl [187]) to determine the leakiness. Thus, a truly periodic model, either analytical or through simulation, has never been done, due to the complexity of periodic fluid dynamics in a complex-shaped object. Overall, our model could closely relate the performance of the antenna with its geometry. However, it cannot deal neither with periodic flow nor with an intermittent chemical signal.

7.5 Functional morphology

7.5.1 Pectinate or cylindrical antennae ?

Samia cynthia and, in a broader sense, Saturniidae, which also bear pectinate antennae, are not the only family to have such antennae. This morphology is actually widespread among the Lepidoptera [183]. Interestingly, pectinate antennae independently appeared 13 times [119] in Lepidoptera. However, many moths using sexual pheromones to find a mate present cylindrical-shape antennae without a pectinate morphology. It is thus necessary to compare the capture capacities of both antennae to understand the benefits of each of them.

The objective here is to determine whether it is better to have a pectinate antenna or a cylindrical one by comparing their respective efficiencies. The capture efficiency of the pectinate antenna was determined in the previous section (Chapter 6). We ran simulations on Comsol (Comsol Inc, Stockholm, Sweden) in order to determine the drag and the mass flux on a cylinder in two cases. First, the cylinder had a diameter equal to the diameter of the flagellum ($200 \pm 30\,\mu m$) and modeled a cylindrical-shaped antenna even though cylindrical shaped-antennae do have other structures such as sensilla and scales which have an influence on the performance [230]. The objective is to determine the additional drag and mass capture due to the rami and the sensilla. The capture efficiency of the cylindrical antenna was calculated by dividing the capture rate of the antenna by the flux of pheromone going through a surface equal to the frontal area of the cylindrical antenna. In a second step, we ran simulations on a cylinder as long and as large as the outer contour of a pectinate antenna and determined the drag and the mass capture. In all cases, in order to improve the quality of the mesh and the numerical convergence of the simulations, we suppressed the sharp edges at the two extremities of the cylinders by adding a sphere at the two extremities. The sphere diameter was equal to the diameter of the cylinder and we decreased the length of the cylinder by the added length due to the presence of the two spheres at the extremities of the cylinder. In the simulations, we used a diffusive coefficient of $4.5 \times 10^{-6}\,m^2\,s^{-1}$ which was defined in Chapter 6.

The reference flux chosen to define the efficiency of a cylinder was taken as the far-field flux through an area equal to the frontal area of the cylinder. This frontal area is thus a square of sides the diameter and the length of the cylinder(Figure 7.16). Figure 7.17 shows that the capture efficiency of a pectinate antenna (yellow curve) is not always higher than the one of a bare flagellum (blue curve) which models a cylindrical antenna. This result, though surprising, was already inferred by Mankin and Mayer [231]. It shows that, contrarily to what is usually expected, pectinate antennae are not always more efficient than cylindrical antennae at capturing pheromone molecules in air. Bare flagella are more efficient at low velocities whereas pectinate antennae perform better at higher ones. In-

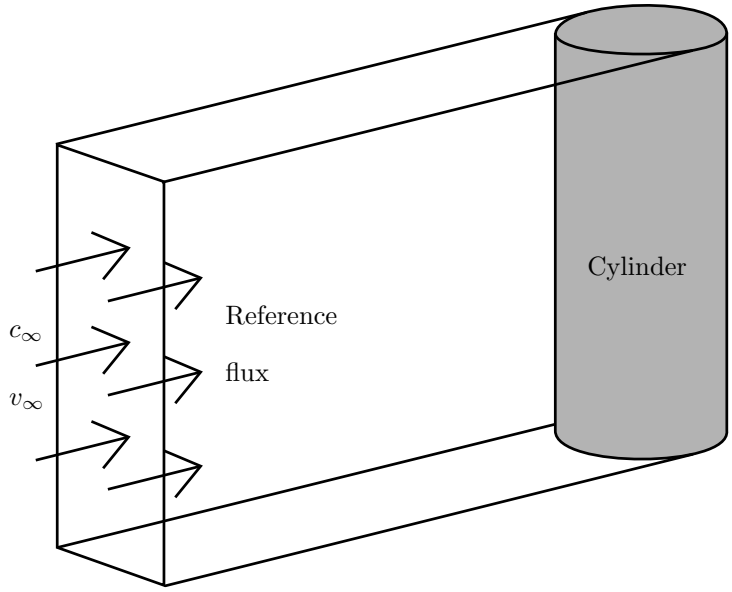

Figure 7.16: Definition of the reference flux.

terestingly, a single transversal ramus (orange curve)) is more efficient at low and medium velocities and single sensilla (violet curve) are always more efficient than a pectinate antenna and can reach efficiencies higher than 100%: because diffusion is efficient at small scale, more pheromone molecules than the one contained in the reference flux reach the surface of the sensillum.

However, pectinate antennae do exist in many moth families. This paradoxical observation may come from the fact that the absolute amount of pheromone m captured by the antenna per unit of time might be the key parameter [104]. Equation 7.5 shows that it is the product of both the efficiency of the antenna η_{ant} and the surface of the antenna S which is important and not the efficiency of the antenna η_{ant} alone.

$$m = \eta_{\text{ant}} S c_\infty v_\infty \tag{7.5}$$

with c_∞ the far-field concentration of pheromone and
v_∞ the far-field air velocity.

The main benefit of pectinate antennae may lie in the absolute amount of captured pheromones (Figure 7.18) and not in their relative efficiency. Transversal cylinders are very efficient (high η_{ant}) but the amount of captured pheromone is limited by their size (small S). To increase the amount of captured pheromone, a pectinate design is well-adapted as it has a medium efficiency (medium η_{ant})

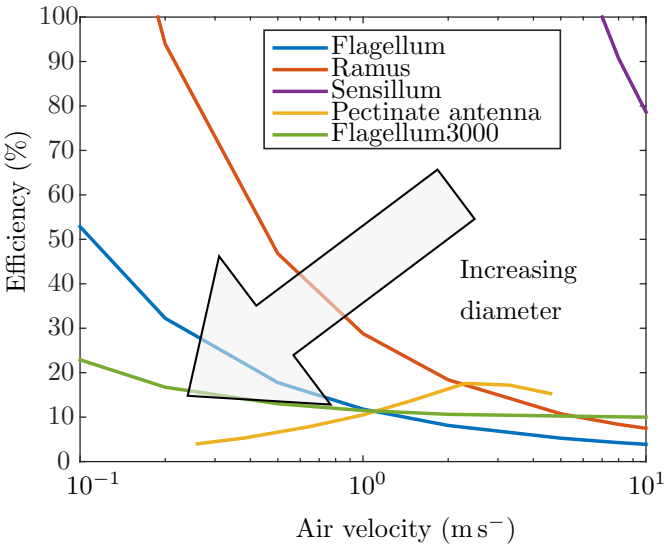

Figure 7.17: Efficiency of the pectinate antenna compared to the one of a single flagellum, ramus or sensillum transversal to the flow. Flagellum3000 refers to a flagellum which would be as long as a normal flagellum but with a diameter equal to the width of a pectinate antenna which is around 3000 µm large.

with a large surface exchange between the antennae and the air (high S). Thus, a pectinate antenna captures at least two times and up to more than one order of magnitude more molecules than a bare flagellum. We also compared a bigger cylindrical antenna with the pectinate one to make sure that a thicker antenna would not be better than a pectinate one. We can thus conclude that a pectinate design is a good solution to increase the absolute amount of captured pheromone molecules.

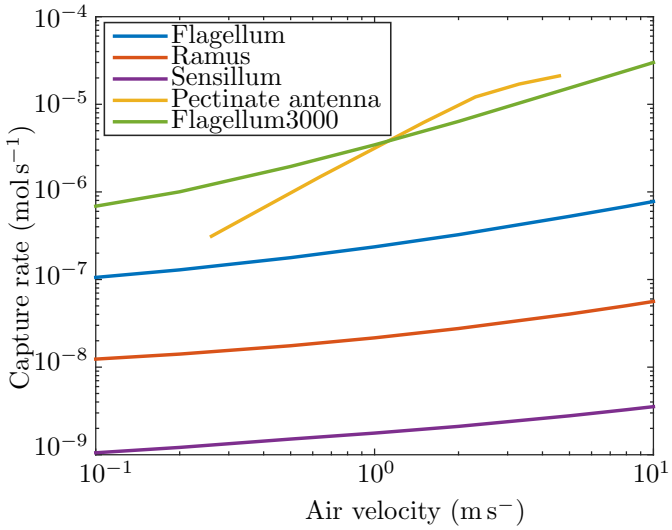

Figure 7.18: Mass captured by the different structures: a bar flagellum, a ramus, a sensillum transversal to the flow, a pectinate antenna and a flagellum with a diameter of 3000 µm. The far-field concentration was set at 1 mol m^{-3}.

7.5.2 Orientation of the sensilla

Because previous models [11, 102] considered the sensilla to be transversal to the flow of air, we wanted to investigate whether longitudinal sensilla would make a difference, as they are oriented towards the flow in *Samia cynthia*. Thus, we ran simulations on a cylinder with equal size as a sensillum and determined its drag and mass capture either in a transversal flow or in a longitudinal one. Here again, transversal sensilla capture at most velocities more pheromone than longitudinal ones (Figure 7.19) but they also have a higher drag (Figure 7.20). The capture of a transversal sensillum is only up to two times the capture by a longitudinal one, whereas there is half an order of magnitude of difference in terms of drag so, if bearing pectinate antennae implies a high price in terms of drag during orientation flight, having sensilla longitudinal to the flow is a good compromise.

7.5.3 Efficiency, antennae surface and pheromone diffusive coefficient

We have previously shown that efficiency is not the only important parameter of an antenna, as an antenna with intermediate efficiency but wide surface could capture more pheromone than a highly-efficient but small one. Symonds *et al*[119] showed that the surface of the antenna is correlated with the size of the moth and that big moths are more likely to have pectinate antennae and, reversely, small moths are more likely to have cylindrical ones. A possible reason for such a difference might lie in the drag generated by the antennae. Pectinate antennae might have too high a drag for small moths, even though such cases do exist: some eucharitids

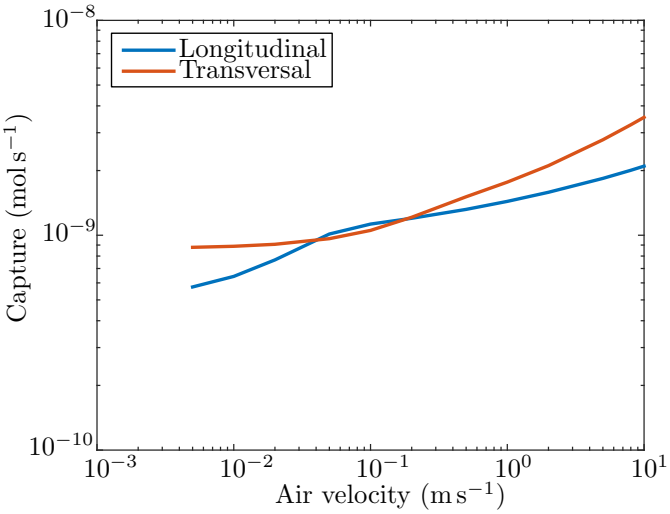

Figure 7.19: Pheromone captured by a transversal and a longitudinal sensillum. The far-field concentration is set at 1 mol m^{-3}.

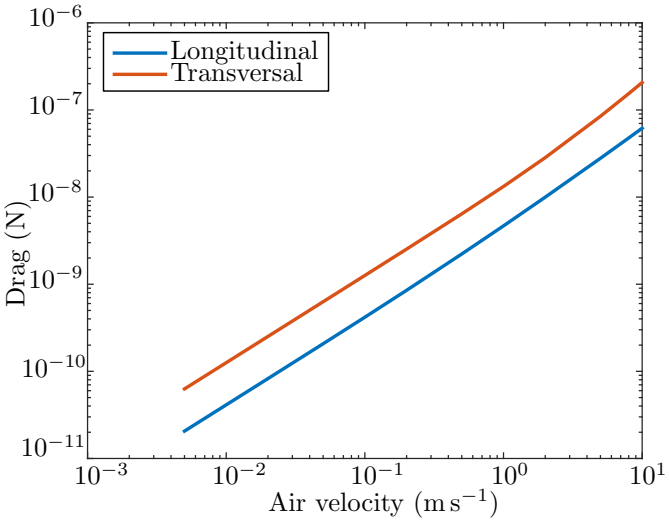

Figure 7.20: Drag of a transversal and a longitudinal sensillum.

wasps do possess pectinate antennae and measure only a few millimeters long [232].

Focusing now on moths bearing pectinate antennae, we investigated the link between the size of the antennae and the diffusive coefficient of the pheromones. The diffusive coefficient of the pheromone is an important parameter. On one hand, a low diffusive coefficient ensures that the chemical signal does not spread and reach low concentrations too fast. Thus, for a given concentration of detection and compared to a pheromone with a high diffusive coefficient, the chemical signal of a pheromone with low diffusive coefficient can travel further away. From a different point of view, we can also notice that, for a given distance, the concentration of the highly-diffusive pheromone is lower and, thus, the moth needs a bigger antenna to capture the same amount of pheromone compared to the case of a pheromone with low diffusive coefficient. On the other hand, a pheromone with low diffusivity crosses the boundary layer around the sensilla more slowly, *i.e.* the antenna is less efficient at capturing it. Thus, for a fixed concentration, in order to capture a given number of molecules, the antenna needs to be bigger for pheromone with low diffusivity compared to pheromone with high diffusivity. According to Symonds *et al* [119], the first argument is the more likely to be true as they found that "*among species with elaborate antennae, longer antennae were typically associated with [...] pheromone compounds with lower molecular weight*" which were assumed to have a higher diffusive coefficient. Another assumption of that study was that the length of an antenna was closely linked to its surface. Although it cannot be entirely wrong, this assumption does not take into account the width of the antenna. For example, Sphingiidae moths have long thin antenna whereas *Antheraea polyphemus* has very large ones. Thus, the length of the antenna might not be an accurate enough proxy for the surface among the Lepidoptera.

The surface of the antenna and the diffusive coefficient of the pheromone are most likely linked and two further parameters should also be taken into account: the distance of detection and the lowest concentration detectable by a moth. These two parameters are related, might vary among species and are difficult to measure. Although the distance of detection has been measured [32] for a few species, it is experimentally difficult to measure it consistently and it might also strongly depend on the wind velocity and direction at the moment of the measurement. The distance of detection is linked with the lowest concentration detectable by a moth. For a fixed diffusive coefficient, the lower the concentration of detection, the further away the moth can detect the pheromones. Symonds *et al* [119] used the pheromone titre in the gland of the females as a proxy for the pheromone concentration and the density of moth for the distance of detection. However, the authors found no link between the pheromone titre and the type and size of the antennae. Pheromone titre might not be a good indicator of pheromone release as most of the pheromone production is actually catabolized and not released [80]. Regarding the density of moths, the authors [119] themselves agree on the difficulty to obtain a reliable measure.

As a conclusion, there certainly are links between the surface of the antenna, the diffusivity of the pheromone and the distance of detection. However, the latter parameter is so difficult to determine that any definitive conclusion is currently not possible. Capture-recapture experiments could be conducted to determine the distance of detection but the experiment should be replicated many times to take into account the variations of environmental parameters such as temperature, humidity, wind speed and wind direction and the biological variations of the moths depending for example on the time after emergence. Maybe experiments in large-scale wind tunnel could offer a more controlled environment but it might not be possible to build very long tunnels.

7.5.4 Comparison with other types of antennae

In this work, we have focused on pectinate antennae which have an olfactory function. However, among the Insects, the diversity of antennae with good olfactory capacities is much larger [63]. Lamellate antennae are of particular interest. They have a shape very different from cylindrical antennae, which means that they should also have a different behavior regarding olfactory molecule capture. Their large surface and high number of sensilla should be beneficial from an olfactory point of view [233]. It is interesting to note that lamellate and pectinate antennae might be two solutions for the same problem of capturing molecules in air. They both increase their surface by bearing many branches which also allow air to flow. However, pectinate antennae have trichodea sensilla which are hair-like sensilla whereas lamellate antennae (from beetles of the genus *Rhipicera*) rely mainly on sensilla placodeum which are flat sensilla although they still exhibit some sensilla trichodea [233].

The difference in design might come from phylogenetic reasons as Lepidoptera have either cylindrical-shaped or pectinate antennae [119] whereas other groups have evolved more designs such as the lamellate antennae that are present in Coleoptera [233]. However, the nature of the chemicals detected by the antennae might also have an influence through the diffusive coefficient which affects the olfactory efficiency of an antenna. In the case of the Lepidoptera, sexual pheromones are mostly medium-sized molecules around 200 to 300 $\mathrm{g\,mol^{-1}}$ [119]. In the case of lamellate antennae, the sexual pheromone is not always known [233] and might be composed of plant chemicals [91, 92].

Much work has also been done on crustaceans which bear appendages used to collect food or detect odors [187, 206, 234]. However, crustaceans are mainly aquatic arthropods and underwater olfaction faces different challenges compared to olfaction in air: water has a lower kinematic viscosity than air but diffusive coefficient are usually 1 000 times smaller than in air, around $10^{-9}\mathrm{m^2s^{-1}}$. Crustaceans exhibit a specific behavior called flicking reminiscent of active olfaction (sniffing) described above. Their appendages are composed of closely-packed hairs, the aesthetascs. Flicking is divided in two phases. The first stroke, the down stroke,

allows water to flow between the aesthetascs and renew the water whereas the return stroke is much slower and keeps the water still in the appendage, giving enough time to the odorant molecules to diffuse to the aesthetascs [234]. The role of leakiness is of primary importance in water as the appendages shift from a leaky array of aesthetascs to an almost non-permeable one. Interestingly, some crustaceans live out of water and it is thus possible to study how the appendages of crustaceans evolved to be efficient in air. A study on hermit crabs [192] showed that their appendages are not leaky, neither during the downstroke nor during the return stroke. Molecules are indeed captured from the side of the appendage thanks to the higher diffusive coefficient of chemicals in air. In a more general way, a model compared olfaction in air and in water [201] and found that appendages in water rely heavily on leakiness to bring new molecules close to the aesthetascs and require a long time for the molecules to diffuse. In air, diffusive coefficients are higher so leakiness is not such a limiting parameter anymore. It is worth noticing that this study does not consider pectinate (or lamellate) antennae for which the authors expected both leakiness and diffusion to have major influence. In our work, we have indeed shown that this is actually the case.

7.6 Conclusion

We developed a method to combine the two levels of the antenna and determined the efficiency of an entire pectinate antenna. Comparison with a cylindrical antenna showed the major benefit of a pectinate antenna is its increased surface contact which compensates for the decrease in relative efficiency at capturing pheromone molecules. Contrary to cylindrical antennae or crustacean appendages in water, leakiness and diffusion are both important mechanisms for a pectinate antenna, which justifies a posteriori our approach to determine the efficiency of our antenna.

Bibliography

[1] C. Loudon. Antennae. In Vincent H. Resh and Ring Cardé, editors, *Encyclopaedia of Insects*. Academic Press, 2003.

[2] J.F. Laliberté, K.L. Kraemer, J.W. Dawson, and D. Miyata. Design and Manufacturing of Biologically Inspired Micro Aerial Vehicle Wings Using Rapid Prototyping. *International Journal of Micro Air Vehicles*, 5(1):15–38, 2013.

[3] M. Sahlabadi and P. Hutapea. Novel design of honeybee-inspired needles for percutaneous procedure. *Biomimetics & Bioinspiration*, 13:036013, 2018.

[4] Z. Qin, B.G. Compton, J.A. Lewis, and M.J. Buehler. Structural optimization of 3D-printed synthetic spider webs for high strength. *Nature Communications*, 6(May):1–7, 2015.

[5] C. Richter and H. Lipson. Untethered Hovering Flapping Flight of a 3D-Printed Mechanical Insect. *Artificial Life*, 17(2):73–86, 2011.

[6] N. Oxman, M. Kayser, J. Laucks, and M. Firstenberg. Robotically controlled fiber-based manufacturing as case study for biomimetic digital fabrication. In *Green Design, Materials and Manufacturing Processes*, pages 473–478. CRC Press (London), 2013.

[7] M. Jaffar-Bandjee, T. Steinmann, K.J.M. Gijs, and J. Casas. Microphysics of the olfactory antenna of the moth Samia cynthia. *In press.*

[8] S.K.V. Aditya, J. Ignasov, K. Filonenko, J.C. Larsen, E. Baird, J. Hallam, S. Büsse, A. Kovalev, S.N. Gorb, L. Duggen, and P. Manoonpong. Bio-Inspired Design and Kinematic Analysis of Dung Beetle-Like Legs. *The 2nd International Symposium on Swarm Behavior and Bio-Inspired Robotics*, 2017.

[9] B.E. Gravel, P.Y. Wong, P.T. Starks, and J.A. Pechenik. The use of artificial shells for exploring shell preference in the marine hermit crab Pagurus longicarpus (Say). *Annales Zoologici Fennici*, 41(3):477–485, 2004.

[10] H.J. Bestmann, A.B. Attygalle, J. Schwarz, W. Garbe, O. Vostrowsky, and I. Tomida. Pheromones, 71. Identification and synthesis of female sex pheromone of eri-silkworm, Samia cynthia ricini (Lepidoptera: Saturniidae). *Tetrahedron Letters*, 30(22):2911–2914, 1989.

[11] J.D. Murray. Reduction of dimensionability in diffusion processes: antenna receptors of moths. In *Nonlinear Differential Equation Models in Biology*, pages 83–127. Oxford University Press, Oxford, 1977.

[12] J.A.C. Humphrey and H. Haj-Hariri. Detection and Real Time Processing of Odor Plume Information by Arthropods in Air and Water. In *Proceedings of the AFI-2002 Mini-Symposium on Advanced Fluids Information—Fusion of EFD and CFD*, pages 47–67, 2002.

[13] C. Loudon and M.A.R. Koehl. Sniffing by a silkworm moth: wing fanning enhances air penetration through and pheromone interception by antennae. *Journal of Experimental Biology*, 203(19):2977–2990, 2000.

[14] S. Vogel. How much air passes through a silkmoth's antenna? *Journal of Insect Physiology*, 29(7):597–602, 1983.

[15] A.M. Ray, M.D. Ginzel, and L.M. Hanks. Male Megacyllene robiniae (Coleoptera: Cerambycidae) Use Multiple Tactics When Aggressively Competing for Mates. *Environmental Entomology*, 38(2):425–432, 2009.

[16] T. Ahmed, T.T. Zhang, Z.Y. Wang, K.L. He, and S.X. Bai. Morphology and ultrastructure of antennal sensilla of Macrocentrus cingulum Brischke (Hymenoptera: Braconidae) and their probable functions. *Micron*, 50:35–43, 2013.

[17] L.L. Ren, Y. Wu, J. Shi, L. Zhang, and Y.Q. Luo. Antenna morphology and sensilla ultrastructure of Tetrigus lewisi Candèze (Coleoptera: Elateridae). *Micron*, 60:29–38, 2014.

[18] X. Yuan, S. Zhang, Z. Zhang, X. Kong, H. Wang, G. Shen, and H. Zhang. Antennal morphology and sensilla ultrastructure of the web-spinning sawfly Acantholyda posticalis Matsumura (Hymenoptera: Pamphiliidae). *Micron*, 50:20–28, 2013.

[19] J. Casas and O. Dangles. Physical Ecology of Fluid Flow Sensing in Arthropods. *Annual Review of Entomology*, 55(1):505–520, 2010.

[20] William A. Harris. The maxillae of Drosophila melanogaster as revealed by scanning electron microscopy. *Journal of Morphology*, 138(4):451–456, 1972.

[21] Z. Syed and W.S. Leal. Maxillary palps are broad spectrum odorant detectors in culex quinquefasciatus. *Chemical Senses*, 32(8):727–738, 2007.

[22] H. Ai. Sensors and sensory processing for airborne vibrations in silk moths and honeybees. *Sensors*, 13(7):9344–9363, 2013.

[23] S.J. Gould and R.C. Lewontin. The Spandrels of San Marco and the Panglossian Paradigm : A Critique of the Adaptationist Programme. *Proceedings of the Royal Society of London B*, 205(1161):581–598, 1979.

[24] K. E. von Baer. *Über Entwickelungsgeschichte der Thiere.* Königsberg: Bornträger, 1828.

[25] R. Owen. Notes on the anatomy of the Nubian Giraffe. *The Transactions of the Zoological Society of London*, 2(3):217–243, 1839.

[26] M.J. Wedel. A Monument of Inefficiency: The Presumed Course of the Recurrent Laryngeal Nerve in Sauropod Dinosaurs. *Acta Palaeontologica Polonica*, 57(2):251–256, 2012.

[27] J. Maynard Smith, R. Burian, S. Kauffman, P. Alberch, J. Campbell, B. Goodwin, R. Lande, D. Raup, and L. Wolpert. Developmental constraints and evolution: a perspective from the mountain lake conference on development and evolution. *The Quaterly Review of Biology*, 60(3):265–287, 1985.

[28] J.F. Harrison, A. Kaiser, and J.M. VandenBrooks. Atmospheric oxygen level and the evolution of insect body size. *Proceedings of the Royal Society B*, 277(1690):1937–1946, 2010.

[29] C. Gans, R. Dudley, N.M. Aguilar, and J.B. Graham. Late Paleozoic atmospheres and biotic evolution. *Historical Biology*, 13(2-3):199–219, 1999.

[30] R. Sears and J. Calambokidis. COSEWIC Assessment and Update Status Report on the Blue Whale, Balaenoptera musculus, Atlantic Population, Pacific Population in Canada. Technical report, Committee on the Status of Endangered Wildlife in Canada., Ottawa, 2002.

[31] P.J. Gullan and P.S. Cranston. External anatomy. In *The insects: an outline of entomology*, chapter 2, pages 23–52. Wiley-Blackwell, 2010.

[32] C. Wall and J.N. Perry. Range of action of moth sex-attractant sources. *Entomologia Experimentalis et Applicata*, 44(1):5–14, 1987.

[33] R.S. Beaman, P.J. Decker, and J.H Beaman. Pollination of Rafflesia (Rafflesiaceae). *American Journal of Botany*, 75(8):1148–1162, 1988.

[34] S.L. Wee, S.B. Tan, and A. Jürgens. Pollinator specialization in the enigmatic Rafflesia cantleyi: A true carrion flower with species-specific and sex-biased blow fly pollinators. *Phytochemistry*, 153(January):120–128, 2018.

[35] N.F. Hadley. Cuticular Lipids of Terrestrial Plants and Arthropods: a Comparison of Their Structure, Composition, and Waterproofing Function. *Biological Reviews*, 56(1):23–47, 1981.

[36] R.K. Vander Meer and L. Morel. Nestmate recognition in ants. In Robert K. Vander Meer, Michael D. Breed, Mark Winston, and Karl E. Espelie, editors, *Pheromone Communication in Social Insects*, pages 79–103. CRC Press, Boca raton, 1998.

[37] M. Ozaki and A. Wada-Katsumata. Perception and olfaction of cuticular compounds. In Gary J. Blomquist and Anne-Geneviève Bagnères, editors, *Insect Hydrocarbons: Biology, Biochemistry, and Chemical Ecology*, chapter 10, pages 207–221. Cambridge University Press, 2010.

[38] F. Bénédet, T. Leroy, N. Gauthier, C. Thibaudeau, E. Thibout, and S. Renault. Gustatory sensilla sensitive to protein kairomones trigger host acceptance by an endoparasitoid. *Proceedings of the Royal Society B*, 269(1503):1879–1886, 2002.

[39] A. Brockmann, C. Groh, and B. Fröhlich. Wax perception in honeybees: Contact is not necessary. *Naturwissenschaften*, 90(9):424–427, 2003.

[40] A.S. Brandstaetter, A. Endler, and C.J. Kleineidam. Nestmate recognition in ants is possible without tactile interaction. *Naturwissenschaften*, 95(7):601–608, 2008.

[41] C. Johnston. Original communications: Auditory Apparatus of the Culex mosquito. *Journal of Cell Science*, 1:97–102, 1855.

[42] M.C. Göpfert, H. Briegel, and D. Robert. Antennal vibrations in mosquitoes. *The Journal of Experimental Biology*, 202:2727–2738, 1999.

[43] C. Dreller and W.H. Kirchner. Hearing in honeybees: localization of the auditory sense organ. *Journal of Comparative Physiology A*, 173(3):275–279, 1993.

[44] S.A. Kolmes. Ecological and Sensory Aspects of Prey Capture by the Whirligig Beetle Dineutes discolor (Coleoptera : Gyrinidae). *Journal of the New York Entomological Society*, 91(4):405–412, 1983.

[45] S.P. Sane, A. Dieudonné, M.A. Willis, and T.L. Daniel. Antennal Mechanosensors Mediate Flight Control in Moths. *Science*, 315:863–866, 2007.

[46] A. Dieudonné, T.L. Daniel, and S.P. Sane. Encoding properties of the mechanosensory neurons in the Johnston's organ of the hawk moth, Manduca sexta. *Journal of Experimental Biology*, 217(17):3045–3056, 2014.

[47] H.-G. Heinzel and H. Böhm. The wind-orientation of walking carrion beetles. *Journal of Comparative Physiology A*, 164(6):775–786, 1989.

[48] D. Clarke, H. Whitney, G. Sutton, and D. Robert. Detection and Learning of Floral Electric Fields by Bumblebees. *Science*, 340:66–69, 2013.

[49] P.L. Newland, E. Hunt, S.M. Sharkh, N. Hama, M. Takahata, and C.W. Jackson. Static electric field detection and behavioural avoidance in cockroaches. *Journal of Experimental Biology*, 211(23):3682–3690, 2008.

[50] U. Warnke. Effects of Electric Charges on Honeybees. *Bee World*, 57(2):50–56, 1976.

[51] C. Jackson and D. McGonigle. Direct monitoring of the electrostatic charge of house-flies (Musca domestica L.) as they walk on a dielectric surface. *Journal of Electrostatics*, 63:803–808, 2005.

[52] U. Greggers, G. Koch, V. Schmidt, A. Dürr, A. Floriou-Servou, D. Piepenbrock, M.C. Göpfert, and R. Menzel. Reception and learning of electric fields in bees. *Proceedings of the Royal Society B*, 280(1759):20130528, 2013.

[53] H. Rajabi, A. Shafiei, A. Darvizeh, S.N. Gorb, V. Dürr, and J.-H. Dirks. Both stiff and compliant: Morphological and biomechanical adaptations of stick insect antennae for tactile exploration. *Journal of the Royal Society Interface*, 15(144), 2018.

[54] J. Okada and Y. Toh. Active tactile sensing for localization of objects by the cockroach antenna. *Journal of Comparative Physiology A*, 192(7):715–726, 2006.

[55] D.B. Zurek and C. Gilbert. Static antennae act as locomotory guides that compensate for visual motion blur in a diurnal, keen-eyed predator. *Proceedings of the Royal Society B*, 281(1779), 2014.

[56] H. Altner and R. Loftus. Ultrastructure and function of insect thermo- and hygroreceptors. *Annual Review of Entomology*, 30:273–295, 1985.

[57] C. Merlin, R.J. Gegear, and S.M. Reppert. Antennal circadian clocks coordinate sun compass orientation in migratory monarch butterflies. *Science*, 325(5948), 2009.

[58] N.E. Stork. The structure and function of the adhesive organs on the antennae of male Harpocera thoracica (Fallen) (Miridae; Hemiptera). *Journal of Natural History*, 15(4):639–644, 1981.

[59] D.A. Humphries. The mating behaviour of the hen flea Ceratophyllus gallinae (Schrank) (Siphonaptera: Insecta). *Animal Behaviour*, 15:82–90, 1967.

[60] F. Brocher. Recherches sur la respiration des insectes aquatiques adultes. Les Haemonia. *Annales de biologie lacustre*, Tome V:5–26, 1912.

[61] F. Brocher. Respiration des insectes aquatiques adultes. L'hydrophile. *Annales de biologie lacustre*, Tome V:220–258, 1912.

[62] E. N. Pavlovsky. On the Biology and Structure of the Larvae of Hydrophilus caraboides L. *Quaterly Journal of Microscopical Science*, 66:627–655, 1922.

[63] M.A. Elgar, D. Zhang, Q. Wang, B. Wittwer, H.T. Pham, T.L. Johnson, C.B. Freelance, and M. Coquilleau. Insect Antennal Morphology : The Evolution of Diverse Solutions to Odorant Perception. *Yale Journal of Biology and Medecine*, 91:457–469, 2018.

[64] A. Schaller. Sinnesphysiologische und psychologische untersuchungen an wasserkäfern und fischen. *Zeitschrift für vergleichende Physiologie*, 4:370–464, 1926.

[65] E. Ritter. Untersuchungen über den chemischen sinn beim schwarzen kolbenwasserkäfer hydrous piceus. *Zeitschrift für vergleichende Physiologie*, 23:543–570, 1936.

[66] D. Schneider. Insect antennae. *Annual review of entomology*, 9(1):103–122, 1964.

[67] P.J. Gullan and P.S. Cranston. Sensory systems and behavior. In *The insects: an outline of entomology*, chapter 4, pages 91–120. Wiley-Blackwell, 2010.

[68] I. Mori. Olfaction. In Sydney Brenne and Jefferey H. Miller, editors, *Encyclopedia of genetics*, pages 1368–1370. Academic Press, 2001.

[69] J. H. Visser. Host Odor Perception in Phytophagous Insects. *Annual Review of Entomology*, 31(1):121–144, 1986.

[70] R.B. Barrozo and C.R. Lazzari. The response of the blood-sucking bug Triatoma infestans to carbon dioxide and other host odours. *Chemical Senses*, 29(4):319–329, 2004.

[71] M. Hilker, C. Kobs, M. Varama, and K. Schrank. Insect egg deposition induces Pinus sylvestris to attract egg parasitoids. *The Journal of Experimental Biology*, 205(4):455–461, 2002.

[72] R. Mumm and M. Hilker. The significance of background odour for an egg parasitoid to detect plants with host eggs. *Chemical Senses*, 30(4):337–343, 2005.

[73] M. Zuk and G.R. Kolluru. Exploitation of sexual signals by predators and parasitoids. *The Quaterly Review of Biology*, 73(4):415–438, 1998.

[74] M.D. Bentley and J.F. Day. Chemical ecology and behavioral aspects of mosquito oviposition. *Annual Review of Entomology*, 34:401–421, 1989.

[75] P. Karlson and M. Lüscher. "Pheromone": a new term for a class of biologically active substances. *Nature*, 183(4653):55–56, 1959.

[76] Gary J. Blomquist and Anne-Geneviève Bagnères, editors. *Insect Hydrocarbons*. Cambridge University Press, 2010.

[77] F.E. Regnier and J.H. Law. Insect pheromones. *Journal of Lipid Research*, 9(5):541–551, 1968.

[78] M.R.E. Symonds and M.A. Elgar. The evolution of pheromone diversity. *Trends in Ecology and Evolution*, 23(4):220–228, 2008.

[79] T.D. Wyatt. Fifty years of pheromones. *Nature*, 457(7227):262–263, 2009.

[80] S.P. Foster, K.G. Anderson, and J. Casas. The Dynamics of Pheromone Gland Synthesis and Release: a Paradigm Shift for Understanding Sex Pheromone Quantity in Female Moths. *Journal of Chemical Ecology*, 44(6):525–533, 2018.

[81] K.H. Dahm, D. Meyer, W.E. Finn, V. Reinhold, and H. Röller. The Olfactory and Auditory Mediated Sex Attraction in Achroia grisella (Fabr.). *Naturwissenschaften*, 58(5):265–266, 1971.

[82] Paul D.N. Hebert. Egg dispersal patterns and adult feeding behaviour in the Lepidoptera. *The Canadian entomologist*, 115(11):1477–1481, 1983.

[83] T. Tammaru and E. Haukioja. Capital Breeders and Income Breeders among Lepidoptera : Consequences to Population Dynamics. *Oikos*, 77(3):561–564, 1996.

[84] R.F. Chapman. *The Insects: Structures and Functions*. Cambridge University Press, 4th edition, 1998.

[85] J. Kochansky, J. Tette, E.F. Taschenberg, R.T. Cardé, K.-E. Kaissling, and W.L. Roelofs. Sex Pheromone of the Moth Antheraea Polyphemus. *Journal of Insect Physiology*, 21:1977–1983, 1975.

[86] J.A. Klun, O.L. Chapman, K.C. Mattes, P.W. Wojtkowski, M. Beroza, and P.E. Sonnet. Insect Sex Pheromones: Minor Amount of Opposite Geometrical Isomer Critical to Attraction. *Science*, 181(4100):661–663, 1973.

[87] C. Löfstedt. Population variation and genetic control of pheromone communication systems in moths. *Entomologia Experimentalis et Applicata*, 54(3):199–218, 1990.

[88] A.K. Minks and R.T. Cardé. Disruption of Pheromone Communication in Moths: Is the natural Blend really most Efficacious? *Entomologia Experimentalis et Applicata*, 49:25–36, 1988.

[89] M. Michereff Filho, E.F. Vilela, G.N. Jham, A.B. Attygalle, A. Svatoš, and J. Meinwald. Initial Studies of Mating Disruption of the Tomato Moth, Tuta absoluta (Lepidoptera: Gelechiidae) Using Synthetic Sex Pheromone. *Journal of the Brazilian Chemical Society*, 11(6):621–628, 2000.

[90] Z. Yang, M. Bengtsson, and P. Witzgall. Host plant volatiles synergize response to sex pheromone in codling moth, Cydia pomonella. *Journal of Chemical Ecology*, 30(3):619–629, 2004.

[91] J. Ruther, A. Reinecke, and M. Hilker. Plant volatiles in the sexual communication of Melolontha hippocastani: Response towards time-dependent bouquets and novel function of (Z)-3-hexen-1-ol as a sexual kairomone. *Ecological Entomology*, 27(1):76–83, 2002.

[92] A. Reinecke, J. Ruther, and M. Hilker. The scent of food and defence: green leaf volatiles and toluquinone as sex attractant mediate mate finding in the European cockchafer Melolontha melolontha. *Ecology Letters*, 5:257–263, 2002.

[93] V. Singh, R. Vig, V. Mohini, I.R. Trehan, and G.L. Kad. Syntheses of (4E,6E,11Z)-4,6,11-hexadecatrienyl acetate and (4E,6E,11Z)-4,6,11-Hexadecatrienal, female sex pheromones of eri-silkworm, Samia cynthia ricini (Lepidoptera: Saturniidae). *Proceedings of the Indian Academy of Sciences*, 104(1):57–60, 1992.

[94] T. Ando, S. Inomata, and M. Yamamoto. Lepidopteran Sex Pheromones. *Topics in Current Chemistry*, 239:51–96, 2004.

[95] C. Schal and R.T. Cardé. Rhythmic extrusion of pheromone gland elevates pheromone release rate. *Experientia*, 41:1617–1619, 1985.

[96] W.E. Conner, R.P. Webster, and H. Itagaki. Calling behaviour in arctiid moths: the effects of temperature and wind speed on the rhythmic exposure of the sex attractant gland. *Journal of Insect Physiology*, 31(10):815–820, 1985.

[97] J. Murlis, J.S. Elkinton, and R.T. Cardé. Odor Plumes And How Insects Use Them. *Annual Review of Entomology*, 37(1):505–532, 1992.

[98] A. Celani, E. Villermaux, and M. Vergassola. Odor landscapes in turbulent environments. *Physical Review X*, 4(4):1–17, 2014.

[99] L. Conchou, P. Lucas, C. Meslin, M. Proffit, M. Staudt, and M. Renou. Insect Odorscapes: From Plant Volatiles to Natural Olfactory Scenes. *Frontiers in Physiology*, 10(August), 2019.

[100] M.A. Willis and T.C. Baker. Effects of intermittent and continuous pheromone stimulation on the flight behaviour of the oriental fruit moth, Grapholita molesta. *Physiological Entomology*, 9(3):341–358, 1984.

[101] N.J. Vickers and T.C. Baker. Male Heliothis virescens maintain upwind flight in response to experimentally pulsed filaments of their sex pheromone (Lepidoptera: Noctuidae). *Journal of Insect Behavior*, 5(6):669–687, 1992.

[102] A.Y.L. Cheer and M.A.R. Koehl. Fluid flow through filtering appendages of insects. *Journal of Mathematics Applied in Medicine and Biology*, 4(3):185–199, 1987.

[103] R.A. Steinbrecht. Pores structures in insect olfactory sensilla: A review of data and concepts. *International Journal of Insect Morphology and Embryology*, 26(3-4):229–245, 1997.

[104] J. Boeckh, K.-E. Kaissling, and D. Schneider. Insect olfactory receptors. *Cold Spring Harbor symposia on quantitative biology*, 30:263–280, 1965.

[105] G. Adam and M. Delbrück. Reduction of dimensionality in biological diffusion processes. In Alexander Rich, Norman R Davidson, and Linus Pauling, editors, *Structural chemistry and molecular biology*, pages 198–215. WH Freeman, San Francisco, 1968.

[106] R.P. Futrelle. How molecules get to their detectors: the physics of diffusion of insect pheromones. *Trends in Neurosciences*, pages 116–120, 1984.

[107] M.M. Maitani, D.L. Allara, K.C. Park, S.G. Lee, and T.C. Baker. Moth olfactory trichoid sensilla exhibit nanoscale-level heterogeneity in surface lipid properties. *Arthropod Structure and Development*, 39(1):1–16, 2010.

[108] P. Pelosi and R. Maida. Odorant-binding proteins in insects. *Comparative Biochemistry and Physiology B*, 111(3):503–514, 1995.

[109] W.S. Leal. Odorant Reception in Insects: Roles of Receptors, Binding Proteins, and Degrading Enzymes. *Annual Review of Entomology*, 58(1):373–391, 2013.

[110] K.-E. Kaissling and E. Priesner. Die Riechschwelle des Seidenspinners. *Naturwissenschaften*, 57(1):23–28, 1970.

[111] J.S. Kennedy and D. Marsh. Pheromone-Regulated Anemotaxis in Flying Moths. *Science*, 184(4140):999–1001, 1974.

[112] C.T. David, J.S. Kennedy, and A.R. Ludlow. Finding of a sex pheromone source by gypsy moths released in the field. *Nature*, 303(30):804–806, 1983.

[113] L.P. S. Kuenen and R.T. Cardé. Strategies for recontacting a lost pheromone plume: casting and upwind flight in the male gypsy moth. *Physiological Entomology*, 19(1):15–29, 1994.

[114] R. Kanzaki. Behavioral and neural basis of instinctive behavior in insects: Odor-source searching strategies without memory and learning. *Robotics and Autonomous Systems*, 18(1-2):33–43, 1996.

[115] R. Kanzaki. Coordination of wing motion and walking suggests common control of zigzag motor program in a male silkworm moth. *Journal of Comparative Physiology - A*, 182(3):267–276, 1998.

[116] M. Birch. Pre-courtship use of abdominal brushes by the nocturnal moth, Phlogophora meticulosa (L.) (Lepidoptera: Noctuidae). *Animal Behaviour*, 18:310–316, 1970.

[117] W.E. Conner, B. Roach, E. Benedict, J. Meinwald, and T. Eisner. Courtship pheromone production and body size as correlates of larval diet in males of the arctiid moth, Utetheisa ornatrix. *Journal of Chemical Ecology*, 16(2):543–552, 1990.

[118] W.E. Conner. Ultrasound: its role in the courtship of the arctiid moth, Cycnia tenera. *Experientia*, 43:1029–1031, 1987.

[119] M.R.E. Symonds, T.L. Johnson, and M.A. Elgar. Pheromone production, male abundance, body size, and the evolution of elaborate antennae in moths. *Ecology and Evolution*, 2(1):227–246, 2011.

[120] M.H. Farias, R.S. Teixeira, J. Koiller, and A.M. Santos. Brief review of uncertainty quantification for particle image velocimetry. *Journal of Physics: Conference Series*, 733(1), 2016.

[121] I. Grant. Particle image velocimetry: a review. *Proceedings of the Institution of Mechanical Engineers: Journal of Mechanical Engineering Science*, 211:55–76, 1997.

[122] X. Cao, J. Liu, N. Jiang, and Q. Chen. Particle image velocimetry measurement of indoor airflow field: A review of the technologies and applications. *Energy and Buildings*, 69:367–380, 2014.

[123] R.J. Bomphrey. Insects in flight: Direct visualization and flow measurements. *Bioinspiration and Biomimetics*, 1(4):1–9, 2006.

[124] T. Steinmann, J. Casas, G.J.M. Krijnen, and O. Dangles. Air-flow sensitive hairs: Boundary layers in oscillatory flows around arthropod appendages. *The Journal of Experimental Biology*, 209(21):4398–4408, 2006.

[125] J. Casas, T. Steinmann, and O. Dangles. The aerodynamic signature of running spiders. *PLoS ONE*, 3(5):3–8, 2008.

[126] P. Henningsson, D. Michaelis, T. Nakata, D. Schanz, R. Geisler, A. Schröder, and R.J. Bomphrey. The complex aerodynamic foot print of desert locusts revealed by large-volume tomographic particle image velocimetry. *Journal of the Royal Society Interface*, 12(108):1–11, 2015.

[127] T. Steinmann, J. Casas, P. Braud, and L. David. Tomo-PTV measurement of a drop impact at air-water interface. In *Proceeding of the13th International Symposium on Particle Image Velocimetry*, 2019.

[128] J.R. Welty, G.L. Rorrer, and D.G. Foster. *Fundamentals of momemtum, heat, and mass transfer*. Wiley, 6th edition, 2014.

[129] F.G. Howarth. Cave insects. In V.H. Resh and R.T. Cardé, editors, *Encyclopedia of insects (Second edition)*, pages 139 – 143. Academic Press, 2009.

[130] K.I. Jönsson, E. Rabbow, R.O. Schill, M. Harms-Ringdahl, and P. Rettberg. Tardigrades survive exposure to space in low Earth orbit. *Current Biology*, 18(17):729–731, 2008.

[131] J.F.V. Vincent and U.G.K. Wegst. Design and mechanical properties of insect cuticle. *Arthropod Structure and Development*, 33(3):187–199, 2004.

[132] S.N. Gorb. Insect-Inspired Technologies: Insects as a Source for Biomimetics. In A Vilcinskas, editor, *Insect Biotechnology*, pages 241–264. Springer, 2011.

[133] A. Dijkshoorn, P. Werkman, M. Welleweerd, G. Wolterink, B. Eijking, J. Delamare, R. Sanders, and G.J.M. Krijnen. Embedded sensing: Integrating sensors in 3-D printed structures. *Journal of Sensors and Sensor Systems*, 7(1):169–181, 2018.

[134] A. Anastasiou, C. Tsirmpas, A. Rompas, K. Giokas, and D. Koutsouris. 3D Printing: Basic concepts Mathematics and Technologies. In *IEEE 13th International Conference on Bioinformatics and Bioengineering*, http://dx.doi.org/10.1109/BIBE.2013.6701672, 2013.

[135] W. Gao, Y. Zhang, D. Ramanujan, K. Ramani, Y. Chen, C.B. Williams, C.C.L. Wang, Y.C. Shin, S. Zhang, and P.D. Zavattieri. The status, challenges, and future of additive manufacturing in engineering. *Computer Aided Design*, 69:65–89, 2015.

[136] J. Jin and Y. Chen. Highly removable water support for Stereolithography. *Journal of Manufacturing Processes*, 28:541–549, 2017.

[137] D. Espalin, J. Ramirez, F. Medina, and R. Wicker. Multi-Material, Multi-Technology FDM System. *Rapid Prototyping Journal*, 20(3):236–244, 2014.

[138] L. Mogas-Soldevila and N. Oxman. Water-based Engineering & Fabrication: Large-Scale Additive Manufacturing of Biomaterials. *Materials Research Society Proceedings*, 1800:1–6, 2015.

[139] P. Sitthi-Amorn, J.E. Ramos, Y. Wang, J. Kwan, J. Lan, W. Wang, and W. Matusik. MultiFab : a machine vision assisted platform for multi- material 3D printing. *ACM Transactions on Graphics (TOG)*, 34(4):129, 2015.

[140] K. Rajan, I. Roppolo, A. Chiappone, S. Bocchini, D. Perrone, and A. Chiolerio. Silver nanoparticle ink technology: state of the art. *Nanotechnology, Science and Applications*, 9:1–13, 2016.

[141] R.L. Truby and J.A. Lewis. Printing soft matter in three dimensions. *Nature*, 540(7633):371–378, 2016.

[142] C. Lee and J.A. Tarbutton. Electric poling-assisted additive manufacturing process for PVDF polymer-based piezoelectric device applications. *Smart Materials and Structures*, 23(9), 2014.

[143] M. Vaezi, S. Chianrabutra, B. Mellor, and S. Yang. Multiple material additive manufacturing - Part 1: a review. *Virtual and physical prototyping*, 8(1):19 – 50, 2013.

[144] G. Pohl and W. Nachtigall. Spider Webs : Tent Roofs. In *Biomimetics for Architecture & Design : Nature-Analogies-Technology*, chapter 5.7.2, pages 173 – 175. Springer, 2015.

[145] U.G K Wegst and M.F. Ashby. The mechanical efficiency of natural materials. *Philosophical Magazine*, 84(21):2167–2181, 2004.

[146] U.G.K. Wegst, H. Bai, E. Saiz, A.P. Tomsia, and R.O. Ritchie. Bioinspired structural materials. *Nature Materials*, 14(1):23–36, 2015.

[147] X. Liu, H. Gu, M. Wang, X. Du, B. Gao, A. Elbaz, L. Sun, J. Liao, P. Xiao, and Z. Gu. 3D Printing of Bioinspired Liquid Superrepellent Structures. *Advanced Materials*, 30(22), 2018.

[148] B.G. Compton and J.A. Lewis. 3D-printing of lightweight cellular composites. *Advanced Materials*, 26(34):5930–5935, 2014.

[149] N. Du, X.Y. Liu, J. Narayanan, L. Li, M. Lek Min Lim, and D. Li. Design of superior spider silk: From nanostructure to mechanical properties. *Biophysical Journal*, 91(12):4528–4535, 2006.

[150] C. Mandrycky, Z. Wang, K. Kim, and D.H. Kim. 3D bioprinting for engineering complex tissues. *Biotechnology Advances*, 34(4):422–434, 2016.

[151] E. Desimone, K. Schacht, T. Jüngst, J. Groll, and T. Scheibel. Biofabrication of 3D constructs: fabrication technologies and spider silk proteins as bioinks. *Pure and applied chemistry*, 87(8):737 – 749, 2015.

[152] V. Dikshit, N.A. Prasanth, J.D. Kumar, Y.L. Yap, and W.Y. Yeong. Investigation of quasi static indentation on 3D printed honeycomb based truncated-pyramid square structure. In *Proceedings of the 2nd International Conference on Progress in Additive Manufacturing*, pages 116–121, 2016.

[153] S.D. Gittard, R.J. Narayan, A. Ovsianikov, and B.N. Chichkov. Rapid Prototyping of Biomimetic Structures: Fabrication of Mosquito-like Microneedles by Two-Photon Polymerization. In *Materials Research Society Proceedings V1239*, pages VV01–11, 2010.

[154] A. Zolfagharian, A.Z. Kouzani, S.Y. Khoo, A.A.A. Moghadam, I. Gibson, and A. Kaynak. Evolution of 3D printed soft actuators. *Sensors and Actuators, A: Physical*, 250:258–272, 2016.

[155] M. Schaffner, J.A. Faber, L. Pianegonda, P.A. Rühs, F. Coulter, and A.R. Studart. 3D printing of robotic soft actuators with programmable bioinspired architectures. *Nature Communications*, 9(1):878, 2018.

[156] J.G. Cham, S.A. Bailey, J.E. Clark, R.J. Full, and M.R. Cutkosky. Fast and Robust: Hexapedal Robots via Shape Deposition Manufacturing. *The International Journal of Robotics Research*, 21(10-11):869–882, 2002.

[157] J. Aguilar, T. Zhang, F. Qian, M. Kingsbury, B. McInroe, N. Mazouchova, C. Li, R. Maladen, C. Gong, M. Travers, R.L. Hatton, H. Choset, P.B. Umbanhowar, and D.I. Goldman. A review on locomotion robophysics: The study of movement at the intersection of robotics, soft matter and dynamical systems. *Reports on Progress in Physics*, 79(11):110001, 2016.

[158] F. Li, W. Liu, Xi. Fu, G. Bonsignori, U. Scarfogliero, C. Stefanini, and P. Dario. Jumping like an insect: Design and dynamic optimization of a jumping mini robot based on bio-mimetic inspiration. *Mechatronics*, 22(2):167–176, 2012.

[159] H.T. Lin, G.G. Leisk, and B.A. Trimmer. GoQBot: A caterpillar-inspired soft-bodied rolling robot. *Bioinspiration and Biomimetics*, 6(2), 2011.

[160] T. Umedachi, V. Vikas, and B.A. Trimmer. Softworms: The design and control of non-pneumatic, 3D-printed, deformable robots. *Bioinspiration and Biomimetics*, 11(2):0, 2016.

[161] S.A. Bailey, J.G. Cham, M.R. Cutkosky, and R.J. Full. Biomimetic Robotic Mechanisms via Shape Deposition Manufacturing. In *International Symposium on Robotics Research*, pages 321–327, Snowbird,Utah, 1999.

[162] R.R. Ma, J.T. Belter, and A.M. Dollar. Hybrid Deposition Manufacturing: Design Strategies for Multimaterial Mechanisms Via Three-Dimensional Printing and Material Deposition. *Journal of Mechanisms and Robotics*, 7(2):021002, 2015.

[163] T.A. Ward, M. Rezadad, C.J. Fearday, and R. Viyapuri. A Review of Biomimetic Air Vehicle Research: 1984-2014. *International Journal of Micro Air Vehicles*, 7(3):375–394, 2015.

[164] H. Liu, S. Ravi, D. Kolomenskiy, and H. Tanaka. Biomechanics and biomimetics in insect-inspired flight systems. *Philosophical Transactions of the Royal Society B*, 371(1704):20150390, 2016.

[165] P. Gopalakrishnan and D.K. Tafti. Effect of Wing Flexibility on Lift and Thrust Production in Flapping Flight. *AIAA Journal*, 48(5):865–877, 2010.

[166] K.C. Moses, S.C. Michaels, M. Willis, and R.D. Quinn. Artificial Manduca sexta forewings for flapping-wing micro aerial vehicles: How wing structure affects performance. *Bioinspiration and Biomimetics*, 12(5):aa7ea3, 2017.

[167] E. Salami, P.B. Ganesan, T.A. Ward, R. Viyapuri, and F.I. Romli. Design and mechanical analysis of a 3D-printed biodegradable biomimetic micro air vehicle wing. *IOP Conference Series: Materials Science and Engineering*, 152(1), 2016.

[168] R. Niiyama, Y. Kawahara, and Y. Kuniyoshi. Multimaterial 3D Reconstruction of Beetle Flapping-Wing Mechanisms. In *8th International Symposium on Adaptative Motion of Animals and Machines*, pages 48–49, 2017.

[169] L.J. Burton, N. Cheng, C. Vega, J. Andrés, and J.W.M. Bush. Biomimicry and the culinary arts. *Bioinspiration and Biomimetics*, 8(4), 2013.

[170] G.J.M. Krijnen and R.G.P. Sanders. Recent Developments in Bio-Inspired Sensors Fabricated by Additive Manufacturing Technologies. *Advances in Science and Technology*, 100:197–206, 2016.

[171] T.L. Spencer, N. Lavrik, and D.L. Hu. Synthetic moth antennae fabricated as preconcentrator for odor collection. In *ISOEN 2017 - ISOCS/IEEE International Symposium on Olfaction and Electronic Nose*, pages 1–3, 2017.

[172] Y.M. Song, Y. Xie, V. Malyarchuk, J. Xiao, I. Jung, K.J. Choi, Z. Liu, H. Park, C. Lu, R.H. Kim, R. Li, K.B. Crozier, Y. Huang, and J.A. Rogers. Digital cameras with designs inspired by the arthropod eye. *Nature*, 497(7447):95–99, 2013.

[173] S. Juodkazis. Manufacturing: 3D printed micro-optics. *Nature Photonics*, 10(8):499–501, 2016.

[174] J. Luo, Y. Guo, and X. Wang. Rapid fabrication of curved microlens array using the 3D printing mold. *Optik*, 156:556–563, 2018.

[175] D. Gu. Materials creation adds new dimensions to 3D printing. *Science Bulletin*, 61(22):1718–1722, 2016.

[176] R. Domingo-Roca, B. Tiller, J.C. Jackson, and J.F.C. Windmill. Bio-inspired 3D-printed piezoelectric device for acoustic frequency selection. *Sensors and Actuators, A: Physical*, 271:1–8, 2018.

[177] B. Kwak and J. Bae. Design of hair-like appendages and comparative analysis on their coordination toward steady and efficient swimming. *Bioinspiration and Biomimetics*, 12(3), 2017.

[178] E.O. Campos. *Plant-Pollinator Interactions in an Ecological and Evolutionary Context: The Promising Role of 3D-Printing Technology and Mathematical Modeling*. PhD thesis, University of Washington, 2017.

[179] M.J. Domingue, D.P. Pulsifer, M.S. Narkhede, L.G. Engel, R.J. Martín-Palma, J. Kumar, T.C. Baker, and A. Lakhtakia. Fine-scale features on bioreplicated decoys of the emerald ash borer provide necessary visual verisimilitude. In *Bioinspiration, Biomimetics and Bioreplication 2014*, volume 9055, page 905507. International Society for Optics and Photonics, 2014.

[180] F. Momeni, S.M. Mehdi Hassani.N, X. Liu, and J. Ni. A review of 4D printing. *Materials and Design*, 122:42–79, 2017.

[181] A. Sydney Gladman, E.A. Matsumoto, R.G. Nuzzo, L. Mahadevan, and Jennifer A. Lewis. Biomimetic 4D printing. *Nature Materials*, 15(4):413–418, 2016.

[182] J.M. Gere and B.J. Goodno. *Mechanics of materials*. Cengage Learning, seventh edition, 2009.

[183] R.T. Cardé and T.C. Baker. Sexual communication with pheromones. In William J Bell and Ring T Cardé, editors, *Chemical ecology of insects*, pages 355 – 383. Springer US, 1984.

[184] A.G. Mayer. On the Mating Instinct in Moths. *Psyche*, 9:15–20, 1900.

[185] M.A.R. Koehl. Small-scale fluid dynamics of olfactory antennae. *Marine and Freshwater Behaviour and Physiology*, 27(2-3):127–141, 1996.

[186] C. Cummins, M. Seale, A. Macente, D. Certini, E. Mastropaolo, I.M. Viola, and N. Nakayama. A separated vortex ring underlies the flight of the dandelion. *Nature*, 562(7727):414–418, 2018.

[187] A.Y.L. Cheer and M.A.R. Koehl. Paddles and rakes: Fluid flow through bristled appendages of small organisms. *Journal of Theoretical Biology*, 129(1):17–39, nov 1987.

[188] K.-E. Kaissling. The sensivity of the insect nose: the example of Bombyx mori. In A Gutiérrez and S Marco, editors, *Biologically Inspired Signal Processing for Chemical Sensing*, chapter 3, pages 45–52. Springer, Berlin, Heidelberg, 2009.

[189] C. Loudon and E.C. Davis. Divergence of streamlines approaching a pectinate insect antenna: Consequences for chemoreception. *Journal of Chemical Ecology*, 31(1):1–13, 2005.

[190] J. Casas, T. Steinmann, and G.J.M. Krijnen. Why do insects have such a high density of flow-sensing hairs? Insights from the hydromechanics of biomimetic MEMS sensors. *Journal of the Royal Society Interface*, 7(51):1487–1495, 2010.

[191] M.H. Dickinson, F.-O. Lehmann, and S.P. Sane. Wing rotation and the aerodynamic basis of insect right. *Science*, 284(5422):1954–1960, 1999.

[192] L.D. Waldrop and M.A.R. Koehl. Do terrestrial hermit crabs sniff? Air flow and odorant capture by flicking antennules. *Journal of the Royal Society, Interface*, 13(114):20150850, jan 2016.

[193] M. Jaffar-Bandjee, J. Casas, and G.J.M. Krijnen. Additive manufacturing: state of the art and potential for insect science. *Current Opinion in Insect Science*, 30(October):79–85, 2018.

[194] R. Byron Bird, W.E. Stewart, and E.N. Lightfoot. *Transport phenomena*. Wiley, 2nd edition, 2002.

[195] Stratasys. https://www.stratasys.com/3d-printers/objet260-connex3, 2019.

[196] Openscad. https://www.openscad.org/, 2015.

[197] R.J. Adrian. Particle-imaging techniques for experimental fluid mechanics. *Annual Reviews of Fluid Mechanics*, 23:261–304, 1991.

[198] R.D. Keane and R.J. Adrian. Theory of cross-correlation analysis of PIV images. *Applied Scientific Research*, 49(3):191–215, 1992.

[199] J.A. Goldman and M.A.R. Koehl. Fluid Dynamic Design of Lobster Olfactory Organs: High Speed Kinematic Analysis of Antennule Flicking by Panulirus argus. *Chemical Senses*, 26(4):385–398, 2001.

[200] M.A. Reidenbach, N. George, and M.A.R. Koehl. Antennule morphology and flicking kinematics facilitate odor sampling by the spiny lobster, Panulirus argus. *Journal of Experimental Biology*, 211(17):2849–2858, 2008.

[201] L.D. Waldrop, Y. He, and S. Khatri. What Can Computational Modeling Tell Us about the Diversity of Odor-Capture Structures in the Pancrustacea? *Journal of Chemical Ecology*, 44(12):1084–1100, 2018.

[202] T.L. Spencer, N. Mohebbi, G. Jin, M.L. Forister, A. Alexeev, and D.L. Hu. Moth-inspired methods for particle capture on a cylinder. *In press.*

[203] T.C. Baker and R.G. Vogt. Measured behavioural latency in response to sex-pheromone loss in the large silk moth Antheraea polyphemus. *Journal of Experimental Biology*, 38:29–38, 1988.

[204] J.R. Barber, B.C. Leavell, A.L. Keener, J.W. Breinholt, B.A. Chadwell, C.J.W. McClure, G.M. Hill, and A.Y. Kawahara. Moth tails divert bat attack: Evolution of acoustic deflection. *Proceedings of the National Academy of Sciences*, 112(9):2812–2816, 2015.

[205] J. Boeckh, K.-E. Kaissling, and D. Schneider. Sensillen und Bau der Antennengeißel von Telea polyphemus. *Zoologische Jahrbücher/Abteilung für Anatomie und Ontogenie der Tiere*, 78:559–584, 1960.

[206] R.C. Schuech, M.T. Stacey, M.F. Barad, and M.A.R. Koehl. Numerical simulations of odorant detection by biologically inspired sensor arrays. *Bioinspiration and Biomimetics*, 7(1), 2012.

[207] O. Miyatake and H. Iwashita. Laminar-flow heat transfer to a fluid flowing axially between cylinders with a uniform surface temperature. *International Journal of Heat and Mass Transfer*, 33(3):417–425, 1990.

[208] T. Alam, Yi. Zhao, and P.S. Takhar. Water and oil permeability of poroelastic potato discs. *International Journal of Food Properties*, 20(3):633–644, 2017.

[209] A.A. Gubaidullin, A.S. Gubkin, D.E. Igoshin, and P.A. Ignatev. Permeability of model porous medium formed by random discs. *AIP Conference Proceedings*, 1939(March), 2018.

[210] J. Murlis and C.D. Jones. Fine–scale structure of odour plumes in relation to insect orientation to distant pheromone and other attractant sources. *Physiological Entomology*, 6(1):71–86, 1981.

[211] D. Schneider and K.-E. Kaissling. Der Bau der Antenne des Seidenspinners Bombyx mori L. III. Das Bindegewebe und das Blutgefäß. *Zoologische Jahrbücher/Abteilung für Anatomie und Ontogenie der Tiere*, 77:111–132, 1959.

[212] R.A. Steinbrecht. Zur morphometrie der antenne des seidenspinners, Bombyx mori L.: Zahl und Verteilung der Riechsensillen (Insecta, Lepidoptera). *Zeitschrift für Morphologie der Tiere*, 68(2):93–126, 1970.

[213] E.M. Sparrow, A.L. Loeffler, and H.A. Hubbard. Heat transfer to longitudinal laminar flow between cylinders. *Journal of heat transfer*, 83(4):415–422, 1961.

[214] H. Sadeghifar, N. Djilali, and M. Bahrami. A compact closed-form Nusselt formula for laminar longitudinal flow between rectangular / square arrays of parallel cylinders with unequal row temperatures. *International Journal of Thermal Sciences*, 100:248–254, 2016.

[215] K.-E. Kaissling. Pheromone Reception in Insects: the example of silk moths. In Carla Mucignat-Caretta, editor, *Neurobiology of chemical communication*, chapter 4, pages 99–146. CRC Press/Taylor & Francis, 2014.

[216] M.J. Tang, M. Shiraiwa, U. Pöschl, R.A. Cox, and M. Kalberer. Compilation and evaluation of gas phase diffusion coefficients of reactive trace gases in the atmosphere: Volume 2. Diffusivities of organic compounds, pressure-normalised mean free paths, and average Knudsen numbers for gas uptake calculations. *Atmospheric Chemistry and Physics*, 15(10):5585–5598, 2015.

[217] Robert C. Reid, J.M. Prausnitz, and Bruce E. Poling. *The properties of gases and liquids*. McGraw-Hill, 1987.

[218] B. Cushman-Roisin. Environmental transport and fate, Chapter 2: Diffusion. *Thayer School of Engineering Dartmouth College, University Lecture*, 2012.

[219] A. Lozano, B. Yip, and R.K. Hanson. Acetone: a tracer for concentration measurements in gaseous flows by planar laser-induced fluorescence. *Experiments in Fluids*, 13(6):369–376, 1992.

[220] J.P. Crimaldi. Planar laser induced fluorescence in aqueous flows. *Experiments in Fluids*, 44(6):851–863, 2008.

[221] L.A. Torres, B.A. Fleck, D.J. Wilson, and D.S. Nobes. Calibration of a planar laser induced fluorescence technique for use in large scale water facilities. *Measurement*, 46(8):2597–2607, 2013.

[222] N.A. Fuchs and I.B. Stechkina. A note on the theory of fibrous aerosol filters. *Annals of Occupational Hygiene*, 6(1):27–30, 1963.

[223] C.W. Oseen. Über die Stokes' sche Formel und über eine verwandte Aufgabe in der Hydrodynamik. *Arkiv för Matematik, Astronomi och Fysik*, 6:1, 1910.

[224] R. Rougerie. *Phylogénie et biogéographie des Saturniinae (Lepidoptera: Bombycoidea, Saturniidae): Approche morphologique et moléculaire*. PhD thesis, Muséum National d'Histoire Naturelle, 2005.

[225] N. R. Silvester. Some hydrodynamic aspects of filter feeding with rectangular-mesh nets. *Journal of Theoretical Biology*, 103(2):265–286, 1983.

[226] S. Kanaujia and K.-E. Kaissling. Interactions of pheromone with moth antennae: Adsorption, desorption and transport. *Journal of Insect Physiology*, 31(1):71–81, 1985.

[227] J. Bau, K.A. Justus, C. Loudon, and R.T. Cardé. Electroantennographic resolution of pulsed pheromone plumes in two species of moths with bipectinate antennae. *Chemical Senses*, 30(9):771–780, 2005.

[228] A.S. Hill, R.W. Rings, S.R. Swier, and W.L. Roelofs. Sex pheromone of the black cutworm moth, Agrotis ipsilon. *Journal of Chemical Ecology*, 5(3):439–457, 1979.

[229] P.S. Callahan. Insect antennae with special reference to the mechanism of scent detection and the evolution of the sensilla. *International Journal of Insect Morphology and Embryology*, 4(5):381–430, 1975.

[230] Q. Wang, Y. Shang, D.S. Hilton, K. Inthavong, D. Zhang, and M.A. Elgar. Antennal scales improve signal detection efficiency in moths. *Proceedings of the Royal Society B*, 285, 2018.

[231] R.W. Mankin and M.S. Mayer. The insect antenna is not a molecular sieve. *Experientia*, 40:1251–1252, 1984.

[232] J. Torréns and J.M. Heraty. Description of the species of dicoelothorax Ashmead (Chalcidoidea, Eucharitidae) and biology of D. platycerus Ashmead. *ZooKeys*, 2012(165):33–46, 2012.

[233] A. Ramsey, T.F. Houston, A.D. Ball, T. Goral, M.V.L. Barclay, and J.P.L. Cox. Towards an Understanding of Molecule Capture by the Antennae of Male Beetles Belonging to the Genus Rhipicera (Coleoptera, Rhipiceridae). *The Anatomical Record*, 298(9):1519–1534, 2015.

[234] M.T. Stacey, K.S. Mead, and M.A.R. Koehl. Molecule capture by olfactory antennules: Mantis shrimp. *Journal of Mathematical Biology*, 44(1):1–30, 2002.

Chapter 8

Abstract

In some moth species, male adults possess pectinate antennae which detect the tiny amounts of sexual pheromones emitted by females. A critical step in the olfaction process is the capture of pheromone molecules which depends heavily on the shape of the antennae. In this work, we investigated whether and how the shape of the pectinate antenna influences its efficiency at capturing pheromone molecules. Pectinate antennae are however complex to study because they are multi-scale objects spanning over four orders of size. In the species *Samia cynthia*, the antenna is 1 cm long whereas the sensilla, which are hair-like structures hosting the detectors, are 150 µm long and only 3 µm thick. To simplify the studies of antenna – air-flow interactions we split them into macro- and microstructure and studied them separately.

In both cases, we used Additive Manufacturing to build artificial scaled up models and Particle Image Velocimetry to determine their respective leakiness, the proportion of air that flows through a permeable object instead of around it, at varying air velocity as encountered by moths in nature. We then adapted a heat transport model to solve the mass transport problem of pheromone capture by the microstructure. We found that the efficiency of the antenna is limited by both the leakiness of the antenna, which increases with air velocity, and the local capture, which is the proportion of molecules captured in the part of the airflow passing through the antenna and which decreases with air velocity. Eventually, the micro-structure does not have a strong maximum efficiency at a specific air velocity but, instead, is moderately efficient over the large range of air velocities encountered by a moth. Using Finite Element Method simulations, we developed a method based on the relation between drag and leakiness to combine the two levels and determine the capture efficiency of the entire antenna. We compared it with cylindrical ones and showed that a pectinate antenna is a good design to increase the surface of the antenna without significantly decreasing the capture efficiency.

Chapitre 9

Abstract in French

Chez certaines espèces de papillons, les mâles adultes possèdent des antennes pectinées leur permettant de détecter d'infimes quantités de phéromones sexuelles émises par les femelles. Une étape critique de ce processus d'olfaction est la capture de molécules de phéromone, qui dépend fortement de la forme des antennes. Dans ce travail, nous avons examiné si et comment la forme des antennes pectinées influait sur leur efficacité à capturer les molécules de phéromone. Les antennes pectinées sont toutefois complexes à étudier car ce sont des objets multi-échelles couvrant quatre ordres de grandeur en terme de taille. Chez l'espèce *Samia cynthia*, l'antenne a une longueur de 1 cm, tandis que les sensilles, structures ressemblant à des poils et abritant les détecteurs, ont une longueur de 150 µm et seulement 3 µm d'épaisseur. Pour simplifier l'étude des interactions antenne-écoulement, nous les avons scindées en macro et microstructures et nous les avons étudiées séparément.

Dans les deux cas, nous avons utilisé l'Impression 3D pour construire des modèles artificiels à plus grande échelle et la Vélocimétrie par Image de Particules pour déterminer leurs perméabilités respectives, c'est-à-dire la proportion d'air traversant un objet perméable au lieu de le contourner, à des vitesses variables rencontrées par les papillons dans la nature. Nous avons ensuite adapté un modèle de transport de chaleur pour résoudre le problème du transport de masse lié à la capture de phéromone par la microstructure. Nous avons constaté que l'efficacité de l'antenne est limitée à la fois par la perméabilité de l'antenne, qui augmente avec la vitesse de l'air, et par la capture locale, qui est la proportion de molécules capturées dans la partie du flux d'air traversant l'antenne et qui diminue avec vitesse de l'air. Finalement, la microstructure n'a pas une efficacité maximale élevée à une vitesse d'air donnée mais plutôt une efficacité moyenne sur la vaste plage de vitesses d'air rencontrées par un papillon. En utilisant des simulations par Eléments Finis, nous avons développé une méthode basée sur la relation entre la traînée et la perméabilité pour combiner les deux niveaux et déterminer l'efficacité de capture de toute l'antenne. Nous l'avons comparée à des antennes cylindriques et avons montré qu'une antenne pectinée était un bon design pour augmenter la

surface de l'antenne sans réduire de manière significative l'efficacité de capture.

Chapter 10

Abstract in Dutch

Mannelijke volwassenen van sommige nachtvlindersoorten hebben pectinaatantennes, die de kleine hoeveelheden seksuele feromonen detecteren, die door de vrouwelijke nachtvlinders worden uitgezonden. Een cruciale stap in het reukproces is het vangen van feromoonmoleculen, het succes daarvan is sterk afhankelijk zijn van de vorm van de antennes. In dit werk hebben we onderzocht of en hoe de vorm van de pectinaatantenne de efficiëntie van het vangen van feromoonmoleculen beïnvloedt. Pectinate-antennes zijn echter moeilijk te bestuderen omdat ze zijn obgebouwd uit objecten van verschillende grote, die meer dan vier verschilledne ordergrootte in lengte beslaan. In de soort *Samia cynthia* is de antenne 1 cm lang, terwijl de sensilla, haarachtige structuren die de detectoren hosten, 150 µm lang zijn en slechts 3 µm dik. Om de studies van antenne - luchtstroom interacties te vereenvoudigen, hebben we ze opgesplitst in macro- en microstructuren en apart bestudeerd.

In beide gevallen hebben we Additive Manufacturing gebruikt om kunstmatige schaalmodellen te bouwen. Daarnaast hebben we Particle Image Velocimetry gebruikt om hun respectieve lek, het deel van de lucht dat door een permeabel object stroomt in plaats van eromheen, te bepalen bij verschillende luchtsnelheden, zoals de nachtvlinders deze ook in de natuur ervaren. Vervolgens hebben we een warmtetransportmodel aangepast om het probleem van het massatransport, van de feromonen door de microstructuur, op te lossen. Aan de hand van deze metingen kunne we concluderen dat de efficiëntie van de antenne wordt beperkt door zowel het lek van de antenne, die toeneemt met de luchtsnelheid, als de lokale afvang, wat het percentage van de moleculen is dat wordt gevangen in het deel van de luchtstroom dat door de antenne gaat en dat afneemt met luchtsnelheid. De microstructuur heeft geen maximale efficiëntie bij een specifieke luchtsnelheid, maar is in plaats daarvan matig efficiënt over een groot bereik aan luchtsnelheden. Met behulp van Finite Element Method-simulaties hebben we een methode ontwikkeld op basis van de relatie tussen weerstand en lek om de twee niveaus te combineren en de opname-efficiëntie van de gehele antenne te bepalen. We vergeleken het met

cilindrische antenne en toonden aan dat een pectinaatantenne een goed ontwerp is om het oppervlak van de antenne te vergroten zonder de opname-efficiëntie aanzienlijk te verminderen.

Chapter 11

Acknowledgments

Jérôme, thank you very much for everything you have done for me. First of all, you gave me a chance to apply for your PhD position as I was wandering across the world, in the countryside of Japan. I didn't know anything about you or your lab before starting my PhD and I am happy that you happened to be my supervisor. More importantly, you showed me the value of my work when I could not see it. I might have been a weird PhD student for you but, eventually, we managed to understand and adapt to each other.

Gijs, thank you too. I enjoyed having your alternative point of view on my work. Thanks for sharing with **Jérôme** and me the highs and lows of a joint PhD and for giving me the opportunity to experience the Dutch way of life. I also arrived in your lab without any prior knowledge about you or even your university and, once again, I was positively surprised. In your lab especially, I learned to be more autonomous so thank you for this precious teaching.

Thomas, had you not been here, I don't know how I would have done my PIV experiments. It was also nice to have someone to talk to about vortices and more general physics problem. I'll always remember your nice words shouted from your office. I must also thank you and **Miguel** for the help in the last moments of my PhD.

Thank you **Remco** for helping me with the SEM and many other things. I'm also grateful to **Sander** and **Gerben** who helped me to print my antennae.

Of course, this thesis has been successfully completed thanks to the help of many other people. I would like to thank **Huib Vanvossen** for having tried a few times to print my antennae with the Nanoscribe. Thank you, **Marc Ankone**, for attempting to scan my antenna with the microCT. Many thanks to **Chee Kent Young** for spending some much time printing some cylinders for me on the Miicraft. I would also like to thank **Magaly Caravanier** and **Bénédicte**

Montigny for letting me use their rolling-ball viscometer to measure accurately the kinematic viscosity of my rapeseed oil. **Rodolphe Rougerie**, thank you for having allowed me to explore the Saturniidae collection of the National Museum of Natural History. Seeing so many designs of pectinate antennae gave me some insights on which characteristics should be important from a physical point of view. I must not forget **Henk-Willem Veltkamp** who gave me some tips to improve my Comsol models and who shared his powerful computer with me. Last, I would like to thank **Rustem Uzbekov** for spending some time on my antenna samples to fix and slice them to perform some Transmission Electron Microscopy.

I give big thanks to all the senior researchers who spent some of their precious time to discuss my problems: prof. **Christelle Suppo**, dr. **Stephen Foster**, prof. **Stefan Luding**, prof. **Theo van deer Meer** and dr. **Hanneke Gelderblom**.

Doing a joint PhD also implies to have more paperwork and to be aware of the administrative procedures of both universities. Thus, I must sincerely thank **Sylvie Lot**, **Nathalie Duchesne**, **Marjorie Tolmont** and **Aïcha Belloufi** on the French side, and **Susan Godschalk** and **Jolanda Boelema-Kaufmann** on the Dutch side. I was sometimes late in my administrative documents but I always found patient people happy at helping me to solve my never-ending problems. I should also mention **Claire Durand** and **Elisabeth Huguet** for their help with the administrative documents related to my Erasmus grants.

I would like to thank the people from the IRBI where I enjoyed a nice working atmosphere. I'm grateful to **Carole**, **Simon**, **Guy** and **Fabrice** for the help when I was rearing moths or doing my experiments. I would also like to thank the group of PhDs and post-docs of the lab: thanks to **Florent** for hosting me in your flat and for the nice trip in Lyon, to **Caro** for the breakfasts we had together, to **Antoine** for the nice discussions but also for the trip we made together in the Netherlands, to **Aurélia** for showing me a gravid pond turtle and many snakes, to **Sophie** for the climbing sessions, to **Lucas** for the time we spent in Rennes at the SFEE conference and for showing me nice TV shows, to **Anthony**, you told me that *L'Attaque des titans* was a nice manga, *c'est pas faux !*, to **Fanny** for showing me that eating oak acorns is not so weird, to **Lorène**, I hope next time we'll find more chestnuts and mushrooms, to **Cristela** and **Diane** for the nice time in Copenhagen, to **Vanessa** for your touchiness about Southern France matters (I hope to show you one day what the real South is), to **Beatriz** and her weird kitty, to **Marie-Anne**, I'm still hoping one day we'll climb together, to **Manon** for all the times you made me laugh, to **Thomas** for bringing me to Terres du son and to many others, among them **Alexandra**, **Anna**, **Paul**, **Sophie**, **Ludovic**, **Julien**, **Guillaume** and **Lou**. In a more general way, thank you to the many people of the lab with whom I had nice interactions.

I must also thank the people from my second lab, the RAM group. Thank you all for welcoming me in your group, for the Friday drinks, the badminton sessions, the video games and the dinners. Thanks to **Frieda**, **Maaike**, **Haye**,

Vincent, **Stefan**, **Françoise**, **Gerjan**, **Marcel**, **Rob**, **Hengameh**, **Nicolò**, **Momen**, **Leon**, **Astrid**, **Esther** and, once again, **Jolanda**.

Florence, I own you so much. You were the first person to give me a chance to do some research in ecology despite my background in physics and mathematics. I also deeply enjoyed the time spent at the research station of Foljuif. Thank you for everything!

The first time I have ever climbed was with you, **Suzanne**, and, since then, I haven't stopped. So thank you for sharing with me one of your passions and I hope one day we meet again to climb a big wall together! Because of you, the first thing I did when I began my PhD was to join the French Alpine Club of Tours. I thank them very much for all the good time I spent there and the patience they had for teaching me how to climb better. In this regard, I deeply thank **Jérôme** and **Cyrille**. But I don't forget all the others: **Henri**, **Léna**, **Kanav**, **Justine**, **Laurent**, **Natacha**, **Greg** and **Laeticia**, **Stephen**, **Xavier**, **Christophe**, **Samuel**, **Dominique**, **Benjamin**, **Jérôme**, **Hélène**, **Pascal**, **François**, **Frédéric**, **Sébastien**, **Sabine**, **Joffrey**, **Sylvain** and many others.

Your wooden house is wonderful, **Jelle**, and I keep talking about it to my friends. I felt very calm and peaceful there and it is indeed a perfect place to teach taiqi and qigong. Many thanks to you and **Paul** for the good time we had together.

Inès, we have been neighbors for almost three years but we met only one month before I moved out, a day when you were practicing the trombone and I was curious about it. Please, next time, try to practice a bit more often! Anyway, thank you for pulling me back in the magic world of brass bands. It was a huge pleasure to play again some music. And thank you and **Chloé** for all the meals we shared!

Talking about music, I would like to thank the **Kakel** group. We don't meet very often but it is always a great pleasure to see you again, guys!

Josh, we may have lived together only three months but I have good remembrance of all our discussions. You definitely changed my mind about your home country and I hope to visit it one day. Anyway, thank you very much for your time used to print my antennae, it was a great help! Thanks also to the other members of the Jungle, namely, **Guido** and **Michaela**, **Jorien**, and **Bahruz**.

You have been such a support for me, **Lucille**, especially in the Netherlands, and you may not even have known it! It was always a great pleasure to visit you in Wageningen or in Plymouth. Your home was like a familiar place where I could relax and read interesting comics! By the way, I must also thank **Marta** for allowing me in your sharehouse.

Yolain, we met randomly and, as *le hasard fait bien les choses*, we lived together as housemates for almost the next four years! I am glad to have seen the evolution of your farming project and happy that now you seem to have found a good balance in your life. It was good to see you doing your best and putting so much effort, despite all the difficulties, in what you believe will make a better future for all and special thanks to **Maman Yolain** and **Tata**! Many thanks also to your friends who shared our house: **Ilham**, **Aurore**, **Claire**, **Lorie**, **Sarah**, **Elodie**, **Aurélie 1** and **2**, **Agathe**, **Fanny**, **Cachou**, **Mathilde** and **Mathilde**, **Lucie**, **Anaïs** and **Caroline**.

Of course, I have to thank my family. **Papa**, **Maman**, **Tannvir** and **Myriam**, you may not understand why I did a PhD and what I will do afterwards but I don't have all the answers either. Anyway, you always supported me in my studies and in my more personal projects and I am happy to know that I can always rely on you. And thanks for hiking with me all across the world.

Thanks to all of you !

Chapter 12

About the author



Mourad Alexandre Jaffar-Bandjee was born in Lyon, France, on January 15th 1990. At the age of four, Mourad and his family moved to Reunion Island and settled in Saint-Denis de la Réunion. There, he grew up (with his two sisters) surrounded by the Indian Ocean and the great volcanoes of the island and discovered the joys of hiking.

After graduating from the high school lycée Leconte de Lisle in 2007, he had the opportunity to move in the heart of Paris, in the Quartier Latin, to study physics and mathematics (MPSI/MP) in the preparatory school (CPGE) Louis-le-Grand. After a national exam, Mourad entered in the Ecole d'ingénieur (College of Engineering) Ecole Centrale Paris (now renamed CentraleSupélec).

During this Engineering Master program, he decided to take a gap year and experienced research in ecology at the laboratory Ecologie, Systématique, Evolution of the University Paris-Sud where he worked on the influence of waves on the community of microalgae in shallow lakes. Back to Ecole Centrale Paris, he completed a joint Master degree in theoretical ecology with the University Paris-Sud co-directed by the University Paris VII (now renamed Sorbonne Université), AgroParisTech, the Ecole Normale Supérieur de Paris and the Muséum National d'Histoire Naturelle. He also had the wonderful opportunity of doing his Master thesis in Australia at

the Fenner School of Environment and Society (the Australian National University) where he studied how disturbance influences the genetic diversity within a population by developing a theoretical model.

After hesitating between Ecology and Biophysics, Mourad began and completed his joint PhD at the University of Tours (Institut de Recherche sur la Biologie de l'Insecte) and the University of Twente (Department of robotics and Mechatronics) where he studied how the shape of pectinate antennae of moths influence the flux of air in order to capture more pheromone molecules.

Missing outdoors activities, he also took the opportunity of living in the two flattest places he had ever been (Tours and the Netherlands) to join the French Alpine Club and start climbing.

Mourad JAFFAR-BANDJEE

Transport de phéromone au sein des antennes pectinées multi-échelles

Résumé

Chez de nombreuses espèces de papillons, les adultes mâles possèdent des antennes pectinées leur permettant de sentir les phéromones sexuelles émises par les femelles. La capture des molécules de phéromone est une étape critique qui dépend étroitement de la forme de l'antenne. Cependant, les antennes pectinées sont des objets multi-échelles dont les différents éléments couvrent quatre ordres de grandeur. Nous avons travaillé sur Samia cynthia et décomposé son antenne en deux niveaux, la macro- et la microstructure. Dans les deux cas, nous avons construits des modèles artificiels à plus grande échelle par impression 3D et avons utilisé la Vélocimétrie par Image de Particules pour déterminer leur perméabilité, une mesure du flux passant à travers un objet. Nous avons adapté un modèle de transfert de chaleur au transfert de masse des phéromones sur la microstructure. Par simulations FEM, nous avons combiné les deux échelles pour déterminer l'efficacité de capture de l'antenne entière. Une comparaison avec une antenne cylindrique nous a montré que l'antenne pectinée est un bon design pour augmenter la surface de contact sans trop diminuer l'efficacité de capture.

Mots-clés : Olfaction, Antenne, Dynamique des fluides, Phéromone

Résumé en anglais

In some moth species, male adults possess pectinate antennae which detect sexual pheromones emitted by females. A critical step in the olfaction process is the capture of pheromone molecules which depends heavily on the shape of the antenna. Pectinate antennae are however difficult to study because they are multi-scale objects spanning over four orders of sizes, depending on the structural elements. We focused on the species Samia cynthia and split its antenna in two levels, the macro- and the microstructures, and studied them separately. In both cases, we used Additive Manufacturing to build artificial scaled up models and Particle Image Velocimetry to determine their respective leakiness, the proportion of flow passing through, instead of around, an object. We then adapted a heat transport model to calculate the mass transport problem of pheromone capture by the microstructure. Using FEM simulations, we combined the two levels and determine the capture efficiency of the entire antenna. We compared it with a cylindrical one and showed that a pectinate antenna is a good design to increase the surface of the antenna without decreasing too much the capture efficiency.

Key words : Olfaction, Antenna, Fluid dynamics, Pheromone